OBSERVATIONS AND MODELING OF THE GAS
DYNAMICS OF THE BARRED SPIRAL GALAXY NGC 7479

By

SEPPO JALMARI LAINE

A DISSERTATION PRESENTED TO THE GRADUATE SCHOOL
OF THE UNIVERSITY OF FLORIDA IN PARTIAL FULFILLMENT
OF THE REQUIREMENTS FOR THE DEGREE OF
DOCTOR OF PHILOSOPHY

UNIVERSITY OF FLORIDA

1996

To my wonderful parents
Raimo and Ritva Laine.

TABLE OF CONTENTS

LIST OF TABLES

LIST OF FIGURES

OBSERVATIONS AND MODELING OF THE GAS
DYNAMICS OF THE BARRED SPIRAL GALAXY NGC 7479

By

SEPPO JALMARI LAINE

December, 1996

Chairman: Stephen T. Gottesman
Major Department: Astronomy

The structure, gas kinematics and dynamics of the barred spiral galaxy NGC 7479 have been investigated in this dissertation. The central, bar-dominated region contains little atomic gas. The atomic gas is circularly rotating within the main disk, except on the strong, dominant spiral arm. The gaseous arm is inclined to the main plane of the galaxy. Numerical models suggest that the warped arm is related to a tidal distortion by a recent minor satellite merger. The nucleus is a radio continuum point source. Outside the nucleus, the radio continuum follows the bar dust lanes. There are also anomalous regions of radio continuum emission just outside the bar. The molecular gas is strongly concentrated in the nucleus and along the bar dust lanes that lead the stellar bar in rotation. The gas in the bar is radially streaming along the bar. A fast-rotating molecular disk has been found in the nucleus. The molecular gas along the bar coincides spatially with ionized hydrogen emission and the bar dust lanes. The optical and near-infrared images show a very asymmetric spiral arm structure. The western arm is much better organized than the spiral structure on the eastern side. Peculiar dust lanes cross the bar. Self-

consistent N-body simulations reproduced the observed asymmetric spiral arm structure and the long bar when a small satellite, near the plane of the disk, was allowed to merge with the main galaxy. Comparison of the gas flow between the observations and a model employing an observationally derived external potential demonstrates that the corotation radius is at 1.1 times the radial length of the bar.

CHAPTER 1
INTRODUCTION

Nature and Scope of the Problem

The objective of this dissertation is to understand the physical processes that drive and maintain the structure and dynamics in the barred spiral galaxy NGC 7479. I have examined the distribution of gas, stars and star formation, and how they relate to each other. The next section demonstrates that it is important to understand bars in galaxies, because they cause large changes in the mass distribution and kinematics. I have acquired observations of the atomic, molecular and ionized gas, and the stellar component. The interpretation of the observations has been aided by numerical simulations that can incorporate both the gaseous and stellar components. I chose NGC 7479 as the target of my investigation because it has a long, strong bar, and easily observable atomic, molecular and ionized gas emission. It is also relatively large and close to us, and it has not been a target of a comprehensive study before.

Bars in Spiral Galaxies

A considerable fraction of disk galaxies are classified as barred spirals. According to Sellwood and Wilkinson (1993), 1/3 are strongly barred and a considerable fraction of the rest are weakly barred. The remaining fraction includes many galaxies which are highly inclined, making bar detection very difficult. Imaging of galaxies in the near-infrared (Pompea & Rieke 1990; Rix 1993; Rix & Rieke 1993) is likely to reveal an even larger fraction of barred disk galaxies. Therefore, it is important to study the effect of the bar potential on the structure and dynamics of the disk.

The origin of the bar in disks of galaxies is the result of either 1) an inherent bar instability or 2) tidal forcing in an interaction with an adequately massive companion. Despite considerable research in the area, the bar instability remains poorly understood. Only parameters which control it have been devised (Sellwood & Wilkinson 1993). Such parameters are a) the halo-to-disk mass ratio: a massive halo suppresses bar formation; however, a halo seems to be present in the outer disk, but observations do not require a halo component in the inner disk, where the bar is; b) the magnitude of stellar velocity dispersions: a disk with high dispersional velocities remains stable against the bar instability and c) the existence of an inner Lindblad resonance (ILR; the dynamical resonances are defined in Chapter 6) wave barrier that breaks the feedback loop, as explained next. One possible explanation for the bar instability is the "swing amplifier", the transformation of leading disturbances into trailing disturbances and the ensuing amplification when the unwinding rate of the disturbance and the epicyclic angular frequency (κ) of the stars are close to a resonance (Toomre 1981; Binney & Tremaine 1987). This process can sustain a stable bar if there is a feedback loop that generates new leading disturbances. If the trailing wave can propagate through the center, it will emerge as a leading disturbance on the other side, and the loop is closed.

An alternative, but physically more insightful, approach to the bar formation problem was taken by Lynden-Bell (1979). He suggested that bars grow through trapping of orbits. His idea is based on the existence of double inner Lindblad resonances. Interestingly, Combes and Elmegreen (1993) obtained models resembling late-type barred galaxies in their simulations where the bar pattern speed is only little above the $\Omega(r) - \kappa(r)/2$ curve, where $\Omega(r)$ is the angular rotation speed of the material at distance r from the center, determined by the axisymmetric component of the potential. They claim that these bars can not be a result of orbit trapping, since the models they consider have no ILRs. The

reliability of their models suffers from an arbitrary truncation of the disk at a relatively small distance. It seems that the significance of Lynden-Bell's mechanism for the origin of bars in the galactic disks remains unclear.

The extent of the bar appears to be controlled by either the form of the rotation curve (Sellwood 1981), or the disk exponential scale length (Combes & Elmegreen 1993), or both, as they may be related to each other. Once the bar has become moderately strong,[1] it can cause dramatic changes in the global structure and evolution of the galaxy. A better physical understanding of the effects of bars is achieved through studies of the orbital structure of particles in the barred potential. Contopoulos and his collaborators (Contopoulos & Mertzanides 1977; Contopoulos 1980; Contopoulos & Papayannopoulos 1980) have shown that the circular orbits in an axisymmetric potential will become an elongated x_1 family of orbits in the presence of a bar perturbation. This family is oriented along the bar between corotation (the radius where the angular speed of circular rotation equals the pattern speed of the bar) and, if it exists, the outer of the inner Lindblad resonances (OILR). The stronger the bar perturbation, the more elongated along the bar is the x_1 family of orbits. The orbits may have small loops at the apocenters. The orientation of the orbits will change by 90° at every major dynamical resonance (corotation, ILR, outer Lindblad resonance (OLR); Contopoulos & Mertzanides 1977; Sanders & Huntley 1976; Athanassoula 1992a). The dissipative gas component cannot follow those closed orbits which have loops. Shocks form at the intersections of orbits. Gas is also unable to change its orbital orientation suddenly by 90°. Rather, the gas orbits will change gradually (Sanders & Huntley 1976). Orbit crowding and shocks will occur, and the

---

1. The strength of the bar is measured by the ratio of the length of the semi-major axis to the semi-minor axis in the near-infrared where emission from the massive, old stellar population usually dominates: the greater the ratio, the stronger the bar; in the numerical simulations and in theoretical models, the strength of the bar is measured by the ratio of tangential to radial forces; again, the greater the ratio, the stronger the bar perturbation.

result around the ILRs will be leading, or trailing, gaseous bars or spirals, which account for the dust lanes of several observed barred spirals. In fact, Athanassoula (1992b) has suggested that the existence of ILRs can be deduced from the dust lane morphology.

Gas will lose energy and angular momentum in shocks. The stellar bar will exert a gravitational torque on the leading gaseous arm or bar, robbing it of angular momentum. This is thought to be the basis for gas inflows in barred galaxies. As suggested by Shlosman et al. (1989), the same scenario may repeat itself at smaller and smaller scales, driving gas inflow very close to the nucleus. Near the center (usually within one kiloparsec), the gas resides in a nearly axisymmetric potential, and the accreting gas will form a central axisymmetric disk, which may experience its own "bar instability" that can drive further inflow. Observations (Kenney et al. 1992; Ishizuki et al. 1990a,b; Lo et al. 1984; Sofue 1996; this dissertation) have detected nuclear molecular bars or disks. By the inflow processes and the associated star formation, a substantial bulge component may form. The formation of a strong central mass concentration will cause a widely separated pair of ILRs. The orbital orientation between these ILRs will be 90° out of phase with the bar, therefore weakening the bar, especially if the distance between the ILRs is large. If one considers the three-dimensional structure of the bar and the disk, the ILR region in the disk plane will couple with vertical ILRs, and induce chaotic orbits through resonance overlapping. This may eventually lead to a dissolution of the bar (Friedli 1994; Friedli & Benz 1993). There is strong numerical evidence that galaxy bars are an important agent in the dynamical evolution of galaxies (Friedli & Benz 1993, 1995).

To understand the details of the dynamical evolution of barred spiral galaxies, high angular and spectral resolution and good sensitivity observations are needed. Detailed studies of the dynamics in barred galaxies have been made earlier by, e.g., Ball (1984, 1986, 1992) on NGC 3359 and England (1986, 1989a,b) on NGC 1300. Their obser-

vational material consisted mostly of atomic hydrogen (H I) observations in the C and D configurations of the Very Large Array (VLA) of the NRAO[2], complemented by I band images of the galaxies. With a numerical hydrodynamic code (the "beam-scheme," Sanders & Prendergast 1974; Huntley 1977), they produced models that fitted the observed gas morphology and kinematics reasonably well. However, these investigations did not have information on some very important dynamical components. For example, they did not have any observations of the molecular gas, which constitutes most of the neutral gas in the inner regions of several spiral galaxies (e.g. NGC 1365, NGC 7479) and which can contribute a substantial mass fraction to the dynamical mass inside the central few hundred parsecs (Turner 1994). Incidentally, NGC 1300 and 3359 may be deficient in molecular gas, although CO emission has been detected in NGC 1300 (J. Knapen, private communication). Recent investigations of gas dynamics in spiral galaxies have employed a multiwavelength approach, complemented by state-of-the-art numerical modeling (Mulder 1995a; Lindblad 1996). This powerful methodology is used in this dissertation. In future, analyses with nonlinear analytical theory should be used together with numerical modeling to investigate the multiwavelength data.

One of the controversial issues addressed by the earlier studies is the bar's ability to drive the spiral structure. Some past investigations (Sanders & Huntley 1976; Huntley et al. 1978; Schwarz 1981) seem to indicate that bars do indeed drive spiral structure, but often the bar alone does not seem to excite a spiral response out to very large radii (see also Lindblad 1996). To solve this problem, several authors have added an oval or spiral potential into the numerical models (Roberts et al. 1979; England 1990b; Ball 1992; Lindblad 1996). The oval potentials should be detectable with the current

instruments, but they are not usually seen. Alternatively, Sellwood and Sparke (1988; see also Sellwood & Wilkinson 1993) argue that the spiral and the bar are independent patterns, and they may have different pattern speeds. The work by Tagger et al. (1987) and Sygnet et al. (1988) suggests that when the corotation radius of the bar coincides with the ILR of the spiral pattern, there is a nonlinear coupling of modes and two pattern speeds. In a similar way, a nuclear bar can be coupled to the main bar. In NGC 1398, Moore and Gottesman (1995) suggest that the OLR of the bar coincides with a resonance of the spiral arms (ILR or corotation). Observational support for differing pattern speeds between the nuclear bar and the main bar comes from Wozniak et al. (1995), Friedli et al. (1996) and Friedli (1996), who find no preferred projected angle between the primary and the secondary bar.

The pattern speeds themselves remain elusive, and are difficult to derive from observations. The following methods have been tried: matching of rings to dynamical resonances (Buta 1993); the method developed by Tremaine and Weinberg (1984), based on the continuity equation; Canzian's (1993) method based on spiral patterns in the velocity residuals; Elmegreen and Elmegreen's (1990) method of matching spurs and bifurcations into dynamical resonances, see also Elmegreen and Elmegreen (1995); and matching gas dynamical models to observations (e.g. Knapen et al. 1995; Sempere et al. 1995a,b; Lindblad et al. 1996). The last approach is nonlinear, whereas the Tremaine-Weinberg and Canzian approaches rely on the linear theory. It seems that rings in disk galaxies trace the locations of the ILR(s) (nuclear ring), the boxy 4:1 or corotation resonance (inner ring) and the OLR (outer ring). Unfortunately, matching the features is not always so straightforward, as shown recently by Moore and Gottesman (1995). All the other methods have difficulties of their own, as they may assume special geometries, projection angles etc. Probably the most reliable way of finding the pattern speed is

through the application of several of these methods. One can then only hope that they do not give discrepant values for the pattern speeds.

Since bars are effective in channeling the gas into the central kiloparsec, the nuclei of galaxies are often sites of active star formation. The common occurrence of star bursts in barred galaxies was first reported by Sérsic and Pastoriza (1965, 1967). Later, Heckman (1980) noticed a similar effect. Balzano (1983) found an excess of barred morphologies among starburst galaxies relative to the field galaxy population. The IRAS satellite revolutionized the field of infrared astronomy, and revealed that barred galaxies had a higher infrared luminosity and hotter dust than the unbarred galaxies (de Jong et al. 1984; Hawarden et al. 1986). Devereux (1987) found an increased amount of $10~\mu m$ emission in 40% of early-type barred spirals. The radio continuum studies often show enhanced emission in the nuclei of barred spiral galaxies (Hummel et al. 1990).

The nuclear radio continuum emission often comes from supernova remnants in a circumnuclear ring, which most likely occurs at the radius of the ILR, or in the presence of two ILRs, in the annulus between these resonances. If star formation is very efficient, most of the gas may be converted to stars, and the gas inflow practically stops. Further inflow may result if the gas mass is large enough for the gas self-gravity to cause an instability in the circumnuclear gas disk. From here, inflow may be driven by the bars within bars scenario (Shlosman et al. 1989) or inelastic and dissipative collisions between the gas clouds (Wada & Habe 1992). Simultaneous activity in the nucleus (Active Galactic Nuclei, AGN) and star formation may also occur. Disentangling these two phenomena has proved to be difficult, but it will be addressed in Chapter 6.

Recently, some numerical codes have included simple star formation schemes to model the effects of star formation on the dynamics of the stellar and, especially, the gaseous disk. Various star formation criteria have been used. Heller and Shlosman

(1994) used the Jeans criterion for star formation. Friedli (1994; see also Friedli & Benz 1993, 1995) has used Toomre's (1964) criterion for star formation, which, as he argues, is more appropriate for a rotating disk galaxy than Jeans criterion. Mihos and Hernquist (1994b) developed a star formation criterion based on the proposed Schmidt's star formation law, where the star formation is proportional to the gas density to some power, usually a number between one and two. Mihos and Hernquist (1994b) chose 1.5 for the numerical value of this power. Since star formation is not well understood, especially the final collapse before the formation of a protostar, the scenarios in use are very sketchy. Schmidt's law is only an approximation to observations, and not based on any physical law. However, inclusion of star formation effects can change the evolution of a gas-rich galaxy in a dramatic way, as was demonstrated by Heller and Shlosman (1994).

Finally, before discussing the previous observations of NGC 7479, I would like to add a word of caution. Our understanding of the dynamical evolution of disk galaxies is based largely on snapshot observations and numerical simulations. Both leave much to be desired. The observations are not a time sequence, from which the current evolutionary status could be derived. They only give us a view of a *two-dimensional* projection of an inherently *three-dimensional* object at one instant of time from one viewing angle. The velocity information is even more limited, as information is obtained in only one direction, the line of sight. Numerical models are based on runs which utilize a few tens of thousands or, at best, a few million particles. Therefore, we are modeling a galaxy that consists of massive star clusters and Giant Molecular Clouds (GMCs). The effects of the discreteness are difficult to evaluate, and one can only hope that the simulations represent the reality, in some statistical sense. The detailed modeling appears to be beyond our capabilities, at least presently. Star formation, as discussed above, is not well understood,

and may cause additional uncertainties. A lot of work remains to be done before we can assess the reliability of numerical simulations and models. However, numerical models do test some qualities and quantities of observed galaxies, and they will be useful in ruling out alternative theories, or at least restricting them.

Review of Earlier Observations of NGC 7479

The galaxy investigated in this dissertation is NGC 7479. The object of the present study is to gain a better understanding of the structure, gas dynamics and star formation in a barred spiral galaxy. NGC 7479 offers an excellent opportunity to obtain this goal. Its classification in the *Third Reference Catalogue of Bright Galaxies* (RC3; Vaucouleurs et al. 1991) is SBS5, corresponding to SBc in the Hubble scheme, and its van den Bergh luminosity class is 1.8 (I-II). In *A Revised Shapley-Ames Catalog of Bright Galaxies* (RSA; Sandage & Tammann 1987) NGC 7479 is classified as SBbc(s) , luminosity class I-II. In the catalog *H I Observations of Galaxies* (Huchtmeier & Richter 1989), various authors have classified NGC 7479 as SBc, SBbc, Sbc and Sc. The uncertainty in the morphological classification may stem from the asymmetric spiral structure: the western arm is luminous and well defined, whereas the arm on the eastern side appears to bifurcate (or even "trifurcate"), and the arms remain weak and ill defined. No companion is seen in the Palomar Observatory Sky Survey (POSS) plates within $45'$ (400 kpc), and no major galaxy with a comparable line-of-sight velocity within $2°$ (1.1 Mpc). This probably means that NGC 7479 is not (and has not been for a while) in close gravitational interaction with any major galaxy. The size at the 25th B band magnitude per square arc second level is $4'.1 \times 3'.1$ according to RC3. The total apparent magnitude (uncorrected for extinction) is $11.60 \pm .05$ (RC3). The heliocentric systemic recession velocity is about 2380 km/s. The IRAS fluxes are 1.49, 3.60, 15.1 and 24.3 Jy at 12, 25, 60 and 100 μm,

respectively. Based on the IRAS (25 μm)/(12 μm) ratio, 2.4, Hawarden et al. (1986) have classified NGC 7479 as a starburst galaxy. Independently, Devereux (1989) classifies it also as a star burst, based on a high 10 μm flux for the nucleus. However, Keel (1983a) has found that the excitation of optical lines in the nucleus corresponds to a LINER (Low Ionization Nuclear Emission Region) classification. In Table 1.1 I summarize the observed properties of NGC 7479, as known before my investigation.

In this dissertation the nature of the galaxy will be studied, within the limitations of the currently available data. NGC 7479 offers a good opportunity to explore the structure and dynamics of its interstellar medium, because it 1) is relatively large (4′ in diameter), 2) is suitably inclined (45°), 3) has a distinct, long bar, 4) has a relatively large H I integrated flux (about 37 Jy km/s) and 5) has been detected in CO, which serves as a tracer for the molecular hydrogen. In addition, the abundant star formation in the bar and especially along the spiral arms, and the (controversial) star burst classification make it a good candidate for detailed studies of the interplay between the dynamics and star formation under a barred potential.

The earliest individual study of NGC 7479 was made by Burbidge et al. (1960). They estimated the mass of the bar (2.22 x 10^{10} M$_\odot$), assuming it is a prolate spheroid rotating end over end. They also noticed a peculiar drop in the velocities on the northeast side, beyond the end of the bar. No further discussion on this feature was written, but it may have been caused erroneously by a nearby bright foreground star. Other photometric studies of NGC 7479 have been made by Baumgart and Peterson (1986), Beckman and Cepa (1989, 1990), Benedict (1982), Blackman (1983), Okamura (1978), Duval and Monnet (1985), Quillen et al. (1995) and Sempere et al. (1995a). Baumgart and Peterson (1986) noted that the disk component of NGC 7479, when observed in the red, can not be extrapolated to the central region, because it would contribute more

luminosity than is actually observed there. They also note that the luminosity profile along the bar is influenced by absorbing dust and emitting H II regions, but on the average it is exponential. They see isophote twisting in the bulge, which has been reported also by Wozniak et al. (1995) and Benedict (1982). Beckman and Cepa (1989, 1990) find evidence for triggering of star formation by a density wave. They observe a change in the peak of B and I band fluxes with the distance from the spiral shock front. This is seen along the southwest arm for a distance of several kiloparsecs, strongly suggesting that the star formation is triggered by the spiral density wave. Beckman and Cepa (1989, 1990) assume that the corotation radius is at, or near, the end of the bar. This, according to them, means that the arms are leading, since the shock front is on the concave side of the arms. More recent investigations, such as Combes and Elmegreen (1993), Elmegreen and Elmegreen (1995) and del Rio (1995) place the corotation radius farther out in the disk, which means that Beckman and Cepa's (1989, 1990) results are still consistent with a trailing density wave theory model. Numerical simulations always produce trailing spiral arms, unless the galaxy is involved in a retrograde interaction.

An older bar, displaced to the west of the "blue bar," is suggested by Benedict (1982). He also sees significant differences in the star formation properties of the northern and southern half of the galaxy. Also, there appears to be more extinction on the eastern side of the galaxy, which is the far side if the spiral pattern is trailing. Recent HST observations (Benedict 1995, private communication) will most likely shed light on these problems.

Blackman (1983) finds that the bar optical flux is about 40% of the total optical flux of NGC 7479, a remarkably large value. He explains the east-west disk light discrepancy by noting that the bright western spiral arm affects the integrated surface brightness. A new component, a plateau, is found between the bar and the western spiral arm. One

possible explanation for the plateau is stars on unstable orbits between the corotation and the OLR. The U-B and B-V colors suggest that NGC 7479 underwent a big burst of star formation about 10^9 years ago, lasting about 10^8 years.

Okamura (1978) argues that the bar consists of an older, red population, on top of which are stars from the younger population I. The eastern (bifurcated) spiral arm suffers from heavy extinction by dust. Duval and Monnet (1985) find a clearly distinguishable bulge component in NGC 7479. They also argue that there is a warp in the outer stellar disk. The mass-to-light ratios for the bar and the disk appear similar, and they argue that a linear approximation for the bar perturbation is adequate.

Quillen et al. (1995) suggest a past merger for NGC 7479, which could have created the asymmetric spiral structure. They also find a strong red dust lane slightly displaced toward the leading edges of the bar, which most likely is the location of a hydrodynamic shock. Finally, they estimate the torque of the bar on the leading gas, and arrive at an inflow rate of (4 ± 2) M$_\odot$ yr^{-1}. Sempere et al. (1995a) find that the corotation radius in NGC 7479 lies beyond the end of the bar. They also note that the streaming motions along the bar are not very well detected, owing to an unfavorable orientation of the bar with respect to the line of nodes. Hua et al. (1980) find that the ratio of Hα/[NII] is about 3.0 along the bar, indicating the existence of H II regions, whereas this ratio drops to well under 1 in the nucleus, which means that the excitation may be provided by other means than star formation. They also remark that the combined emission from these lines in the nucleus is weaker than the emission along the bar. They present a rotation curve based on their observations of the bar region.

Among other studies that include NGC 7479 are, e.g., Elmegreen and Elmegreen (1985), Young and Devereux (1991) and Telesco et al. (1993). These papers discuss the optical morphology, CO flux and infrared emission properties of NGC 7479. In

addition, there exist numerous papers that have included NGC 7479 in a sample for H I flux (e.g. Mirabel & Sanders 1988), radio continuum (e.g. Condon 1987) or infrared flux measurements (e.g. Devereux 1987, 1989). Athanassoula (1994) has found that in a large sample, NGC 7479 is one of only two barred spirals whose bar dust lanes are close to the bar major axis and which most likely do not have ILRs.

Outline of the Investigation

The methods that I have employed to inspect the structure and kinematics of NGC 7479 consist of the analysis of atomic hydrogen 21 cm, CO and Hα spectral line observations together with optical and near-infrared wide-band images and numerical modeling with a tree-SPH code that includes both gaseous and stellar particles. Chapter 2 presents and discusses the atomic hydrogen 21 cm observations together with radio continuum data. Atomic hydrogen is mostly found in the outer disk beyond the bar-dominated region, where its kinematics reveal that the strong western arm is inclined to the main plane. The radio continuum is concentrated in the nucleus and in the bar. Surprisingly, there are regions outside the bar that produce radio continuum emission. These regions are not clearly seen in any other data that I have gathered. I suggest that these regions are related to the star formation effects caused by a recent merger.

CO emission maps are presented and discussed in Chapter 3. I explain the kinematics of the molecular gas with a fast-rotating nuclear disk and strong radial motions along the bar. No molecular gas is seen outside the bar. The optical and near-infrared images in Chapter 4 reveal the distribution of stars and star formation. Star formation is concentrated along the western spiral arm and the bar. The Hα kinematics reveal strong radial motions along the bar. The bar motions are modeled in Chapter 5, and the corotation radius of the bar is found at 1.2 times the bar length. Self-consistent simulations with a small satellite

Table 1.1: General properties of NGC 7479.

Type, luminosity class[a,b]	SBS5, 1.8; SBbc(s), I-II
Environment[c,j]	Isolated
Coordinates[k] (B1950),R.A.	$23^h02^m26.37^s$
Dec.	$+12°03'10''.6$
(J2000.0), R.A.	$23^h04^m56.63^s$
Dec.	$+12°19'22''.7$
Heliocentric radial velocity[a]	2378 ± 3 km/s
Distance[l]	20.0 Mpc
Linear scale[l]	97 pc/arcsec
Optical size at μ_B =	$4'.1 \times 3'.1^a$
25 mag arcsec^{-2}	$4'.4 \times 3'.4^c$
Inclination[m]	45°
Position angle[c]	25°
B_T[a]	$11.60 \pm .05$
H I flux[e]	36.5 Jy km/s
H I linewidth[e] at 50 % level	345 km/s
H I mass[h]	8.8×10^9 $M_\odot$
CO flux[f]	850 ± 160 Jy km/s
CO linewidth[g]	330 km/s
H_2 mass[f]	2.5×10^{10} $M_\odot$
IRAS 12 μm flux[f]	1.49 Jy
IRAS 25 μm flux[f]	3.60 Jy
IRAS 60 μm flux[f]	15.1 Jy
IRAS 100 μm flux[f]	24.3 Jy
L_{IR}[f]	8.91×10^{10} $L_\odot$
Hα flux[f]	1.4×10^{-12} ergs cm^{-2} s^{-1}

Table 1.1 (Continued).

Dynamical mass[i]	1.4×10^{11} $M_\odot$
Central activity	LINER[n]
	Star burst[o]
Position angle of the bar[d]	$6°$
Unprojected length of the bar[p]	5.5 kpc
Bar axial ratio[m]	0.25

[a] RC3.
[b] RSA.
[c] Nilson (1973).
[d] Burbidge et al. (1960).
[e] Average values from Huchtmeier & Richter (1989).
[f] Young et al. (1989).
[g] Young et al. (unpublished).
[h] H I mass from $M_{HI} = 2.36 \times 10^5$ D^2 S_{HI}, where M_{HI} is in $M_\odot$, D is in Mpc, and S_{HI} is in Jy km/s.
[i] Total mass within the 25 mag arcsec^{-2} isophote from $M = 6.77 \times 10^4$ R D V^2_{max} $M_\odot$, where R is 2.2 arc min, D is 20.0 Mpc and V_{max} is 220 km/s.
[j] Karachentseva (1973).
[k] From NED[3].
[l] de Vaucouleurs (1979).
[m] Duval & Monnet (1985).
[n] Keel (1983a).
[o] Devereux (1989).
[p] Using a projected length of 53'.5, as given by Blackman (1983), and the formulas in Devereux (1989).

galaxy demonstate that the asymmetric spiral structure and the long arm can be driven by a satellite galaxy that is merging with the main galaxy. The results from the earlier chapters are discussed in Chapter 6 and a summary of the main results and directions for future investigations are presented in Chapter 7.

Introduction

Most measurements of the global velocity fields in galaxies have been made at the 21 cm spin-flip transition of the atomic hydrogen atom. The use of this technique was substantially facilitated around 1980, when the Very Large Array (VLA) in New Mexico became operational. It enabled relatively high resolution ($20''$ – $30''$) mapping of the atomic gas contents of spiral galaxies. Despite being widely used, atomic hydrogen is not an ideal tracer of the distribution and velocity fields of gas in spiral galaxies. Several spiral galaxies have central deficiencies of H I emission (Mihalas & Binney 1981), or even holes (e.g., M 81, NGC 2841, NGC 3992) in the center. The reasons for this are not yet fully understood, but it has been suggested (Gottesman et al. 1984) that in barred spirals the bar is forcing the gas to flow either into the nucleus (inside the corotation) or into the outer disk (outside corotation). However, the bar has not evacuated the atomic hydrogen from the central disk in all disk galaxies. There may be a dependency on the Hubble class in the sense that earlier, SBa and SBb galaxies are more likely to have holes. A marginal trend in the ratio of the maximum H I surface density to the density in the center can be seen along the Hubble sequence (Hunter & Gottesman 1996), in the sense that the late-type systems have more gas in the center. On the other hand, Knapen and Beckman (1996) have argued that apart from the tendency of earlier type galaxies to have a more pronounced central H I depression, there is no correlation between the presence of the central H I deficiency and other properties, such as the

presence of a bar. The galaxy in the present study, NGC 7479, clearly contradicts the above-mentioned separation between early- and late-type galaxies, since although its type is SBc (relatively late), it has a distinct central H I hole.

Since gas is dissipative, gravitational forces are not the only ones that affect its motions. Ideally we would like to have a pure tracer of gravity in deducing the underlying mass distribution of the galaxy. Stars behave practically like point masses in the general gravitational field of the galaxy, but they are also "supported" by pressure gradients against the centrifugal force. Also, the measurement of stellar velocities is difficult. The only method employed so far is the measurement of the relatively weak stellar atmospheric absorption lines (e.g. the Mg b, 519 nm and Ca triplet lines, around 860 nm; a modern example of this is in Kuijken and Merrifield 1995a,b) through long slit spectroscopy. Since the required integration times are long, the slit can be placed in only a few directions across the galaxy, and complete information on the stellar velocity field will be practically unattainable. Other gas tracers, which complement H I 21 cm line, are the CO millimeter lines, discussed in Chapter 3, and the Hα line, discussed in Chapter 4. When discussing the observed velocity fields, we must keep in mind the restrictions set by the dissipative nature of gas.

Some properties of the atomic hydrogen 21 cm emission are discussed in Appendix A. Appendix B contains a brief review of the interferometric measurement of the 21 cm emission with the VLA. This discussion will be at a relatively general level, because I followed standard procedures in data reduction. More detailed and excellent reviews are given elsewhere (Hjellming & Basart 1982, Ball 1984, England 1986). A very detailed description of the techniques used is in the collection of lectures (Perley et al. 1989).

Atomic Hydrogen Observations of NGC 7479

NGC 7479 was observed in three different configurations at the VLA from September 14, 1989 to June 4, 1995. The total on-source integration time is 1158.5 minutes = 19h 18m 30s. 216 minutes of on-source time were obtained in the C configuration on September 14, 1989, 357.5 minutes in the B configuration on August 11, 1994, 358 minutes in the B configuration on August 13, 1994 and 227 minutes in the D configuration on June 4, 1995. The observations in the C configuration were made by Dr. Jeff Kenney, using the 2AC correlator setting giving 64 Hanning-smoothed channels with a velocity resolution of 10.4 km/s and both the right- and left-hand circularly polarized components. The central heliocentric velocity, using the extragalactic (optical) velocity definition, was

$$v_{rad} = c \frac{\lambda - \lambda_0}{\lambda_0} = 2380 \ km/s. \tag{2-1}$$

The observed coordinates were (B1950) R.A. 23h 02m 26.8s, Dec. +12° 03' 06''. This position is $7'' - 8''$ off the center of the galaxy, as determined from optical images. This offset is useful if there are instrumental artifacts at the field center. The observing parameters for the various runs are summarized in Table 2.1. The brightness sensitivity of the B configuration observations is substantially lower than the brightness sensitivity in the C and D configurations. The noise level in the B configuration observations is about 5 K, whereas the noise in D configuration is only about 0.15 K. This means that only the brightest emission will be detected and resolved. Also, the B configuration observations are not sensitive to the largest spatial scale emission, so there is less flux to be detected.

As mentioned earlier, the data in the September 14, 1989 run were gathered by Dr. Jeff Kenney, who kindly granted us permission to use his data. These data were re-edited and calibrated together with our August 1994 B configuration observations at the VLA.

Table 2.1: VLA observing parameters for NGC 7479.

Array	B	C	D
Total number of antennas	27	26	26
Observing dates	Aug 11, 13 1994	Sep 14 1989	Jun 4 1995
Total duration, on-source [hr]	16.0, 11.9	6.0, 3.6	5.1, 3.8
Integration time [sec]	30	120	30
Heliocentric velocity [km/s]	2380	2380	2380
Observing mode	2AC	2AC	2AC
On-line Hanning smoothing	Yes	Yes	Yes
FWHP of primary beam [']	32	32	32
Flux of 3C 48 [Jy]	16.1493, 16.1479	16.1483	16.1483
Flux of 3C 286 [Jy]	14.9105	14.9103	-
Flux of 2251+158 [Jy]	-	1.5301	-
Flux of 2328+107 [Jy]	1.0991, 1.1147	-	1.2288
Phase calibrator	2328+107	2251+158	2328+107
Min. projected spacing [kλ]	0.347	0.270	0.165
Max. projected spacing [kλ]	52.3	17.5	4.85
Field Center RA [1950]	23^h 02^m 26.8^s	23^h 02^m 26.8^s	23^h 02^m 26.8^s
Field Center DEC [1950]	12° 03′ 06″	12° 03′ 06″	12° 03′ 06″
Total bandwidth [MHz]	3.125	3.125	3.125
Band center [MHz]	1409.35	1409.35	1409.35
Number of velocity channels	63	63	63
Channel separation [km/s]	10.47	10.47	10.47
Channel separation [kHz]	48.828	48.828	48.828
Velocity resolution [km/s]	10.47	10.47	10.47
Total number of visibilities	495316	37307	115111

Since I wanted to combine all the data from different configurations together, I used the same observing parameters for the VLA in the subsequent runs.

Calibration

The data from different configurations were reduced separately. First, I edited the data. The observations on June 4th, 1995 were made when the Sun was about 82° away from NGC 7479. The short baselines in the D configuration are sensitive to interference, and even though the Sun was well outside the field of view, the sidelobes of the beam still contained considerable emission from the Sun, since it is a very strong continuum source. Therefore, the shortest baselines were badly contaminated. In the range 0–0.57 kλ all visibilities having visibility amplitude values above 0.1 Jy were flagged. The data for calibrators were also clipped at short baselines. This editing was done for channel 0, which was solely used in the calibration.

Next I determined the flux for the primary, and then the antenna-based amplitude and phase gain factors. As a last step of the calibration, I determined the bandpass correction by dividing through by channel 0.

Imaging

After calibration, the three u-v data files were combined using the AIPS task DBCON, without any re-weighting of the data. I used channels 7–11 and 53–56 to form the average continuum. From previous mappings of the data I knew that these channels did not contain any line emission. I subtracted the continuum from the channels containing line emission with the task UVLIN that makes the subtraction in the u-v space.

I have made images of the continuum emission using the individual configuration data. In Figure 2.1 I show an example of the continuum emission in the B configuration observations. This map was made by first subtracting the confusing continuum emission in the field. I cleaned the field continuum point sources and subtracted their "clean

components" from the u-v data. The fluxes of the field point sources, determined by fitting two-dimensional Gaussians, are listed in Table 2.2.

Figure 2.1 shows the intriguing open spiral shape of the continuum radiation. This will be discussed below in the section on continuum emission from NGC 7479 and in Chapter 6. Also the possible connection of continuum emission with Supernova 1990U will be shortly addressed.

After the continuum removal the data sets were imaged. The new AIPS imaging task IMAGR was used for this purpose. To achieve maximum sensitivity, I used natural weighting to make one set of channel maps. IMAGR will do the mapping and cleaning in one run, but every channel needs to be imaged separately. Atomic hydrogen emission extends from channel 13 to channel 52. I decided, conservatively, to image channels 10–56. Since the combined data set includes short spacings from the D configuration, I expect that the cleaning algorithm can interpolate across the zero spacing flux. Therefore, I did not add any flux for the zero spacing component. From the channel maps in Figure 2.2 it can be seen that there is no evidence for any negative bowl around the emission, which means that most of the extended flux has been recovered in the observations.

Table 2.2: Continuum point sources in the NGC 7479 field

Source	Right Ascension (B1950.0)	Declination (B1950.0)	Integrated intensity [mJy]
1	23 02 00.63	12 00 41.9	11.55
2	23 02 24.89	12 04 50.0	7.21
3	23 02 15.89	12 08 18.0	6.58
4	23 02 57.34	12 01 53.9	4.07
5	23 02 53.81	12 10 41.9	3.28
6	23 02 01.44	12 07 01.9	2.88
7	23 02 55.98	12 03 09.9	2.17
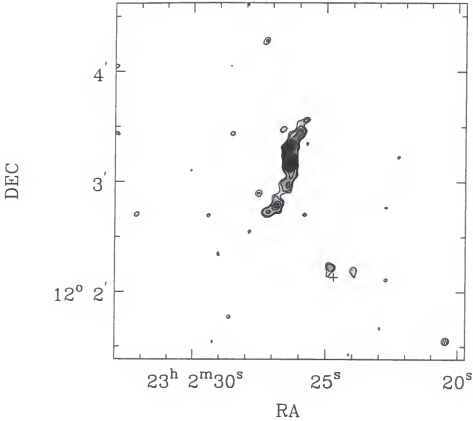
Figure 2.1: The 21 cm continuum image of NGC 7479 from the B configuration data only. The beam size (3″.85 x 4″.30) is indicated by the ellipse at the bottom right corner. The contours are plotted at (3, 4, 6, 8, 10, 16, 24 and 30) times the rms noise, 1.65 × 10⁻⁴ Jy/beam. The position of Supernova 1990U is shown with a plus sign.

The channels were imaged and cleaned in one run after making dirty images of some randomly selected channels and measuring the noise in these channels. The cleaning was stopped when a flux corresponding to 1σ rms noise in the dirty images was reached. This value was 0.0002 mJy/beam. The FWHM (full width at half maximum) values of the clean beam were BMAJ = 9″.7 and BMIN = 7″.4, and the beam position angle −49°. Only a rectangular area covering the emission with some margin was cleaned to speed up the process and reduce redundant cleaning. The resulting cleaned channel maps were then combined with the AIPS task MCUBE. The cleaned maps from the naturally weighted data set are presented in Figure 2.2.
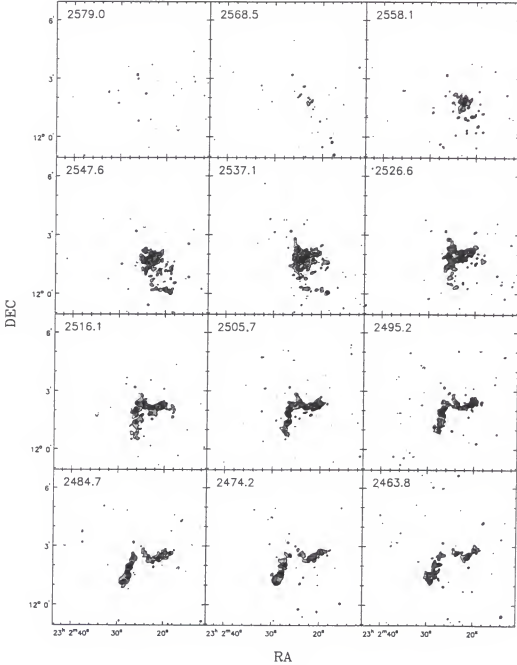
Figure 2.2: The naturally weighted H I channel maps (B+C+D configuration). The contour levels are at (-3, 3, 5, 8, 12 and 15) x the average rms noise in the channels. The star marks the K band peak. The velocities in km/s are at the top left of each frame, and the beam at the bottom right of the last frame.
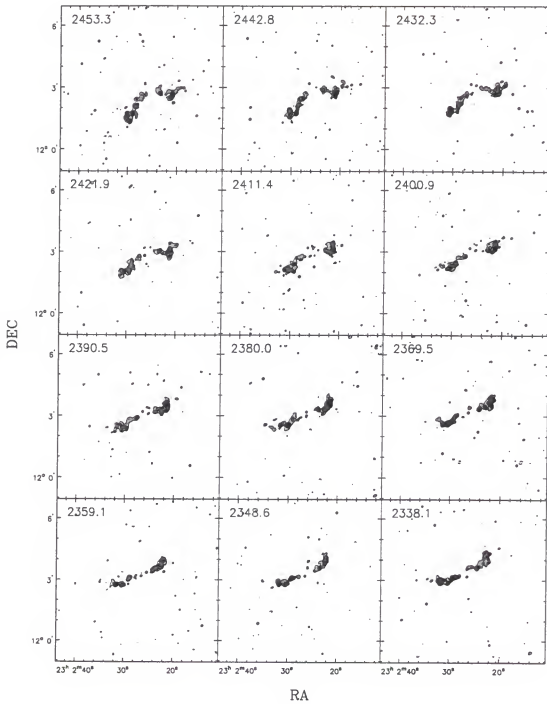
Figure 2.2: (Continued)
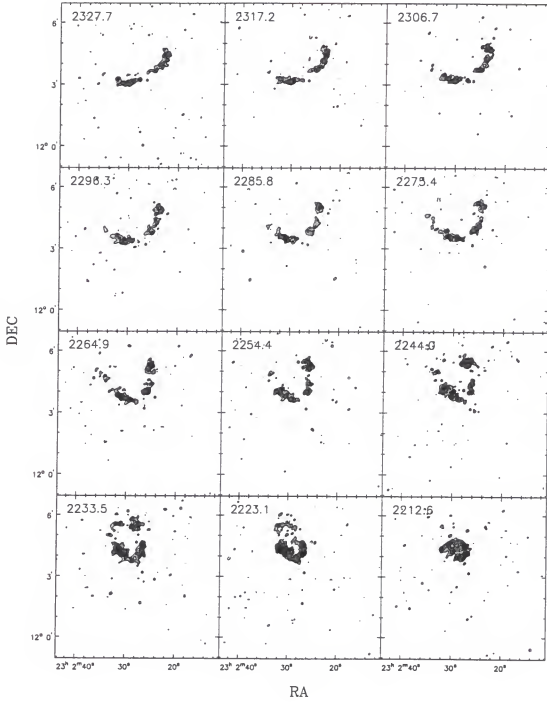
Figure 2.2: (Continued)
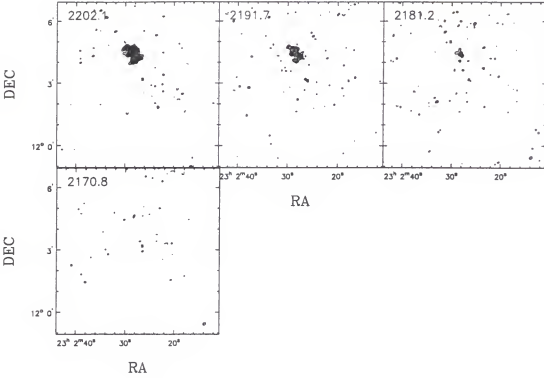
Figure 2.2: (Continued)

Some statistics from the naturally weighted channel maps are shown in Table 2.3. The brightness temperature can be calculated from

$$T_B = \frac{c^2 S_\nu}{2k\nu^2 \Omega_{syn}}, \qquad (2\text{--}2)$$

where S_ν is the flux density per beam and the synthesized beam area Ω_{syn} in arc seconds is

$$\Omega_{syn} = 1.13309 \, \theta_{FWHP_1} \times \theta_{FWHP_2}, \qquad (2\text{--}3)$$

where $\theta_{FWHP1,2}$ are the major and minor axis half power beam widths, respectively.

From Table 2.3 it can be seen that the peak brightness temperature is 37.4 K. If the mean temperature of gas in the interstellar medium is 80 K (Crovisier 1981), the optical depth becomes 0.63 (from equation (A–8) in Appendix A). With such a high optical depth the assumption of optically thin radiation is not valid anymore. However, most of

Table 2.3: Statistical properties of the naturally weighted H I channel maps of NGC 7479.

Maximum rms level [mJy/beam]	0.310, at velocity channel 2181.2 km/s
Minimum rms level [mJy/beam]	0.256, at velocity channel 2463.8 km/s
Average rms level [mJy/beam]	0.279
Expected rms level [mJy/beam]	0.260
Average rms level [K]	2.4
Peak Brightness [K]	37.4, at velocity channel 2537.1 km/s

the emission comes from gas which has a much lower brightness temperature, and the use of equations (A–14) and (A–16) in Appendix A to obtain hydrogen surface densities and H I masses is still justified.

In a similar way, maps having a higher resolution but worse sensitivity were created. The imaging parameters in IMAGR that were different from the naturally weighted maps are discussed in the following. The beam size ($5''.9 \times 5''.0$) is smaller than in the naturally weighted maps. For the weighting scheme presented in equations (B–8) to (B–10) in Appendix B, the beam size and the noise are largely controlled by the parameter ROBUST. I made maps of one channel to search for the optimal value of ROBUST, giving a reasonable noise and a relatively small beam. I also tested the effect of tapering on the same map. The results of these experiments are presented in Table 2.4. The taper parameters UVTAPER(1) and UVTAPER(2) affect the weighting in the following way:

$$W_o(i) = W_2(i) \exp\left[C_u u(i)^2 + C_v v(i)^2\right] \tag{2–4}$$

where

$$C_u = \frac{\ln\ (0.3)}{(UVTAPER(1) \cdot 1000)^2} \tag{2–5}$$

and

$$C_v = \frac{\ln\ (0.3)}{(UVTAPER(2) \cdot 1000)^2}. \tag{2–6}$$

Therefore, the UVTAPER parameters specify the u-v radius where the weights have dropped to 30% level. This way the sparsely sampled outer u-v plane can be down-weighted.

Table 2.4: Test of mapping parameters and the corresponding beam sizes and noise levels.

ROBUST	UVTAPER(1,2) [kλ]	BEAM (arc sec x arc sec)	rms noise [mJy/beam]
5 (natural wt)	0	9.7 x 7.4	0.197
-5 (pure uniform)	0	4.8 x 4.1	0.333
-1	0	5.1 x 4.3	0.277
-0.8	0	5.1 x 4.4	0.266
-0.6	0	5.3 x 4.5	0.254
-0.4	0	5.4 x 4.7	0.243
-0.2	0	5.7 x 4.8	0.233
0	0	5.9 x 5.0	0.225
0.2	0	6.4 x 5.3	0.217
0.4	0	6.7 x 5.4	0.212
0.6	0	7.1 x 5.7	0.207
0.8	0	7.7 x 5.9	0.203
1.0	0	8.1 x 6.3	0.201
0	20	9.6 x 8.7	0.269
0	30	7.7 x 6.6	0.243
0	40	6.8 x 5.9	0.232
0	50	6.5 x 5.6	0.228

Based on these experiments, I decided to make maps with the ROBUST parameter set to 0 and no taper. As a cutoff value for the clean algorithm I used a flux level of 0.25 mJy/beam. All channels from 10 to 56 were imaged separately and then combined with MCUBE to build a data cube. Only a rectangular area around emission was cleaned.

Data Analysis and Results

In this section I will generate various data displays and diagrams which will help in the analysis of the obtained data. These results will be discussed in the final part of this section, and compared to data from other wavelengths in Chapter 6. The first step in this process is to generate an image of the total hydrogen distribution and velocity field. These images may be calculated by integrating powers of velocity, weighted by the brightness temperature over the observed velocity range. In this way, the zeroth moment gives for the column density at some location (x,y)

$$N_H(x,y) = 1.8224 \cdot 10^{18} \int\limits_0^\infty T_B(x,y)dV \quad atoms \; cm^{-2} \qquad (2\text{--}7)$$

(Mihalas and Binney, 1981) which is the same as equation (A–14), but expressed as an integral of velocity instead of frequency. The density weighted mean velocity may be calculated from

$$<V(x,y)> = \frac{\int T_B(x,y)V(x,y)dV}{\int T_B(x,y)dV} \qquad (2\text{--}8)$$

and the second moment of the velocity from

$$<V^2(x,y)> = \frac{\int T_B(x,y)V^2(x,y)dV}{\int T_B(x,y)dV}. \qquad (2\text{--}9)$$

Equation (2–9) has contribution from the differential rotation within the beam (beam smearing) and the genuine velocity dispersion of the gas, which should be relatively small, on the order of a few km/s. The formulas given above are valid only if the 21 cm emission is optically thin. In addition, the calculation of a meaningful (rotational) velocity from (2–8) requires that the emission is single-peaked.

The spectrum integration techniques are discussed at length in Bosma (1981) and England (1986). Bosma lists four different ways the signal may be separated from noise for further integration and processing:

1. Individual study of each profile on a computer display.

2. Fitting of Gaussians to the velocity profiles.

3. Using a cutoff above the noise in intensity.

4. Using an acceptance gate in velocity (the "window" method).

From his studies of the various methods, the window method turned out to be the best. The study of individual profiles for a big map is prohibitively time-consuming. Sometimes, the velocity profiles may not be well fitted with Gaussians. The determination of the intensity cutoff is somewhat arbitrary and it will affect the final results. Noise spikes tend to bias the calculated line-of-sight velocity in the cutoff method towards the middle of the velocity range.

I have combined the intensity cutoff method and the window method. First, I created a smoothed cube in which I had convolved the original data cube along the velocity axis with a Hanning function,

$$X_n = 0.25X_{n-1} + 0.5X_n + 0.25X_{n+1} \qquad (2-10)$$

and along the Right Ascension and Declination axis with a two dimensional Gaussian. The FWHM values for this Gaussian were calculated in such a way that the convolved image has a beam size about twice that of the original. Next I examined the convolved cube. All the points that had a value less than twice the channel rms level in this smoothed cube were rejected in the original, unsmoothed data cube. The smoothed cube acted as a mask for the original cube. In the last step, the original data cube pixels were integrated if their value was at least 2.5 x rms noise in these cubes and if there were at least two consecutive channels at that spatial pixel location fulfilling this minimum criterion. This method guaranteed that almost all the single channel noise spikes were rejected (the channels in the original cube should be independent of each other). As final products I obtained the zeroth moment (H I distribution), the first moment (velocity field) and the
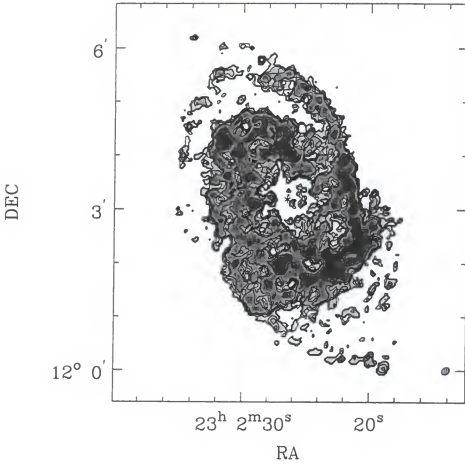
Figure 2.3: The naturally weighted zeroth moment image of NGC 7479. The contour levels are (2, 4, 6, 8, 10, 16, 24 and 30) x the rms level, 7×10^{19} atoms cm^{-2}. The position of the center as determined from the K band image is shown with an asterisk, and the beam size ($9''.7 \times 7''.4$) is indicated by the ellipse at the lower right corner.

second moment (a combination of beam smearing and intrinsic velocity dispersion). I also made a map of the velocity field by fitting Gaussians to the spectra at each spatial pixel location, using the velocity at the peak of the Gaussians as the line-of-sight velocity at that location. This image is displayed in Figure 2.4. The H I distribution is shown in Figure 2.3 and the velocity dispersion in Figure 2.5. The data used in making Figures 2.3 – 2.5 come from the naturally weighted data cube. The zeroth moment high resolution map is shown in Figure 2.6. The units of the zeroth moment images are atoms/cm^2, as
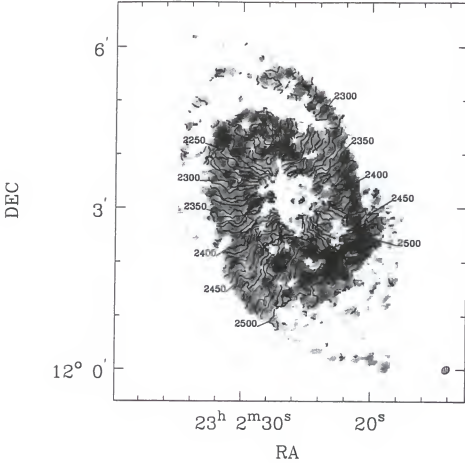
Figure 2.4: The velocity contours overlaid on the naturally weighted grayscale
hydrogen distribution image of NGC 7479. The contour interval is
10 km/s and some of the contour velocities have been labeled. The beam
size (9″.7 x 7″.4) is indicated by the ellipse at the lower right corner.

calculated from equation (2–7). The noise in the integrated images was estimated by
summing two channels at each spatial pixel location and finding the rms level in the
integrated map in a region outside of any signal. This is the minimum noise at any
position, because the noise depends on the number of channels included in the sum at
each spatial pixel location.
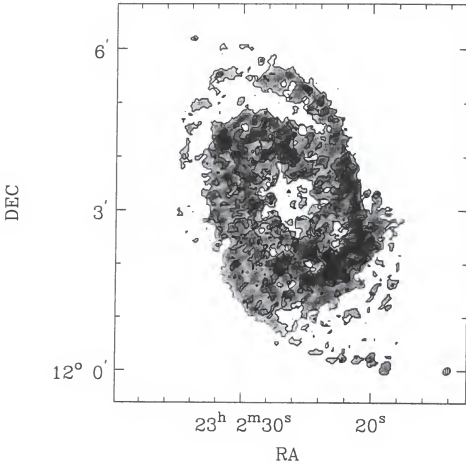
Figure 2.5: The contours of the second moment with respect to velocity map for the naturally weighted data set of NGC 7479 overlaid on the grayscale hydrogen distribution. The contour levels in km/s are 5, 10, 15, 20 and 25. The beam size ($9''.7 \times 7''.4$) is indicated by the ellipse at the lower right corner.

Radio Continuum Emission

The 21 cm continuum image made with the highest available resolution (uniformly weighted B configuration data) was shown earlier in Figure 2.1. I have compared the fluxes from this figure to those obtained by Q. Yin at 2 cm in the C configuration and kindly given to me. Before comparison, the 2 cm image was smoothed to the same resolution ($3''.85 \times 4''.30$) as the B configuration 21 cm image. The data in the 2 cm
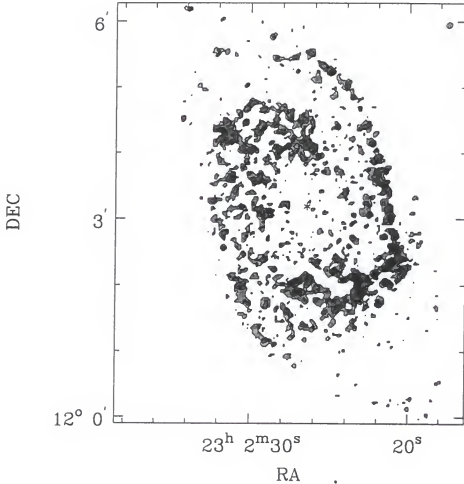
Figure 2.6: The atomic hydrogen distribution in the high resolution map. The contour levels are at (3, 6, 10 and 16) x the rms noise in a two channel integration, 1.8×10^{20} atoms/cm². The nucleus as determined from the peak brightness in the K band image is marked with an asterisk, and the beam size ($5''.9 \times 5''.0$) is indicated by the small ellipse at the upper right corner of the image.

observations are sensitive up to structures $40''$ in size. It appears that in the nucleus the spectral index α, defined by

$$F = C\nu^{\alpha}, \qquad (2-11)$$

is close to zero. In this equation, F is the observed flux, C is a constant, and ν is the frequency. Usually, for thermal radiation, α is zero for optically thin radiation from ionized hydrogen, and two for optically thick radiation. For synchrotron (non-thermal)

radiation, the spectral index is usually about −0.7, depending on the electron energy spectrum. New observations are needed, preferably at 2, 6 and 20 cm with a phased array (where comparable resolutions are achieved), to confirm the character of the emission.

The striking aspects of the 21 cm continuum emission are the open spiral arm morphology and the fact that the ends of the continuum "arms" do not coincide with enhanced emission at any other observed wavelength. Only in CO are there some hints of emission at the location of the continuum arms (Chapter 3). At 2 cm, the morphology of the emission is different. The 2 cm emission is shown in Figure 2.7. It is possible that the 21 cm emission is not continuous, but consists of separate regions that blend together when smoothed with the $4''$ beam.

It is interesting to look for radio emission from supernova 1990U (Gomez & Lopez 1994). As can be seen in Figure 2.1, the location of the supernova seems to be outside the patches of continuum emission on the southern section of the strong spiral arm. The offset is relatively small ($5''$ or about 800 pc). The optical images confirm that the location of the supernova is still within the arm. This supernova was of type Ic, representing an explosion in a binary star system. It seems that the continuum radiation in the 21 cm continuum image is associated with the gas-rich star forming regions that are clearly seen in H I, Hα and optical images. A continuum source in the same location is seen also in the C configuration observations made in 1989 before the supernova, which makes it even more likely that the enhanced radio continuum emission from supernova 1990U is not seen in the B configuration observations from 1994.

Total Mass Calculation with a Refined Cleaning Method

I calculated the total H I flux coming from NGC 7479 using two different techniques. First, the total intensity image can be used for this purpose. To do this, I smoothed the
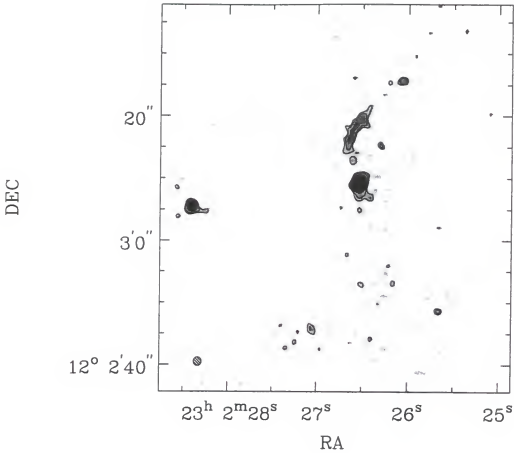
Figure 2.7: The 2 cm continuum image of the center of NGC 7479. The source on the left is most likely a background source. The contour levels are 8.5 x 10^{-5} (3, 4, 6, 8, 10, 16, 24) Jy/beam. The beam size ($1''.4$ x $1''.3$) is indicated by the small ellipse on the lower left corner.

naturally weighted zeroth moment map to a resolution of $45''$ x $45''$. In this way, I guaranteed that the noise will become smaller (noise $\propto \frac{1}{\Omega_{beam}}$, where Ω_{beam} is the beam size) and the low surface brightness features will be detected.

The integrated map was made in a way described earlier. The channel maps were integrated above 2.5 x the 1σ rms noise level. I also included values lower than -2.5σ to guarantee that there is no positive bias from the noise. The requirement of emission in two consecutive channels should remove most of these noise spikes anyway, as discussed before. I then calculated the average integrated flux in a box around the galaxy that had

everything blanked outside the H I disk, which was clearly seen in TV displays of the integrated map. The average integrated flux was then multiplied by the number of pixels containing emission times the pixel size in (arc sec)^2. Since the integrated flux units are Jy × km/s/beam, I divided by the beam size to obtain the total integrated flux, 35.48 Jy × km/s. The uncertainty in this value can be judged by comparing it to the value obtained when the channel maps were integrated above 1.5σ, 35.63 Jy × km/s, and above 3σ, 35.09 Jy × km/s. No correction for the primary antenna pattern has been made in obtaining these fluxes.

The other method follows that introduced by van Moorsel (Jörsäter & van Moorsel 1995). This method was developed to compensate for the overestimation of the fluxes when using strongly non-Gaussian naturally weighted beams. The flux in cleaned maps will be the sum of the clean component, C, and the residual, R. At the end of a CLEAN, the residuals are added to the clean component to give an estimate for the noise level. Unfortunately, the units of the residuals are flux per dirty beam. The dirty beam area, and thus the flux in a pixel, in a naturally weighted data cube can be substantially larger than the area (and the flux) of the clean beam. The unknown true flux, G, can be obtained by scaling the residual flux by a factor ϵ and adding it to the clean flux:

$$G = C + \varepsilon \times R \tag{2-12}$$

The factor ϵ is defined as the ratio of the clean beam area to the dirty beam area. In practice, ϵ can be determined by performing two experiments with cleaned fluxes C_1 and C_2, and residuals R_1 and R_2. Then,

$$G = C_1 + \varepsilon \times R_1 \text{ and } G = C_2 + \varepsilon \times R_2. \tag{2-13}$$

In practice we need to clean only once; the second clean is given by the dirty map, thus $C_2 = 0$ and R_2 is the flux in the dirty image. The previous equations can be solved

for ε and G:

$$\varepsilon = \frac{C_1}{R_2 - R_1} \qquad (2-14)$$

and

$$G = \varepsilon \times R_2. \qquad (2-15)$$

The clean should go deep enough to remove visible beam sidelobes, usually to around $2-3\sigma$. I cleaned a box around the emission in each channel down to 2σ using the data from the C array, which should be sensitive to large enough scales $(15')$ to cover all the emission in NGC 7479. In Table 2.5 I present the results from these cleaning experiments. The final, total flux, multiplied by the channel width to obtain the velocity integrated value, is 35.53 Jy $\times$ km/s, which is comparable to the result obtained from the smoothed moment zero map.

From the integrated flux profile (Figure 2.8) I measured the velocity width at 20% of the peak flux level, 373 km/s. The midpoint line-of-sight heliocentric velocity between the 20% levels is 2380 km/s, which can be compared to the value derived in the next section, from the kinematics, 2371 km/s.

To calculate the total hydrogen mass, I used equation (A-16). The velocity width of the channels is 10.469 km/s. I adopt a final integrated flux value of 35.5 Jy $\times$ km/s. This flux can be compared to previous determinations, made with single antenna radio telescopes. Shostak (1978) obtained a total H I flux of 37.6 Jy $\times$ km/s with the Greenbank 300 ft. telescope, Richter and Huchtmeier (1982) 37.18 ± 2.26 Jy $\times$ km/s with the Effelsberg 100 m radio telescope and 31.56 ± 2.67 Jy $\times$ km/s with the Greenbank 300 ft. telescope. Hewitt et al. (1983) used the Arecibo 300 m telescope to obtain a flux of 44.7 Jy $\times$ km/s and Davis and Seaquist (1983) used the Greenbank 300 ft. and 140 ft. telescopes to obtain total H I fluxes of 30.8 and 37.7 Jy $\times$ km/s, respectively. Haynes

Table 2.5: The channel fluxes from van Moorsel's method.

velocity (km/s)	C_1 (mJy)	R_1 (mJy)	R_2 (mJy)	G (mJy)	ϵ
2568.5	8.95	20.0	37.6	19.1	0.51
2558.1	38.7	64.7	144	70.2	0.49
2547.6	97.7	79.3	264	140	0.53
2537.1	115	102	323	168	0.52
2526.6	101	83.1	292	141	0.48
2516.1	89.9	105	318	134	0.42
2505.7	82.6	74.4	252	117	0.47
2495.2	74.4	65.8	235	103	0.44
2484.7	71.9	71.5	227	105	0.46
2474.2	65.7	78.8	231	100	0.43
2463.8	58.0	65.5	187	89.1	0.48
2453.3	61.1	68.0	193	94.3	0.49
2442.8	53.5	54.4	177	77.2	0.44
2432.3	51.4	55.3	172	75.9	0.44
2421.9	55.9	87.3	209	96.2	0.46
2411.4	53.7	73.1	202	84.3	0.42
2400.9	54.7	75.4	217	83.8	0.39
2390.5	53.2	48.9	178	73.4	0.41
2380.0	49.6	40.7	169	65.3	0.39
2369.5	45.3	28.7	130	58.1	0.45
2359.1	42.1	48.9	145	63.5	0.44
2348.6	39.9	41.3	112	63.2	0.56
2338.1	44.4	54.8	135	74.8	0.55
2327.7	58.4	58.6	204	82.0	0.40
2317.2	46.4	36.5	112	68.6	0.61
2306.7	58.3	42.7	131	86.6	0.66
2296.3	60.6	69.9	179	99.5	0.56
2285.8	43.2	54.8	127	75.9	0.60
2275.4	53.5	49.8	144	81.8	0.57
2264.9	65.6	78.9	219	103	0.47
2254.4	59.5	65.6	168	97.6	0.58

Table 2.5 (Continued).

velocity (km/s)	C_1 (mJy)	R_1 (mJy)	R_2 (mJy)	G (mJy)	ϵ
2244.0	80.8	110	297	128	0.43
2233.5	97.5	67.0	295	126	0.43
2223.1	102	76.5	275	141	0.51
2212.6	67.0	45.2	195	87.2	0.45
2202.1	49.3	48.0	165	69.5	0.42
2191.7	21.5	22.1	77.7	30.0	0.39
2181.2	8.03	17.3	38.7	14.5	0.38
2170.8	4.34	2.55	12.2	5.49	0.45
Total				3.39 Jy	
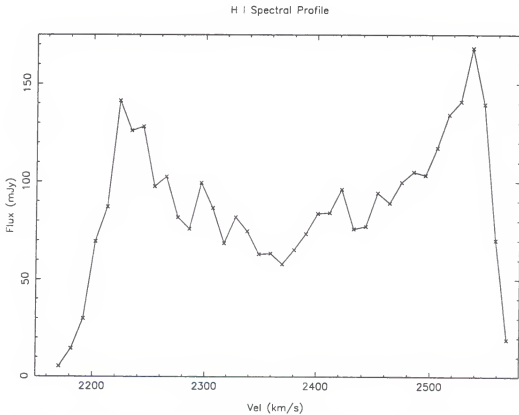
Figure 2.8: The integrated spectral H I flux against the heliocentric velocity in NGC 7479.

and Giovanelli (1984) obtained the value 42.3 Jy × km/s using the Arecibo telescope. In addition to these measurements, a total H I mass of 1.01 x 10^{10} $M_\odot$ is cited by Bottinelli

et al. (1982) using the Nancay 300 m telescope. Adopting the total flux of 35.5 Jy × km/s, I derive a total H I mass, 8.58 x 10^9 $M_\odot$ from equation (A–16). I estimate that the uncertainty in the total mass, based on the noise in the channel fluxes, is 0.3 x 10^9 $M_\odot$. The value derived from the VLA observations is comparable to the single dish measurements, which have a considerable scatter. Therefore, most likely very little, or no emission, has been lost in the interferometric H I observations.

Atomic Hydrogen Gas Distribution and Morphology

The atomic gas disk has a central hole and two extended gaseous arms. Upon close inspection one can see an asymmetry in the H I distribution. An asymmetry is also found in the global flux spectrum (Figure 2.8).

The central hole in H I gas is somewhat unusual since late-type spiral galaxies often have atomic hydrogen all the way to the nucleus. However, there is lots of molecular gas in the bar (see the CO emission maps in Chapter 3). The higher pressure of the interstellar medium in the bar region has caused a phase transition from atomic to molecular gas.

The spiral arm starting at the southern end of the bar is much longer and more easily discernible than the arm(s) starting at the northern end of the bar. The southern arm actually starts near position angle 90° on the eastern side of the galaxy. This arm contains several regions of strong emission. The most striking bright region is in the northwest, near position angle 350°. Moving outwards along the arm, there are no strong optical counterparts to the atomic gas emission after position angle 270°, although some patches of optical emission along the gaseous arm can be seen in the optical images between the position angles 270° and 0°. However, a deep exposure (Benedict, G. F., private communication) reveals an extension of optical light on the northwestern side of the galaxy. In addition, this arm has a sharp kink on the SW side which can be seen

also in the optical images. The arm suddenly changes its direction by $60° - 70°$. To the west of this location, the arm overshoots towards northwest. To the east, the gas arm bifurcates. One branch is coincident with the optical spiral arm, whereas the other branch leads to a location about $30''$ south. This arm seems to end in a large H I region, not readily seen in the stellar distribution. The comparison between the optical and gaseous distributions is given in Figure 2.9.

On the eastern side, one can see three gaseous arms branching off the northern end of the bar. These arms are more easily recognizable in the high resolution image (Figure 2.6). The gas arms can be followed for at least one arc minute. In the southeast, a thin, long gas arm separates from the main atomic hydrogen disk. This arm does not have
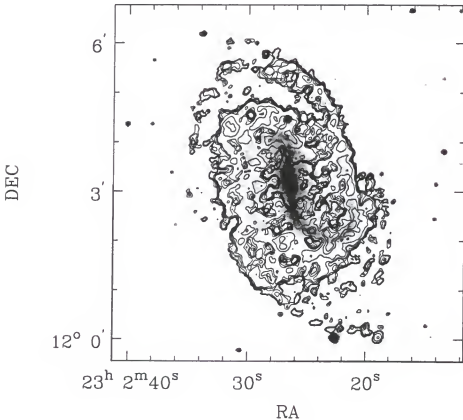
Figure 2.9: The contours of the naturally weighted H I map overlaid on an optical image of NGC 7479. The contour levels are (2, 4, 6, 8, 10, 16, 24 and 30) x the rms level, 7×10^{19} atoms cm^{-2}.

any optical or infrared counterparts. It can be followed for at least two arc minutes. In addition to these features, there are several detached patches of weak emission in the south, between the main body of the gas disk and the long, southern arm.

I present the low resolution H I distribution, made only from the D configuration observations, in Figure 2.10. The data processing was done as described before. In this image, the asymmetric atomic hydrogen distribution can be seen again. Also, the southern gaseous extension is observed. The concentration of the gas at the ends of the bar is obvious, as is the central hole, which fills up at this resolution because of the beam smearing. The total extent of the hydrogen disk, defined at 1% of the peak level at this resolution ($51''.5 \times 44''.3$), is about $7'.3 \times 5'.0$.

Atomic Hydrogen Gas Kinematics

The velocity field of the H I emission contains a wealth of information. We may obtain the following global parameters from it: the systemic velocity, the position of the kinematic center, the position angle of the kinematic major axis, and the inclination. In practice, the position angle and the inclination may be allowed to vary as a function of radius (the tilted ring model). Estimates for the rotation velocity are obtained from a least squares fit to the velocity field. Usually this fit is made in narrow annuli, whose width corresponds to the size of the beam. This procedure is well described in Warner, Wright and Baldwin (1973) and Begeman (1989).

First we give initial guesses for all the parameters mentioned above. Good initial guesses are usually provided by the optical determinations of these parameters. Next we select points that are within the elliptical annuli defined by the orientation parameters (center position, position angle of the major axis and the inclination). For each point
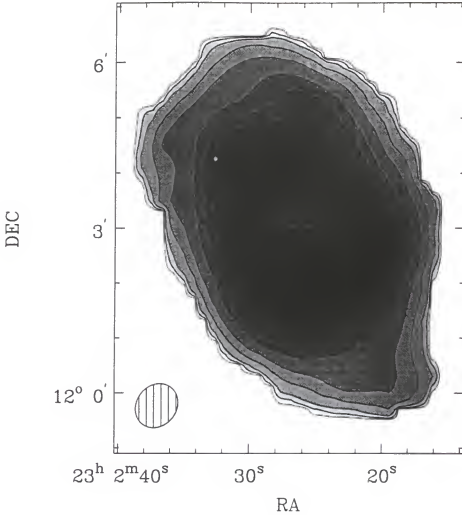
Figure 2.10: The zeroth moment image of the H I distribution from the D configuration observations only. The beam size is $51''.5 \times 44''.3$, and its shape is shown at the lower left corner. The contour and grayscale levels are (0.005, 0.01, 0.02, 0.05, 0.1, 0.2, 0.3, 0.4, 0.5, 0.6, 0.7, 0.8 and 0.9) x the maximum pixel value. The position of the peak radio continuum emission is shown with a small star at the center.

within the annulus, an estimated value for the line-of-sight velocity is calculated from

$$V(x,y) = V_0 + V_C(r)sin(i)cos(\theta) + V_R sin(i)sin(\theta). \qquad (2-16)$$

Here x and y are the coordinates of a position on the plane of the sky, V_0 is the systemic velocity, V_C is the circular velocity at the distance r of the annulus from the center, i is the inclination, and θ is the angular distance of the point from the kinematical major axis on (the part of this axis in the receding half of the galaxy), measured on the plane of the

galaxy. The angle θ is related to the other parameters through the following equations:

$$cos\,(\theta) = \frac{-(x - x_0)\,sin\,(\phi) + (y - y_0)\,cos\,(\phi)}{r},\qquad(2\text{--}17)$$

$$sin\,(\theta) = \frac{-(x - x_0)\,cos\,(\phi) - (y - y_0)\,sin\,(\phi)}{r\,cos\,(i)}.\qquad(2\text{--}18)$$

In these equations, x_0 and y_0 denote the position of the center, and ϕ is the position angle of the receding part of the major axis, measured counterclockwise from north on the plane of the sky.

Next, the estimated line-of-sight velocity is subtracted from the observed line-of-sight velocity at every position (pixel), and the difference squared is added to the χ^2 measure for that ring. A least squares minimization is made using these parameters. The pixels may also be assigned different weights. The most common weighting scheme takes weights from the corresponding integrated surface density image. Often higher weights are given for the points near the kinematical major axis, since on the major axis only the tangential component of the velocity in the plane of the galaxy is observed. Therefore, by suppressing the importance of points near the minor axis, where the line-of-sight velocity contains contributions from radial motions only, we expect to obtain a more reliable estimate of the circular rotation velocity (which, of course, is purely tangential). However, the tangential streaming terms remain in the fitted velocities, and one can only hope that they are small in magnitude. It is also possible to use a wedge around the minor axis to exclude points from the fit. Naturally, if we expect to investigate radial motions, we have to concentrate on points near the minor axis.

To achieve a better idea of the H I velocity field in NGC 7479, I smoothed the naturally weighted data cube from $8''.5$ resolution to circular $15''$ and $30''$ FWHM beams. I then made images of the velocity field by fitting Gaussians to the spectra at each spatial pixel position. The spectral profiles were approximately Gaussian in shape, and no
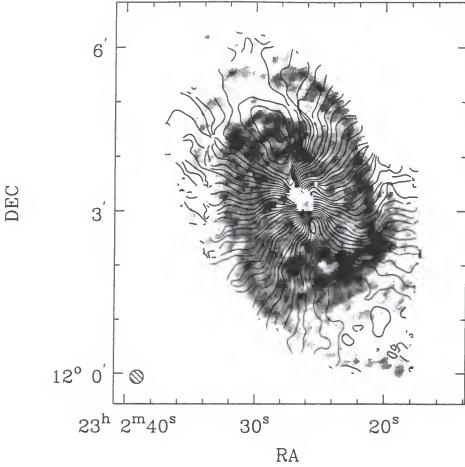
Figure 2.11: The 15″ resolution H I velocity field contours superposed on the 8″.5 resolution naturally weighted integrated surface density map (grayscale). The contours range from 2210 km/s to 2550 km/s in 10 km/s intervals. The beam size is shown on the lower left.

systematic effects are expected from this technique. The 15″ resolution image of the velocity field is shown overlaid on top of the 8″.5 grayscale image in Figure 2.11. A similar image with the 30″ resolution data is shown in Figure 2.12.

These images show that the signal-to-noise ratio in the original 8″.5 resolution image is too low to see the distortions in the velocity field clearly. The 15″ resolution and the 30″ images show clearly that the H I disk velocity field has been perturbed severely on the western side along the strong spiral arm. For this reason, the global rotational field may be difficult to determine reliably. Therefore, I decided to emphasize the data on
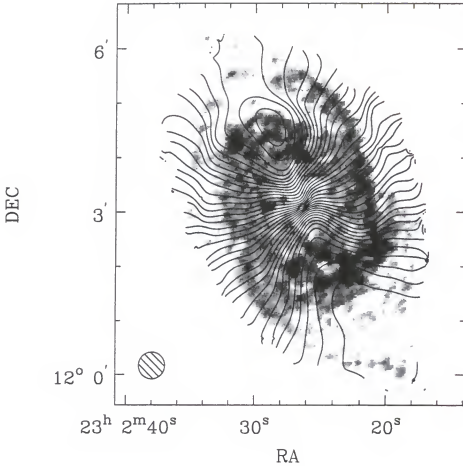
Figure 2.12: The 30″ resolution H I velocity field contours superposed on the 8″.5 resolution naturally weighted integrated surface density map (grayscale). The contours range from 2200 km/s to 2570 km/s in 10 km/s intervals. The beam size is shown on the lower left.

the southeastern side of the line of nodes. On that side, the velocity contours are fairly smooth with only small kinks which are possibly related to streaming motions around the weak eastern arms or perturbations from a merging satellite galaxy. I employed the GIPSY task ROTCUR to determine the run of velocities out to 130″, using data in 10″ wide annuli in the 8″.5 resolution naturally weighted data set. GIPSY is described by van der Hulst et al. (1992). The use of the high resolution data set is justified because serious beam smearing is avoided. The beam smearing causes underestimation of velocities in the steeply rising part near the center.

Tests leaving the inclination as a free parameter, and using data from the whole galaxy, showed that inclination rises to very high values near the center, where little gas is found and the effects of the gas streaming along the bar could be very severe. A plot of the fitted inclinations, using the $15''$ resolution velocity field, is shown in Figure 2.13. The position angle, if left as a free parameter, varies much less. It fluctuated between 195° and 203°, with values very close to 202° at radii where the inclination seems to stay at a fairly constant value near 51°.

The position angle cannot be unambiguously determined by using data from only one side of the major axis. Therefore, this parameter was determined using data from both sides of the major axis. The results from this fit are shown in Tables 2.6, 2.7 and in Figure 2.14. In Table 2.7, V_{rot} is the circular velocity and σ is the dispersion of the least squares sum that can be used as a conservative estimate for the error in the rotational velocities.

To make the final rotation curve solution, I used $\cos \theta$ weights, and fixed the inclination at 51° and the position angle of the line of nodes at 202° (22°). These values should be compared to the optically estimated values, inclination 35° − 45° (Richter & Huchtmeier 1982; Grosbøl 1985) and position angle 16° − 39° (Burbidge et al. 1960; Grosbøl 1985). I believe the kinematically obtained values are more reliable than the values obtained by the optical isophote fitting programs. The latter values suffer from perturbations caused by the bar, spiral arms, and interactions. Of course these perturbations are visible in velocity fields as well, but they are easier to recognize and the statistics are better if many annuli are used.

The orientation parameters that were obtained using only data with $\sin \theta < 0$ were checked against the values obtained when the whole velocity field was used, or only the half with $\sin \theta > 0$. Solutions were also sought with different weighting schemes, such as uniform weights, and weights based on the moment zero image. All these tests gave
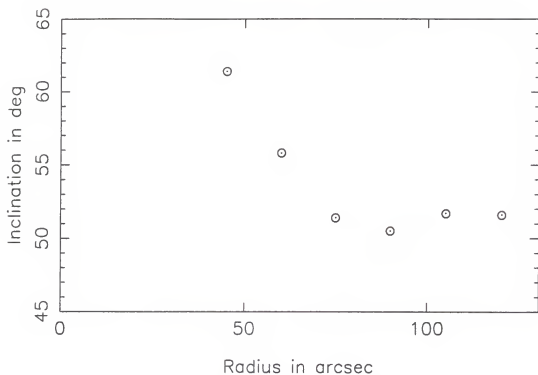
Figure 2.13: The variation of inclination if left as a free
parameter after fixing the center position and systemic velocity.

Table 2.6: The positional and orientation parameters of the rotation curve.

Kinematic Center R.A.	23h 02m 26.52s
Kinematic Center Dec.	12° 03′ 7″.9
Heliocentric systemic velocity	2367 km/s
Inclination	51°
Position angle (receding side)	202°

similar results, but larger rms values than $\cos \theta$ weighting in the southeast half of the galaxy. If left free, the inclination in the innermost radii is above 60°. This high value is probably related to the elliptical streaming motion along the bar.

At radii larger than $130''$ from the center, the velocity field changes its character dramatically. This may be seen best in the $30''$ resolution image (Figure 2.12), which
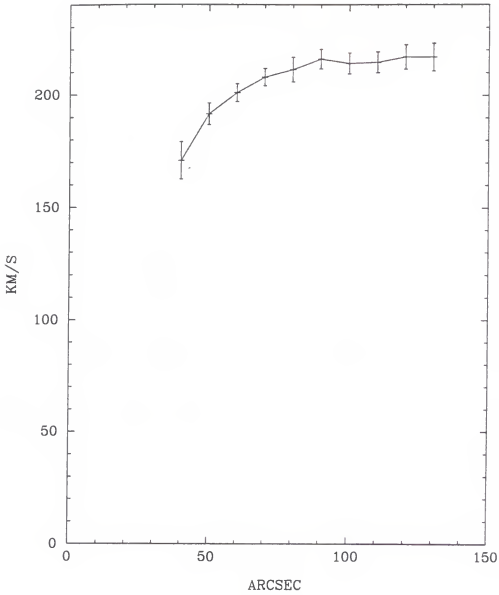
Figure 2.14: The deprojected $8''.5$ rotation curve out to a
radius of $130''$. See Table 2.6 for parameters used in the fit.

shows that in the northeast part of the galaxy, the velocity contours suddenly bend by
$60° - 90°$ toward north and then further out the contours bend back towards their earlier
position angles. This happens along the patchy gaseous arm that wraps around the galaxy
in the north. Similar dramatic bends are seen toward a higher line-of-sight velocity in
the north and north-west parts or the gaseous arm.

Often these kinds of bends in the velocity contours are interpreted in terms of a warp of the outer H I layers. The warp can be caused by the triaxial nature of the halo component or by interaction with another galaxy. The possibility of a warp cannot be excluded in the north, although I was unable to generate a warp model that reproduces the observed velocity field. In Chapters 5 and 6 I explore the possibility that the H I arm consists of gas that has been pushed to a different plane by the tidal forces from a companion whose orbit was inclined to the plane of the main galaxy.

The receding half of the velocity field does not have any obvious sign of a warp. Instead, the contours do not close, but open up, thereby indicating a slightly rising or flat rotation curve. In addition, the position angle of the major axis shifts towards higher values, from about $190°$ near the center to $215° - 220°$ at the outer radii. This is seen most clearly in the $15''$ and $30''$ resolution data (Figures 2.11 and 2.12). In Figure 2.12, and also in the other images of the velocity field, the contours to the west and southwest of the center, near the position of the gaseous – optical spiral arm, have moved toward

Table 2.7: The parameters of the rotation curve. See
Table 2.6 for the orientation parameters used in the fit.

Radius ($''$)	V_{rot} (km/s)	σ(V) (km/s)
40	171.0	8.3
50	191.7	4.8
60	201.1	4.0
70	208.0	3.8
80	211.3	5.4
90	215.9	4.3
100	214.0	4.6
110	214.5	4.6
120	216.9	5.4
130	216.9	6.1

lower velocities, as if the arm was not receding as fast as the rest of the disk. This could be caused by the lower inclination of the arm. Alternatively, if the emission in the H I arm is in the same plane as the main neutral gas disk, the tangential velocity is lower on the arm or there is substantial radial flow towards the arm. I discuss these issues in Chapter 6.

The channel maps in Figure 2.2 reveal a strong kink in the emission around 2506 km/s. This coincides spatially with the bifurcation seen in the H I distribution (Figures 2.3 and 2.6). Its location is well beyond the end of the bar, which makes it unlikely that the bar perturbation could have caused it, since there is no counterpart on the other side of the disk. Therefore, this perturbation must be related to the effects of the strong spiral arm.

One explanation for the bends in the velocity contours is density wave streaming motions. I tried to fit the velocity perturbations to the first order (linear) density wave streaming motion, described by (Rohlfs 1977)

$$V_{s.m.} = V_t(r) \, sin \, (2\theta - 2\theta_0(r)) \, cos \, (\theta) \, sin \, (i) +$$
$$V_r(r) \, cos \, (2\theta - 2\theta_0(r)) \, sin \, (\theta) \, sin \, (i), \tag{2-19}$$

where $V_t(r)$ and $V_r(r)$ are the tangential and radial amplitudes of the streaming motion, respectively, and $\theta_0(r)$ is the zero-point for the perturbation (the position angle of the arm ridge at radius r from the center). No physically meaningful, consistent solutions were found. It appears that the receding half of the velocity field has been severely perturbed by the strong western arm.

I also tried to improve the fit to the inner regions which showed consistently high inclinations, in terms of bar streaming motions. The expansion of the Fourier series representation of the velocity field to second order gives (Long 1991)

$$V_{bar}(r) = [V_{tbar} cos \, 2(\theta - \theta_0(r)) \, cos \, (\theta) + V_{rbar} sin \, 2(\theta - \theta_0(r)) \, sin \, (\theta)] \, sin \, (i). \tag{2-20}$$

Here $V_{tbar}(r)$ is the tangential amplitude of the bar perturbation at radius r, V_{rbar} is the radial amplitude of the bar perturbation at radius r and $\theta_0(r)$ is the position angle of the bar in the plane of the galaxy, measured from the kinematical major axis. The observed difference in the position angle of the major axis and the position angle of the bar, β, is related to the angle θ_0 through

$$tan(\theta_0) = \frac{tan(\beta)}{cos(i)}. \tag{2–21}$$

(Burbidge et al. 1960). No satisfactory fit could be achieved. The bar streaming cannot be extracted, since the angle between the line of nodes and the major axis of the bar is perhaps less than 20°, close to the singular situation of 0°, for which Long's procedure does not work.

Position-Velocity Plots of H I Emission

In Figure 2.15 I show a position-velocity plot taken along the minor axis, using a position angle 115°. It can be seen that the bar streaming motion has caused the little nodes at higher velocities on the western side near the central hole and at lower velocities on the eastern side. In addition to these, a small radial streaming component near one of the arms on the eastern side can be seen. The sign of this streaming is such that the gas is moving toward us. The unprojected magnitude is about 30 km/s. Assuming that the arms are trailing, this implies inflow in the plane of the galaxy. This position coincides with a major dust lane on the eastern side and could be related to an infalling motion in a trail left behind by a merging satellite. On both sides the profile shifts toward higher velocities at large distances from the center. On the western side, this reflects the generally higher line-of-sight velocity in the gaseous arm. On the eastern side the situation is less clear. A patch of emission from the long peculiar gaseous arm is on the far left in the minor
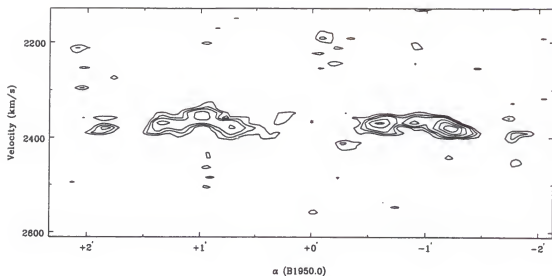
Figure 2.15: A position-velocity slice across the minor axis in the naturally weighted data cube at position angle 115°. The center position corresponds to the kinematical center at R.A. 23^h 02^m 26.52s, Dec. +12° 03′ 7″.9. The contour levels are 0.28 (1σ rms) x (−2, 2, 3, 4, 6, 8, 10) mJy/beam. Negative contours are shown as dashed lines.

axis slice. No sign of continuum absorption in the center is seen, most likely because there is no detectable atomic hydrogen gas.

A cut through the major axis is shown in Figure 2.16. Again, the central hole in the H I distribution is visible. This cut was made at position angle 205°. The projected linear velocity gradient across the central region is about 3 km/s/arc sec. The emission in the southwest has a remarkably flat character, out to the H I arm, seen at a distance of about 200″. The emission in the northeast has more bends and bumps, and a falling character, most clearly seen at the position of the H I arm, at a distance of 160″. No H I absorption is found near the location of the central continuum emission.

Atomic Hydrogen Gas Velocity Dispersion

The observed velocity dispersion is showed in Figure 2.5 for the naturally weighted set. The peak dispersion in the naturally weighted image (26.2 km/s) occurs at R.A.
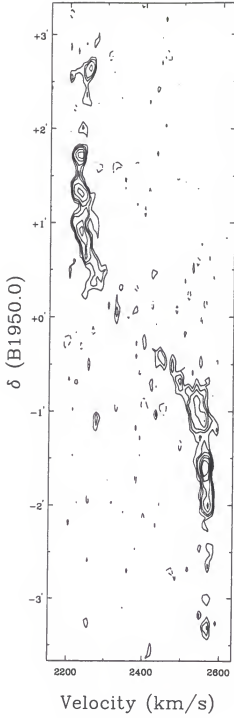
Figure 2.16: A position-velocity slice across the major axis in the naturally weighted data cube at position angle 205°. The center position along the y axis corresponds to the kinematical center at R.A. 23^h 02^m 26.52s, Dec. +12° 03′ 7″.9. The contour levels are 0.28 (1σ rms) x (−2, 2, 4, 6, 8, 10) mJy/beam. Negative contours are shown as dashed lines.

23^h 02^m $23^s.11$, near some of the strongest emission in the southern part of the western arm. In this area, emission is detected from nine successive channels, therefore having a very large velocity width (perhaps as large as 90 km/s). A typical velocity dispersion in the part of the disk where the rotation curve is flat is about 8–9 km/s. This is an upper limit for the true, intrinsic velocity dispersion. Our finite channel width and the beam width contribute to the observed velocity dispersion. Farther out in the disk, the effect of beam smearing is relatively small, since the velocity curve is flat, and curvature effects are small. Therefore, the average velocity dispersion, which has contributions from both the perpendicular and in-the-plane components, is unlikely to be very different from typical spiral galaxy gas vertical dispersions, 5 – 10 km/s, as measured for face-on galaxies (Lewis 1984).

Detection Experiment

Motivated by speculation of a recent interaction in Quillen et al. (1995) and the asymmetric nature of the spiral structure, I made a search for low luminosity, hydrogen-rich satellite galaxies around NGC 7479. These observations were made on June 4, 1995. For the detection experiment I chose a large bandwidth, 6.25 MHz, with thirty-one 195.3 kHz (41.9 km/s) channels. The total time on-source was 29.5 minutes. 2328+107 was used as a phase calibrator and its observations bracketed that of NGC 7479. 3C 48 (0134+329) was observed once at the beginning of the detection experiment to obtain flux and bandpass calibration. Data reduction proceeded in the same way as described in the previous section. Parameters used in these observations are given in Table 2.8.

I made a naturally weighted map after subtracting the continuum from the line channels in the u-v-space. The data were gridded with $12''$ x $12''$ cells into a 256 x 256 pixel map, covering a total field of $51'$ x $51'$. This map was inspected for noise

Table 2.8: VLA observational parameters in the detection experiment.

Target	NGC 7479
Observing date	June 4, 1995
Field Center, R.A. (1950)	$23^h\ 02^m\ 26.8$ s
Dec. (1950)	$12°\ 03'\ 06''$
Number of Antennas	26
Shortest Baseline	0.035 km
Longest Baseline	1.03 km
FWHP (primary beam)	$30'$
Central Velocity Channel	2380 km/s
Number of channels	31
Velocity separation of channels	41.9 km/s
Total integration time on target	29.5 min.
Synthesized beam	$52''.7 \times 46''.9$
Position angle of beam	$45°$
Channel rms noise	0.1 K

in the channel maps, and after determining the average noise level, 0.0006 mJy/beam (0.1 K), the whole data cube was cleaned down to one sigma rms noise level (0.0006 mJy/beam). The 1σ noise in the cleaned maps is 0.00042 mJy/beam.

Simpson (1995) has made a search for weak 21 cm atomic hydrogen emission with the VLA. She proved the Gaussian nature of the noise. I also studied the character of the noise in the channel maps. An example is shown in Figure 2.17. The noise can be well approximated by a Gaussian. Therefore, I used Gaussian statistics in evaluating the probability of a high flux value as a true detection. Following Gaussian statistics,
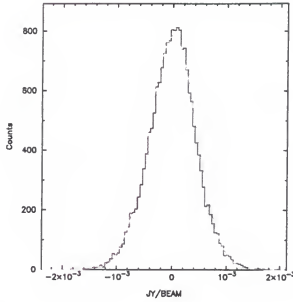
Figure 2.17: Histogram and a Gaussian fit to the noise
in channel 23 of the detection experiment data set.

in a map 256 x 256 = 65536 pixels in size, one would expect 0.04 pixels per channel
to appear above the 5σ level. Thus, if a pixel with flux above the 5σ level were to be
found, it would very likely be a detection.

I inspected the channel maps using this detection criterion as a first cut. I treated
pixels with values > 4σ as possible detections and performed further tests to investigate
whether any of these were true detections.

One would expect velocity continuity in a true detection. The true linewidths, v_c,
can be calculated from

$$\Delta v_{obs} = \sqrt{(2v_c)^2 + (\Delta v_{ch})^2}\,. \qquad (2\text{--}22)$$

where Δv_{obs} is the observed velocity width and Δv_{ch} is the channel width (41.9 km/s).
If the observed velocity width is 2 x 41.9 = 83.8 (the satellite appears in two successive
channels), the intrinsic velocity width (or rotational velocity) is only about 35–40 km/s,
which is very low. On these grounds I expected to see emission in at least two successive

channels in the same location, or very near to it. An inspection of the channels of the cube revealed that there are no 5σ peaks in the same location in two or more successive channels, but there might still be weaker emission in adjacent channels.

To determine whether this is true, I looked at the spectra in a phase space covering four pixels in both right ascension and declination directions beyond the last detected 5σ pixel, and three velocity channels (about 126 km/s) below and above the detected emission. Some of the detection candidates did not show emission in the nearby region in adjacent channels at even 3σ level. I discarded these as noise spikes.

NGC 7479 was also observed in the same run with a different correlator setting, giving 10.4 km/s channels. These observations have noise that is independent of the detection experiment. By averaging four channels in this other set of observations, I looked for emission at the locations of the detection candidates in the detection experiment data. No flux above 2σ noise level was found at the locations of the suspect emission. I conclude that NGC 7479 does not have any hydrogen-rich companions within $\pm 12'$ (115 kpc) of its center and ± 440 km/s of its systemic velocity. An upper H I mass limit for any satellite is obtained if the highest integrated flux in the moment zero map is averaged over a reasonable positive signal area. The result using the formula (A-16) in Appendix A is $(2.4 \pm 0.7) \times 10^8$ $M_{\odot}$, where the error corresponds to one sigma noise in the moment map. This upper limit is probably very conservative, as slightly negative values were actually found at the location of this peak in the other, independent D configuration moment zero map.

In conclusion, it appears that NGC 7479 does not have any interacting companions that possess significant amounts of neutral hydrogen. This conclusion is supported by the preliminary results of Benedict (1995, private communication), who independently undertook a deep photometric search for faint companions around NGC 7479, and

found none. The asymmetric spiral structure, strong bar, and the strong concentration of molecular gas in the center must then be explained by a recent merger, where the companion has been tidally disrupted, or by intrinsic dynamical evolution of NGC 7479. More discussion on these issues can be found in Chapters 5 and 6.

Discussion of the Atomic Hydrogen Observations

While the atomic hydrogen 21 cm observations have revealed many important perturbations in the gas disk of NGC 7479, longer integration times are needed in order to study the 21 cm emission at high resolution and sensitivity. The B configuration observations are useful in revealing the location and structure of the most intense emission, but they do not detect and resolve the lower level emission in spatial scales up to $2'$ to which the B configuration is sensitive. Therefore, we must await further improvements in detector sensitivity.

The first striking feature in these observations is the asymmetric structure of the H I emission. This is seen also in the optical and near-IR data (Chapter 4). There are basically two explanations for this structure. It must be either a result of the intrinsic evolution of an isolated disk galaxy, or the outcome of an interaction/merger. The situation is somewhat similar to the morphology of Magellanic barred spirals (e.g. Odewahn 1994, 1996). These galaxies often have an offset bar (not seen in NGC 7479) and one strong spiral arm, with one or more minor arms starting from the ends of the bar, which is exactly what is seen in NGC 7479.

However, asymmetries in the H I distribution and spectra are not unusual. Richter and Sancisi (1994) discuss asymmetries in disk galaxies, mostly based on evidence from single dish H I global spectra. They conclude that H I asymmetries can be seen in at least 50% of disk galaxies in a sample that includes about 1700 galaxies. They suggest that

these features may be long-lived, and stem from the era of galaxy formation. The features are not only seen in the gas and young star distributions, but also in the near-infrared, which samples the older stellar population. Therefore, either interactions and mergers must have been much more common than generally accepted, or the galaxy potentials must be asymmetric (m=1 instability).

It would be tempting to explain several peculiar features with the help of a recent interaction. The main argument against this interpretation is the lack of any visible companion near NGC 7479. The only remaining alternative is the possibility of a merger that has disrupted the (gas-rich) companion. I suggest that the strong, long western arm is the tidal counter-arm created by the inward spiraling companion. If the companion was reasonably massive, it could have contributed to the formation of the bar, which presumably is young (less than $5-10 \times 10^8$ years, Friedli & Benz 1995; Friedli, private communication). These issues are further addressed in Chapters 5 and 6 that present results from numerical simulations.

The velocity field shows a peculiar behavior of decreasing inclination with distance from the center. Also, the two halves (receding and approaching) have very different velocity fields. The most likely explanation is again a perturbation by a recent interaction. It would be most rewarding to obtain stellar kinematical data and compare them to gas kinematics. The gas may not trace reliably the dynamics of the galaxy, because (as noted before) gas suffers dissipation in shocks. Our lack of knowledge of the three-dimensional structure makes the interpretation of the velocity field even more uncertain.

CHAPTER 3
MOLECULAR GAS OBSERVATIONS

Introduction

The previous chapter on atomic hydrogen observations revealed a wealth of details about the distribution and kinematics of the interstellar gas in NGC 7479. However, this galaxy has a central hole in its atomic hydrogen distribution. Therefore, another tracer of gas distribution and kinematics must be used in the central, bar-dominated region. A natural candidate is molecular gas, which is known to be more centrally concentrated in spiral galaxies than the atomic hydrogen. Most of the molecular gas is hydrogen molecules, H_2. Unfortunately, molecular hydrogen does not have any readily detectable transitions in the optical or radio regimes. It has no permanent electric dipole moment, and the lowest quadrupole transitions (relatively weak) occur in the near-infrared. In addition, H_2 has been detected in absorption in the UV, but these lines require observations from space, and, as all other ultraviolet observations, suffer from the limitations set by interstellar scattering and absorption (extinction) at these short wavelengths. Thus we must observe the second most common molecule, carbon monoxide (CO). Although the H_2/CO abundance ratio is of the order of $10^5 - 10^6$, CO has a permanent dipole moment, and its rotational states are quantized in such a way that the energy differences produce mm-wave radiation. As I discuss in Appendix C, CO can be used as a tracer for the most abundant molecule, H_2, although not without problems. Another tracer for the interstellar gas, ionized hydrogen, will be discussed in the next chapter.

Molecular gas is of interest also because it is thought that star formation occurs in the dense molecular clouds of the interstellar medium (ISM). Therefore, the distribution of molecular gas should reveal locations within the galaxy where star formation might occur. Naturally, other factors will have to be taken into account as well, such as the differences between the shearing time-scales and free-fall time-scales, rotation, magnetic fields etc., but molecular material can nevertheless serve as a first order tracer for the likelihood of star formation.

Since we are forced to use radio observing techniques, the instrumental resolution will set a restriction to the detail at which we are able to study the molecular gas properties in external galaxies. Again, use of aperture synthesis techniques is desirable. This technique is discussed in Appendix B. The theory of the 2.6 mm CO emission, and molecular mass estimation from the 2.6 mm emission are discussed in Appendix C. In this chapter I will describe the calibration and imaging procedures and then discuss the results from the CO observations. These observations will be compared to other observations and simulations in Chapters 5 and 6.

Molecular Gas Observations of NGC 7479

The Owens Valley Radio Observatory[1] (OVRO) Millimeter Array, near Big Pine, California, consists of six 10.4–meter dish antennas. The telescopes can be stationed along an East-West baseline and along a North-South baseline that ends at the East-West baseline. The maximum baselines are 200 m East-West and 235 m North-South. Each telescope has two receivers, one for the 3 mm band (85–115 GHz) and the other for the 1 mm band (200–270 GHz). The telescope setup cycles through three different configurations, where A configuration is the most compact, and C configuration has the

---

longest baselines. The pointing accuracy of the telescopes is about $5''$. Spectral coverage for these observations was obtained by 128 channels, each having a channel width of 4 MHz (10.4 km/s). Further details about the technical aspects of the array are in Padin et al. (1991).

NGC 7479 was observed in all three configurations, A (Oct. 7 1994), B (Nov. 23–24 1994) and C (Jan. 18–19 1995). The total integration times at each of the three observed positions and other observing parameters are given in Table 3.1. The observations in each configuration consisted of one track (about eight hours). The total single sideband temperatures, including the effects of the atmosphere, were typically 350–500 K. The pointing was checked at the beginning of a track. The strong quasar 3C454.3 served as a passband and gain calibrator, and also as a secondary flux calibrator. It was observed every 19 minutes. Weather conditions during the observations were very good for each of the three tracks, and no technical problems were encountered during these observations. Five antennas were available in the A configuration and six in both the B and the C configuration. Variations in the sky opacity and receiver gain were corrected through measurements of an ambient temperature chopper wheel.

Calibration and Mapping

The data from each track were calibrated separately. The calibration procedure is described in Scoville et al. (1993). The passband was derived from observations of the passband calibrator. Next, an antenna-based amplitude and phase calibration were done using the gain calibrator. As maximum acceptable amplitude and phase errors I used $10°$ and 20%. Finally, observations of the planet Neptune and the secondary flux calibrator 3C 454.3 were used in the flux calibration. A minimum requirement for the coherence (roughly the ratio of the scalar-averaged to vector-averaged visibility over about four

Table 3.1: Observing parameters for the OVRO 2.6 mm CO observations of NGC 7479.

Parameter	Value
Pointing center 1	R.A. 23^h 02^m $25^s.99$
	Dec. $+12°$ $02'$ $24''.2$
Pointing center 2	R.A. 23^h 02^m $26^s.30$
	Dec. $+12°$ $03'$ $09''.0$
Pointing center 3	R.A. 23^h 02^m $26^s.61$
	Dec. $+12°$ $03'$ $53''.7$
Central frequency	114.37 GHz
Central velocity (LSR)	2340 km/s
Configurations used	A, B, C
Total number of antennas	A=5, B=6, C=6
Field of view	$63''$
Baseline lengths	4.0 - 92.7 kλ
Total integration time, p.c. 1	350 min.
Total integration time, p.c. 2	360 min.
Total integration time, p.c. 3	360 min.
Absolute flux calibrator	Neptune, T_B = 114 K
Gain, passband and secondary flux calibrator	3C 454.3
Velocity resolution	10.4 km/s
Total observed bandwidth	464 MHz = 1206.4 km/s

minutes of integration) of 90% for a point source was used to guarantee that the flux calibration is based on good quality data and gives us reliable flux values for the galaxy.

I used AIPS to produce channel and integrated maps of the CO emission. The u-v data sets include the continuum adjacent to the frequency band of the line observations, channel 0 and four separate, partly overlapping line data sets; altogether six u-v data sets per position. I made maps of the continuum with the task 'MX' and no cleaning. These maps did not reveal any emission within the limits of the noise. This means that no continuum subtraction was necessary for the line data.
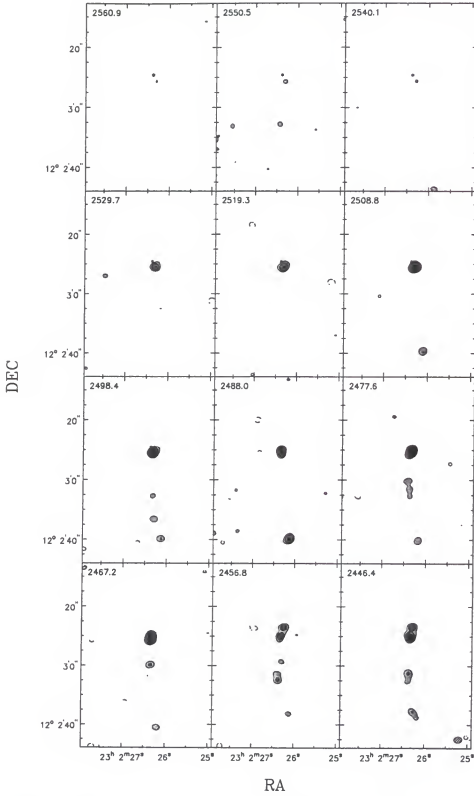
Figure 3.1: The channel maps of the naturally weighted CO cube. The contour levels are 0.015 x (-3, 3, 5, 8, 12, 15) mJy/beam. The star marks the K band nucleus. The central channel velocity is at the top left, and the beam at the bottom right of the last frame.
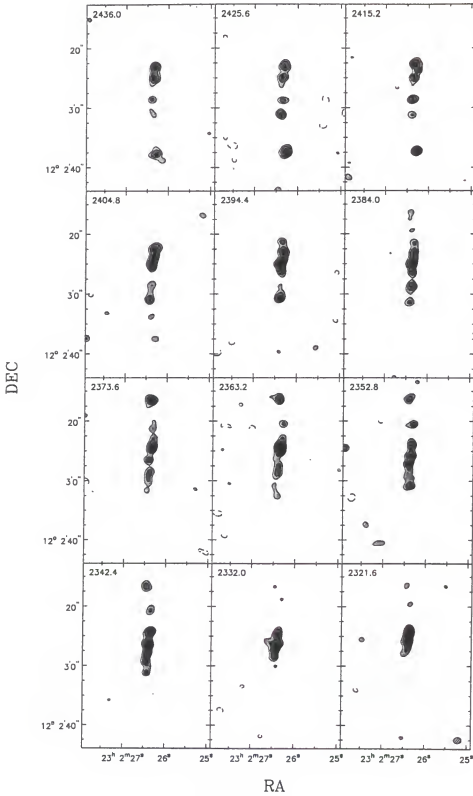
Figure 3.1: (Continued)
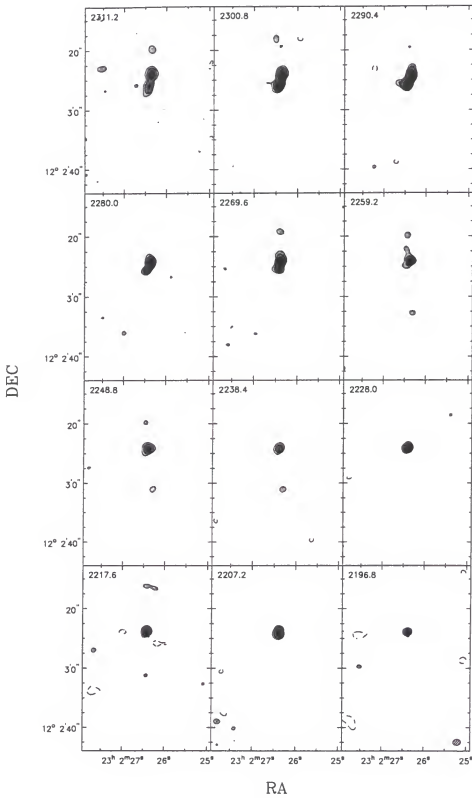
Figure 3.1: (Continued)
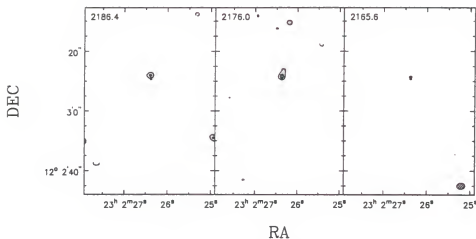
Figure 3.1: (Continued)

I made maps of the combined u-v data with the task MX. Natural weighting was used. Uniform weighting does not give a significantly higher resolution because of the array configuration. Natural weighting produces the highest sensitivity and is therefore justified. I used 0.015 mJy/beam (about 1.4 x rms noise in the final, cleaned maps) as the stopping criterion for the cleaning iterations. The final beam size and other map parameters are given in Table 3.2. I used the AIPS task 'LTESS' to build a mosaic image of the three observed positions. LTESS also corrects for the attenuation of the primary beam, whose FWHM is 63″. The channels containing emission in this mosaic data cube are displayed in Figure 3.1, and the parameters of the maps are listed in Table 3.2.

Molecular Gas Moment Maps of NGC 7479

The moment maps of the CO $(1 \rightarrow 0)$ emission in NGC 7479 were made much in the same way as the H I emission maps. The naturally weighted data cube was first smoothed along the velocity axis using Hanning smoothing. The velocity-smoothed cube was then smoothed spatially with a beam that made the effective resolution $6″ \times 6″$. The rms noise in the smoothed cube was checked and pixels in the original cube that had flux values below 2 x rms noise at the corresponding location in the smoothed cube

Table 3.2: Parameters of the ^{12}CO channel maps.

Parameter	Value
Size of synthesized beam	$2''.7$ x $2''.1$
Linear size of synthesized beam	262 pc x 204 pc
Position angle of synthesized beam	-85°
Weighting used to make maps	Natural
Rms noise in channel maps	0.011 = 0.18 K
Expected rms noise in channel maps	0.016 = 0.26 K
Peak brightness temperature	3.83 K
Radio continuum flux density[a]	< 4 mJy

[a]A 5σ upper limit is given for a point source

were blanked. Finally, the data cube was integrated over the velocity axis, requiring that the pixel value be at least 2.5 x rms noise and that there is emission in at least two consecutive velocity channels at the same spatial location. This way most of the noise spikes that show up in one channel only at any spatial location were eliminated. The resulting integrated molecular CO emission map, velocity field and second moment map are displayed in Figures 3.2 – 3.5. The velocity field near the nucleus is shown magnified in Figure 3.4. The units of the integrated emission map have been converted to N(H$_2$) cm^{-2} with the "standard conversion factor" (Bloemen et al. 1986; Scoville et al. 1987; Kenney & Young 1989), calculated from

$$N(H_2)cm^{-2} = 2.8 \times 10^{20} \int T_B(CO)dv \ K \ kms^{-1}. \qquad (3-1)$$

The uncertainties in this conversion have been discussed in Appendix C. For the metal-rich nuclear region of the NGC 7479 the formula above may cause the molecular hydrogen column density and the molecular mass to be slightly overestimated.
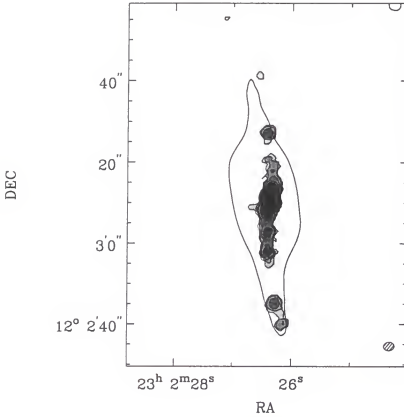
Figure 3.2: The naturally weighted integrated map of CO $(1 \rightarrow 0)$ emission. The contour and grayscale levels are 40 x 10^{20} (1, 2, 4, 8, 12, 24, 36) H_2 molecules cm^{-2}. The contour around the CO emission is the 17.1 mag $arcsec^{-2}$ contour of the K band image, showing the location of the stellar bar. The beam is shown at the bottom right corner of the map.

Results and Discussion

Total Flux

The total CO flux was calculated by summing up the flux in the channel maps. The fluxes in each channel were measured in a large rectangular area around the emission seen on the TV display, with dimensions of the box up to $30''$ (R.A.) x $60''$ (Dec.). The fluxes found are given in Table 3.3, and the spectrum is plotted in Figure 3.6. The total integrated flux is (275 ± 40) Jy km/s. The flux from FCRAO single dish observations for the central $45''$ of NGC 7479 is (430 ± 65) Jy km/s (Kenney 1996, private communication). The uncertainties in the interferometer flux include point source calibration errors ($\pm 15\%$) and the uncertainty in the signal-to-noise ratio (5%). The
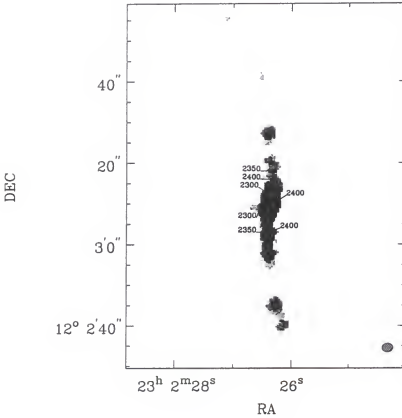
Figure 3.3: The naturally weighted velocity field at about 2."5 resolution superposed on a grayscale map of the CO emission. Only the lowest emission levels have been plotted in the grayscale map. The velocity contours have been plotted from 2220 km/s to 2510 km/s in 10 km/s intervals. Some of the velocity contours have been labelled in km/s. The beam size is indicated by the ellipse at the bottom right corner.

errors were added quadratically. The estimated channel fluxes are generally precise to within 5%. The uncertainty in the single dish flux is caused by the conversion from Kelvins to Janskys, where a source distribution somewhere between a point source and a uniform distribution is assumed over the beam area (diameter $45''$). Another source of error is again point source calibration.

At least $(64 \pm 20)\%$ of the flux has been detected by the high resolution OVRO interferometer observations. The remaining flux could be in spatial frequencies "resolved out" by the interferometer. Alternatively, the single dish value could be wrong, and the interferometer may have recovered essentially all the flux. Since I believe the missing flux
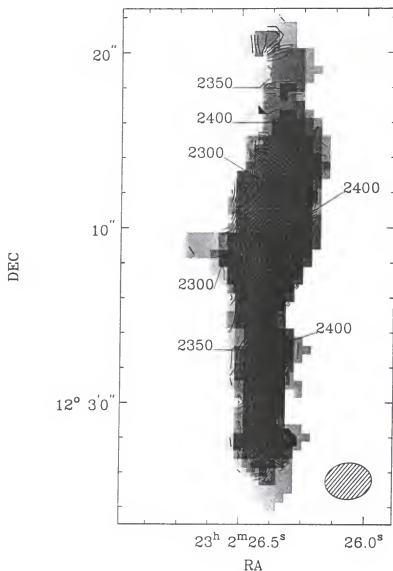
Figure 3.4: A magnified image of the central CO velocity field superposed on the integrated emission map. The contours and grayscale are the same as in Figure 3.3.

will not affect the detected high resolution CO kinematics, I will not make an attempt to search for the possibly missing flux.

Molecular Gas Distribution

The zeroth moment map was presented earlier in Figure 3.2. To complement this map I have generated another map, showing the peak emission at each spatial location. This map is shown in Figure 3.7.
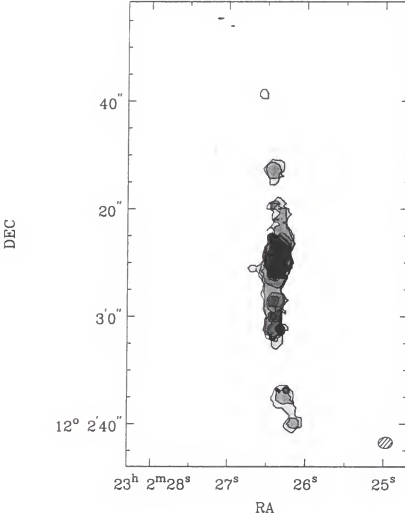
Figure 3.5: The naturally weighted second moment map of CO emission in NGC 7479. The contours and grayscales are 5, 10, 20, 30, 40, 50, 60, 70, 75, 80, 90 and 100 km/s. The beam is shown at the lower right corner.

All the CO emission occurs along nearly linear ridges that are displaced towards the leading edges of the bar (assuming that the spiral arms are trailing). Near the center, the emission smoothly crosses the center along a position angle $-10°$, connecting the two linear ridges.

The emission is highly clumpy. In the moment zero image we can identify at least seven separate clumps. If we use the standard CO-to-H_2 conversion factor, and multiply the resulting masses by 1.35 to correct for Helium and other molecular gas, the masses

Table 3.3: CO channel fluxes.

Ch. vel. [km/s]	Flux [Jy]	Ch. vel. [km/s]	Flux [Jy]
2560.9	0.057	2352.8	1.364
2550.5	0.069	2342.4	1.278
2540.1	0.092	2332.0	0.846
2529.7	0.239	2321.6	1.011
2519.3	0.321	2311.2	1.043
2508.8	0.688	2300.8	0.937
2498.4	0.643	2290.4	0.676
2488.0	0.590	2280.0	0.437
2477.6	0.630	2269.6	0.584
2467.2	0.658	2259.2	0.474
2456.8	0.870	2248.8	0.531
2446.4	0.825	2238.4	0.417
2436.0	1.112	2228.0	0.150
2425.6	1.443	2217.6	0.092
2415.2	0.963	2207.2	0.242
2404.8	0.885	2196.8	0.119
2394.4	1.059	2186.4	0.072
2384.0	1.400	2176.0	0.158
2373.6	1.267	2165.6	0.051
2363.2	1.319		

of these clumps vary from 5 x 10^7 $M_\odot$ to 5 x 10^8 $M_\odot$. The mass in the nucleus (within 6'' of the central peak) is about 2 x 10^9 $M_\odot$. The total mass of molecular gas, calculated from a moment map in which all the data have been integrated, is about 4 x 10^9 $M_\odot$. The nuclear emission accounts for approximately 50% of the detected CO emission. These masses are lower limits, if all the flux has not been recovered in the interferometer observations and the CO to H_2 conversion factor is correct.

In Figure 3.7 we see that in addition to the nuclear peak of emission there appear to be two other weak peaks symmetrically placed around the nucleus, some 3'' − 4''
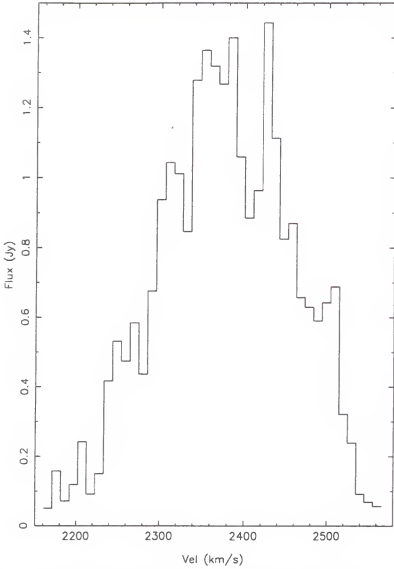
Figure 3.6: The spectrum of the CO emission detected with the OVRO millimeter interferometer. The channel fluxes have uncertainties on the order of 5 %.

towards south-southeast and north-northwest. These locations may indicate a zone where the gas streaming in the circular orbits near the center and the gas in the elongated orbits associated with bar intersect. However, no great concentration of star formation is seen near these points. This could be caused by high shear in these regions, or alternatively by high collision velocities that disrupt the clouds. The large amount of dust could also hide the regions of star formation.
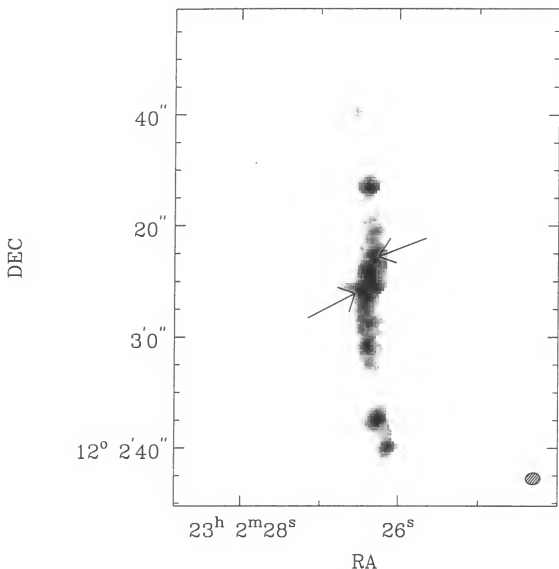
Figure 3.7: A map of CO emission made by taking the peak flux density value at every spatial pixel location. The location of the symmetrical peaks, discussed in the text, are shown with arrows.

The CO emission near the center of the galaxy, seen in the moment zero map, has a bar-like shape, elongated along the north-south direction. Since this feature is only marginally resolved, no definite conclusions can be drawn on the existence of a nuclear molecular bar. No stellar nuclear bar at a similar orientation can be found in the optical or near-infrared images (Chapter 4). Therefore, it is more likely that the elongated gaseous feature is caused by the combination of gas in the nuclear disk, discussed further in
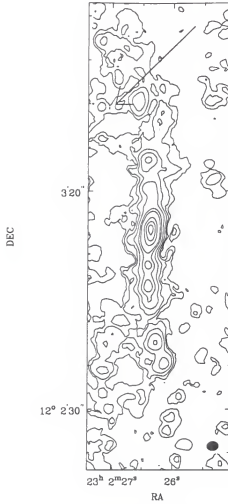
Figure 3.8: A sensitive map of CO emission made with the help of a mask, as explained in the text. The contour values are 3.94 (peak) x (0.01, 0.02, 0.04, 0.08, 0.16, 0.24, 0.5, 0.7 and 0.9) Jy km/s. The arrow shows the track of the perpendicular dust lane discussed in the text.

the section on CO kinematics, and radial gas streaming along the bar dust lanes in the stellar bar.

Weaker CO emission can be seen in Figure 3.8. This map was made using another cube as a mask. The masking cube was constructed from the original by Hanning smoothing along the velocity axis and then spatially smoothing the emission in each channel with a $6''$ x $6''$ beam. After this all pixels that had a value below 2 x the rms noise in the smoothed cube were blanked in the original cube. After blanking, the moment map was made by integrating all the unblanked pixels.

Emission in Figure 3.8 can be detected along the optically visible (Chapter 4) perpendicular dust lane at the end of the northern bar dust lane, and near the southern tip of the central radio continuum feature, at 23h 02m 27s, 12° 02′ 45″. A region of low emission is seen near the northern bar end. Emission in the bar-spiral arm transition zone is not detected in the south.

Molecular Gas Kinematics

Velocity field

Some of the general kinematic characteristics can be seen in the velocity field maps (Figures 3.3 and 3.4). The only area where the velocity contours are well organized is the center, where a mirrored S-shaped structure can be seen. The position-velocity maps, together with the tightly packed set of parallel velocity contours in the center, imply a rapidly rising rotation curve. The position angle of this rapidly rotating central disk may be estimated from the orientation of the tightly packed set of velocity contours, which, in the presence of circular rotation, should be oriented along the kinematical minor axis. A rough estimate by drawing a line perpendicular to the velocity contours gives a position angle 204° (the receding half) for the major axis of the central CO disk. This is almost identical to the kinematical major axis found for the atomic hydrogen component in Chapter 2, 202°. Therefore, it appears that the central CO and the outer H I disks are in the same plane.

Outside the central 2″ (also roughly the beam size), the velocity contours bend strongly to form the top and the bottom of the mirrored S-shaped figure. This implies that there is another kinematical component in addition to the disk with circular rotation near the center. Since the CO emission occurs close to the major axis of the galaxy, the observed velocity will trace mostly the azimuthal motions, but it will also have

a small, highly projected, radial component. From orbital theory (Contopoulos & Papayannopoulos 1980; Contopoulos 1983; Teuben & Sanders 1985; Athanassoula 1992a) we know that the dominant family of orbits supporting the bar, x_1 in the notation of Contopoulos, is elongated along the bar. Minor modifications take place when there is a shock (e.g. Roberts et al. 1979). Again, further discussion of this issue can be found in Chapter 6.

The emission outside the mirrored S-shaped region occurs mostly at velocities close to 2350 to 2400 km/s in the first moment map. Some emission is seen at velocities below 2350 km/s at the northern tip of this region, and some at velocities above 2400 km/s near the southern tip. These velocities are not consistent with the circular rotational velocities expected within the central $40''$ radius from the H I rotation curve, since the circular velocities (the rotation curve) must rise rapidly here to reach the 170 km/s value in H I observations at $40''$. A much better understanding of the motions in the nucleus and along the bar is given by the position-velocity plots, which are presented next.

<u>Position – velocity plots</u>

Often more information on the kinematics can be found in position-velocity plots than in the moment maps. Position-velocity plots close to the major axis (at a position angle 25°), close to the minor axis (position angle 115°) and along the bar are presented in Figures 3.9 – 3.11. All the plots go through the peak CO emission point as determined from the map of integrated CO distribution.

The plot along the CO major axis gives a hint of the existence of two separate kinematic components. The first one is a velocity gradient across the central few arc seconds that shows rotation in the same sense as the outer H I disk (higher velocities towards smaller declinations, and vice versa). The velocity width of this emission is

roughly 380 km/s, as can also be seen in the channel maps. If we assume that the rotation takes place in the same plane as the outer disk, the total width of the emission becomes about 500 km/s, which implies rotation velocities of 250 km/s near the center. Perhaps part of this width is contributed by the large streaming motions near the center. As we recall from Chapter 2, the H I rotation curve rises only out to about 220 km/s. If the kinematic center of rotation is at about 2375 km/s as was found in Chapter 2 for the H I gas (CO velocities are in LSR units and can be obtained from the heliocentric velocities by addition of 4.5 km/s), the CO emission seems to extend much farther out toward lower velocities than toward higher velocities. This could mean that there is an offset of about 20–30 km/s between the kinematical centers of the H I and CO disks, since the CO centroid velocity is close to 2345 km/s. A similar effect, but of a smaller magnitude, is found by Hurt et al. (1996) in Maffei 2, which has an offset of 11 km/s between the systemic velocities of the CO and the H I components. Hurt et al. attribute this difference to a recent gravitational disruption, or interaction. However, for both Maffei 2 and NGC 7479, the spatial position of the kinematical center is the same within positional uncertainties for both the CO and H I emission.

The second component can be seen as an extension towards lower declinations and lower velocities and higher declinations and higher velocities around the center in the major axis plot. This component can also be seen in the position–velocity plot along the bar. In the south, after a short excursion towards lower velocities, the emission shifts back toward higher velocities, most likely because the noncircular motions are not as extreme farther away from the center. However, the emission along the bar never reaches the enormous width it has near the center. The practically unresolved clumps of emission along the bar dust lanes have velocities close to the systemic velocity, from 2350 km/s to 2420 km/s. Based on the models presented in Chapter 5, the large radial motions along

the bar are the main contributors to the velocities along the bar. The models show that the radial velocities along the bar may have projected components of ±150 km/s.

The minor axis plot, perhaps somewhat surprisingly, shows a large velocity width in the center. A literal interpretation would mean that we see radial motion at all velocities from 0 to ±200 km/s. This situation appears unlikely. Instead, we are probably seeing the effects of beam smearing. In each observed channel, the beam (about $2''.5$) will cause emission to be seen even at locations ($\pm 1''$) where there is no emission. If these observations were made with a beam that resolved the emission, we would see only a constant plateau of emission along the systemic velocity. The only plateau visible in the minor axis plot occurs at 2300 km/s. It is likely caused by the radial streaming motions.

The first moment velocity field map can be somewhat misleading. The mirrored S-shaped velocity field we see near the center gives the impression of there being a lot of emission at intermediate velocities at locations toward north and south of the center. In Figure 3.11, I have plotted a slice along the bar in the first moment map on top of the bar position-velocity plot. This plot shows that the velocities in the first moment map do not always follow the velocities of the most abundant emission. Rather, the first moment image follows the central, circularly rotating component near the center, and after that it smoothly switches to follow the emission from the bar streaming component.

Molecular Gas Velocity Dispersion

As can be seen in Figure 3.5, the CO velocity dispersion attains very high values near the center. This can be attributed mostly to the large velocity gradient of the circular motion (beam smearing), and the transition from the circular kinematics of the central molecular disk to the elongated streaming motions in the barred region.

To obtain an estimate of the intrinsic velocity dispersion of the molecular gas, we must use the clumps of emission lying farther out in the bar. Here, a more typical value for the dispersion is 10–12 km/s, which is on the high end of the values for CO and H I velocity dispersions. The H I intrinsic dispersion found in Chapter 2 was about 8 km/s. The large values for the CO dispersion could be due to the perturbed motion caused by the vicinity of the bar shock or star formation winds along the bar.

Kenney et al. (1993) modeled the distribution, kinematics and the velocity dispersion in NGC 3504. The molecular gas is remarkably well behaved near the center of NGC 3504, and a simple model can be built. However, the molecular gas in NGC 7479 is behaving in a different way. The gas distribution is strongly elongated along the bar dust lanes, and the kinematics show very large effects by noncircular motions and the central,
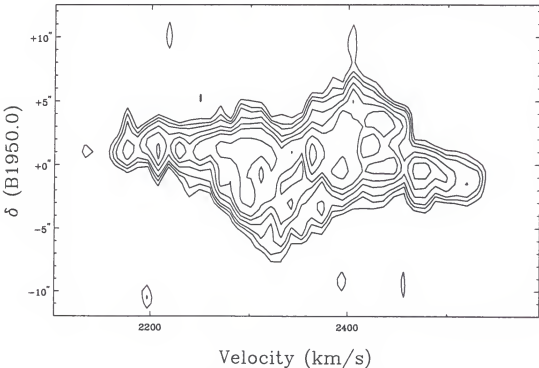
Figure 3.9: The major axis CO position-velocity plot. The contours are at 0.011 x (2, 3, 4, 6, 8, 10, 14, 18, 22, 24) Jy/beam.
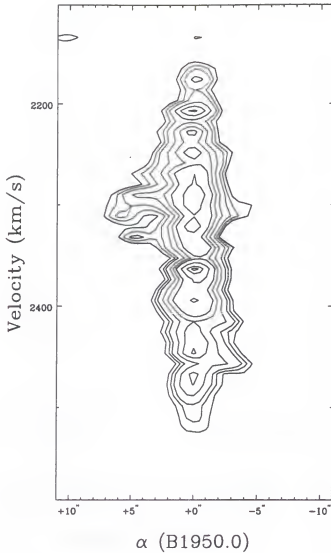
Figure 3.10: The minor axis CO position-velocity plot. The
contours are at 0.011 x (2, 3, 4, 6, 8, 10, 14, 18, 20) Jy/beam.

fast-rotating molecular disk is hardly resolved. For these reasons I do not attempt to make

any simple model for the molecular gas near the center of NGC 7479. Modeling with a

fully nonlinear SPH scheme is presented in Chapter 5 and discussed further in Chapter 6.

Dynamical Effects of the Bar on the Molecular Gas

Interferometric studies of molecular gas near the centers of (barred) spiral galaxies

(e.g. Lo et al. 1984; Ball et al. 1985; Canzian et al. 1988; Ishizuki et al. 1990a,b;
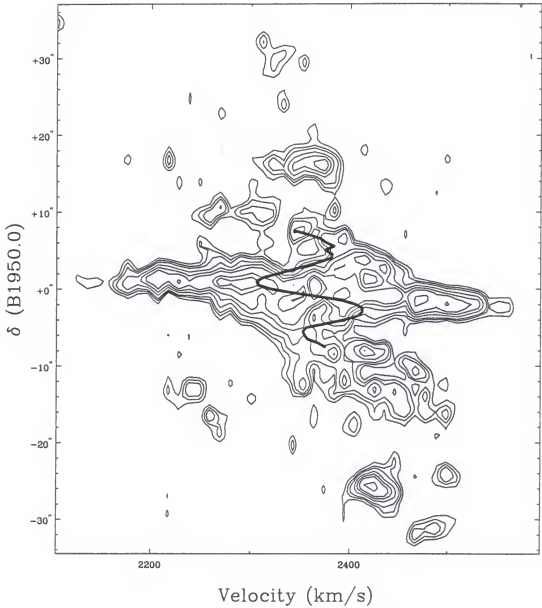
Figure 3.11: The CO position-velocity plot along the bar. The contours
are at 0.011 x (2, 3, 4, 6, 8, 10, 14, 16) Jy/beam. Values from a slice at the same
position angle (177°) across the first moment map have been plotted as a thick line.

Devereux et al. 1992; Kenney et al. 1992, Kenney et al. 1993; Regan & Vogel 1995;

Sakamoto et al. 1995; Benedict et al. 1996) have revealed a wealth of morphologies and

kinematic structures. These have been summarized by Kenney (1996a,b). The different

morphologies include patchy molecular gas rings (NGC 4314, NGC 4321, twin peaks near

the regions where the bar dust lanes intersect the nuclear ring (NGC 3351, NGC 6951), emission along the bar dust lanes (M 83, M 101), molecular gas arms trailing the stellar arms (IC 342, NGC 6946) and centrally concentrated emission (NGC 3504, NGC 4102).

The gas behavior appears to depend on the dynamics through the existence of resonances. In the vicinity of ILRs, the self-gravitational effects in the gas were predicted by Shlosman et al. (1989) and later modeled by Knapen et al. (1995). If there are inner Lindblad resonances, the gas will tend to accrete at radii near these resonances. These resonances cannot completely prevent the gas from falling towards the center. Further inflow is possible through gas instabilities, with the help of dissipation and self-gravity (Wada & Habe 1992, 1995; Sakamoto et al. 1995; Wada 1996). The gas also collects in the leading bar dust lanes, which are the locations of shocks. Star formation is not always observed in these dust lanes, especially in the earlier Hubble type barred spirals (Phillips 1996). One reason for this could be that the strong shear in the shocks and the high velocities with which the molecular clouds impact the bar may prevent star formation (Tubbs 1982; Athanassoula 1992b; Kenney & Lord 1991). Other explanations include an insufficient gas density for triggering of gravitational instabilities (Kennicutt 1989, 1990; Kenney & Lord 1991) or gas passing through the bar perturbation much quicker than through spiral arms. After passing the center and shock of the gas, the gas streamlines diverge and the collapse of a molecular cloud can no longer be supported (Kenney & Lord 1991).

The inflow rates of the gas are usually not directly observable. The gas loses angular momentum by the gravitational torques on the leading dust lanes inside corotation (Combes 1994) and possibly through hydrodynamic torques in the bar dust lanes (Regan et al. 1997). Some other investigations have concluded that the hydrodynamic forces have a negligible contribution (Barnes & Hernquist 1991; Hernquist & Mihos 1995), but

they considered the global hydrodynamic torque, not the local torque in the bar dust lanes. The gas is shocked in the leading dust lanes and loses angular momentum and energy. An inflow results, but averaged over the whole orbit of the gas cloud, it amounts to only a few km/s (Athanassoula 1994), possibly more in NGC 7479 (Quillen et al. 1995). The different inflow rates in the earlier results could arise from using a steady-state or an time–dependent potential, or from the assumed ISM properties (effective viscosities).

The shock lanes are often associated with velocity jumps in the ionized gas. These have been observed in the ionized gas, e.g., in NGC 1365 (Jörsäter 1984) and in NGC 6221 (Pence & Blackman 1984). There, velocity gradients of 130 km/s over a distance of $90''$ can be detected. Because the dust lanes are parallel to the major axis of the bar, and the bar is relatively close to the kinematical major axis of NGC 7479 ($20°$ – $25°$, the observations are mostly sensitive to azimuthal motions (across the bar), and should therefore be ideal for determining shock velocity discontinuities. Unfortunately, the resolution is only $2''.7$ across the shock lanes. Also, CO may not be an ideal tracer of shocks, if the molecular gas is mostly in massive molecular clouds that behave like ballistic particles. Only the diffuse gas experiences the shock. This gas is better examined with Hα position-velocity slices in Chapter 4.

To study the kinematical behavior of the molecular gas across the bar dust lanes, I took several position-velocity slices across the bar. The positions where the slices were taken are shown in Figure 3.12. The slices themselves are presented in Figures 3.13–3.15. The emission across the shock is not resolved. However, CO emission can be found in a narrow column only a few arc seconds wide but with a velocity width of more than 100 km/s. This could be an effect of shocks, but it is probably caused by the contribution from both outgoing and ingoing radial orbits within the beam across the bar. The evidence for shocks remains elusive in the CO observations. Higher resolution is needed.
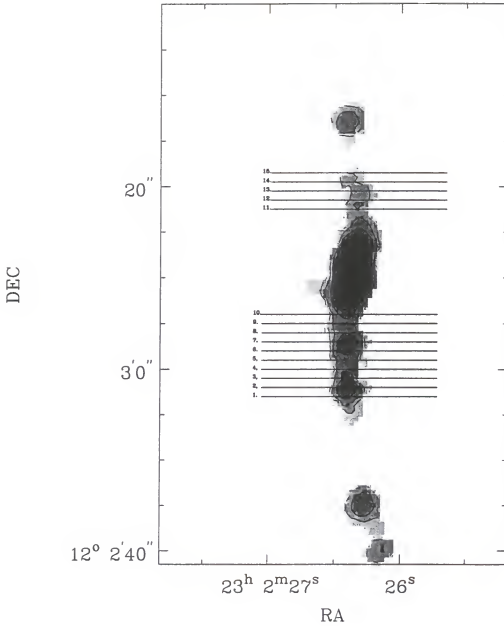
Figure 3.12: The positions of the slices taken to examine the effects of shocks in the CO are shown on top of the zeroth moment CO map. The grayscale and contour levels are the same as earlier in Figure 3.2.

As argued recently by Sofue (1996) and earlier by Sørensen et al. (1976), if a strong bar is aligned with the major axis of the disk, it should be possible to estimate the bar pattern speed from observations of gas shocked regions of the bar dust lanes. This is true because the gas in the shock is not moving azimuthally very much with respect to
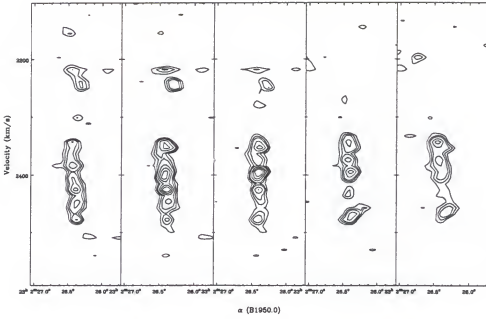
Figure 3.13: Position-velocity plots of slices 1.–5. (see Figure 3.12). The contour levels are 0.011 x (2, 3, 4, 6, 8, 10) Jy/beam.
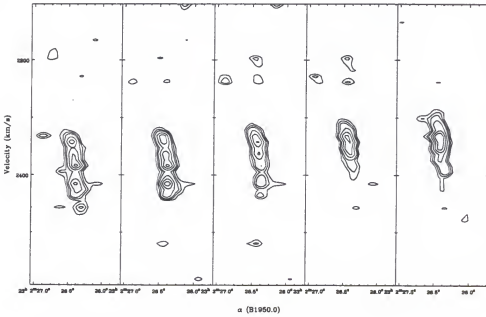
Figure 3.14: Position-velocity plots of slices 6.–10. (see Figure 3.12). The contour levels are 0.011 x (2, 3, 4, 6, 8, 10) Jy/beam.

the bar. Thus the main azimuthal, or tangential, movement is that of the bar. The radial motions will be undetectable if the bar lies along the major axis of the disk.
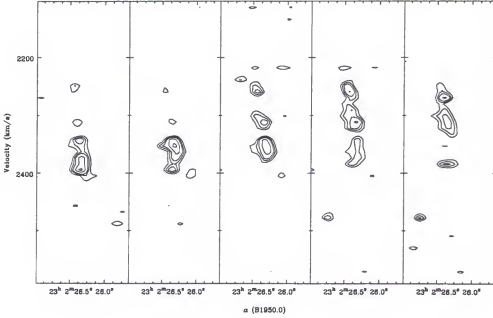
Figure 3.15: Position-velocity plots of slices 11.–15. (see Figure 3.12). The contour levels are 0.011 x (2, 3, 4, 6, 8, 10) Jy/beam.

NGC 7479 is a good candidate for detecting such velocities. The angle between the bar shock lanes and the major axis of the disk is only about 30° in the plane of the galaxy. The radial motions are expected to cause some uncertainty in the results. The emission along the bar is presented in Figure 3.11. It can be seen that a velocity gradient, much shallower than that in the central CO disk, is detectable along the bar. However, not all emission outside the central disk is concentrated along a single, well-defined line. This probably means that there is an appreciable contribution from radial motions, at least near the center, where the inverse-S shaped distortion is seen in the first moment map. On the other hand, the outermost detected emission is close to the end of the bar (±30″ from the center), where azimuthal motion across the bar may be considerably larger. Using only points within about 10″ − 25″ from the center, a rough estimate for the pattern speed is

about 2 km/s/arcsec, which is corrected for the inclination of the disk (51°). This would mean that the corotation is very far out in the disk, at radii over $100''$. This contradicts the results obtained for the bar pattern speed obtained earlier by, e.g., Sempere et al. (1995) and Aguerri et al. (1996), who place the corotation near $55''$ to $65''$. However, because of the large radial streaming motions occurring along the bar, the uncertainties in this estimate for the pattern speed are large. In Chapter 4 I find that the radius of the bar is only about $40'' - 45''$ and the simulation results presented in Chapter 5 give a pattern speed that brings the corotation radius close to the end of the bar, near $50''$.

The molecular gas mass in the center can be a large fraction of the total dynamical mass (Turner 1994; Kenney 1996b). Under these conditions, the self-gravity of the molecular gas becomes important and drives further inflow towards the center (Shlosman et al. 1989; Shlosman et al. 1990; Heller and Shlosman 1994; Knapen et al. 1995; Wada and Habe 1992). The gas fraction in the central disk of NGC 7479 can be calculated from the observed linearly rising part of the CO emission in the major axis plot, and with the standard CO luminosity to H_2 mass conversion factor. The velocity width near the center, as seen from Figure 3.9, is about 380 km/s. If the rotation takes place in the same plane as the outer H I disk, we must correct for the inclination by dividing by sin 51°. Then the rotation velocity will become roughly half of that value, 245 km/s. Because of beam smearing, it is somewhat difficult to assess the radius of this maximum velocity, but the emission appears to come from a disk ± 1 arc second from the center. Using a distance of 32 Mpc, the central mass becomes

$$M_{dyn} = \frac{rv^2}{G} = 2.2 \cdot 10^9 M_\odot. \tag{3-2}$$

The molecular mass from equation (3–1), applied to the central $2'' \times 2''$, and correcting for helium by a factor of 1.35, becomes 3.3 x 10^8 $M_\odot$. Molecular gas forms a considerable

part of the total mass in the center, 15%. However, the uncertainties in this calculation are large. The radius of the central linearly rising part of the rotation curve is uncertain by at least 50%, and the areas used for calculating the dynamical mass and the molecular mass are different by 75%. In addition to all this, the uncertainty in the CO to H_2 conversion factor is a factor of two.

The relationship of star formation and molecular gas abundances will be discussed in Chapter 6, and the comparison of CO data to numerical simulations will be made in Chapter 5.

OPTICAL AND NEAR-INFRARED OBSERVATIONS

Introduction

The previous chapters have discussed the interstellar gas distribution and kinematics
in NGC 7479. Because gas is dissipative, its response to the gravitational potential
is different from the stars. While this property can be employed to derive important
information about the dynamics and star formation, observations of the stellar component
are imperative if we are to understand the gravitational potential and the stellar populations
of a galaxy. For example, the linear theory of stellar orbits can not be applied to the
gaseous components. Unfortunately, extinction of the stellar light within the observed
galaxy causes great uncertainties in the interpretation of the results based on optical
observations. This problem is less severe, but not completely negligible, at near-IR (1 –
5 μm) wavelengths. Rapid progress in the near-IR regime has been made during the last
10–15 years, and near-infrared array cameras and spectrometers have become available.
A lot of work remains to be done in this area, for example, pushing the wavelength limit
to longer and longer values. Ultimately, we may be able to do high resolution far-IR
and submillimeter mapping from space.

The technology to make extensive spectral mappings of the stellar component in
optical wavelengths remains to be developed. The best results so far have come from
long-slit spectroscopy, where the spectra are taken along a narrow slit, cutting the image
of the galaxy at a certain angle. Complete mapping of galaxy disks using this technique
would require prohibitive amounts of observing time. In the near future, we can look

forward to the arrival of near-infrared spectral arrays, which can map the spectra across the array, pixel per pixel. The sensitivity of these arrays will hopefully soon reach the limit when we can start mapping the faint outer regions of distant galaxies (10 – 100 Mpc) with high spatial resolution (less than 100 pc).

The resolution of the optical and near-IR images is generally much better than in radio observations. With the help of the Hubble Space Telescope and some clever image processing, details smaller than $0.''1$ can be resolved. Since $0.''1$ at a distance of 10 Mpc is about 5 pc and 50 pc at 100 Mpc, the sample of galaxies that can be studied in detail will greatly increase. These high resolution studies can address, for example, the following problems:

1. Can a central disk in the galaxy nucleus be seen in active galaxies? What is the color of the central disk?

2. What are the motions of the stars in different parts of a stellar bar and in the halo?

3. What is the phase difference of new born stars, the dust lanes, and gas accumulations in the spiral arms?

In this investigation, the optical and near-infrared images are mainly used to compare the gas distribution to the stellar distribution. Also, the regions of star formation are identified from their color indices and $H\alpha$ emission, and their location compared to the gas observations presented in Chapters 2 and 3. The near-IR observations have been used as the basis for extracting the stellar bar potential in NGC 7479, used in Chapter 5 in the gas simulations. The dust lane structure, as revealed by the color indices and optical images, will also be addressed in this chapter.

First, I will discuss the data reduction of the UKIRT J, H and K images, as these were obtained specifically for this investigation. I will briefly describe the other data

sets, which have been kindly given to me by various colleagues around the world. I will then present the optical and near-infrared images, and also some color index images. The technique of obtaining a gravitational potential from these images will be reviewed. Finally, I will present a data cube of Hα observations of NGC 7479, kindly given for my use by Dr. Stuart Vogel and Mr. Mike Regan from the University of Maryland. These images will be used in Chapter 6 to compare the ionized hydrogen gas distribution and motion to other gaseous and stellar tracers of the dynamics and star formation in NGC 7479.

UKIRT Near-Infrared Observations of NGC 7479

The United Kingdom Infrared Telescope (UKIRT) is a 3.8–meter infrared telescope on Mauna Kea, Hawaii, at an altitude of 4,194 m. It is an f/35 Cassegrain telescope. The effective aperture is reduced by the chopping secondary mirror to 3.75 m. The seeing on Mauna Kea at 2.2 μm can be as good as $0.''5$. It is about $0.''8$ in the images taken for this project. The pointing accuracy of the telescope is of the order of $1''$, and it tracks to within $2''$ per hour, and considerably better if an autoguider is used.

As the detector, the new 256 x 256 InSb array in the IRCAM3 instrument was used. The array operates at a temperature of 35 K. Imaging can be done through J (1.25 μm), H (1.65μm), K (2.2 μm) and L′ (3.8 μm) broad band filters. The pixel scale is $0.''286$/pixel. The limiting magnitude for a point source, assuming a $0.8''$ seeing and a $2''$ software aperture, is 18.2 mag for a 5σ detection in 100 seconds in the K band. For J and H the limiting magnitudes are higher by 1.6 and 0.8 mag, respectively.

NGC 7479 was observed through the Service Observing program (a program to allocate short scientific observations without writing a formal proposal to a time allocation committee) at the UKIRT telescope on July 14 1994 in J, H and K bands. The observed

position, the exposure times, the calibration star and other observing parameters are presented in Table 4.1.

Table 4.1: Parameters in the UKIRT J, H and K observations of NGC 7479.

Parameter	Value
Observed RA (B1950)	$23^h02^m26.6^s$
Observed Dec. (B1950)	$+12°03'15.''6$
Exposure time (J)	20 sec
Exposure time (H)	15 sec
Exposure time (K)	10 sec
Number of exposures per frame (J)	3
Number of exposures per frame (H)	4
Number of exposures per frame (K)	6
Total integration time on source (J)	5 min.
Total integration time on source (H)	5 min.
Total integration time on source (K)	10 min
Calibration star FS 31[a] K mag	14.039 ± 0.010
FS 31 RA (B1950)	$23^h09^m50.4^s$
FS 31 Dec. (B1950)	$+10°30'46''$

[a]Landolt (1983); Turnshek et al. (1990).

For absolute magnitude calibration, standard stars were observed from the lists of Landolt (1983) and Turnshek et al. (1990). The two closest in time and celestial coordinates were FS 29 and FS 31. Unfortunately, the exposure times used for FS 29 were found to be erroneously long, and the data corrupted by saturation. Therefore, only FS 31 was used in the calibration.

The observations of NGC 7479 and the surrounding sky were made in blocks of ten observations using the sequence OBJ/SKY/OBJ/SKY... Each "frame" consisted of a number of exposures so that the total integration time was 60 seconds per frame. Small offsets (±5″ in the sky frames) were made between each frame to allow for median

filtering. Small offsets ($\pm 3''$) were included in the object frames to enable bad pixels to be smoothed out. The observed sky position was $100''$ east of the observed galaxy position, outside the visible disk of the galaxy (although at very long exposures some faint emission at this distance could be found, but it is unlikely to affect the photometry done with the short exposures here). The airmass during the observations was steady and around $1.00 - 1.05$, and has not been corrected for in the subsequent analysis.

I subtracted the nearest dark images from the galaxy and sky frames. After dark subtraction, I median-combined the sky frames taken in the J, H and K bands into three flat fields. In this process, I rejected the lowest and highest pixel values to eliminate spurious values caused, for example, by cosmic rays. After this I divided the individual sky and galaxy frames by the flatfield image in each band. I calculated the mode in each flatfielded sky frame. This mode was taken as a representative sky value and subtracted from the galaxy frame nearest in time. Next I checked the positions of several stars on the galaxy images and moved the images so that the positions of the control stars overlapped. I then combined the shifted images. With the help of images of FS 31 I converted the units on the images to magnitudes.

I checked the calibration against the data from Forbes et al. (1992). The results from this comparison are presented in Table 4.2

As it can be seen, the integrated magnitudes in the J and H bands agree with each other to better than 0.10 mag between the data from Forbes et al. and the new observations. However, in the K band the difference appears to be larger in the sense that Forbes et al. magnitudes are brighter than my magnitudes. Forbes et al. observed NGC 7479 at the Cerro Tololo observatory 4 m telescope. The reason for the discrepancy is not clear. The rms errors in the measurement of the standard star magnitudes in the new observations are at least an order of magnitude smaller than the 0.1 mag difference. Forbes et al. report

Table 4.2: Comparison of the J, H and K observations with the data from Forbes et al. (1992).

Aperture	$3''$	$6''$	$12''$
Band	J		
Forbes et al.	13.44 mag	12.45 mag	11.55 mag
New UKIRT data	13.34 mag	12.43 mag	11.55 mag
Band	H		
Forbes et al.	12.58 mag	11.63 mag	10.83 mag
New UKIRT data	12.50 mag	11.67 mag	10.84 mag
Band	K		
Forbes et al.	11.92 mag	11.15 mag	10.36 mag
New UKIRT data	12.00 mag	11.25 mag	10.49 mag

an rms error in the standard star measurements of ±0.06 mag. Forbes et al. corrected the magnitudes for the atmospheric extinction, but since the airmasses for the standard stars and the galaxy were practically identical, and the observations were made within an hour of each other, it is doubtful that the neglect of this correction in the new observations could have affected my magnitudes. Other systematic error sources, as discussed by Forbes et al., include errors in the sky background level. As suggested by Regan and Gruendl (1995), ideally the observations of the galaxy and the sky should be made in a mosaic, because the sky background may vary in short time scales. Therefore, errors in the sky background are a possible source for the discrepant integrated magnitude values. Another candidate for the difference between the two sets of observations is the intrinsic variability of the galactic nucleus. Since the K band may include some contribution from the hot dust, it may be affected by the radiation from the central engine more than the J and H bands. NGC 7479 has been classified as a LINER galaxy by Keel (1983a). Eracleous et al. (1995) have suggested a duty cycle for the LINER activity. Although this explanation remains unlikely because the observations were taken within a few years of each other, it warrants further higher resolution investigations, preferably

with the Hubble Space Telescope, of the nucleus of NGC 7479. The nucleus will be further discussed in Chapter 6.

The final possible explanation for the fainter UKIRT magnitudes is the lack of calibration stars. As the calibration is based on the observations of a single standard star, the systematic error can be large. However, I consider errors on the order of 0.1 mag to be acceptable, as the results of this investigation do not critically depend on the photometrical accuracy. Errors as small as these are often found when comparing the data from different authors, and it may be difficult to judge which data set has the correct calibration.

I have calculated the noise in the images by selecting empty areas in the sky frames and measured the rms noise in these regions. The true noise is then computed by dividing the rms noise by $\sqrt{N}$, where N is the number of frames averaged to obtain the final image. Finally I converted this noise into mag/(arc second)^2 with the help of the calibrated zero-point. The final noise values are J: 22.18 mag/(arc second)^2; H: 21.68 mag/(arc second)^2; K: 21.26 mag/(arc second)^2. The calibrated J, H and K images from these observations are presented in Figures 4.1 – 4.6, and the corresponding color index images in Figures 4.7 – 4.9. The results from these observations are discussed in the next section.

The color index images were made using the following algorithm in GIPSY:

$$result = -2.5 \cdot log[(img1 - bground1)/(img2 - bground2)] \qquad (4–1)$$

where img1,2 are the images in counts/sec units and bground1,2 are the background values determined on the image. The seeing in all images is around $0.''8$, so no smoothing to the same resolution was needed.

In addition to these near-IR images, I have acquired J, H and K images of the whole galaxy, taken by Quillen et al. (1995). Here I will show only the K band image (Figure
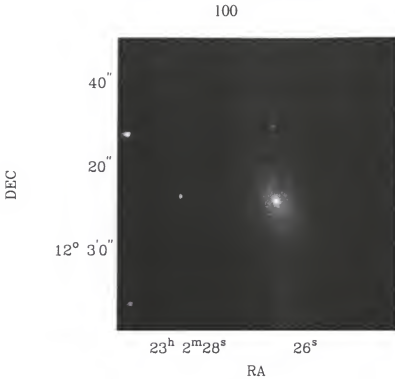
Figure 4.1: A J band image of the nucleus and the bar in NGC 7479.
The range in magnitudes shown is from 14.3 to 26.2 mag/(arc sec^2).

4.10), which was used in extracting the gravitational potential for the simulations. This procedure in described in some detail in Quillen et al. (1994, 1995) and in Chapter 5 of this dissertation. The FWHM of stars in these images is about $2.''6$, and the pixel size $1.''5$, so they are spatially undersampled.

Results from the UKIRT Observations

The dust lanes along the bar are still clearly visible in the J band image. In the nucleus, the isophotes seem to move towards a position angle 45°, which is also seen in the H and K band images. Although the extinction caused by dust is generally ten times less in K band magnitudes than in the V band magnitudes, the apparent change in the isophotes may still be the effect of dust extinction. Apparently there is a lot of warm dust near the center, since NGC 7479 was clearly detected in the mid-IR observations by Telesco et al. (1993). Devereux (1987, 1989) has also concluded that this galaxy
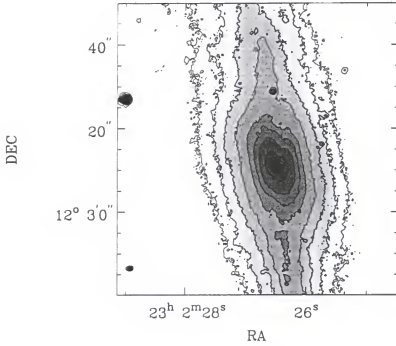
Figure 4.2: A grayscale and contour J image of the nucleus and bar in NGC 7479. The contour intervals are (14.5, 14.7, 15.1, 15.45, 15.8, 16.2, 16.6, 17.1, 17.4, 17.7, 18.1, 18.5, 18.9 and 19.3) mag/(arc sec^2).
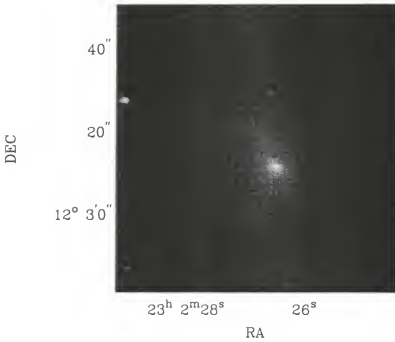
Figure 4.3: An H band image of the nucleus and the bar in NGC 7479. The range in magnitudes that are shown is 13.8 to 20.3 mag/(arc sec^2).
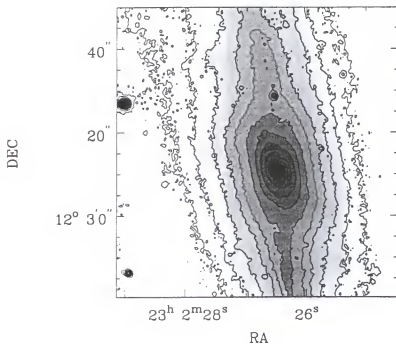
Figure 4.4: A grayscale and contour H image of the nucleus and bar in NGC 7479. The contour intervals are (13.9, 14.1, 14.45, 14.75, 15.1, 15.45, 15.75, 16.1, 16.45, 16.75, 17.1, 17.45, 17.75, 18.1, 18.45 and 18.75) mag/(arc sec^2).
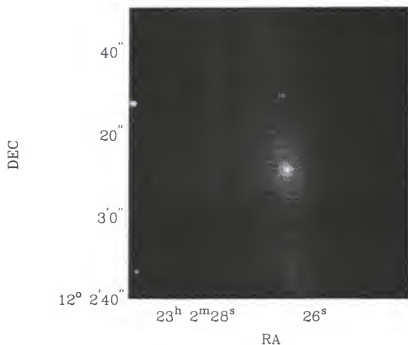
Figure 4.5: A K band image of the nucleus and the bar in NGC 7479. The range in magnitudes that are shown is 12.9 to 22.0 mag/(arc sec^2).
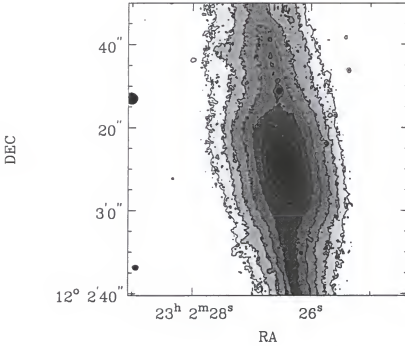
Figure 4.6: A grayscale and contour K image of the nucleus and bar in NGC 7479. The contour intervals are (13.3, 13.7, 14.0, 14.6, 15.0, 15.4, 15.8, 16.15, 16.5, 16.9, 17.3, 17.7, 18.1 and 18.5) mag/(arc sec^2).

has a dusty nucleus that is heated by an internal source to cause the large and centrally concentrated 10 μm flux.

Wozniak et al. (1995) and Friedli et al. (1996) have studied the isophote twists in several disc galaxies including NGC 7479. They conclude that NGC 7479 is too dusty to interpret the isophotal twist as a triaxial structure or a nuclear bar. The high inclination should also prevent a nuclear bar from being seen. Friedli et al. (1996) claim that if the inclination is greater than 45°, the characteristic features of the double bar disappear. Roche et al. (1991) detect strong silicate absorption at 9.7μm in the mid-infrared in the nucleus of NGC 7479. This strong absorption may indicate a visual extinction of a few tens of magnitudes. The dust is still slightly visible in a high contrast K band image on the computer screen. However, Baumgart and Peterson (1986) have interpreted the twist in the position angle of the isophotes as a sign of a triaxial bulge. I conclude that there
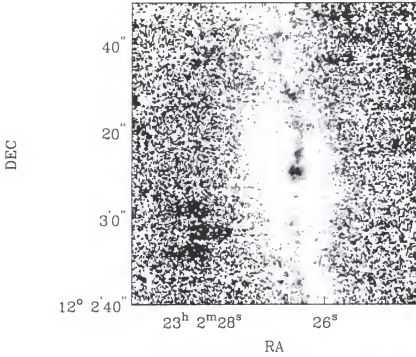
Figure 4.7: A grayscale J–H color index image of the nucleus and the bar environment in NGC 7479. The grayscale colors indicate color indices between 0 (white) and 1.2 (dark grey).
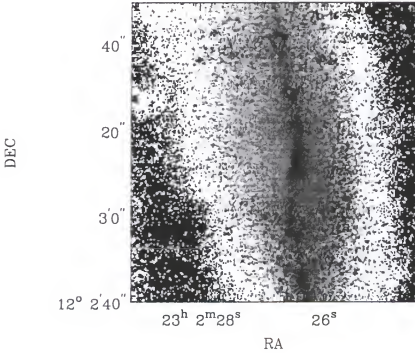
Figure 4.8: A grayscale J–K color index image of the nucleus and the bar environment in NGC 7479. The grayscale colors indicate color indices between 0 (white) and 2.2 (dark grey).
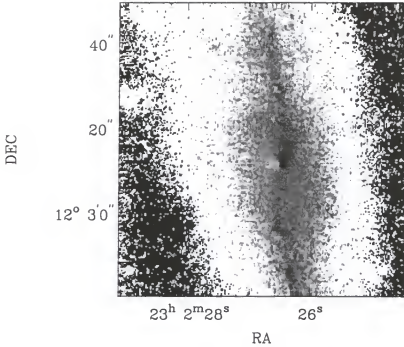
Figure 4.9: A grayscale H–K color index image of the nucleus and the bar environment in NGC 7479. The grayscale colors indicate color indices between 0 (white) and 1.1 (dark grey).

is no definite evidence for a triaxial bulge or a nuclear bar near the center of NGC 7479, because of the large uncertainties caused by the high extinction and the high inclination.

A luminous H II region can be seen in all the near-IR images close to the location of the northern dust lane about $15''$ north of the nucleus. The young stars of this H II region can be seen as a very blue spot on the red bar and red dust lanes in the color index maps. Counterparts in the CO emission and Hα images can also be found, although there may be some displacement between the gas peak and the stellar emission peak. This is further discussed in Chapter 6. Enhancement in the infrared images is also seen at an almost symmetrically placed location on the southern dust lane, but the emission is considerably weaker. No major dynamical resonances are expected at this radius, so the symmetry may be just a coincidence. I speculate that this northern blob is part of the remains of a recently disrupted companion. The southern half of the bar appears to be 0.2–0.3 magnitudes brighter than the northern half in all the near-IR bands. Elmegreen
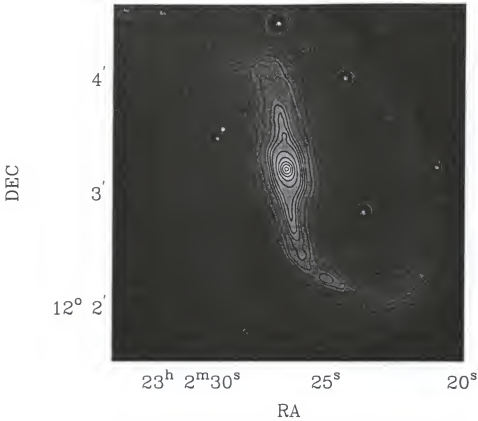
Figure 4.10: A K band image of NGC 7479. The contours are drawn at 14.9, 15.3, 15.7, 16.1, 16.5, 16.9, 17.1, 17.3, 17.5, 17.9, 18.2, 18.6, 19.0, 19.5 and 20.0 mag/(arc sec^2).

and Elmegreen (1985) have classified the surface brightness profile along the bar in NGC 7479 as flat. This means it is not decreasing as fast as the (exponential) disk around it. Earlier photometrical studies by Okamura (1978) and Blackman (1983) also showed this character.

An intensity profile along the bar is shown in Figure 4.11. The disparity in the surface brightness can be seen clearly in this image. The CO emission is also stronger and more extensive along the southern bar branch. The reason for this is unclear, but it could be related to the asymmetry seen in the spiral arms (the western arm being much more luminous and better defined than the structure on the eastern side) and indirectly to a minor merger scenario. The Hα emission appears to be stronger in the northern branch
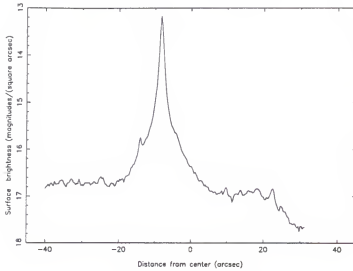
Figure 4.11: An intensity profile along the bar in the K band
image. North is towards the positive distances from the center.

of the bar, so the brightness variation can not be explained completely by enhanced star
formation. The strongest emission along the bar in the J, H and K images is shifted from
the major axis of the bar toward the bar dust lane, almost coinciding with it. So star
formation may contribute to the emission at these bands as well. However, as can be
seen in the color index images, especially J-K and H-K, the dust lanes can clearly be
seen as redder features than the rest of the bar. Part of this certainly comes from the
extinction and reddening by the cold dust and emission from hot dust, but part of it may
be contributed by emission from H II regions and red supergiants.

It is somewhat difficult to disentangle the various components that contribute to the
observed near-IR colors. In general, light from the giant stars of spectral classes K and
M of the old stellar population dominates the emission from nuclei, bulges and bars of
galaxies. This can be modified by contributions from 1) younger population supergiant
stars (luminosity class I); 2) young, massive blue stars (spectral classes O, B and A);
3) thermal radiation from dust heated either by X rays and UV radiation from a central
non-thermal source, or UV and optical radiation from OB stars from a recent starburst;

4) free-free and free-bound thermal bremsstrahlung from electrons in H II regions. The observed light and colors may also be affected by extinction that usually reduces the blue emission more than red, because the extinction is approximately proportional to $\lambda^{-1.85}$ (Landini et al. 1984), where λ denotes the wavelength.

The J-H colors of the dust lane are around 0.67–0.75. This color decreases to 0.61–0.62 in the bar outside the dust lane. Therefore, the difference between the dust lane and the surrounding region is about 0.06 magnitudes. Quillen et al. (1995) found this difference to be only 0.03, and combined with the much larger difference in the J-K color between these regions they argued that this is inconsistent with extinction difference only. The current observations could be interpreted in terms of extinction effects (see also below). However, the differences are almost within the errors and they cannot be given high significance. The J-H colors are fairly normal for a bulge stellar population, consisting mostly of giant stars (Telesco & Gatley 1984; Aaronson 1977). There could also be a significant contribution from supergiants, but their colors are very similar to those of giant stars, and additional data, such as near-IR spectra of the CO absorption feature near 2.3 μm are needed to separate the two. Outside the bar, the signal-to-noise ratio is so low that no definite conclusions can be drawn.

The J-K color of the dust lane is close to 1.0, and this color drops down to 0.9 in the bar around the dust lane, in agreement with Quillen et al. (1995). The most interesting effect can be seen in the H-K colors. These colors are found to be 0.35–0.45 in the dust lanes. According to Telesco and Gatley (1984) these H-K colors together with normal J-H colors could mean a significant contribution to the emission from hot dust and H II regions, indicating vigorous star formation activity. Devereux (1989) interpreted the H-K excess in starburst galaxies in terms of extra extinction from dust and thermal emission from hot dust and bremsstrahlung free-free and free-bound radiation

from electrons interacting with the atoms in H II regions. The energizing source in the nucleus could be nonstellar but in the bar it is likely to be young ionizing stars along the dust lanes in the bar. A 10–20% contribution to the emission from hot dust is capable of moving the observed H-K colors in the dust lanes from those of an old stellar population to 0.35–0.45 (Telesco & Gatley 1984).

U, B, V, R and I images of NGC 7479

I have acquired images of NGC 7479 in U(0.360 μm), B(0.440 μm), V(0.550 μm), R(0.700 μm) and I(0.880 μm) bands from collaborators. A set of B, V, R and I images were obtained by Pierre Martin and Daniel Friedli at the Steward Observatory 2.3 m telescope on Kitt Peak on October 13, 1993. The data reduction was done by the observers. They also provided the calibration factors. The seeing in these images is around 1.''5, and the pixel scale is 0.''3/pixel. The images cover a rectangular area of about 114'' x 175'' around the center of NGC 7479. Some of these images are presented in Figures 4.12 – 4.15.

I have obtained another set of U, B, V, R and I band images covering almost the whole visible disk. These data were kindly given to me by Drs. Varela and Prieto at the Instituto de Astrofisica de Canarias. The observations were taken during the night of 16–17 August, 1990, at the 2.5 m Isaac Newton telescope (Varela et al. 1996). The pixel scale is 0.''54/pixel, and the observations cover a field of about 300'' x 210''. The integration times varied from 1800 s in the U band to 400 s in the R and I bands. As a calibration star, Feige 24 (Landolt 1983) was used. The dark and sky subtraction and flatfielding were performed by the observers. I have reduced the image pixel units to mag/(arc sec^2) with the following formulas:

$$mag/arcsec^2 = -2.5 \cdot log\left[\frac{C_g}{T_g A_{pix}}\right] - K_g X_g + C - A_g \qquad (4\text{–}2)$$
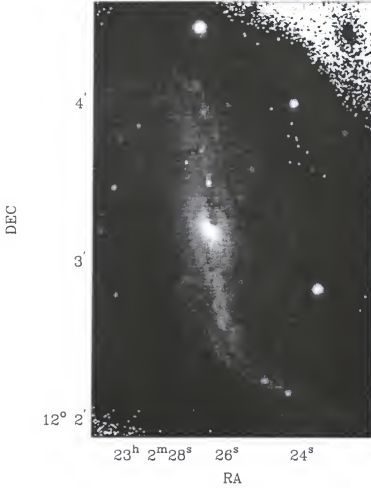
Figure 4.12: A V band image of the nucleus and the bar of NGC 7479. The range of magnitudes shown is 17.5 – 26.3 mag/(arc sec²).

and

$$C = m_c + 2.5 \cdot log\left(\frac{C_*}{T_*}\right) + K_* X_* \tag{4-3}$$

Here C_g and C_* are the counts from the galaxy and star, respectively, T_g and T_* are the integration times on the galaxy and the star, respectively, K_g and K_* are the extinction coefficients determined for that night, X_g and X_* are the airmasses for the galaxy and the star, respectively, A_{pix} is the size of the pixel in arc sec², m_c is the apparent magnitude of the calibration star, and A_g is the galactic extinction calculated from the formulas

$$A_V = 0.0998(cosec(|\,b\,|) - 1) \tag{4-4}$$
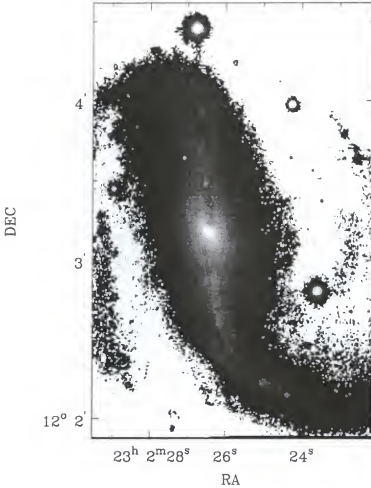
Figure 4.13: An I band image of the nucleus and the bar of NGC 7479. The range of magnitudes shown is $16.0 - 25.8$ mag/(arc sec^2).

(b = Galactic latitude of NGC 7479, $-42°.84$) and $A_U = 1.56A_V$, $A_B = 1.33A_V$, $A_R = 0.74A_V$ and $A_I = 0.47A_V$. Some of these images are presented in Figures 4.16 and 4.17.

In addition I have generated color index images using the formula 4.1. Shown here are the U-I (Figure 4.18) and B-V (Figure 4.19) images.

H–Alpha Data on NGC 7479

I have collected a set of Hα data on NGC 7479. These data include an Hα image by Rozas et al. (1996), and Hα Fabry-Perot observations by Vogel and Regan (private communication). Here I will present the high resolution Hα image by Rozas et al.
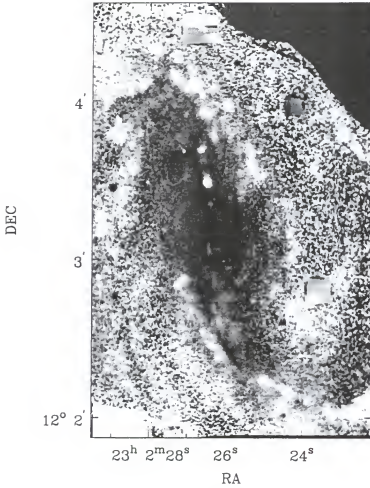
Figure 4.14: A B-V color index image of the nucleus and the
bar in NGC 7479. Color indices between 0 and 1.2 are shown.

(kindly given to me by Dr. J. Knapen) and the Hα velocity field from the Fabry-Perot
observations.

High Resolution H–Alpha Image

These data were gathered on September 9, 1990 with the Taurus narrow band imager
attached to the 4.2 m William Herschel Telescope in La Palma. The integration time was
1200 s for the line and the same for the adjacent continuum. The pixel size is 0.″279 x
0.″279. The resolution is about 0.″9. This image is shown in Figure 4.20.

DEC

4'

3'

12° 2'

23ʰ 2ᵐ28ˢ 26ˢ 24ˢ

RA
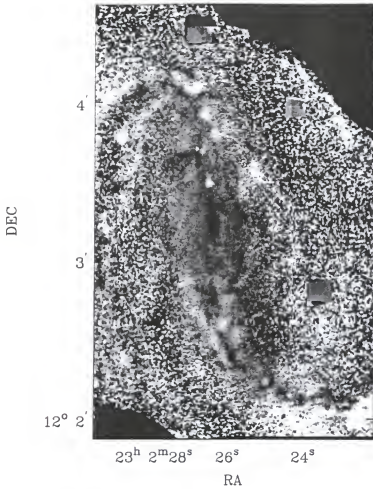
Figure 4.15: A V-R color index image of the nucleus and the
bar in NGC 7479. Color indices between 0 and 1 are shown.

Fabry-Perot Data of NGC 7479

In this section I present the velocity field from Fabry-Perot Hα observations kindly
given to me by Stuart Vogel and Mike Regan. These observations were made with
the Maryland-Caltech Fabry-Perot Spectrometer (see e.g. Vogel et al. 1995) attached
to the Cassegrain focus of the 1.5 m telescope at Palomar Observatory on September
29–30, 1994. 40 exposures were taken, each with a 500 second integration time. The
detector was a thinned Tektronix 1024 x 1024 CCD with 24 μm pixels, giving a pixel
scale of $1.''88$ per pixel. The velocity planes were separated by 12.0929 km/s. The
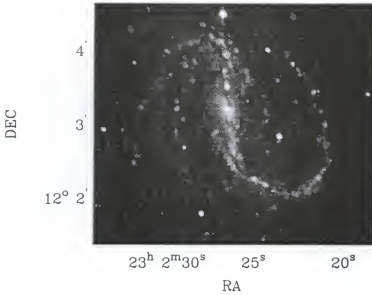
Figure 4.16: A U band image of NGC 7479. The range of magnitudes shown is 16.1 – 26.6 mag/(arc sec^2).
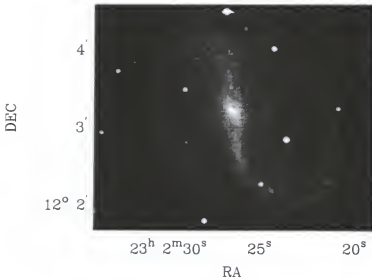
Figure 4.17: An I band image of NGC 7479. The range of magnitudes shown is 17.0 – 25.0 mag/(arc sec^2).

velocity uncertainty (rms) is roughly 1–2 km/s, and the images were smoothed to 11.″8 resolution so that even the weak emission can be recorded in these images. I also made position-velocity slices across the bar. The images are presented in Figures 4.21–4.25.
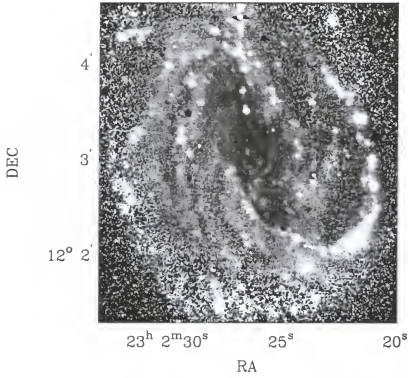
Figure 4.18: A U-I color index image of NGC 7479. The range shown is −1.5 − 3.0.
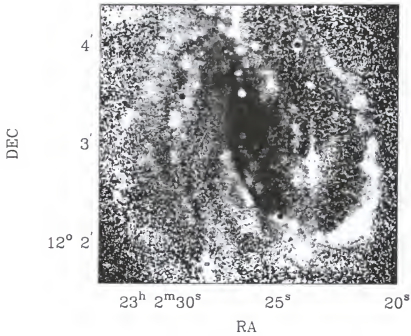
Figure 4.19: A B-V color index image of NGC 7479. The range shown is 0.0 − 1.5.
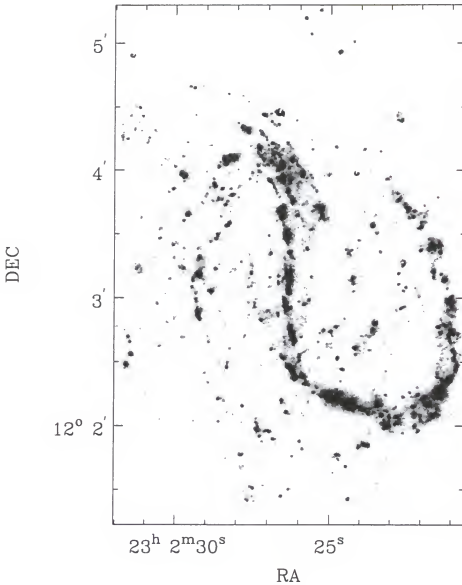
Figure 4.20: A high resolution Hα image of NGC 7479.

Discussion of the Optical Observations

Results from Optical Observations

The radius of the bar from these images appears to be about $35'' - 40''$. This radius marks the end of the straight linear part of the dust lanes and the associated emission from young stars and H II regions (e.g. Figure 4.12). This radius differs from the estimates
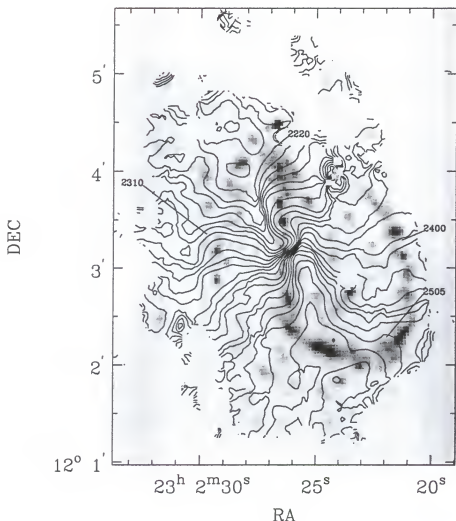
Figure 4.21: A low resolution (11."8) Hα velocity field superposed on a
grayscale Hα image of NGC 7479 with 3."6 resolution. Some of the
velocity contours have been labeled with corresponding velocities in km/s.

made by several other authors (Burbidge et al. 1960, Duval & Monnet 1985; del Rio

1995) who estimated that the end of the bar is close to $60''$ in radius. Deprojection of

the apparent radius with a $51°$ inclination does not change the result very much, because

the line of nodes ($22°$) is close to the major axis of the bar ($7°$).

The spiral arms seem to "overshoot" the end of the bar in both north and south. They

continue outside the bar close to the radius where the bulge becomes visible. This kind

of structure can be seen at early times in the bar simulations presented in Chapter 5. The
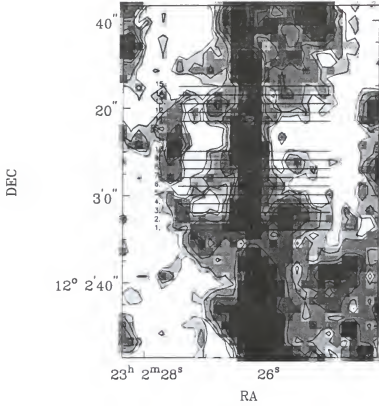
Figure 4.22: A low resolution Hα image showing the positions of position-velocity slices taken across the bar. The grayscale and contours are in arbitrary units.
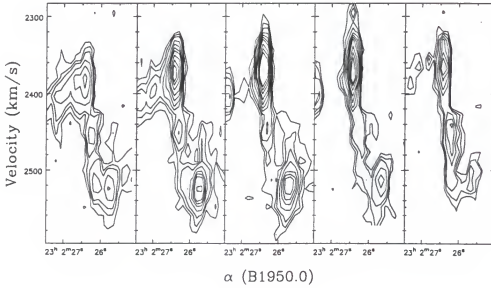
Figure 4.23: Position-velocity plots of slices 1-5, left to right (see Figure 4.22). The contours in arbitrary units are at 100, 150, 200, 300, 400, 500, 600, 800, 1000 and 1200.
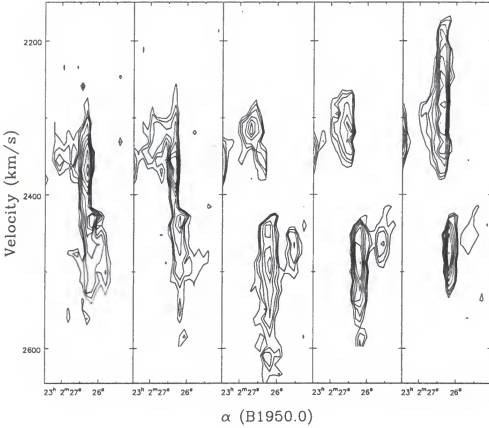
Figure 4.24: Position-velocity plots of slices 5-10, left to right (see Figure 4.22). The contours in arbitrary units are at 100, 150, 200, 300, 400, 500, 600, 800, 1000 and 1200.

dust lanes are slightly displaced towards the leading edges of the bar (assuming that the spiral arms are trailing). The southern bar dust lane seems to bifurcate about $14''$ to the south of the nucleus. This bifurcation is not clearly seen in the JHK images, indicating that the branch towards west is composed of cold dust. The dust in the major bar dust lane is heated by star formation. The bar dust lanes disappear near the aforementioned radius of the bar, $35'' - 40''$. At the ends of the bar, the spiral arm dust lane passes between the two, separating the bar and the arm components. There is a strong dust lane, perpendicular to the bar dust lane, at a radius of about $30''$ north of the nucleus. This dust lane is also weakly present in the CO map, Fig. 3.9. The dust lane following the strong SW spiral arm seems to change from the leading side to the trailing side between
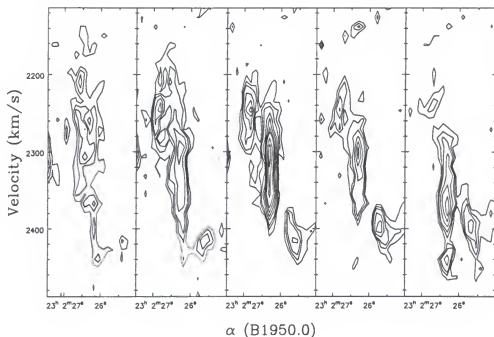
Figure 4.25: Position-velocity plots of slices 10-15, left to right (see Figure 4.22). The contours in arbitrary units are at 100, 150, 200, 300, 400, 500, 600, 800, 1000 and 1200.

two strong H II regions about $65''$ (projected) from the center. This can be clearly seen in the Hubble V and I band images (Benedict 1996, private communication).

There are several dust lanes perpendicular to the strong bar and spiral arm south of the nucleus. These dust lanes curve towards north. They can be seen mostly on the western side, but some sections appear on the eastern side as well. Moving outwards along the strong western spiral arm in its southern section, after the strong H II regions, mentioned above, there is a strong minimum in light near the center of the arm. The extent of this region is only about $3''$. In addition to these features, there are a couple of arm branches to the southwest of the nucleus, approximately at radii $35''$ and $60''$. Near the nucleus, the northern bar dust lane appears to extend closer to the nucleus and most likely extends all the way to the nucleus, as is seen in the near-IR images. In the optical wavelengths, the contribution from young bright stars and the bright, but relatively small, nucleus and bulge can compensate for the dust absorption.

The B-V image shows a large red component, elongated along a position angle 25°, with B-V colors > 0.63 and U-I > 1.6. Near the nucleus the B-V color is about 0.9, moderately red, and it reddens up to 1.0 in the northern bar dust lane. The perpendicular dust lane to the north of the nucleus, connecting to the bar dust lane from the east is also clearly seen with red B-V colors between 0.85 and 0.95. The H II regions near the dust lane in the bar have blue colors, 0.15-0.25 in B-V, down to 0.28 in V-R and -0.5 in U-I. The red component suddenly disappears at about $60''$ radius in the north and in the south. This component is bordered by the blue-colored spiral arms and their extensions. The colors in the blue spiral arms range from 0.1 to 0.5 in B-V and from -0.85 to 1.2 in U-I. Several separate H II regions, or blue spots, can be seen.

As is discussed by del Rio (1995), the pitch angle of the western spiral changes dramatically by at least 20° at a distance of about $85''$ from the center. On the eastern side, the spiral arms have several branches, as is also seen in the H I images (see Figure 2.6), and Hα (Figure 4.20).

H–Alpha Distribution

In Hα, the asymmetric spiral structure may be seen perhaps most clearly. Also the "overshooting" of the arms past the end of the bar is obvious. In the bar, the emission follows linear ridges that are obviously displaced toward the leading edges of the bar, as are the optical (and near-IR) dust lanes. The spatial offset between the various components will be further discussed in Chapter 6, as will be the correlation between the Hα, optical, H I and CO emission.

The Hα emission from the center is not very strong. This weakening of the line emission intensity could be due to dust absorption. As I discussed above, there is evidence that the dust absorption in the center can be several magnitudes in the visual

light. Alternatively, star formation in the center may not be very vigorous. There is evidence that perhaps most of the nuclear emission in the Hα images comes from the N II lines (rest frequencies 654.8 and 658.4 nm; Filippenko & Sargent 1985; Ho et al. 1993). This could imply that the dust in the center is excited and heated by non-thermal radiation from emission in an accretion disk around a supermassive black hole. Further observations, preferably in the infrared bands, of the excitation conditions in the circumnuclear environment are needed.

The most intense emission comes from the SW spiral arm, about $65''$ from the center, where two bright H II regions are seen also in the optical images. Another source of very strong emission is the H II region in the bar about $15''$ north of the nucleus. This shows up as a point source in the optical images. The emission is well organized along the western spiral arm, but in the east, the H II regions do not seem to form any continuous feature. A large plateau of lower level ionized hydrogen emission is seen near the northern end of the bar. It is remarkable that the spiral arms seem to continue well beyond the end of the bar, and the branch coming from the south is even passing the nucleus on the eastern side. Similar behavior can be seen in the numerical simulations (Chapter 5) during the early times, when the bar perturbation is slowly introduced. Short "armlets" are also seen between the western arm and the bar. In the optical wide-band images continuous dust lanes are seen to run parallel to and accompany these armlets. The bifurcation of the western arm in the south is not nearly as obvious as it is in the H I images. The total detected Hα luminosity, after blanking below a flux level of 1×10^{-17} ergs/sec/cm^2, is 2.7×10^{41} ergs/s (cf. 4.6×10^{41} ergs/s, Kennicutt & Kent 1983, extrapolated and corrected for extinction).

H–Alpha Kinematics

The signal-to-noise ratio of the Hα image limits the study of ionized gas kinematics to the central $60''$ radius. Again, we can see that the isovelocity contours in Figure 4.21 are parallel to each other in the center, implying circular rotation with a linearly rising rotation curve. The position angle of the receding side of the kinematical major axis appears to be somewhat larger ($210°$) than what it was for the CO data ($204°$). However, the difference is small and within the errors of the measurement.

Outside the central circularly rotating disk, there are two tongues or narrow fingers of high and low line-of-sight velocity contours protruding toward the center. The "wings" of these features have sharp bends when they cross the bar. The most likely explanation for these features is streaming associated with orbits following the bar (most likely x_1 orbits, as discussed before). The Hα (and H I) velocities on the southeastern side of the kinematical major axis are relatively normal. Some kinks in the velocity field may be seen at the locations of the diffuse eastern spiral armlets. In contrast, to the west and northwest of the major axis, the velocity field appears to be severely disturbed. Although the velocity field does not extend very far, disturbances associated with the strong western arm, similar to H I observations, are seen.

The position-velocity slices may be a little misleading, since unlike radio images, in optical images the channels are not independent of each other, and one sees very large FWZPs (full widths between zero points). However, the FWHM values should be relatively reliable. The velocity resolution is around 25 km/s. Large jumps are again seen across the bar dust lanes and star forming regions near the center (Figures 4.22–4.25). The magnitude of the jumps is at least 100 km/s. The spatial resolution of the images ($3''.6$) is too low to clearly resolve the shocks. CO observations showed very similar

velocity structures across the shocks in the sense that the high velocities on the western side of the jump are converted to low velocities on the eastern side of the shocks. This behavior is seen along the southern dust lane. On the northern side the interpretation is more difficult, and the kinematic evidence for shocks is weaker. Again, most of these large velocity ranges are caused by radial streaming along the bar.

A comparison between the H I and Hα velocity fields at the same $11''.8$ resolution reveals that the average velocity difference between the two maps is less than 5 km/s, and the rms dispersion is around 10 km/s. Considering that the velocity resolutions are 10 and 25 km/s, respectively, the velocity fields agree fairly well with each other, although at some locations the ionized gas has different kinematics. It is possible that the more compact ionized gas is more influenced by local velocity fields associated with stellar winds and star formation, especially near the shocks (Jörsäter & van Moorsel 1995).

Because of the strong perturbations caused by the bar, it is very difficult to obtain a reliable rotation curve, especially because the bar is so close to the line of nodes. Tests have shown that the orientation parameters found with the H I data are good approximations to the Hα rotation as well. When I fixed the inclination and the position angle, in addition to the central position and systemic velocity, to the values found for the atomic hydrogen kinematics, the agreement between the circular velocities obtained was within 10 km/s. As suggested by Lindblad (1996), leaving the rotation curve or the mass distribution as a free parameter within the bar radius in models will probably give the best results. Long (1991) has developed a technique for obtaining the true rotation curve under bar disturbances, but to close his set of equations he assumes that there is no net radial inflow (or outflow). This is almost certainly incorrect for a galaxy like NGC 7479 with a long, strong bar. Consequently, I will not attempt to obtain a detailed fit for the rotation curve within about $40'' - 50''$ radius, where the effects of the bar are very large.

CHAPTER 5
NUMERICAL SIMULATIONS

Introduction

I have described a considerable amount of observational work on NGC 7479 in the previous three chapters. This chapter is devoted to numerical simulations of gas and stars, and some elementary star formation.

This area has grown a lot since the pioneering work of the first "simulators" in the 1970's. Major workers in this field have been Athanassoula (1992a,b), who has found that the existence of offset shocks (dust lanes) in the bar potential depends on whether there are inner Lindblad resonances; Combes (Combes & Gerin 1985), who has developed a "sticky particle code," where gas cloud collisions can lead to coalescence; Friedli (Friedli & Benz 1993, 1995) who has studied the secular evolution under the barred potential, for example, the creation of an ILR and dissolution of the bar; Hernquist (1989, Hernquist & Mihos 1995), who has studied how galactic mergers can increase star formation activity; Huntley (Huntley et al. 1978; Sanders & Huntley 1976), who has studied the gas flow in barred spirals; Noguchi (1987, 1988) who has studied the question of how bars can fuel nuclear activity in disk galaxies; Roberts (Roberts et al. 1979) who has studied the shock structure in the gas component under a barred potential; Sanders (Sanders & Huntley 1976; Sanders & Tubbs 1980) who has also investigated the effects of the bar potential on the gas distribution and kinematics; Schwarz (1984, 1985) who has simulated the response of the spiral structure to the bar potential using a sticky-particle code; Sellwood (1981; Sellwood & Sparke 1988) who has studied, for example, the connection between

125

the bar instability and the rotation curve, and the pattern speeds of the bars and spiral arms in disk galaxies; Shlosman (Shlosman & Noguchi 1993; Heller & Shlosman 1994) who has studied the radial flows of gas into the nucleus and the possibility of feeding an AGN with the help of nested bars, van Albada (Roberts, Huntley and van Albada 1979; van Albada & Roberts 1981) who has studied the gas flow properties in barred spiral galaxies; and Wada (Wada & Habe 1992, 1995) who has investigated how the gas can reach the central engine in a barred potential by clumping and collisions. The group at the University of Florida, consisting of professors Gottesman, Hunter and Contopoulos, together with several students, has tried to model the gas flow in several barred galaxies (NGCs 1073, 1300, 1398, 1784, 3319, 3359, 3992, 4731 and 7479; Ball 1984; Ball 1992; Contopoulos et al. 1989; England 1986, 1989b; England et al. 1990; Hunter et al. 1988; Kaufmann & Contopoulos 1996). These investigations have clearly revealed how the gas is shocked in the linear shocks (dust lanes) along the bar and how the gas loses angular momentum and falls toward the center. The bar instability seems to be a natural explanation for the ubiquity of bars, and the various resonances created by the rotating bar potential may explain the ring structures often observed in barred galaxies.

My simulations addressed two central questions about NGC 7479. First, I have investigated how the gas behaves in the bar potential derived from the near-infrared observations of NGC 7479. The main goal of this investigation is to find out what the pattern speed of the bar is and where the dynamical resonances are by comparing the observed CO and Hα morphology and kinematics to the observations. In the second part of this chapter, I report the results from some runs where a self-consistent disk galaxy interacts with a small mass companion. The purpose of this study was to explore the possibility that the asymmetric spiral morphology of NGC 7479 is a result of a relatively recent interaction with a small mass companion galaxy.

The numerical code that I used in these simulations is a tree-SPH N-body program. The code and the tree-SPH method used to calculate the models are discussed in Appendix D. This code was kindly given to me by Dr. Clayton Heller, who wrote it and used it in his dissertation project (1991) and later modified it and used it to study gas dynamics in a disk galaxy (Heller & Shlosman 1994). The code is under constant development, and I have used the latest version.

Simulations of the Gas Flow in NGC 7479

One of the original goals in this investigation was to simulate the behavior of gas in the gravitational potential of NGC 7479. Ideally, this simulation should be made fully consistently, i.e. using a mixture of gas and stars with star formation and no external potential. In practice, finding the initial conditions that lead to something like a real galaxy in the sky is virtually impossible. However, simulations of the gas behavior in fully self-consistent potentials have been made by, e.g., Heller and Shlosman (1994) and Friedli and Benz (1993, 1995).

For NGC 7479, I decided that the best approach is to use a realistic potential gathered from the observations, and study the gas behavior in this potential. The best approximation for the stellar mass is obtained from near-infrared images, especially those in the K band. It has been shown that the K band luminosity traces the stellar mass in various components, such as bars and spiral arms (Rix 1993). However, the mass-to-luminosity ratio remains uncertain. It is, however, conceivable that this ratio is constant across most of the disk of the galaxy. This is so because the time scale for mixing is relatively short. One potential problem in mapping the stellar mass surface density with the K band images is the contribution to this light from other than old K and M type giants and dwarfs. Foremost in this respect are the K supergiants, which presumably

trace the young population I component. The near-infrared colors of red supergiants and giants are very similar. To distinguish between the two, the CO absorption feature near 2.3 μm could be used. Unfortunately, these data are not available for NGC 7479. It would be interesting to obtain 2.3 μm spectral observations in the future to see which stellar population dominates.

The potential used in my simulations was taken from the work of Quillen et al. (1995). Assuming a constant z thickness of the disk, one can rewrite the potential

$$\Phi(x) = -G \int \frac{\rho(x')d^3x'}{|x - x'|} \tag{5–1}$$

in the plane of the galaxy as

$$\Phi(x, y, z = 0) = -G \int \sum (x', y') g(x - x', y - y') \, dx'dy' \tag{5–2}$$

where the convolution function g(r) is

$$g(r) = \int\limits_{-\infty}^{\infty} \frac{\rho_z(z) \, dz}{\sqrt{r^2 + z^2}}, \tag{5–3}$$

where r is the radius in the plane of the galaxy. The vertical density profile has been normalized to one ($\int\limits_{-\infty}^{\infty} \rho_z(z) \, dz = 1.$). The vertical distribution is approximated with an isothermal sheet,

$$\rho_z(z) = \frac{1}{2h} sech^2 \left(\frac{z}{h} \right). \tag{5–4}$$

For the vertical scale height the value h = 4$''$ was used. This value is 1/12 times the exponential disk scale length of the galaxy. This assumption is consistent with optical and near-infrared observations of edge-on disks (Barnaby & Thronson 1992). The small bulge in NGC 7479 was neglected, so the potential may not be accurate within the central 8$''$. This is an important region if one wants to study the nuclear gas flows, but for purposes of obtaining the pattern speed its influence should not affect the results. The

K band image from the observations of Quillen et al. (1995) was first deprojected using an inclination of 45° and a position angle of 39°. These values are somewhat different from those that I have found in the observations (inclination = 51° and position angle = 22°). This introduces some uncertainty to the results. To convert the observed surface density profile into a mass surface density profile, the mass-to-luminosity (M/L) ratio was assumed to be 1.35 in solar units for both the axisymmetric and nonaxisymmetric components. This corresponds to the mass-to-light ratio of a single burst model with an age of 12 Gyr and metallicity [Fe/H] = − 0.25 (Worthey 1994). The surface mass density was then convolved with the vertical distribution function using Fast Fourier Transform techniques. Finally, the potential was calculated from equation (5–2), and divided into the Fourier components given by

$$\Phi(r, \theta) = \Phi_0(r) + \sum_{m=0,2,4,6} \Phi_{mc}(r) \, cos(m\theta) + \Phi_{ms}(r) \, sin(m\theta). \qquad (5-5)$$

A polynomial fit was then made to the coefficients of the Fourier decomposition. The polynomials are given by $\sum_{n=0}^{8} a_n r^n$, where r is in units of 10 kpc with coefficients in units of $(225.1734 \text{ km/s})^4$ (the unit used in the simulations with G=1; the time unit is 4.34285×10^7 years and the mass unit is $1.17889 \times 10^{11} \text{ M}_{\odot}$). The coefficients of the polynomials are listed in Table 5.1. The potential with the full bar perturbation is shown in Figure 5.1. To check the results, orbits were integrated in the potential and compared to the observations (Quillen et al. 1995).

The simulations were started from a circular disk with a radius of 10 kpc. This includes the bar, but only part of the spiral arms. The particles were put into this disk with a constant surface density, which was derived from the total mass of the molecular gas (see Chapter 3), $4.0 \times 10^9 \text{ M}_{\odot}$. The bar potential is introduced gradually, according to

$$\frac{Bar \; force \; (t)}{Final \; bar \; force} = \left(3 - \frac{2t}{t_{bar}} \right) \left(\frac{t}{t_{bar}} \right)^2. \qquad (5-6)$$

Table 5.1: The polynomial coefficients.

	$\Phi_0(r)$	$\Phi_{2c}(r)$	$\Phi_{2s}(r)$	$\Phi_{4c}(r)$	$\Phi_{4s}(r)$	$\Phi_{6c}(r)$	$\Phi_{6s}(r)$
a_0	-1.9464E5	7.43551E2	3.18402E2	-1.60335E1	-2.62696	-3.01984E1	-2.33545E1
a_1	2.27589E4	-3.25498E3	-1.80053E3	3.25654E2	1.65286E2	1.27177E2	-8.55019E1
a_2	-9.9051E2	-1.54599E3	3.49872E2	-5.02498E2	-2.91382E2	-8.46057E1	7.96445E1
a_3	-1.5920E2	6.32367E2	4.17750E1	6.21195E1	6.59966E1	-1.35513E1	-3.19208E1
a_4	2.91980E1	-7.38982E1	-1.22464E1	2.71821E-1	-1.5704E-1	5.98043	6.17960
a_5	-2.19174	5.39590	9.73524E-1	4.53509E-1	-6.8008E-1	-6.6187E-1	-6.5797E-1
a_6	9.8238E-2	-7.9660E-1	-1.0439E-1	-1.0217E-1	-6.1201E-3	5.84325E-2	6.70802E-2
a_7	-2.8551E-3	8.76642E-2	1.12704E-2	2.50247E-3	6.11178E-3	-4.5807E-3	-6.5485E-3
a_8	4.0117E-5	-3.3016E-3	-4.2032E-4	1.47209E-4	-2.3892E-4	1.43992E-4	2.72291E-4
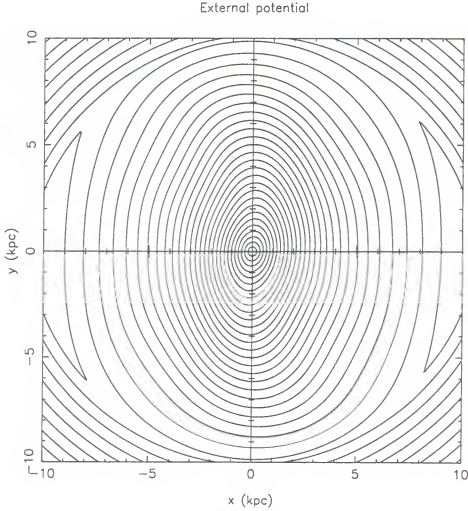
Figure 5.1: Contours of the potential with the full bar perturbation used in the simulations.

Results and Discussion

I studied the gas flow with various pattern speeds to find the right morphology. The gas self-gravity and star formation were turned off. The results from some runs are shown in Figures 5.2 – 5.14. The gas distribution and the line-of-sight velocity field at late times can be compared to Figures 3.2 and 3.4, and the structure at early times to the optical images, e.g., Figure 4.12 and 4.16. These runs had 20,480 gaseous particles. I made one run for the best fitting pattern speed, 27.0 km/s kpc^{-1}, with half the number of particles, 10,240. The gas morphology and the star formation distribution resembled closely those of the 20,480 particle run. Thus, the results and conclusions do not depend on the number of particles very sensitively. I also investigated the effects of a larger viscosity, by giving values of $(\alpha, \beta) = (1.0, 3.0)$ for one run instead of the $(\alpha, \beta) = (0.5, 1.0)$ used in other runs. These larger viscosity coefficients resulted in high viscous interactions between the clouds, preventing the formation of the leading edge gas morphology and resulting in a fast evolution of the gas distribution. I could not find a match to the observed gas morphology at any instant of time. In a test simulation where the bar forces were added in full by $t = 7$ instead of the usual $t = 13$, the evolution at the beginning took place much faster, as expected. At later times, the test model showed a bar morphology similar to the regular model where bar forces were added by $t = 13$.

Pattern speed from the simulations

The most important goal of these particular simulations was to find the pattern speed of the bar. I compared the frames that best resembled the observations to the observed gas/dust lane morphology (Figures 3.2, 4.8), velocity field (Figures 3.3, 3.4 and 4.21) and star formation distribution (Figure 4.20). Since the gas distribution is evolving fairly rapidly as gas falls into the nuclear region, I did not pay as much attention to the global
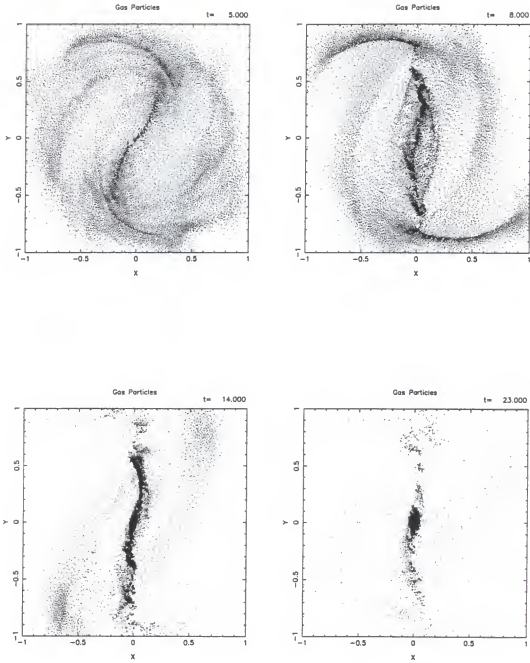
Figure 5.2: The unprojected gas particle distribution with pattern speed = 18.0 km/s kpc^{-1}. The bar potential is vertical in all the frames shown here. The bar forces were turned completely on at $t = 13$. The time is shown at the upper right corner of each frame. The viscosity coefficients are $(\alpha, \beta) = (0.5, 1.0)$. The unit time corresponds to 4.34×10^7 years and the unit length to 10 kpc.
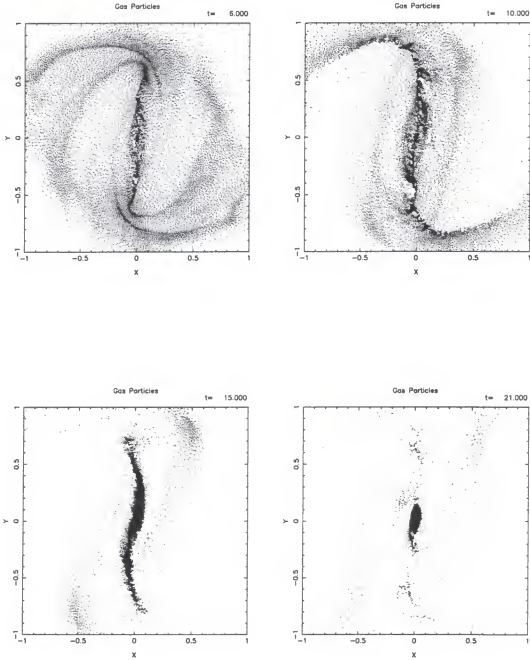
Figure 5.3: The unprojected gas particle distribution with pattern speed = 20.3 km/s kpc^{-1}. The bar potential is vertical in all the frames shown here. The bar forces were turned completely on at t = 13. The time is shown at the upper right corner of each frame. The viscosity coefficients are $(\alpha, \beta) = (0.5, 1.0)$. The units are the same as in the previous figure.
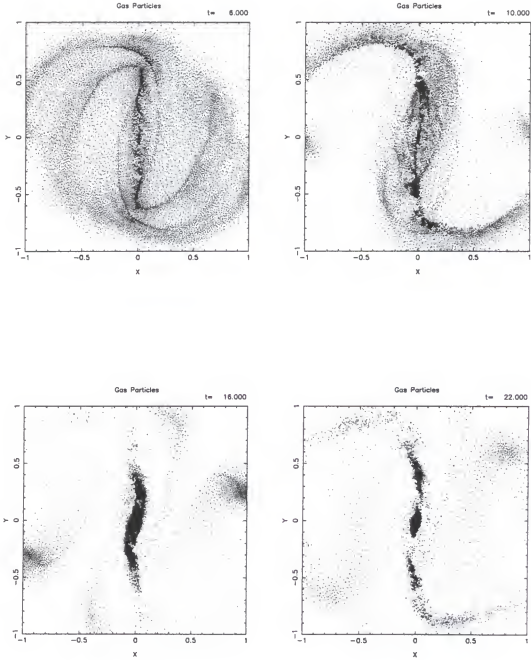
Figure 5.4: The unprojected gas particle distribution with pattern speed = 22.5 km/s kpc^{-1}. The bar potential is vertical in all the frames shown here. The bar forces were turned completely on at t = 13. The time is shown at the upper right corner of each frame. The viscosity coefficients are $(\alpha, \beta) = (0.5, 0.5)$. The units are the same as in the previous figure.
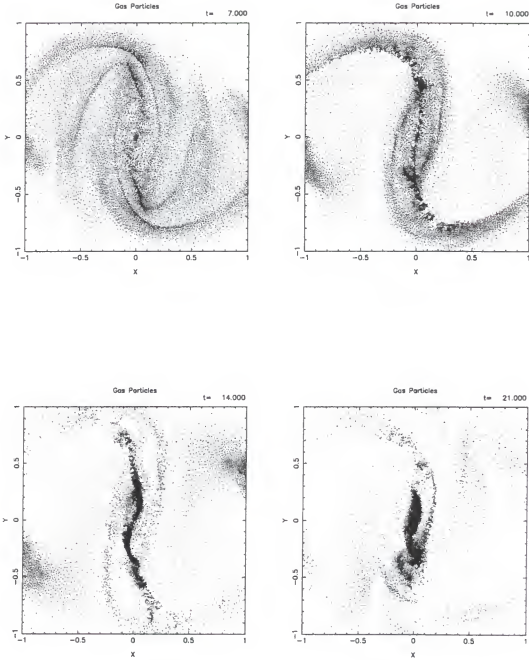
Figure 5.5: The unprojected gas particle distribution with pattern speed = 24.8 km/s kpc^{-1}. The bar potential is vertical in all the frames shown here. The bar forces were turned completely on at t = 13. The time is shown at the upper right corner of each frame. The viscosity coefficients are $(\alpha, \beta) = (0.5, 1.0)$. The units are the same as in the previous figure.
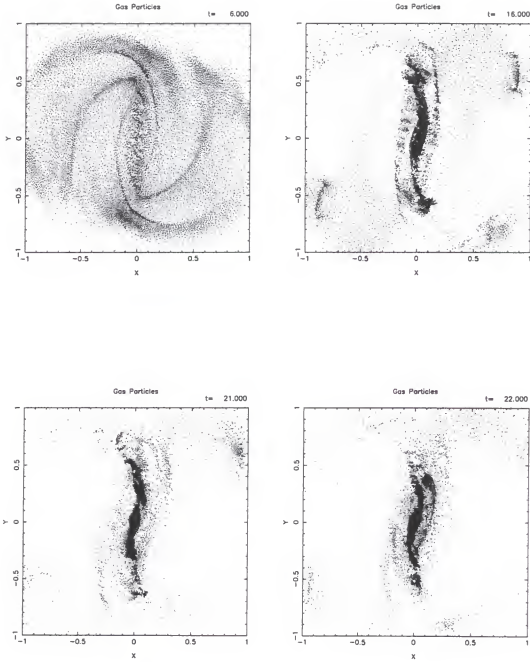
Figure 5.6: The unprojected gas particle distribution with pattern speed = 27.0 km/s kpc^{-1}. The bar potential is vertical in all the frames shown here. The bar forces were turned completely on at t = 13. The time is shown at the upper right corner of each frame. The viscosity coefficients are $(\alpha, \beta) = (0.5, 1.0)$. The units are the same as in the previous figure.
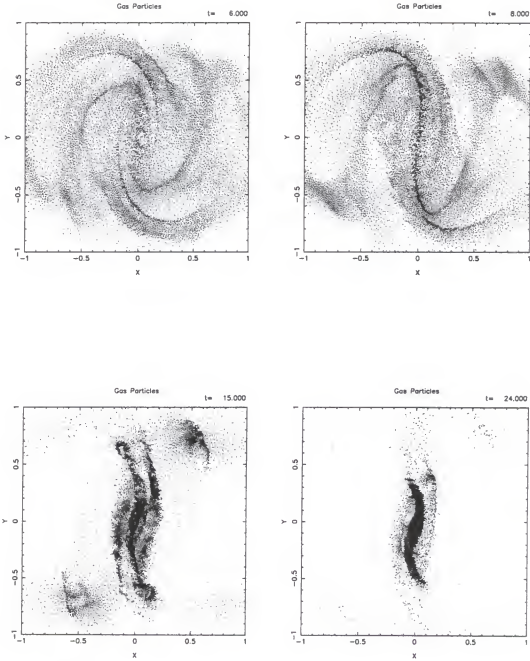
Figure 5.7: The unprojected gas particle distribution with pattern speed = 29.3 km/s kpc^{-1}. The bar potential is vertical in all the frames shown here. The bar forces were turned completely on at t = 13. The time is shown at the upper right corner of each frame. The viscosity coefficients are $(\alpha, \beta) = (0.5, 1.0)$. The units are the same as in the previous figure.
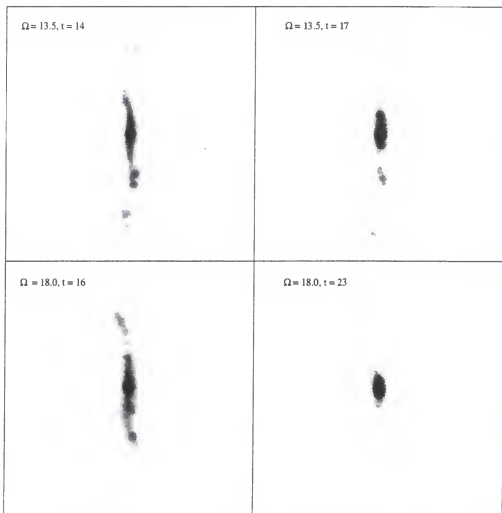
Figure 5.8: A grayscale plot of particle surface density, projected to the same orientation as the observations using inclination = 51°, position angle = 22°, and the angle between the bar and the line of nodes in the plane of the disk = −35°. The units of the pattern speed Ω_p are km/s kpc^{-1}, and the times are also shown.

gas distribution as I did to the dust lane structure. The main arguments for a high bar pattern speed (27.0 km/s kpc^{-1}) are:

1. The leading straight dust lane structure extends to smaller and smaller radii as the pattern speed is increased. The CO observations together with the near-IR colors and Hα images show that the straight part in the center, connecting the leading dust/gas lanes in the outer part, is about $20''$ – $25''$ in length. This can be obtained if the pattern speed is around 27 km/s kpc^{-1}.
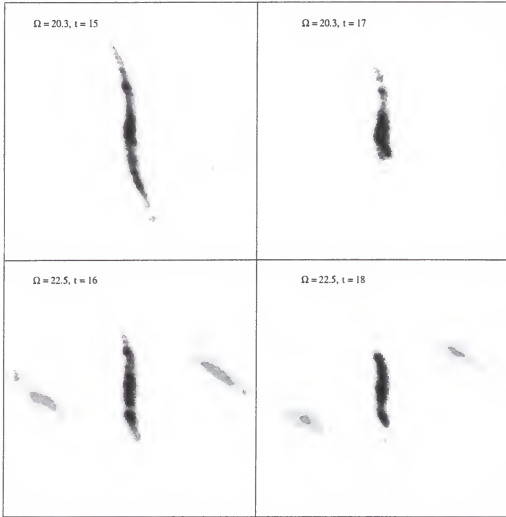
Figure 5.9: A grayscale plot of particle surface density, projected to the same orientation as the observations using inclination = 51°, position angle = 22°, and the angle between the bar and the line of nodes in the plane of the disk = −35°. The units of the pattern speed Ω_p are km/s kpc^{-1}, and the times are also shown.

2. The line-of-sight velocity field has a small range along the bar and around the nucleus if the pattern speed is low. This is probably related to the low circulation speed of gas clouds trapped to the bar as the pattern speed is low. Best agreement with observations can again be achieved for pattern speeds close to 27 km/s kpc^{-1}. It is also of interest to note that the low pattern speed models have an abrupt change from radially outward velocities to radially inward velocities near the apocenter of their orbits in the bar (large curvature), whereas the high pattern speed models show a
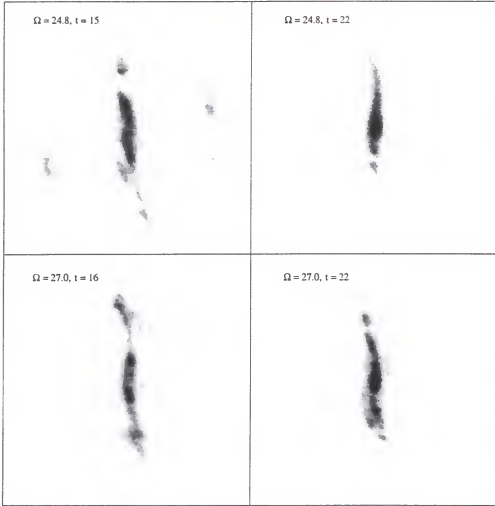
Figure 5.10: A grayscale plot of particles surface density, projected to the same orientation as the observations using inclination = 51°, position angle = 22°, and the angle between the bar and the line of nodes in the plane of the disk = –35°. The units of the pattern speed Ω_p are km/s kpc^{-1}, and the times are also shown.

small tangential motion near the location of the shock. This may be seen in Figure 5.13. A similar behavior was observed by Athanassoula (1992a) in her models.

3. The spiral arm and arc structure driven by the bar at early times (5 – 8 in the time units used here) resembles the observations much better with a high pattern speed (above 24 km/s kpc^{-1}). With low pattern speeds the spiral arms start almost perpendicular to the bar structure, contradicting the observations. The high pattern speed observations produce a spiral arm structure that has the arm overshooting the
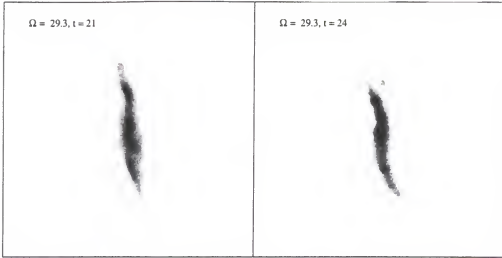
Figure 5.11: A grayscale plot of particles surface density, projected to the same orientation as the observations using inclination = 51°, position angle = 22°, and the angle between the bar and the line of nodes in the plane of the disk = −35°. The units of the pattern speed Ω_p are km/s kpc^{-1}, and the times are also shown.
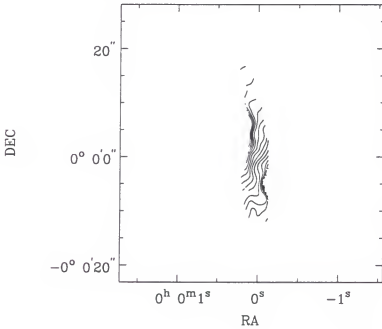
Figure 5.12: The velocity field for the pattern speed 27.0 km/s kpc^{-1}, t=22. The velocity contours are marked at 20 km/s intervals.

bar end slightly, but curving parallel to it near the arm's inner end. Since the arm (and even bar) structure may be driven by a recent or even ongoing minor merger, the structural similarity should not be taken as the main argument for a high pattern

speed, but it is consistent with it.

4. The star formation distribution supports point 1. above. The star formation is located on the linear offset gas/dust lanes, which extend closer to the nucleus as the pattern speed is increased. The best agreement with the observed star formation distribution (see, e.g., Figure 4.20) is achieved when the pattern speed is 27 km/s kpc^{-1}. There is no sharp peak of star formation near the center, as observed. I tried several star formation criteria. They showed various rates of star formation, but agree in morphology. The results shown in Figure 5.14 used the Toomre criterion (see Appendix D) with pattern speed 27.0 km/s kpc^{-1} at time t = 22.
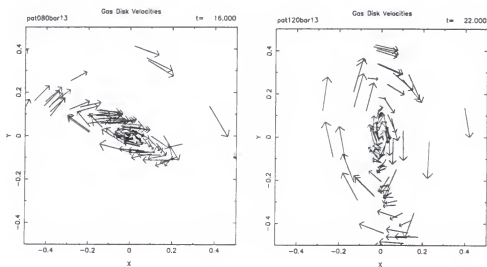
Figure 5.13: A comparison of the velocity fields in the gas bar.

The fact that the dust/gas lanes stay close to the major axis of the bar even for low pattern speeds when the ILR(s) move farther out from the nucleus is probably due to the fact that the bar is very strong. Athanassoula (1992b) has found a similar behavior in her models; the dust lanes remain centered when the bar is strong (for a definition of a strong bar, see Chapter 1). The associated resonance curves can be seen in Figure 5.15.
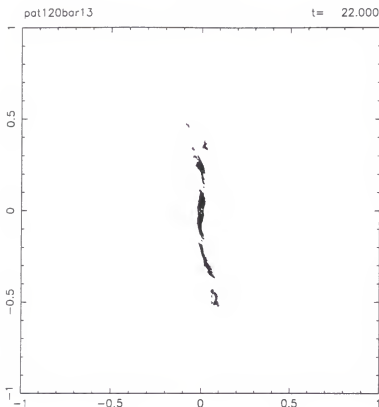
Figure 5.14: The location of star forming regions in the model with pattern speed = 27.0 km/s kpc^{-1} at time t = 22, according to the Toomre criterion. The sound speed used was 10 km/s and the critical Q parameter was 0.5.

The diagram in Figure 5.15 indicates that there is one ILR around 700–800 pc from the center. The other, inner ILR must be very close to the nucleus. Since the bar is so strong, the location of the ILRs is not well determined from frequency diagrams like this. The epicyclic oscillations, described by the frequency κ (for more discussion see Chapter 6) cannot be derived from linear perturbation analysis. The only way to obtain the location of the inner Lindblad resonances in a strong bar potential is to study the behavior of orbits in the potential, and use the extent of the x_2 (in the notation of Contopoulos) family of orbits as the radial extent between the two ILRs. However, as shown by Lindblad and Lindblad (1994) and Wada (1994), the determination of the location of the ILRs using the linear approximation can often give a good first guess if the bar perturbation is not very strong.

Frequency diagram
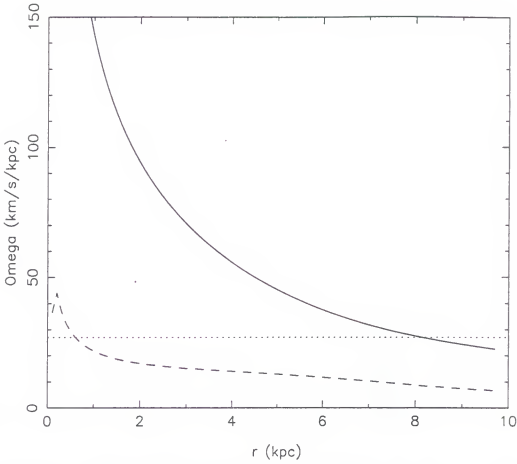
Figure 5.15: A diagram of the frequencies associated with the axisymmetric component of the potential. The angular rotation frequency, Ω, is the solid line, the dashed line represents $\Omega - \frac{\kappa}{2}$ and the dotted line is the pattern speed $\Omega_p = 27.0$ km/s kpc^{-1}.

No dramatic phenomena are observed near the inferred location of the ILR. In bars that have one or more of the following properties

1. large bar axial ratio

2. high pattern speed

3. low central mass concentration, or

4. large quadrupole moment

the x_2 orbits can even vanish altogether. NGC 7479 most likely has all these properties, and therefore there is a good chance that the ILRs themselves do not exist, but the

gas/dust lane morphology can still serve as a tracer of the pattern speed. In the future, a detailed study of the orbits in the (possibly improved) potential of this galaxy should be made to study the existence of the ILRs. If, however, ILRs do exist, a possible ring structure very close to the nucleus (within $0''.5$ of the center; G. F. Benedict, private communication) could be the location of the inner ILR.

Shocks and gas inflow rate

It is of interest to examine the shock structure in the bar. Despite the poor resolution, the CO and Hα observations gave hints that shocks may actually exist in the gas/dust lanes. In Figure 5.16 I present some representative values for the shocks in the gas distribution. The shocks appear to trace the gas/dust lanes well. In contrast, the shock morphology for the lower pattern speed values appears chaotic, and no systematic "lanes" are seen (not shown here). The velocity jumps across the center of the bar and the shock of the bar are often about 250 – 300 km/s radial velocity, but very small in tangential velocity, since the motion is mostly radial in the strong bar. These values are fairly independent of the pattern speed, although the detailed circulation shows that the curvature in the apocenters is larger for the lower pattern speed cases. A typical drop in the magnitude of the velocity across the shock front is on the order of 100 km/s in the models.

The position-velocity diagrams across the bar, presented in Chapters 3 and 4, can be understood with the help of the large jumps in radial velocity. Using an inclination of 51°, as found in Chapter 2, and an angle of 35 ° between the gas bar and the line-of-nodes in the plane of the galaxy (calculated from the projected angle between the line-of-nodes and the bar of about 25° and inclination of 51°), and using the velocities from the models, I find that the jump in the line-of-sight velocity should be about 135–150

km/s at moderate distances from the center (about $10'' - 15''$ in the observations). These jumps occur within $3'' - 5''$, almost within one beam width in the CO observations. The observations show jumps of the order of $130 - 150$ km/s within about $3''$. The emission at low line-of-sight velocities seen in slices 1–3 in Figure 3.13 requires either an unusually large radial inflow speed (more than 250 km/s) or a counter-rotating motion. The first alternative seems more likely, but the origin of this high inflow speed is unclear.

The average mass inflow rate in the slow pattern speed (18.0 km/s kpc^{-1}) simulation between times t = 15 and t = 20 is 6 M$_\odot$/year at 1 kpc radius. For the high pattern speed (27.0 km/s kpc^{-1}) model the average mass inflow rate in the same time interval was 4.5 M$_\odot$/year at the 1 kpc radius. These rates are only slightly higher than those cited by Athanassoula (1992b), and similar to those found by Quillen et al. (1995), who estimated the inflow rate as (4 ± 2) M$_\odot$/year based on the gravitational torque on the gas. They confirm that substantial feeding of the inner kpc is taking place.
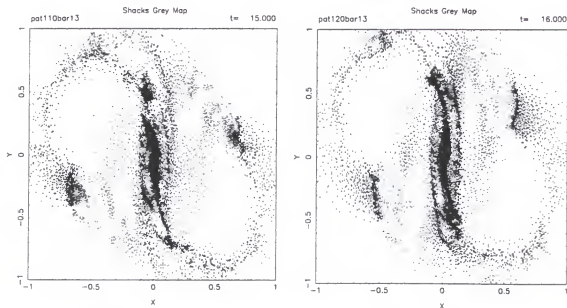
Figure 5.16: Grayscale plots of the shocks for the pattern speeds 24.8 and 27.0 km/s kpc^{-1}. The time is on the upper right corner. The gray level is given by the time derivative of the nonadiabatic component of internal energy.

A short discussion of the results

The models presented above have given a lot of circumstantial evidence that the pattern speed in NGC 7479 is high and the inner Lindblad resonances, if they exist, must be very close to the nucleus. They have also provided explanations of many observed features, such as the jumps across the bar observed in CO emission and in the Hα Fabry-Perot data. I will now briefly discuss the implications of the model results.

As several of the earlier investigations have revealed, bars appear to be rapidly rotating entities. The previous investigation by Sempere et al. (1995), using techniques similar, but not identical, to the ones employed here, obtained a pattern speed of 30 km/s kpc^{-1} for the bar in NGC 7479. 30 km/s kpc^{-1} is at the upper limit of acceptable pattern speeds in my investigation.

If I place the end of the bar at around 45$''$, the favored pattern speed in the range 26 – 28 km/s kpc^{-1} places the corotation probably around 1.1 times the bar radius, which is in the range 1.2 ± 0.2 times the bar radius, predicted by Athanassoula (1992b). A similar result for the barred SB0 galaxy NGC 936 has been found recently by Kuijken and Merrifield (1995b), using a different technique based on the application of the Tremaine-Weinberg method. Lindblad et al. (1996) and Lindblad and Kristen (1996) have used a method similar to mine (although with a different hydrodynamic scheme) to determine, among other things, the pattern speed in NGC 1365 and NGC 1300. They find the corotation radius at 1.21 times the bar radius in NGC 1365 and two "best models" for NGC 1300 with corotation at 1.3 and 2.4 times the bar radius, respectively. I investigated the reliability of the results in the model with 20,480 initial particles by running a model with half the number of particles, 10,240. Some representative particle plots of this run are shown in Figure 5.17. This run indicates that most of the essential characteristics,

such as the gas/dust lane morphology, are recovered. Therefore, 20,480 seems to be an adequate number of particles for recovering the essential aspects of the structure and dynamics of the bar in this potential. Further experiments with even larger or smaller particle numbers should be made, however, to be sure of the limitations of the modeling results.

It appears safe to state that bars have high pattern speeds. This leads to some problems, such as the slowing of the bar by angular momentum lost to the spherical halo through dynamical friction. This question has been recently posed by Sellwood and Debattista (1996). The results from their simulations have shown that the bar slows so dramatically during the age of the Universe that the corotation radius moves out to several times the length of the bar, contrary to observations. This seems to be a serious problem, and future research should be directed towards resolving this dilemma. The bar in NGC 7479 may be relatively young (perhaps less than 10^9 years, as hinted in the next section on the interaction simulations).

The existence and location of the ILRs remains uncertain. Calculations of the stability of the orbits in the potential of the galaxy need to be made. Only these calculations can prove or disprove the existence of the inner Lindblad resonances in a strong barred potential like the one in NGC 7479. If the ILRs exist, they have to be within the central 1 kpc. The location of other resonance regions, such as the ultraharmonic inner 4:1 resonance or the outer Lindblad resonances, are also of interest. Since the bar disturbance is probably almost insignificant at the large radii of the OLRs, they can be obtained from the linear theory. Some uncertainty in these results is introduced by the large velocity disturbances in the western spiral arm. Using the H I rotation curve, which agrees relatively well with Quillen's rotation curve in the region of overlap, I found that the outer Lindblad resonance, where Ω_p (the pattern speed) equals $\Omega + \kappa/2$, is at 15 kpc
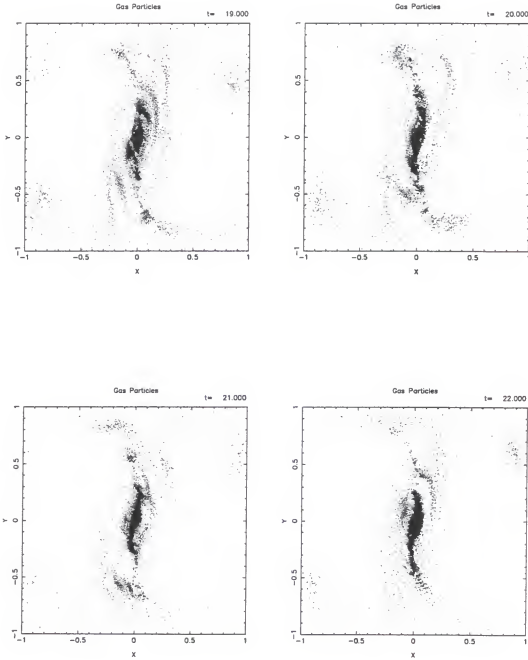
Figure 5.17: A model run with pattern speed = 27.0 km/s kpc^{-1}, but only 10240 particles. The times are shown on the upper right of the frames.

(95$''$). A great part of the spiral structure is outside of this radius. According to wave theories of spiral structure, a two-armed spiral structure in the stellar component in an

isolated disk galaxy can exist only between the inner and outer Lindblad resonances. This principle may not be violated by having the OLR at $95''$, since the spiral structure is not clearly bisymmetric, but rather there is evidence for an interaction driven spiral structure, and the spiral structure is mostly seen in the population I component (gas and young stars).

The models have shown how the gas is driven to form the observed structure, including, but not limited to, the linear bar shock. Therefore, the association of gas and dust and star formation seems natural. The triggering method of star formation is not certain, and this will be further discussed in Chapter 6. The star formation criteria that I used usually trace the highest gas concentration, whereas the observed emission most likely comes somewhat downstream from the shock front. It would be valuable to study in detail the locations of shocks and star forming regions with high resolution observations with the Hubble Space Telescope or the new 10 m class telescopes that can achieve resolutions down to $0.1''$.

The velocity fields in the models show that the gas (and presumably the stellar) flow in the bar is mostly radial, and with the modest resolutions ($2''–3''$) achievable with today's velocity field mapping instruments, large velocity jumps can be seen across the beam. Therefore, the large velocity widths found in the position-velocity plots in Chapters 3 and 4 are mostly due to the superposition of the orbits, not the shocks themselves. In addition, part of the molecular gas is likely to reside in giant molecular clouds or associations, which do not respond to the shocks, but behave like stars or ballistic particles. To detect the shocks, high resolution (less than an arc second) observations of the velocity field across the dust lanes need to be made. The interpretation of these observations will be aided by high resolution numerical modeling, similar to what has been discussed in this chapter.

Of course, we have to be careful not to overinterpret the simulation results. However, as stated above, the overall gas structure seems to be a solid result of this investigation. The interpretation of the resonance regions is much harder, as discussed above. Some of the limiting factors of the simulations include the use of the analytical, external potential instead of self-consistent gas-star interactions through gravitation and star formation. However, one of the major unsolved problems in the studies of galactic dynamics is the generation of initial conditions that lead to something that looks like a real galaxy in the sky. Even if the simulation result looks like the galaxy to be modeled, there is always the question of non-uniqueness. Also, how would the behavior change if we could use 10^{11} particles instead of 10^4 or 10^5? What are the effects of friction and noise and the round-off errors in the simulations with respect to the final result?

Another major unsolved problem is star formation. How should it be handled in the simulations? Clearly, star formation can change the evolution of a disk galaxy dramatically, as demonstrated by, e.g., Heller and Shlosman (1994). Are there other major deficiencies in our knowledge of the physics in galaxies, such as the neglect of magnetic fields?

In my simulations the potential beyond 10 kpc was neglected. It is possible, although unlikely, that the spiral structure could affect the evolution of the gas distribution and dynamics in the bar region. A more serious shortcoming in the models that I made was the failure to include a possible perturbation from a merging satellite galaxy. However, including a major perturbation without a massive halo to stabilize the disk would have led to unpredictable behavior. The K band image can only trace the potential in the disk component. A final deficiency is the use of a two-dimensional model. New phenomena take place in three dimensions, such as vertical resonances and scattering to vertical orbits. It is difficult to estimate the seriousness of the lack of the third dimension. However,

observations give little constraints on the third dimension, and we must wait until future improvements make it possible to construct a realistic three-dimensional model for the potential. An attempt to this direction is being made by the group at the IAC in Spain.

Interaction Simulations

Introduction

I have made simulations of a small satellite galaxy starting in a circular orbit within a normal disk galaxy. These simulations are fully three-dimensional and self-consistent in the sense that no external potential has been introduced. The simulations were made to study if it is feasible that the structure of NGC 7479 is a result of a recent interaction or a merger. This has been suggested recently by Quillen et al. (1995) and it has been brought up in discussions with several people in the field. I wanted to study, in a general case, how an infalling dwarf galaxy will affect the evolution of the primary disk galaxy. Despite a wealth of indirect evidence, the results from the observations of NGC 7479 show no compelling visual evidence of a body that could be identified with the remains of the hypothetical companion galaxy in, or near, the disk of NGC 7479. This implies that if there was an interaction in the recent past, the companion galaxy has been completely disrupted by the effects of tidal shear and dynamical friction. These simulations were made to study whether the observations are consistent with this scenario, by investigating the gas velocity field and the morphological appearance of the stellar and gaseous distributions during the interaction. No claims of associating any detailed features with NGC 7479 are made. Because the available parameter space for the interaction is very large, only a small range of the most plausible initial conditions have been studied.

Initial Conditions for the Simulations

The related question of excitation of activity in minor mergers has been studied by Hernquist and Mihos (1995). They explored the interaction of a disk galaxy with a halo and a companion galaxy whose mass is one tenth of that of the main disk mass. The simulations made by Hernquist and Mihos (1995) provided a good starting point for studying the kind of interactions I am interested in. Therefore, the same galaxy models were used as in the work of Hernquist and Mihos (1995). A more detailed description of the galaxy model can be found in Hernquist (1993). The disks are modeled with an exponential profile in the plane of the disk and by a $sech^2$ distribution in the z direction:

$$\rho_d(r, z) = \frac{M_d}{4\pi h^2 z_0} \exp\left(-\frac{r}{h}\right) sech^2\left(\frac{z}{z_0}\right). \tag{5–7}$$

The horizontal scale length is h and the vertical scale length is z_0. The gaseous disk has the same profile, but a smaller vertical scale length. These disks are imbedded in a self-consistent halo with a density profile

$$\rho_h(r) = \frac{M_h}{2\pi^{\frac{3}{2}}} \frac{\alpha}{r_c} \frac{\exp\left(-\frac{r^2}{r_c^2}\right)}{r^2 + \gamma^2}. \tag{5–8}$$

M_h is the halo mass, r_c is a "cutoff radius," γ is a core radius, and α is a normalization constant. I did not include the bulge component because it is believed to be small for NGC 7479, and most of the evolution caused by the satellite galaxy takes place outside the bulge.

The density profile for the satellite is the same as that of the main disk, but the mass and the length scales have been reduced by a factor of 10. The satellite is initially in a circular orbit around the main disk at a distance of 4 units. The velocities of the particles are initiated using moments of the Vlasov equation and by approximating the velocity distributions as Gaussians (see e.g. Davies 1995).

<u>Runs</u>

I first checked the FTM code against the results of Hernquist and Mihos (1995). I started with an isolated disk having 16,384 particles in the disk and 16,384 particles in the halo. The gas mass was 10 % of the disk mass, presented by 8,192 particles. The halo mass was 5.8 times the disk mass. The physical interpretation of the units is the following: one mass unit = 5.6 x 10^{10} M$_\odot$, one length unit = 3.5 kpc and the time unit is 1.31 x 10^7 years. In these units one velocity unit becomes 262 km/s. The other parameters for the disk and halo component are as follows: $z_0 = 0.2$, $\gamma = 1$, $r_c = 10$. The disk scale length is h = 1. The Toomre parameter varied weakly with radius, and it has been normalized to 1.5 at a radius of 8.5/3.5 (corresponding to the solar radius in our Galaxy). The gas is isothermal at a temperature of 10,000 K. As can be seen in Figure 1 of Hernquist and Mihos (1995), in an isolated disk the gas develops spiral structure, probably from the swing amplification of noise (Hernquist & Mihos 1995), but no net gas inflow can be seen. My results were completely comparable to those of Hernquist and Mihos (1995).

To further compare our results with those of Hernquist and Mihos (1995), we ran a simulation similar to their "standard model" without a bulge. The satelllite had a model density derived from

$$\rho_{sat} = \frac{M_{sat}}{2\pi a^3} \frac{1}{m(1+m)^3},$$
(5–9)

where M$_{sat}$ is the satellite mass, a is a scale length and

$$m^2 = \frac{x^2 + y^2 + z^2}{a^2}.$$
(5–10)

The satellite mass was 0.1 and its scale length a = 0.15, and it was contained within its tidal radius. It started with a circular velocity at a distance of six length units (21 kpc)

from the center and an inclination of 30°. The orbit is prograde, in other words, the direction of rotation is the same as that of the disk of the main galaxy. The results from this simulation for the stellar component are shown in Figure 5.18. From these frames it is obvious that the companion is stripped off its particles during the interaction.

Since the companion seemed to be disrupted early in its evolution when using the structural model of Hernquist and Mihos (1995), I decided to build the companion with the same structure as the main galaxy, but with smaller dimensions. Its mass was first kept at 10 % of the disk mass of the main galaxy, and its size was scaled down by a factor of ten as well. The velocity components were scaled down by $\sqrt{\frac{m}{r}}$, where m is the mass of the satellite (0.1) and r is the scaled down disk scale length. The disk scale length (the length unit for the main galaxy) is 1.0, so r is 0.1 in the formula above. The main galaxy, the satellite and the satellite's orbital motion were all prograde, clockwise as seen along the z-axis. The halo mass was twice the disk mass of the main galaxy. 16,384 particles were used for the main disk and halo, 8,192 gas particles for the gas in the main galaxy, 4,096 particles for satellite gas and 4,096 for satellite stars. The satellite did not have any halo. I did not use any bulge component. Star formation was turned off. Results from this simulation are presented in Figures 5.19 – 5.22, and some parameters of all the runs I made are given in Table 5.2. Plots of a simulations where the companion mass was reduced to 5% of the disk mass are shown in Figures 5.23 – 5.25.

I also made a similar simulation with a counter-rotating satellite. The orbital encounter was still prograde, the only difference being the internal rotation of the satellite, which was spinning in the opposite direction to the spin of the main galaxy and opposite to the sense of the interaction orbit. The results from this run show a very similar response in the main galaxy: a bar forms at the same time as before, together with a strong tidal counterarm. Towards the end of the simulation both of these features disappear as before.
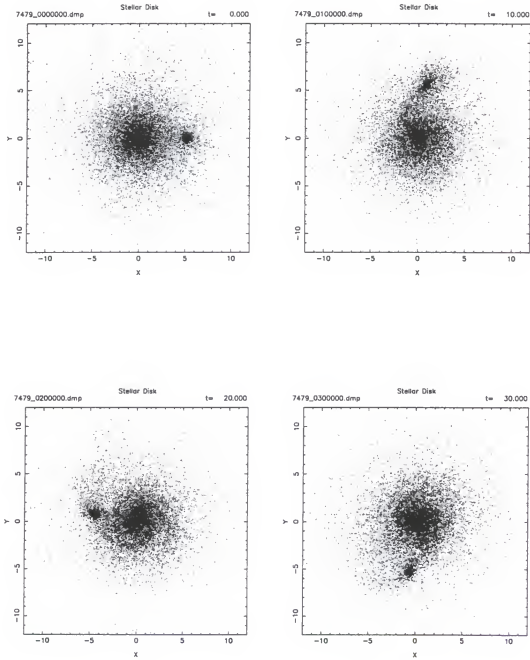
Figure 5.18: The results from a control simulation similar to that made by Hernquist and Mihos (1995). The mass of the companion is one tenth of the mass of the disk of the main galaxy, and the initial orbit is circular, inclined 30° to the plane of the disk.

Table 5.2: Initial parameters of the interaction runs.

Run	Sat. mass	Sat. rot.	Sat. Incl.	M_{halo}/M_{disk}
1	0.1, gas 50%	prograde	10°	2
2	0.1, gas 50%	retrograde	10°	2
3	0.05, gas 50%	prograde	10°	2
4	-	-	-	2

The evolution of the gas and stars of the satellite galaxy is somewhat different. If the satellite is rotating in the prograde sense, part of the gas and stars of the satellite falls into the nucleus of the main galaxy at a relatively early time (between t = 10 and t = 15 in the runs). The gas is trapped in the nucleus and it forms there a rapidly rotating small gas bar. The stars are not captured to the nucleus, but remain in orbits that take them well outside the nuclear region. The retrograde-spin satellite retains almost all of its stellar and gaseous material all the way to its final merger in the nucleus. The final merger takes place a little earlier for the prograde rotating satellite.

The disk thickness increases by less than a factor of two from the beginning to the stage at which the bar is strongest, and by little more than a factor of two from the beginning to the end of the simulation (Figure 5.22).

Discussion of the Interaction Simulations

In this section, I will discuss some of the limitations of the current interaction simulations. A thorough discussion of the meaning of the results with respect to NGC 7479's asymmetric spiral structure and the strong bar is given in Chapter 6, where I also discuss observational evidence for a recent minor merger.

From the beginning, it was clear that a detailed reproduction of the observed gas and stellar morphology from a minor merger would be practically impossible. First, since there is no observable feature that could be reliably identified with the remains of the satellite galaxy, it is a matter of speculation to try to find orbital parameters of the satellite
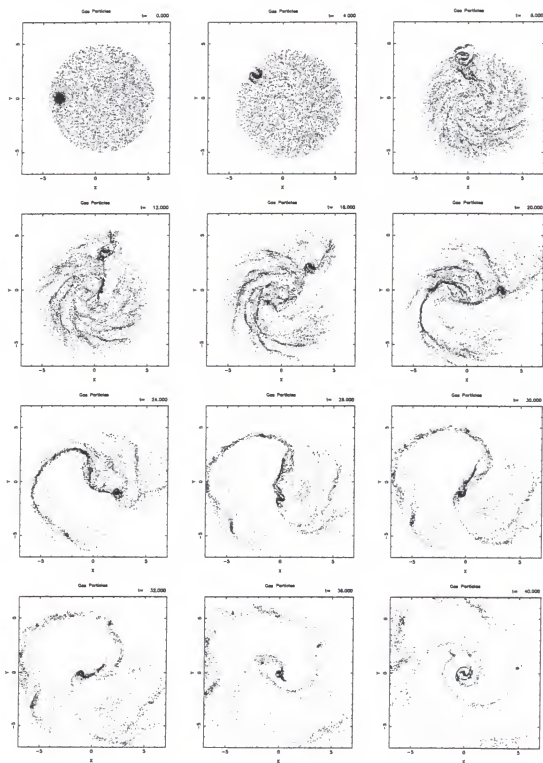
Figure 5.19: Evolution of gas distribution in the prograde encounter. The satellite mass is 10% of the main disk mass, and the motion is prograde for all components. Times are shown on the upper right corner of each frame.
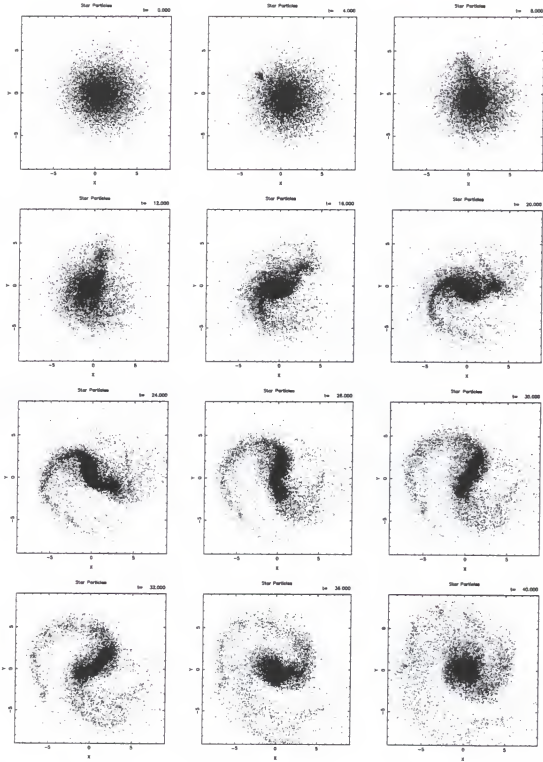
Figure 5.20: Evolution of the main disk star distribution in the prograde encounter. The satellite mass is 10% of the main disk mass, and the motion is prograde for all components. Times are shown on the upper right corner of each frame.
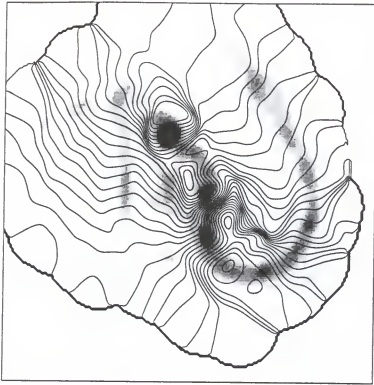
Figure 5.21: The velocity field at 15″ resolution overlaid on a grayscale image of the gas density at time t = 25, companion mass = 10% of the main disk mass, all rotating in a prograde sense. The contours are printed every 10 km/s. Both the velocity field and the surface density have been projected to an orientation similar to the one found in the observations.
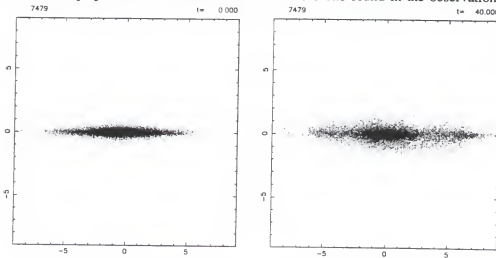
Figure 5.22: Edge-on views of the stellar disk at the beginning of the simulations (left) and at the end of the simulation (right).

that would take it along a track favorable for formation of the asymmetric spiral structure and perhaps even the bar. The mass of the alleged companion is unknown as well,
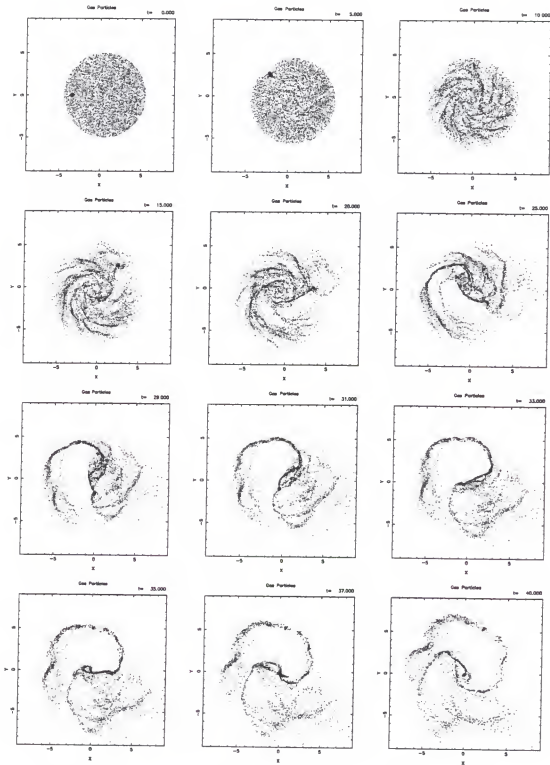
Figure 5.23: Evolution of gas distribution in the prograde encounter. The satellite mass is 5% the main disk mass, and the motion is prograde for all components. Times are shown on the upper right corner of each frame.
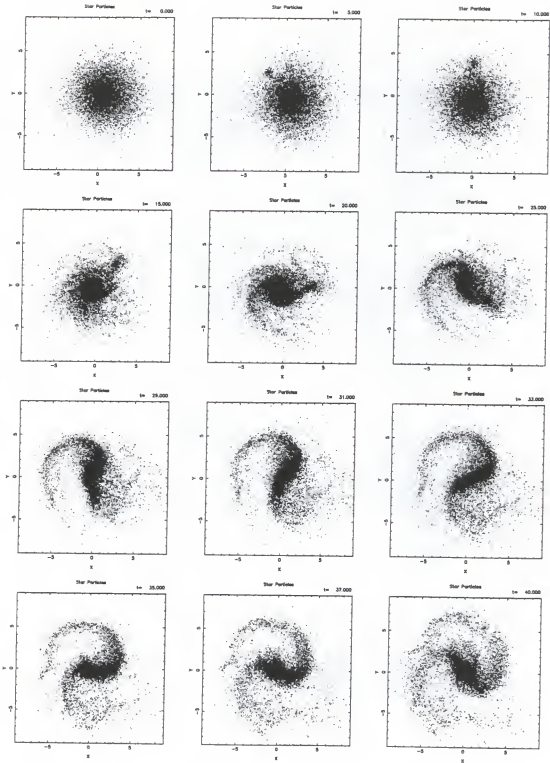
Figure 5.24: Evolution of the main disk star distribution in the prograde encounter. The satellite mass is 5% of the main disk mass, and the motion is prograde for all components. Times are shown on the upper right corner of each frame.
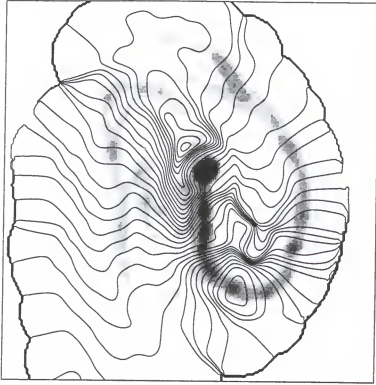
Figure 5.25: The velocity field at 15″ resolution overlaid on a grayscale image of the gas density at time t = 33, companion mass = 5% of the main disk mass, all rotating in a prograde sense. The contours are printed every 10 km/s. Both the velocity field and the surface density have been projected to an orientation similar to the one found in the observations.

although if the interaction scenario is correct, the companion can not be very massive since it appears to have been disrupted. Second, as can be seen from the simulation results that I presented above, the structure of the main galaxy (as well as the structure of the satellite galaxy) can change the outcome in a fundamental way. It is dangerous to build the initial galaxy structure (scale lengths, scale heights, disk mass distribution, halo-to-disk mass ratio etc.) from the conditions that we observe. The simulations that I made have proved that the disk structure, both horizontally and vertically, suffers fairly dramatic changes during the interaction.

Despite all these limitations, the idea that the asymmetric spiral structure is related to a recent accretion of a minor satellite companion seems appealing, especially since there does not seem to be any other mechanism that would build and support such a strong

asymmetry in the disk. As the simulations dramatically demonstrate, and as is further discussed in Chapter 6, the strong western spiral arm most likely is the tidal arm created in a recent interaction event. Perhaps somewhat surprisingly, the companion, despite its small mass, appears to be successful in creating also a strong stellar bar to the system.

The success in creating the observed structure and even some of the kinematics is encouraging. However, there remain some serious problems: the companion is not destroyed in the simulations, but remains as a dense stellar and gaseous concentration until the end of the simulations. A more convincing simulation would show both the creation of the asymmetric and nonaxisymmetric structures and the consequent destruction of the satellite. However, in my earlier experiments with satellites of the type that Hernquist and Mihos (1995) used, I often had the opposite problem: the companion was destroyed well before anything dramatic happened to the structure of the main galaxy. Thus, it seems that the fate of the companion depends very sensitively on its structure. The future models should incorporate satellites with different structural parameters and densities. Another important parameter that can help in disrupting the companion is the presence of a central bulge in the main disk galaxy (G. Hensler, private communication).

Another serious shortcoming in the current models is the wandering of the distortion. The observations suggest that the center of the outer disk and the nucleus disagree by perhaps 1 kiloparsec, but not more. The simulations, however, have the center of the bar move from the center of the halo or the center of the mass by several kiloparsecs. Part of this problem is certainly related to the non-destruction of the satellite. The satellite seems to "drive" the wandering of the bar and the disk in the potential well of the halo. If there is a way to destroy the satellite by star formation or tidal forces before it comes very close to the center of the disk of the main galaxy, this problem would be alleviated substantially. Lowering the mass of the satellite helps this problem somewhat. The

inclination of the orbit may help in disrupting the satellite, but it is not clear whether a high inclination (a strong "tidal" shock when crossing the plane) or a low inclination (constant perturbation by disk material) gives a better chance for disruption. More runs should be made to determine this. Dynamical friction from a more massive halo might also favor the disruption.

The lack of star formation brings considerable uncertainty to the interpretation of these runs. One "positive" impact of star formation could be that it disrupts a large fraction of the companion's gas reserve, thus making the gravitational support of the companion much weaker and subjecting it to tidal disruption. Again, the future runs should include the effects of star formation during the interaction.

Finally, a very limited set of initial conditions was investigated. A more thorough examination should incorporate a systematic variation of the mass ratios, both halo-to-disk and satellite-to-main disk. An inclusion of a bulge component could have dramatic effects on the interaction evolution, as demonstrated by Mihos and Hernquist (1994a). The gas-to-stellar mass ratios of the companion (and the main galaxy) should be varied, and a dark matter component could be included in the companion. The initial orbit could be started from farther away, made more elliptical, and various inclinations should be tried. The scale length of the main disk should also be varied. These are just some of the few parameters that could affect the outcome of the simulation. In the end, it appears that "the dynamical inverse problem" approach (Merritt 1994), where the observations of both the light distribution and the kinematics are used to build the model, rather than checking if the created models match the observations, is the method of choice in the future. However, how to apply this method to nonaxisymmetric systems remains a problem.

SYNTHESIS OF OBSERVATIONS AND MODELING

Nature of the Nucleus

The nucleus of NGC 7479 has been classified as a LINER (low ionization nuclear emission-line region) by Keel (1983a, 1983b). LINERs have strong low-ionization emission lines whose intensity ratios do not resemble those of extragalactic H II regions. Their excitation mechanism remains controversial. Excitation mechanisms that have been suggested include photoionization by a dilute power-law continuum, shock heating, cooling flows, and photoionization by very hot Wolf-Rayet stars and normal O stars (Filippenko 1993 and references therein).

Devereux (1989) has classified NGC 7479 as a starburst galaxy based on its high nuclear 10 μm flux. If LINERs are powered by starbursts, the LINER and star burst classifications agree with each other. However, if the LINER activity is powered by a power law continuum, similar to the power sources in the nuclei of Seyfert galaxies and QSOs, we suspect that the nucleus harbors a supermassive object. The mid-IR observations by Roche et al. (1991) reveal a relatively featureless 8–13 μm spectrum in the nucleus of NGC 7479. They classify NGC 7479 as a member of the silicate absorption group, which consists mostly of Seyfert 2 galaxies.

Radio Continuum Emission Near the Nucleus

The nucleus of NGC 7479 has been mapped with the VLA at 2, 6 and 21 cm. A moderately strong point source coincides with the optical position of the nucleus. Extended emission outside the nucleus comes from star formation. Most of it is

166

nonthermal emission from supernova remnants and the rest is thermal radiation from H II regions.

Determination of a spectral index for the nucleus is difficult. Neff and Hutchings (1992) observed the nucleus at 6 cm and obtained a flux density of 2.8 mJy in a $0''.4$ beam. After smoothing the 21 cm continuum map to a circular $4''.5$ FWHM beam and fitting a Gaussian to the nuclear source I obtained a nuclear flux of 7.9 mJy. The 2 cm map with the similar resolution gives a nuclear flux of 8.1 mJy. The uncertainties in these fluxes are 0.4 mJy, estimated from the errors of the Gaussian fits. The nuclear spectral index from equation (2–39) is close to zero or slightly positive. This implies that the emission from the nucleus has a substantial thermal component. According to Turner and Ho (1994), the thermal fraction of the flux is higher at 2 cm than at lower frequencies.

The flat spectrum implies a compact core of star formation, since the thermal flux comes from bremsstrahlung (free-free recombination emission taking place in the envelopes of H II regions). The brightness temperature of the nuclear emission is a few thousand degrees Kelvin, which is consistent with an H II region. Additional high resolution observations with the VLA at 2, 3.5 and 6 cm have been made and will be analyzed in the near future.

The nuclear 21 cm continuum and CO emission (at the same resolution) are shown in Figure 6.1. The radio continuum radiation follows the CO emission along the bar for about $30''$ (4.8 kpc at a distance of 32 Mpc). The emission peaks are at 23h 02m 26.37s, 12° 03′ $11''.1$ in the CO and 23h 02m 26.36s, 12° 03′ $10''.7$ in the 21 cm radio continuum. These positions coincide within errors.

The K band peak coincides with the radio continuum peak within $0''.2$ (Figure 6.2). The errors in the optical – near-infrared astrometry are on the order of $0''.4$, estimated
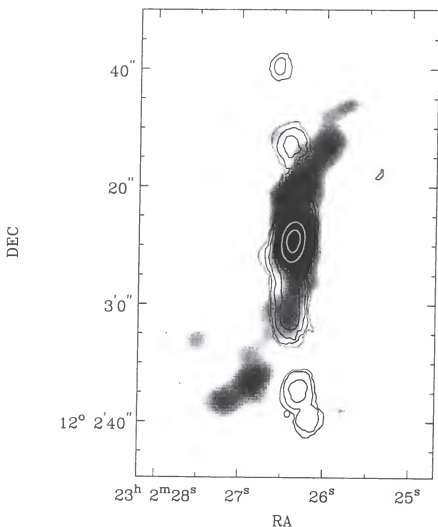
Figure 6.1: The contours of the CO emission overlaid on an exponentially scaled grayscale image of the 21 cm radio continuum from the uniformly weighted B configuration data. The contour levels are 0.16 x (1, 2, 4, 8, 12, 24, 36, 48 and 60) Jy/beam. The CO integrated intensity map was made from a cube that had been smoothed to the resolution of the radio continuum emission (4″.3 x 3″.85).

from Gaussian fits of the stars[1]. The grayscale J-K infrared color index image is shown in Figure 6.3 with radio continuum contours. The central red peak in the color image seems to coincide with the peak radio continuum emission.

1. Astrometry obtained using the Guide Stars Selection System Astrometric Support Program developed at the Space Telescope Science Institute (STScI is operated by the Association of Universities for research in Astronomy, Inc., for NASA).
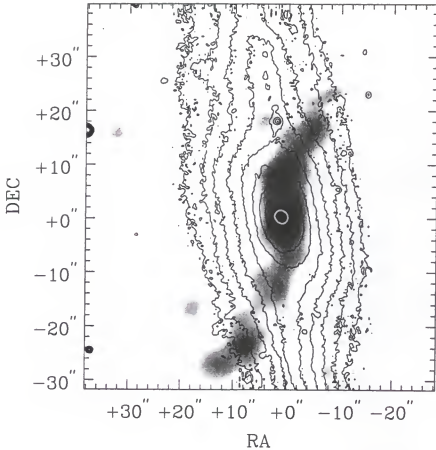
Figure 6.2: The K band image contoured on a grayscale presentation of the 21 cm radio continuum emission. The contours of the K band image are (14.6, 15.0, 15.4, 15.8, 16.15, 16.5, 16.9, 17.3, 17.7, 18.1 and 18.5) mag/(arc sec^2).

The Hα and radio continuum are shown in Figure 6.4. The central Hα peak has shifted toward northwest of the radio continuum peak. However, this shift is less than $1''$ (positional uncertainty is about $0''.5$ in the Hα image). The strong northern bar dust lane, as seen in the optical images from the HST, and optical images presented in Chapter 4, can easily shift the Hα peak. The nuclear Hα source is not very strong (for example, the H II region in the bar about $18''$ north of the nucleus has a higher Hα luminosity). Since the N II to Hα intensity ratio in the nucleus is greater than one (Hua et al. 1980; Filippenko & Sargent 1985), the excitation mechanism in the center must be different from pure star formation. The high resolution Hα image presented here does not include
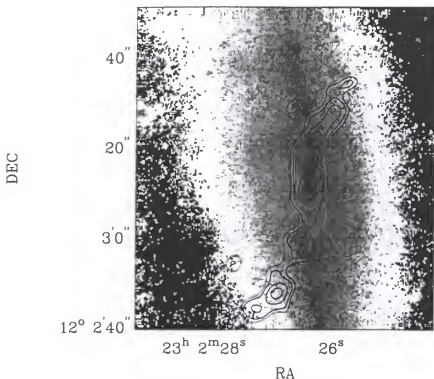
Figure 6.3: The 21 cm continuum image contoured on top of a grayscale image of the J-K color of the central region and the bar. The contours are $1.65 \times 10^{-4} \times$ (3, 4, 6, 8, 10, 16, 24, 30) Jy/beam.

the contribution from the 6583 μm N II line, but it does have a contribution from the (weaker) 6548 μm N II line.

Carbon Monoxide Emission from the Nucleus

In the nucleus, CO emission peaks at the same position with the radio continuum and the K band emission. The central CO morphology is slightly elongated along the north-south direction, matching the dust lanes that lead into the nucleus. The velocity field reveals a central molecular disk, with fast circular rotation, and an orientation close to that of the main galaxy disk. The nuclear disk is accreting gas from the bar, as shown by the kinematics in the position-velocity maps. Tidal shear is reduced in the rigidly rotating central disk. If the high CO intensities truly imply high H_2 column densities, we would expect to see abundant star formation in the nucleus. Since we do not observe this,
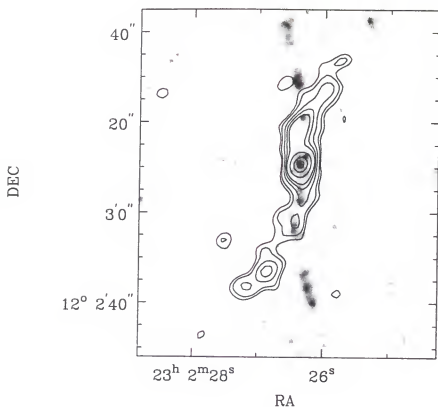
Figure 6.4: The contours of 21 cm radio continuum emission at 1.65 x 10⁻⁴ x (3, 4, 6, 8, 10, 16, 24, 30) Jy/beam over a grayscale of the high resolution Hα image.

other mechanisms or effects such as large extinction must reduce the optical radiation from the star burst.

I present the overlay of the CO emission on the J-K color map in Figure 6.5. The CO emission follows the red-colored dust lanes very closely. Again, the centers coincide within 0″.5. The contours of the Hα emission are shown on the CO image in Figure 6.6. Again, the two coincide very well over most of the length of the bar shown here, and the central peaks are at the same location within uncertainties.

The data show that there is a connection between star formation and CO emission. Clearly, the correlation is not simple, since the CO emission is brightest in the center, but only mild Hα emission is observed there. The most likely reason for this is the extinction. However, the CO emission does not always reflect the H_2 column density.
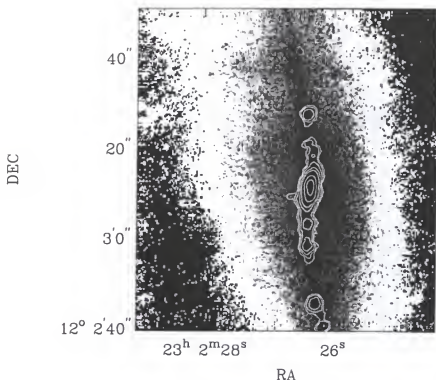
Figure 6.5: The contours of the naturally weighted CO emission overlaid on the grayscale image of the J-K color map. Darker colors are redder regions in the grayscale map. The contour levels are 40×10^{20} (1, 2, 4, 8, 12, 24, 36) H_2 molecules cm^{-2}.

Instead, it depends partly on the excitation conditions and the metallicities (Allen 1992; see also Knapen & Beckman 1996 and references therein). Higher resolution observations of other molecular species are needed to probe the physical conditions in the molecular gas near the nucleus.

Optical and Infrared Data Relating to the Nature of the Nucleus

In Figure 6.7 I show how the peak K band emission compares with the dust distribution (the J-K image). The grayscale level has been adjusted so that the dust lanes become visible. The reddest J-K color coincides with the peak K brightness within $0''.2$ (the positional alignment error).

The association between the dust lanes and the Hα emission is also of interest. This is shown in Figure 6.8. Again, the central peak and the distribution in the bar dust
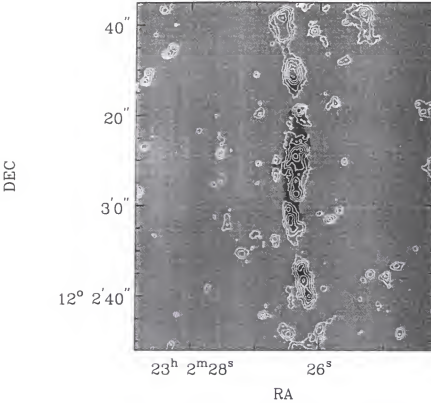
Figure 6.6: The contours of the high resolution Hα emission laid on top of
the grayscale image of the naturally weighted CO distribution. The
contour levels are, in arbitrary flux units, 50 x (2, 4, 8, 16, 32, 64).

lanes agree within alignment errors, which means that there is no offset due to triggering
and the associated time delay of star formation. The optical images also show that the
reddest emission comes from the nucleus (Chapter 4), and that there is no evidence for
blue colors and star formation in the nucleus.

Discussion of the Nature of the Nucleus

The comparison of the different images has confirmed that at all the observed
wavelengths discussed here the emission peaks at the same location in the nucleus, within
about $0''.5$ (80 pc if the distance is 32 Mpc). This can be understood if material falls
into the gravitational potential well of the galaxy. Star formation activity will then take
place in the nucleus. The observed central CO disk velocities allow the existence of a
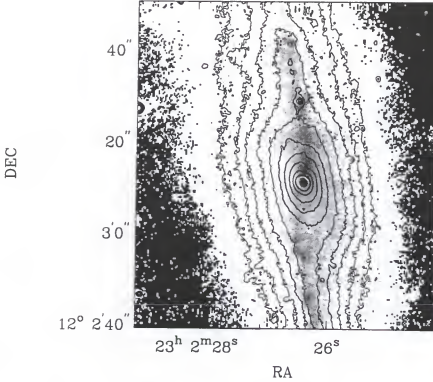
Figure 6.7: The K band contours shown on top of the J-K grayscale image. The darker grayscale shades are redder regions. The contour levels are (14.6, 15.0, 15.4, 15.8, 16.15, 16.5, 16.9, 17.3, 17.7, 18.1 and 18.5) mag/(arc sec)^2.

few times 10^9 $M_\odot$ within the central few hundred pc. The modeling results can not shed further light on the problem of the nature of the nucleus. The simulations where the bar potential was gradually introduced demonstrate that the gas is brought to the center where it accumulates.

Infrared spectroscopy would help in deciding the nature of the nucleus. Useful comparisons are provided by the strength of the molecular hydrogen S(1–0) and S(2–1) lines together with the Brackett γ emission line and the optical lines. In the mid-infrared, the IR fine structure lines of Ar III (9 μm), S IV (10.5 μm) and Ne II (12.8 μm) can reveal the excitation conditions, as demonstrated by Miles et al. (1994).
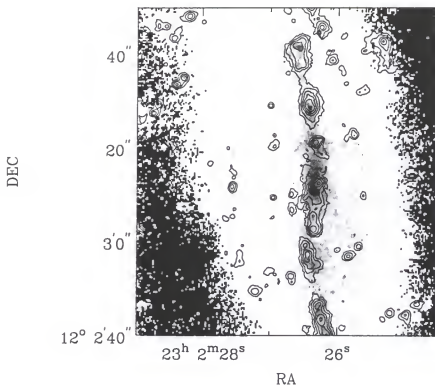
Figure 6.8: The contours of the high resolution Hα image are shown on the grayscale image of the J-K map, adjusted so that the dust lane is well visible. The contour levels are, in arbitrary flux units, 50 x (2, 4, 8, 16, 32, 64).

Physical Conditions of the Bar

Radio Continuum in the Bar

The radio continuum morphology at 21 cm has a curious "leading arm" morphology. A somewhat reminiscent radio continuum feature has been found in NGC 4258. It has been studied extensively, starting with van der Kruit et al. (1972). NGC 4258's radio continuum structure has a counterpart in ionized gas emission, and it has been interpreted as a braided jet near the plane of the disk.

A crude estimate of the spectral index in the bright region just north of the nucleus in NGC 7479 gives a very negative value. Therefore, the emission here is nonthermal. The character of the emission at other locations is less certain because of a lower signal-to-noise ratio.

The figures in the previous section show that the radio continuum emission outside the bar does not have counterparts at any other wavelength. In other mildly active galaxies the high resolution radio continuum follows star formation (Turner & Ho 1994). The large mean free paths of cosmic rays cause them to diffuse far away from their origin. The resulting lower level disk emission, with a brightness temperature of about 1 K (van der Kruit 1973), is below the detection threshold in my 21 cm continuum maps, where one sigma noise corresponds to about 6 K.

The radio continuum emission outside the bar is most likely related to star formation, but for some reason it does not coincide with the star formation. As was discussed before, the anomalous radio clumps outside the bar have counterparts in the CO emission which are located in the bar, both in the northern and in the southern ends of the continuum arms. Also, the dust lanes and current star formation are offset in a similar way from the radio continuum. How is it possible to have radio continuum emission in a region that is 1–2 kpc from the nearest strong star formation region?

If star formation was triggered as pieces of the companion passed through the bar, the young massive stars will explode as supernovae $10^6 - 10^7$ years later. The rotational velocity is correct for this kind of time delay and consequent spatial offset. The newborn stars need to be on nearly circular orbits, whereas most of the matter in the bar is in highly elongated radial orbits. A companion spiraling inwards is on a nearly circular orbit. I suggest that debris from a disintegrated satellite has impacted the bar very recently, and the merger is still going on. It is difficult to estimate the supernova rates and the magnitude of OB star formation before we have reliable spectral indices allowing us to separate the thermal and nonthermal radio components.

Alternatively, the 21 cm radio continuum emission originates in the nucleus. If so, the radio continuum feature represents a (dormant) jet or outflow cone. However, the

bending of the jet (in the leading sense) or emission outside the bar remains a problem. Obtaining radio bursts that extend for several kiloparsecs from the nucleus requires a very energetic source in the nucleus. Since there is no definite evidence for an active galactic nucleus, the "jet" scheme is very unlikely. If there is a jet, we would expect to see it at some other wavelengths. However, there is no evidence for a jet in other wavelengths.

Gas and Dust in the Bar

The molecular gas distribution is very similar to the J-K reddened colors. There is no offset between the straight dust lanes and the molecular gas. Also, the star formation, traced by the Hα emission, follows the molecular gas and the dust lanes very closely. This morphology is different from what is seen in the spiral arms of other galaxies. Lord and Kenney (1991) find that star formation and molecular gas are spatially coincident in one of the arms of M 83, whereas the dust lanes are upstream. The diffuse gas and dust respond to the shock, whereas molecular clouds behave like stellar particles and accumulate in the spiral potential minimum downstream. If the column density of the diffuse gas is low, it is not detected. The overlap of CO and Hα emission in the southern arm segment of M 100 (Rand 1995) can also be interpreted as this location's closeness to the corotation resonance.

If the diffuse gas density becomes very high, it starts to trap the molecular clouds as well. In M 51 (Vogel et al. 1988), the CO emission is well correlated with the dust lanes, whereas star formation takes place downstream. The same is true for the northern arm segment of M 100. This is more reminiscent of the bar in NGC 7479, although the dynamics in the bar region are very different from those in the spiral arms. Several studies have addressed the "steady-state" flow of gas in a barred potential (e.g. Roberts et al. 1979). Since the orbits are elongated along the bar, the incoming gas does not experience a shock similar to the density wave spiral arms. Instead, the shocks form on

the leading side of the bar. This property is related to the crowding of gas streamlines. If there are no ILRs or the ILRs are very close to the center, the dust lanes are centered. Also, the strength of the bar affects the straightness of the dust lanes: the stronger the bar, the straighter are the dust lanes. Since the dust lanes in NGC 7479 are very straight and relatively close to the center, it has a strong bar with no ILRs (or, if ILRs exist, they must be very close to the nucleus where they do not have any easily observable effects, as noted above).

The CO morphology in NGC 7479 is similar to that of M 101 (Kenney et al. 1996). The position-velocity maps show in both cases a linearly rising, spatially unresolved central disk, surrounded by gas with a much shallower velocity gradient. However, in M 101 the bar is much shorter and weaker, and the dust lanes are displaced far from the major axis of the bar toward the leading edges. In NGC 7479 the bar shocks "trap" most of the passing molecular gas, whether diffuse or in giant molecular clouds and associations. This is assisted by the location of the shocks close to the potential minimum of the bar: the material has just passed through the potential minimum and is moving "uphill" when it encounters the shocks and is trapped by the bar potential.

If the tangential streaming motions are in the direction of rotation, clockwise in the images (spiral structure trailing, Pasha & Smirnov 1982), it is relatively easy to show that to produce the observed "wings" of CO emission in Figure 3.11 (the wings extend to approaching velocities on the southern side and receding velocities on the northern side), there must be radial inflow. The magnitude of the velocity of this inflow near the nucleus, within a kiloparsec of the center, must cancel the effect of bar rotation and azimuthal streaming. Assuming that the corotation is found at a radius near $55''$, where the circular rotation velocity is about 200 km/s, and accounting for the projection effects, I find that the projected bar velocity at $6''$ from the center (about 1 kpc) is around 20 km/s.

The unknown azimuthal streaming motion also contributes to the tangential velocity. Therefore, a lower limit for the radial inflow is 25 km/s at this radius. Since the "wings" extend to perhaps 50 km/s on the opposite sides of the velocity diagram (wings represent approaching velocities on the southern side, where rotation and outflow gives receding velocities, and vice versa for the northern side of the bar), radial streaming with velocities well over 100 km/s is possible near the rapidly rotating inner molecular disk.

The strong bar causes the "feeding" of the nuclear molecular disk by exerting torques on the molecular gas that leads the bar in rotation. The resulting inflow speed was calculated in Quillen et al. (1995), and found to be 10–20 km/s. However, due to uncertainties in the adopted pattern speed, the inflow rate can be several times higher than this (Quillen, private communication). Additional acceleration near the nuclear disk increases this estimate further. The fate of the nuclear gas and dust after they reach the central gas disk is an open question that the current observations cannot resolve. According to Regan et al. (1997), 20% of the inflowing material stays near the center and the rest are scattered to bar orbits on the other side of the nucleus. There is only relatively weak Hα emission from the nucleus. Either the large amounts of dust have extinguished the visible signal of star formation, the star burst has not commenced yet, or there is some mechanism that prevents star formation.

It is likely that the recent merger has stirred up and heated the gas and dust in the nucleus, therefore temporarily preventing star formation. Another alternative is a cycle of star burst activity and quiescent periods. If galaxies have such cycles, NGC 7479 is on the verge of the next star burst. The radio continuum measurements reveal a relatively strong central point source. Since the size of this source is probably less than 100 pc, it is not a star burst like the one in M 82, where the star burst emission is spread throughout a region several hundreds of parsecs across (e.g. Rieke et al. 1980; Telesco et al. 1991;

Telesco & Gezari 1992). The results from a study of starburst galaxies by Young and Devereux (1991) show that the lowest star formation efficiency, defined by $L_{IR}/M(H_2)$, in their sample is found in NGC 7479. New observations at wavelengths less affected by dust extinction (infrared, radio) must be made to study the extent and magnitude of the nuclear star formation.

The amount of warm dust in NGC 7479 is 1.9 x 10^7 $M_\odot$ (Young et al. 1986). If we assume that most of it is in the bar, the $M(H_2)/M(dust)$ ratio is about 200, similar to the Milky Way (100). The uncertainties in the above estimate include the neglect of cold dust, and the uncertainty in the CO luminosity to molecular gas mass conversion factor. The contribution of H I gas is negligible within the bar region. There is some atomic hydrogen in the northern part of the bar, and at the location of the southern CO clumps, as can be seen in Figure 6.9. The H I has been converted into H_2 (Elmegreen 1993; Knapen & Beckman 1996; Kenney 1996b).

The conversion of H I to H_2 takes place when the gas is sufficiently self-shielded from dissociating UV photons. The presence of dust is essential for this process, since dust absorbs UV photons, and also "catalyzes" the formation of H_2 molecules on dust grains. In general, the column density of H I surrounding a molecular cloud core is (Kenney 1996b)

$$N_{HI} \propto \left(\frac{n_{gas} R_H}{G_{surf}} \right)^{-1.5}, \tag{6-1}$$

where n_{gas} is the mean gas density in the transition region, R_H is the rate constant for H_2 formation on dust grains, and G_{surf} is the H_2 photodissociation rate at the cloud surface. In the central parts of galaxies, the interstellar pressure compresses gas and the gas density is high enough so that practically all the gas is in the molecular form. Similar arguments can be applied to spiral arms.
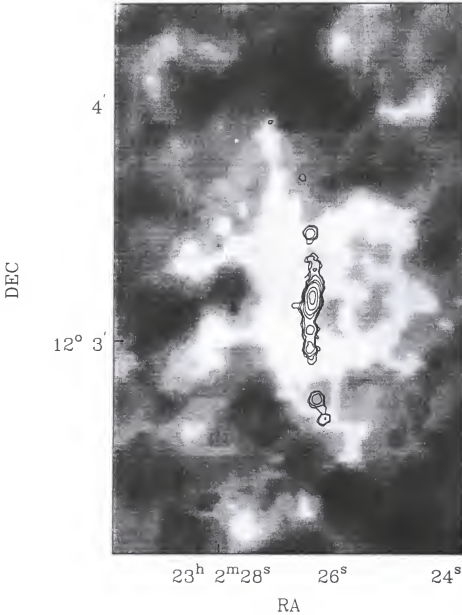
Figure 6.9: The CO contours overlaid on the H I grayscale, only the bar region is shown. The contour levels are at $40 \times 10^{20} \times (1, 2, 4, 8, 12, 24, 36)$ H_2 molecules cm^{-2}.

Optical and Near-Infrared Observations

The most obvious features of the bar in the optical are the straight dust lanes near the major axis of the bar, and the bright star formation regions. A closer examination reveals numerous long dust lanes coming into the bar mostly from the western side. One

very obvious dust feature is seen about $30''$ to the north of the nucleus, perpendicular to the bar (Figure 4.12). A region of accompanying star formation in the bar lies at the end of this dust feature.

Optical color index images presented in Chapter 4 bring out the red color of the region enveloping the bar. The red color is explained by the large amount of dust, since mixing of orbits in stellar disks is expected to remove any population gradients (including color gradients) in a few dynamical times.

In the presence of large amounts of locally patchy extinction due to dust, it is difficult to estimate the age of stellar populations. The estimation of age based on wide band colors is uncertain (Worthey 1994). More detailed spectral information is needed for a reliable identification of stellar populations. The metallicity gradient and age differences can also conspire in producing the observed colors. However, a potentially useful and important study is the investigation of optical line excitation ratios across the bar and in the disk (Martin & Roy 1994). Such studies can also help to estimate the age of the bar (Martin & Roy 1995). Recently, using this technique Martin and Roy (1995) discovered that the bar in NGC 3359 is very young, $\sim 4 \times 10^8$ years. Similar data for NGC 7479 exist, but have not yet been reduced. A cursory look at the data has revealed a dramatic difference in the excitation of the western and eastern spiral structures (P. Martin, private communication).

In the near-infrared bands the stellar bar is brighter by about 0.2 mag/(arc sec^2) on the southern side. The reason for this discrepancy is unknown. The extinction can vary along the bar. This bar brightness asymmetry has its counterpart in the outer asymmetrical spiral arm structure of the galaxy. The numerical simulations in Chapter 5 demonstrated that the spiral arm asymmetries are most likely a consequence of the tidal torque from the companion.

The straight bar dust lane is particularly well seen in the J-K and H-K images. This implies that there is an additional process increasing the luminosity in the K band. Spectral measurements of, e.g., the CO feature at 2.3 μm will allow one to decide whether this extra emission comes from giant stars, supergiants, hot dust or H II regions.

Star Formation in the Bar.

The tracers of star formation in the presented images are Hα, optical U, B and V images and the optical color index images. Because all these are influenced by extinction, no reliable quantitative measurements of star formation can be made. The radio continuum images trace star formation also, but if most of this emission is nonthermal synchrotron radiation from supernova remnants, it will not coincide exactly with the position of original star formation.

At the resolution of the images, and within alignment errors, the location of star formation is very close to that of the dust lanes and the molecular gas. Studies of shocks in barred galaxies include those made by Jörsäter (1984), Lindblad and Jörsäter (1988) and Teuben et al. (1986) of the bar shock in NGC 1365, and Pence and Blackman (1984) of the bar dust lane in NGC 6221. For NGC 1365, the velocity drop perpendicular to the shock is 230 km/s, and for NGC 6221 about 150 km/s. Martin (1996) has argued that star formation near the dust lanes is not related to strong shocks but rather caused by high gas densities at locations where the gas gathers. At these locations star formation is assisted by weak shocks in the ISM. A study of the relationship of the compression shock to star formation was made with numerical simulations by Knapen et al. (1995).

Often, especially in earlier type barred galaxies (SBa and SBb), no or very little star formation is seen along the bar. One reason for this is the lack of gas in the bar. This cannot be the whole explanation in later type galaxies like M 83, where

abundant molecular gas is seen along the bar. Kenney and Lord (1991) gave several possible reasons for the dearth of star formation along the bar in M 83. First, the gas surface density may be below the threshold for gravitational instabilities that lead to star formation. Second, tidal forces are large and they can prevent the clouds from collapsing to form stars. Third, the time scale for the passage of gas through the bar may be so short that there is not enough time for clouds to compress and start the collapse leading to star formation. This is true for dust lanes placed far away from the potential center (major axis) of the bar. If shocks are required to initiate star formation, star formation in bars is deficient because often the shock takes place long after the cloud has passed the potential minimum, whereas in spiral arms the opposite is true. Athanassoula (1992b) has suggested that the strong shear motions around the shocks prevent the collapse of molecular clouds and the subsequent star formation. Tubbs (1982) states that if the gas clouds impact the bar shocks at a very high speed, the clouds are compressed and then disperse before they have time to collapse. This is related to the third possible explanation given by Kenney and Lord (1991).

Why is there so much star formation near the bar dust lanes of NGC 7479? The CO and Hα position-velocity plots across the dust lanes hint that shocks of moderate strength (velocity jumps of 100–150 km/s) can exist there, although these velocity jumps mostly represent the ensemble of radially streaming material across the bar. A straightforward application of the CO to H$_2$ mass conversion factor tells us that the gas surface densities in the bar are at least a few hundred M$_\odot$/pc^2. The usually cited numbers for star formation thresholds, for example, from the Jeans criterion, are one order of magnitude smaller than this. So, although we do not have an accurate estimate for the Jeans critical mass, the surface density in the bar is high enough to cause gravitational instabilities in the absence of other effects.

From the distribution of the star forming regions along the bar in NGC 7479 it is immediately clear that star formation is not symmetric about the nucleus. Therefore, dynamical resonances do not regulate the distribution of H II regions along the bar. The overall efficiency of star formation in the bar is explained by triggering in moderate strength shocks. Because the dust lanes are near the potential minimum of the bar, gas has time to compress before it leaves the bar. This scenario will be observationally confirmed if we find more galaxies that have straight shocks close to the bar major axis and associated star formation (NGC 4123 has centered, straight shocks and some H II regions in the bar almost coincident with the dust lanes).

One reason for the patchy nature of star formation in the bar of NGC 7479 is the extinction by dust. Careful examination of optical images with high contrast on a TV display reveals several major dust lanes coming to the bar from the western side. Sometimes they can be followed on the eastern side. These dust lanes are capable of producing breaks in the optical emission.

Models for the Bar Gas Structure and Inflow

I presented models of the gas distribution and dynamics in the bar with several different pattern speeds in Chapter 5. The initial gas distribution was uniform. As the nonaxisymmetric forces are introduced, the gas quickly forms a bar and a spiral structure, and begins the inflow towards the center along the bar. The gas distribution is rapidly changing and no quasi-stationary state is reached, although in the higher pattern speed models the gas morphology is more persistent. The models with lower pattern speeds create rapidly a very high gas concentration in the nucleus. The gas surface densities in this central gas disk are at least a factor of two higher than the nuclear molecular gas density derived from the CO observations, using the standard conversion factor. In contrast, in the models with fast pattern speeds the nuclear gas surface density is similar

to the observed densities, around 2000 $M_\odot pc^{-2}$. At intermediate times after the full bar perturbation has been introduced ($6 - 8 \times 10^8$ years from the beginning of the simulation), the gas inflow rate is about 5 $M_\odot$/year at 1 kpc.

The large CO velocity width in the position-velocity maps along the bar ($100 - 150$ km/s) is caused by strong radial motions along the bar. Since the beam size is large (about $3''$ or 500 pc across the beam), both the outward streaming and inward streaming components are seen within the same beam. The difference in the radial velocity between these two components can be over 300 km/s. The tangential streaming motion is much smaller, and there is hardly any detectable difference in the tangential motion between the outward and inward streaming gas components. The gas velocity perpendicular to the shock decreases by about 100 km/s in a typical bar shock region along the leading bar shock lanes. However, this jump takes place in a very narrow region, and observations with better than $1''$ resolution are needed to detect these jumps in the velocity. The models support the idea that the narrow dust lanes observed along the leading edges of several barred spiral galaxies are indeed near the location of the bar shocks.

Star formation takes place near these shocks in places where the gas piles up. However, the detailed distribution of star formation with respects to the shock fronts cannot be answered with the simulations and observations made here. Higher resolution simulations and observations need to be made to answer this question. Star formation phenomena and its effects should be included during the simulation. It is puzzling that there is abundant star formation in the bar of NGC 7479, but the gas-rich bar in M 83 does not have much star formation.

Finally, the simulations offer little help for explaining the peculiar inverse-S-shaped CO velocity field near the center. There is a hint of this kind of structure in the velocity field presented in Chapter 5 (Figure 5.12), but the magnitude of the velocity distortion is

much smaller than in the observations. The central gas concentration must have built up early to form a compact mass concentration around the nucleus with a very high rotation velocity. The slower, but steady, accretion rate in the bar simulations is incapable of reproducing the central mass concentration. However, early gas inflow into the nucleus is seen in the interaction simulations, especially from the prograde spinning satellite which loses part of its gas content early. The detached gas falls rapidly (in less than 10^8 years) into the nucleus, where it builds up the central mass.

Spiral Arm Structure and Morphology

In the imaging survey of Pogge (1989), NGC 7479 has the most sharply delineated bar and spiral arms in $H\alpha$. It also has the most highly asymmetric spiral arm pattern in this survey (Quillen et al. 1995). A more detailed study of the symmetry was made by Knapen (1992). He found that there is practically no symmetry in the $H\alpha$ distribution along the spiral arms. Only the peaks near the ends of the bar are symmetrically placed, but they have different luminosities. Elmegreen and Elmegreen (1987) have classified NGC 7479 as an arm class 9 object, which means that it has a grand design spiral arm structure with two symmetric inner arms and multiple long and continuous outer arms. If there is any symmetry at all in the arms, it does not extend very far beyond the ends of the bar.

Del Rio (1995) and Knapen (1992) both found that the arms cannot be fit to a logarithmic spiral. I have confirmed this result using the high resolution H I data. The southwestern spiral arm can be fitted with a logarithmic spiral function out to a deprojected distance of $110''$, where the pitch angle changes from 36° to 22°. This location is easily seen in the integrated intensity maps (Figure 2.3). The arm comes along the western edge of the H I disk from the north, but then has a sharp turn at this location towards the

east-southeast. A strong concentration of H I emission marks this location. An overlay of the H I and Hα images is displayed in Figure 6.10, showing the sharp turn of the arm. The H I arm stays at approximately the same distance from the nucleus from the northwestern corner to its end on the eastern side of the disk.
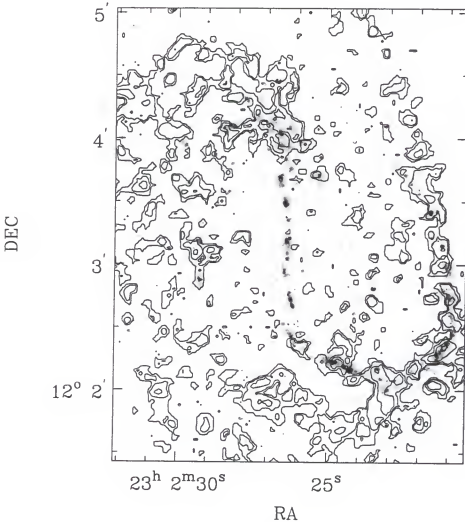
Figure 6.10: The overlay of the high resolution (5″.9 x 5″.0) H I contours on the high resolution Hα image. The contour levels are 1.8×10^{20} (3, 6, 10, 16) atoms/cm^2.

The spiral structure in the atomic hydrogen is best seen in the high resolution image (Figure 2.6). The western spiral arm is composed of a long string of "clumps" that are not resolved in the direction perpendicular to the arm. These have counterparts in Hα

and optical emission out to a position angle of 290°. Here, the optical and H I arms seem to separate, with the optical arm curving back toward the inner radii before it terminates. The velocity field on the western spiral arm shows that its kinematics are different from the main disk. Along the minor axis, where only radial motions are detected, the velocity contours do not seem highly disturbed. This is consistent with the idea that the perturbing companion is on a low inclination orbit with respect to the main disk. Farther out beyond the main disk the contours near the arm bend strongly towards the north, and after that they cross the arm perpendicular to it. For this reason, the line-of-sight velocity on the arm is higher than expected from a normal rotation. South of the minor axis, the velocity contours bend strongly to the south before crossing the arm. This means that the line-of-sight velocity is lower than expected for an undisturbed rotation.

This perturbation is probably related to a different inclination of this arm and to gas moving radially towards the arm. It is unlikely that these perturbations are related to a density wave, since the density wave streaming motions should be seen globally, not only in the arms. The perturbations can be explained with arms inclined to the main disk by about 10°.

The spiral structure on the eastern side is very different. Three sections of gaseous spiral arms emerge from the northern end of the bar region, which itself has more atomic gas than its counterpart on the southern end of the bar. Each one of the three arms turns sharply towards the south and continues for about 90°. On the southern side, a thin, long H I arm extends for more than 3′ from the nucleus. No optical counterpart to this feature is visible.

The dust lane in the southwestern arm is on the leading side of the arm until it splits between the two strong H II regions at about 65″ from the center and moves to the trailing side. It has been suggested that the corotation lies around this radius (Aguerri

et al. 1996; Beckman & Cepa 1990). The spiral arm continues well past the bar end to the eastern side of the bar. A similar structure is seen in the north. These structures are especially well delineated in the Hα, U and B band images in Chapter 4. Quillen et al. (1995) suggested that these linear structures are related to the remnant of a merging dwarf galaxy. The optical spiral structure on the eastern side is incoherent and patchy. The lack of any coherent spiral structure on the eastern side is also seen in the numerical simulations of a merger, presented in Chapter 5.

The largest perturbation in the Hα velocity field takes place just north of the southernmost part of the southwestern spiral arm. The velocity contours bend sharply towards the south on the western side of the line-of-nodes. A similar effect can be seen in the H I velocity field, and H I channel maps. This means that at this location inside the spiral arm, the line-of-sight velocities are lower than expected from circular rotation. The model shows that this effect can be achieved if the motion is mostly radial towards the arm.

Disk and the Near Environment of NGC 7479

The total extent of the gaseous disk, as seen in Figure 2.12, is more than $7'$. This is considerably larger than the optical size ($4'.4$, Nilson 1973). Part of this discrepancy is due to the large beam size of the VLA D configuration map that was used to estimate the extent of the H I disk. But even when that effect is taken into account, the H I distribution seems to extend beyond the optical disk, mostly because of the H I arms in the north and the south. The main H I disk, seen at higher resolution H I maps, has a major axis length of about $4'$, comparable to the extent of the optical disk.

In H I, the main disk has several "holes" with sizes similar to the H I naturally weighted beam size. This clumpy structure of the interstellar medium appears to be

common to all disk galaxies (e.g. Brinks & Bajaja 1986). A typical surface density in the disk is about 7×10^{20} atoms cm^{-2} which corresponds to about 7 M$_\odot$ pc^{-2}. This is probably too low to trigger star formation. Assuming a flat rotation curve with a rotation velocity of 215 km/s beyond 100$''$ and a sound speed in the gas of 7 km/s, the critical density for instability can be calculated from the Toomre stability criterion

$$\Sigma_c = \frac{\kappa c_s}{\pi G} = 147 \times R^{-1}(kpc) \ M_\odot, \qquad (6\text{--}2)$$

This gives values between 7 and 9 M$_\odot$ pc^{-2} within the radii 100$''$ – 130$''$ (16 – 20 kpc in the galaxy). The H I disk boundaries are relatively sharp.

There is a weak high luminosity optical extension in the southern part of the disk at R.A. 23h 02m 26.28s, declination 12° 01$'$ 30$''$ (Figure 4.16). A long dust trail extends inward from this. This dust lane cuts the bar perpendicularly 30$''$ north of the nucleus. It could mark the orbit of the companion. Okamura (1978) and Blackman (1983) give a more detailed account of the features in the disk, including a plateau around the bar. Star formation is strongly concentrated into the bar and in the western arm. A strong and extended concentration of H II regions lies to the north of the northern end of the bar. Here, the orbits inside and outside the bar crowd (a similar situation is seen in M 83, Kenney & Lord 1991).

Search for the Pattern Speed and Dynamical Resonances

The most important dynamical resonances in disk galaxies are the Outer Lindblad Resonance (OLR), the Inner Lindblad Resonance (ILR) and the Corotation Resonance (CR). At the corotation resonance the pattern (bar, spiral arms) is corotating with the matter (gas, stars) that is on circular orbits. It should be noted that the circular speed of rotation, and therefore, the rotation curve, is not the same for the gaseous, dissipative component, and the collisionless component, the stars. Although they may start with the

same circular velocity at some distance, as is usually assumed for the initial conditions in numerical simulations, the velocities soon will become different from each other. This difference is caused by the heating of the stellar component in close encounters. Therefore, one would expect that the observed tangential velocity at any distance from the center of a disk galaxy is smaller for the stars than for the gas. However, the observed differences in the velocity dispersions between the stars (20–30 km/s) and the gas (10 km/s) are not large, so we would not expect to see large differences in the rotational speed. The difference between the gaseous and stellar tangential velocities is a special case of what is called the asymmetric drift, and it has been observed in NGC 4321 (Knapen et al. 1995) and in NGC 4736 (Mulder 1995b), where it is about 40 km/s. The gas is dissipative, and as most models of the interstellar medium have shown, remains at an isothermal temperature. This is a good approximation for the numerical simulations of disk galaxies as well.

In the linear theory for weak gravitational perturbations from axisymmetry, the dynamical resonances are calculated with the help of κ, the epicyclic frequency of a star oscillating around its circular orbit. The derivation of the linearized perturbation equation, and κ, can be found in Mihalas and Routly (1968). The result is

$$\kappa = \left[4\Omega_c^2 + R_c \left(\frac{d\Omega_c^2}{dr} \right)_{R_c} \right]^{\frac{1}{2}} \qquad (6\text{--}3)$$

or in terms of the circular velocities,

$$\kappa = \left\{ 2 \frac{V_c}{R_c} \left[\frac{V_c}{R_c} + \left(\frac{dV}{dr} \right)_{R_c} \right] \right\}^{\frac{1}{2}}. \qquad (6\text{--}4)$$

In these equations, Ω_c is the angular speed of circular rotation at radius R_c from the center of the galaxy, and V_c is the speed of circular rotation at the distance R_c. If the pattern speed of the bar or spiral arms is Ω_p, then an ILR is defined by

$$\Omega_p = \Omega_c - \frac{\kappa}{2}. \qquad (6\text{--}5)$$

This means that for every full rotation of the bar or spiral arm, the star has described two epicycles. The OLR is defined by

$$\Omega_p = \Omega_c + \frac{\kappa}{2}. \tag{6-6}$$

This means that after the pattern has completed two full rotations, the star has described one epicycle. The corotation occurs at a radius where

$$\Omega_p = \Omega_c, \tag{6-7}$$

in other words, the pattern and the matter corotate with the same speed. The value of κ is undefined at this radius and ideally, no epicyclic motion takes place. It must be emphasized that the above formulas are only true for a small perturbation. If the strength of the perturbation exceeds 5–10 % of the axisymmetric force, the above formulas can be used only as approximations, and the true radii of the resonances can be found only through a nonlinear orbit analysis (e.g. Knapen et al. 1995).

Previous Measurements of the Pattern Speed in NGC 7479

Duval and Monnet (1985) place the corotation radius at the end of the bar, which they judge to be at about $56''$. They do not give any compelling arguments for the existence of the corotation resonance at this radius. They obtain no ILRs, and their rotation curve is gently rising until $120''$. Their Hα long slit spectra give rotation velocities around 250 km/s at $120''$ for an assumed inclination of $45°$. The corotation angular speed is about 24 km/s/kpc for a distance of 32 Mpc.

Beckman and Cepa (1989, 1990) assume the same in their studies. More recently, del Rio (1995) has made a photometric study of NGC 7479. She finds the corotation at $85''$ from the center, whereas she places the end of the bar at $59''$. Aguerri et al. (1996) have placed the corotation at $60''$, near the end of the bar. Elmegreen and Elmegreen (1995)

studied the extent of two strong, symmetric spiral arms in spiral galaxies. They conclude that the end of these marks the location of corotation. For NGC 7479, they give as endpoints of the two strong arms $74''$ and $106''$. Apparently, corotation must be located between these two radii. Quillen et al. (1995) assume that the corotation is at the end of the bar near $45''$, and obtain an angular rotation rate of 0.1 Myr^{-1}. Finally, Sempere et al. (1995a) have found the corotation at 9 kpc, which, at their assumed distance, corresponds to about $57''$. They used a similar technique to that used in this dissertation, matching the simulation results to observations. Their simulations used a potential from an R band image, and their gas is modeled by a sticky particle code, similar to that of Combes and Gerin (1985). One common problem for all these determinations is that different position angles for the line-of-nodes and inclination have been used. These affect the derived values slightly. It is remarkable that ILRs were found only by Aguerri et al. (1996). They suggest that the location of the outer ILR is at $15''$. However, they used a simple exponential rotation curve $v(R) \sim R^{\alpha}$, with $\alpha = 0.079$.

Pattern Speed Estimate from This Study

One technique to estimate the pattern speed was first presented by Tremaine and Weinberg (1984). This method relies on the use of the continuity equation and assumes that 1) the disk of the galaxy is flat, 2) the disk has a well-defined pattern speed and 3) that the surface brightness of the tracers obeys the continuity equation. In the presence of a lot of star formation and phase transitions from H I to H_2, this method is less reliable. It works best for SB0 type galaxies. I have chosen not to employ this method for NGC 7479, since this galaxy obviously does not obey the continuity equation in its tracers, as shown by abundant star formation and a stark contrast between its H_2 and H I distributions.

Another method was introduced by Canzian (1993). He utilizes the streaming motions associated with spiral structure, and claims that if one subtracts a model velocity field from the observations, the residuals will form an $m = 1$ spiral mode inside the corotation and $m = 3$ spirals outside the corotation. Since the spiral structure of NGC 7479 is strongly asymmetric and does not have a clear grand design $m = 2$ structure, the application of this method to the data is questionable. Also, the large disturbances seen on the western side may not be related to density wave streaming.

Canzian's method relies on the subtraction of the *axisymmetric* part only from the velocity field. In practice, it is difficult to derive the axisymmetric part only. Instead, the streaming motions are included when one fits the observed velocity field with a model, and therefore, the effects that are sought for may themselves be at least partly subtracted out. An additional complication is the lack of emission inside $40''$ in NGC 7479. In spite of all this, I tried to apply Canzian's method to the H I data. The result is shown in Figure 6.11.

It is impossible to tell if there are spiral features corresponding to streaming motions in Figure 6.11. Even color representations of the residual field do not give a much better result. If anything, there is a hint of a beginning of a spiral feature in the residual map at position angle $60°$ in the middle of the slice of the disk that is shown, $40'' - 130''$. If this is the corotation radius, it is close to $85''$, as suggested by del Rio (1995).

Another possible technique for determining the corotation radius is the use of several optical features: gaps, spurs, bifurcations, kinks of spiral arms, endpoints of star formation, dust lane cross-over points etc. (Elmegreen et al. 1989; Elmegreen & Elmegreen 1990). As mentioned above, Knapen's (1992) measurements revealed a lack of any symmetry in the star formation patterns of the galaxy along the arms on the western and eastern side. This result limits the applicability of the Elmegreens' method
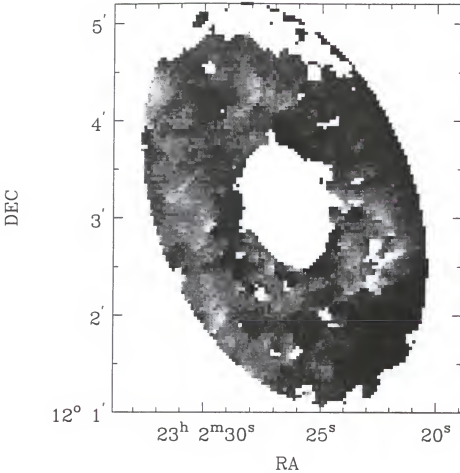
Figure 6.11: The residual H I velocity field from the naturally weighted data. The range of grayscale levels is from −20 km/s to 40 km/s in steps of 4 km/s.

to NGC 7479 seriously. Several kinks in the western arm can be seen, most notably at about $85'' - 90''$. There is also a break in star formation at this radius. But unless this arm is highly inclined, there is no similar pattern on the eastern side. As seen in the optical images near the end of the western arm, there is a bifurcation, with the tail of the spiral arm turning inwards. Some weaker emission follows the H I trail towards north. Again, this feature does not have any counterpart on the eastern side.

The corotation radius from the numerical SPH simulations

The simulations presented in Chapter 5 strongly support the claim that the corotation lies at $55''$ or even closer to the end of the bar. The gas morphology is not consistent with

the observed morphology if the pattern speed is lower. In low pattern speed models, a long linear gas ridge in the center connects the outer gas ridges that are diplaced towards leading edges of the bar. The observations, however, clearly reveal that the leading morphology should extend much closer to the nucleus. The best correspondence between the models and the observation is achieved when the pattern speed is high, 27 ± 3 km/s kpc^{-1}, placing the corotation at the above-mentioned radius, or even a little closer to the bar end.

The star formation morphology in the bar follows closely the gas morphology, even when different star formation criteria are used. The Hα observations reveal the star formation regions, and the best agreement with observations is again reached when the corotation is just beyond the end of the bar. It could be argued that the dust absorption could systematically change the location of the detected Hα emission, but even so, the linear extents of the structures should remain the same, and the best correspondence between the models and the observations would still be obtained by placing the corotation near the bar end.

The shock structure should be closely correlated with the dust lanes in the bar. Again, the shock morphology is in best agreement with the observed dust lane structure when the pattern speed is high. The overall galactic structure at the early times in the simulation when the perturbation is being introduced agrees better with the observed primary spiral arms and secondary spiral arcs when the pattern speed is high. The strong western arm, however, may be the product of a recent interaction or merger, as suggested by the satellite merger simulations and the observational evidence presented later in this chapter. The spiral arms are almost perpendicular to the ends of the bar in the low pattern speed simulations, which is inconsistent with both the observations and the interaction-driven spiral structure.

The low pattern speed simulations also show a very high gas concentration near the nucleus at later times, inconsistent with the observations. These models evacuate almost all the gas from the bar, and after 1 Gyr from the beginning of the simulation there is hardly any gas left in the bar. The higher pattern speed simulations support a more long-lived gas structure in the bar, and are more consistent with the CO observations. The velocity field of the gas in the bar also supports the faster pattern speeds. The range of velocities is fairly low along the bar, but a larger range of line-of-sight velocities for the gas rotating in the bar is achieved when the bar rotates rapidly. The observations of the molecular gas at the largest distances from the center support the larger velocities. The central gas concentration and its kinematics can not distinguish between the low and fast pattern speed models, since the observed line-of-sight velocity field is not created in any model.

From the detailed comparison of the observations with the models an overwhelming amount of evidence favors the high pattern speed, locating the corotation radius at $1.1 - 1.2$ times the bar length. The results from my investigation are more reliable than the previous estimates that relied often on studying only the strong western spiral arm. Especially, if the proposed recent interaction scenario is true, studies treating the spiral arm structure as a bar-driven entity are suspect (Sempere et al. 1995). Perhaps coincidentally, their best match pattern speed, 30 km/s kpc^{-1}, is very close to the value found here. On the other hand, work on one spiral arm only, such as the investigation by del Rio (1995), is very dangerous, since if resonance structures exist, they are expected to be visible on both sides of the galaxy. I believe this has led her to erroneously identify the peculiarities of a possibly interaction-driven spiral arm as resonance features.

If the corotation is around $55''$, its location agrees with the end of the region with very blue colors north of the bar, and a break in the blue colors and star formation just

south of the bar. There also appears to be an ellipse of atomic gas, seen in Figure 2.8, roughly aligned with the major axis and having a semimajor axis close to $55'' - 60''$, and an axial ratio that gives an inclination just above $50°$, all consistent with it being related to the corotation resonance.

Evidence for a Recent Merger with a Gas-Rich Dwarf Galaxy

Introduction and Results from Other Studies

What has caused the remarkable asymmetry in the spiral arm structure? This could be a result of the intrinsic evolution of the disk in isolation, or a result of a perturbation due to an external effect. These were first briefly discussed in Laine and Gottesman (1996). Earn (1993) has studied the maintenance of one-armed patterns in spiral galaxies. He concluded that the rotation curves need to have the correct form to support these patterns. Specifically, if $\Omega(r) - \kappa(r)$ is constant over a large range of radii, then a one-armed spiral can be maintained. I have applied this test to the H I rotation curve of NGC 7479. It turns out that $\Omega(r) - \kappa(r)$ is not constant anywhere in the disk, but rather it is a linear function of the radius. Even if the disk rotation curve is capable of maintaining an m = 1 perturbation, the question of its origin remains. Most likely interactions are responsible for exciting almost all the strong m = 1 symmetries studied. This was found to be true for Magellanic type galaxies by Odewahn (1994, 1996). I know of no reported cases in numerical simulations of isolated galactic disks that have produced long-lived m = 1 asymmetries of the magnitude observed in NGC 7479.

A recent interaction is a much more likely reason for many of the exceptional features seen in NGC 7479. A recent study of one-armed spiral galaxies was made by Phookun (1993). He studied a sample of five one-armed spiral galaxies, NGC 3162, NGC 4027 (Phookun et al. 1992), NGC 4254 (Phookun et al. 1993), NGC 4654 (Phookun & Mundy

1995) and NGC 5713. It turned out that every one of these galaxies is interacting with its environment, usually with a companion galaxy or a large H I cloud. NGC 4027 appears to have a ring of accreted gas around the disk, in a plane inclined to the main disk. Gas from an intergalactic H I cloud is accreting to the perimeter of NGC 4254. NGC 4654 is traveling through dense intergalactic gas with a high speed, and therefore it assumes a peculiar morphology. There is no evidence for a lack of a massive halo in any of these galaxies. In the absence of a massive halo the m = 1 perturbations are favored in the scenario of swing amplification. Phookun suggests that the dominance of the one-armed mode is caused by the excitation of weak leading waves by an interaction. These leading waves can then grow larger by swing amplification if there is no damping ILR in the center and the feedback loop is closed.

Simulations of mergers between a small mass companion and a spiral galaxy have appeared in the literature during the last few years. Mihos and Hernquist (1994) and Hernquist and Mihos (1995) have studied a compact stellar companion merging with a spiral galaxy using a tree-SPH numerical code. They find that the presence of a substantial bulge component can prevent or prolong the development of a central starburst. This is most likely due to the ILRs where the gas stays some time before falling to the center (Kenney et al. 1992; Knapen et al. 1995; Shlosman et al. 1989). Their stellar companion has 10% of the mass of the disk of the main galaxy, and largely survives to the center.

The results of Sofue (1994) indicate strong tidal stripping of ballistic gas clouds from a companion which impacts the disk of the main galaxy in a high inclination orbit. He extends his work to the M 31 system. He suggests that the infalling motion heats the gas so that it becomes ionized. Therefore, Hα emission may not always indicate star formation. Sofue (1994) also interprets the dark cloud spirals seen in the central region of M 31 as trails left behind the stripped clouds of an infalling companion.

Thakar and Ryden (1996) studied the problem of formation of massive counterrotating disks in spiral galaxies. They describe the gas as ballistic particles that lose a fraction of their speed in collisions. They find that merging of a gas-rich dwarf galaxy heats the disk of the main galaxy significantly, and for this reason they do not consider mergers as a viable option in producing a significant counterrotating component. However, further simulations employing smaller stellar content and smaller dark halos for dwarf galaxies proved to be more successful in reproducing the observed amounts of counterrotating material in disk galaxies. There appears to be a discrepancy between the observations that often show very high M/L ratios for dwarf galaxies and these simulations.

Observational Evidence for a Recent Merger in NGC 7479

The strongest evidence for a recent interaction comes from the high resolution H I observations. They show a long gaseous arm that seems to have different kinematics from the main gas disk. A small difference in the inclination could explain these observations. An intrinsic H I warp can do this, but there is no integral sign –like or any other symmetry in the warp as is usually observed. Therefore, gas could have been forced to an inclined orbit as a response to the tidal forces of a gas-rich companion galaxy on an inwards spiraling orbit (initially close to a circle). Before the satellite galaxy is disrupted, the tidal forces from it can create a strong counterarm in the main galaxy on the opposite side from it. The core of the companion can survive the inward plunge as shown by the simulations in Chapter 5. However, in NGC 7479, the core must have been broken up into pieces that spiral in towards the nucleus, since no core is seen.

The integrated H I intensity maps show strong gaseous concentrations in the southwest part of the disk near the end of a nearly straight part of the gaseous and stellar arm. These morphological peculiarities are associated with strongly disturbed kinematics. Figure 6.11

shows that the velocities in this part of the disk vary between +20 km/s and −40 km/s around the angle-averaged rotation curve. Nowhere else in the disk are such extended perturbations observed. These strong tidal streaming motions can be caused by an external perturber, as I demonstrated in Chapter 5.

The optical images show a strong one-armed pattern with irregular short armlets on the opposing side. As I discussed before, these kinds of observations have almost always been explained with an interaction scenario. The simulations presented in Chapter 5 strongly suggest that the merger is relatively recent (it took place within the last few times 10^8 years), and the effects of the merger are still visible, because the dynamical time scale for mixing is large in the outer disk where most of the arm structure lies. The optical images also show an anomalous pattern of dust lanes perpendicular to the bar and the southwest spiral arm, often associated with Hα emission in the bar or spiral arm. In the scenario I suggest, the dust trails are left behind by inwards spiralling, tidally broken up pieces of the companion that trigger star formation in the denser environment of a bar or spiral arm. The bar itself has been formed as a result of an interaction, although more simulational work needs to be done to study the possibility of minor companions triggering strong bars.

The strong concentration of molecular gas in the center is related to the torques caused by the bar. However, since there is no irrefutable evidence for strong star formation in the center, it looks like the pileup of gas has been relatively recent, and therefore, the bar is relatively young. This further supports the assumption of a recent merger scenario. Finally, Martin (private communication) has made optical spectral measurements of several H II regions in NGC 7479, and his preliminary results indicate that the [O III]/Hβ ratio is considerably higher in the western arm than in the H II regions on the eastern side of the galaxy. While there may be several possible explanations for

this effect, it is consistent with the existence of strong shocks along the western arm, probably caused by the recent tidal effects and radial streaming of gas into the bar.

Discussion of the Interaction Simulations

The results presented in Chapter 5 provide strong support for the interaction hypothesis. The evidence includes both the generation of a strong one-armed structure, and the creation of a long bar near the center of the disk. The model velocity field also partially supports the interaction-induced spiral arm structure. The greatest problem in these simulations was the fact that the companion is not disrupted before it reaches the nucleus of the main galaxy during the merger process. This is clearly contrary to observations, which show few signs of a companion in the disk.

The first runs with a companion that has a mass 10% of that of the main disk, and 50% gaseous, bring out a morphology similar to the observations of the main galaxy. However, the distortion that forms is highly off-centered at later times, which is inconsistent with the observations. The change of the spin direction of the companion does not seem to change any essential features in the merger. The bar forms in about 20 time units, which corresponds to less than 3×10^8 years if we use the same physical units as in Hernquist and Mihos (1995). After another 1.5×10^8 years the bar is destroyed as the companion spirals into the nucleus. The destruction of the bar due to increased central mass is a well-known result (e.g. Friedli & Benz 1993). The growth of the mass in the bulge moves the locations of the ILRs out along the bar, thus destroying the x_1 family of orbits that supports the bar. In NGC 7479, this is unlikely to take place soon, since the companion has been disrupted and its stellar and gaseous material has been spread out into the disk. However, the massive concentration of molecular gas in the nucleus of NGC 7479 indicates that an evolution similar to the model runs is taking place and

in the future, after more gas has accreted to the nucleus, the bar will start to fatten and weaken. It appears that the bar in NGC 7479 is young.

The wandering of the bar and arms is perhaps somewhat reduced when the satellite mass is only 5% of the main disk mass, but they still wander by a few kiloparsecs, which is inconsistent with the observations. Either 1) we see the bar in a very early stage of evolution, 2) the companion has been disrupted before it can start "driving" the wandering of the distortion or 3) some of the parameters of the simulation are fundamentally wrong. While the first two explanations could well be true, attention should be paid to the third possibility. The first parameter that could be in error and would probably remedy the wandering of the disk and the distortion is the halo-to-disk mass ratio. I fixed it to two, since systems with low halo-to-disk mass ratios are more likely to develop bars. It is possible that the bar had formed before the interaction took place. If so, the spiral arm and the bar can have different pattern speeds. The simulations reported in Chapter 5 cannot exclude two pattern speeds. However, since there is no convincing evidence for that scenario, and the simulations demonstrate that a structure closely resembling the observed one is easily created in a minor merger, it is more likely that both the bar and the strong western arm were formed in the merger process.

The numerical simulations that I have made of the system without any companion prove that even with a small halo-to-disk mass ratio of two, the system is stable against bar formation at least for the duration of the simulation (some 5×10^8 years). Several short spiral armlets developed in the disk. These were generated most likely by the swing amplification of noise in the initial conditions. But nothing like the strong one-armed morphology seen in NGC 7479 ever appears during the simulations if there is no external perturbation. Also, the stability and longevity of the asymmetric structure is in serious doubt, at least if the disk kinematics do not support a $nm = 1$ feature. Therefore, it is

very difficult to escape the conclusion that the western spiral arm must have been created by a recent interaction.

The inclination of the satellite orbit was restricted to $10°$ in these simulations. Various values around $0°$ inclination could give slightly different results, but it is unlikely that the inclination of the companion is high, since this only provides a short impulse to the disk while the satellite crosses the disk plane, although a higher inclination could possibly contribute to the destruction of the companion. It is also unlikely that the companion is much more massive, since it would then be even more difficult disrupt it, and it would cause more disk heating and an unacceptable increase in the main disk scale height, as found by Thakar and Ryden (1996). The structure of the companion is another unknown. Less centrally concentrated satellites are more likely to be disrupted as they spiral close to the center of the main galaxy.

The characteristics of the bar that is formed are not necessary similar to those of the observed bar in NGC 7479. However, the bar that forms is strong (a large ratio of the major to minor axis length). The gas morphology in this bar does not seem to settle to anything that could be compared with the observations, because the model bar is created and then destroyed in a few times 10^8 years. A better idea can be obtained from the other set of simulations that I made to investigate the pattern speed of the bar. In those simulations, the bar structure was assumed to be stable, which may not be true. The bar in NGC 7479 is likely more long-lived than the bars that I obtained in the interaction simulations.

The model velocity field indicates that the gas is flowing toward the strong tidal arm, thus forming the strong kink seen a little inside the arm in the south. A similar velocity feature can be seen in the observations. However, this velocity structure could be seen regardless of the origin of the one-armed feature, and cannot therefore taken as

definite evidence for an interaction. Once the gas reaches the arm in the simulations, it forms a shock in the arm, that turns the velocity vector more along the arm, and the gas is flowing inward. The gas in the outer arm is in nearly circular orbits, but it appears to be at a different inclination from that of the main disk. If this trend extends out to the outermost arm gas, it explains the different kinematics of the gas there, as seen in the H I observations in Chapter 2. A higher inclination of the satellite orbit forces the gas farther out in the arm to become non-planar. There is also a velocity disturbance along the presumed path of the satellite on the eastern side, in the sense of higher line of sight velocities. A hint of this disturbance is seen in the $15''$ resolution H I velocity field in Chapter 2.

Finally, the lack of star formation in the models must be addressed. Star formation will tend to break up high density gas concentrations. This could help in disrupting the satellite. Based on the simulations, it is likely that star formation is seen all along the strong tidal spiral arm and in the bar, as observed. Since there are no extreme gas concentrations in the arm, it is unlikely that the arm would be disrupted by the winds from young stars and energy from supernova explosions in the starburst regions.

CHAPTER 7
SUMMARY AND DIRECTIONS FOR FUTURE WORK

Results

My goal in this work was to gain insight into and understanding of the structure and dynamics of NGC 7479. I aimed at finding dynamical processes that could improve our understanding of the barred structure, and its effects on the stars and the ISM, in barred spiral galaxies. Towards this goal I gathered an extensive set of observations from high resolution 21 cm measurements to the U band images of the whole galaxy. The interpretation of these data was significantly aided by the numerical simulations that I made of the gas flow in the bar and of the merger with a satellite galaxy. I will summarize the main points from each chapter, emphasizing the connection between the observed properties and the simulated models. I feel that even more physical insight and a more quantitative understanding would have resulted if analytical calculations of the behavior of stars and gas in the observed potential had been made. The nonlinear theory of stars and gas in the resonances remains mostly undeveloped (see, however, Contopoulos 1975), mostly because of the enormous complexity when terms of the second order and higher are taken into account. Also, our knowledge of the gas dissipation has been incorporated often by just some kind of a simple frictional coefficient. The derivation of a more sophisticated analytical theory for strong bars should be made. Its neglect here may be justified by the circumstantial evidence for a recent interaction, which would further complicate things.

207

Atomic Hydrogen and Radio Continuum Observations

As a by-product of H I observations I obtained a 21 cm continuum map at $4''$ resolution. This map revealed an unexpected two-armed structure in the bar region. The arms bend in the opposite sense to the main spiral arm structure. The emission along the bar comes from thermal radiation associated with the star forming regions and nonthermal emission from supernovae. Since no high resolution measurements of several closely spaced radio frequencies are available, it is not possible to separate the amount of thermal and nonthermal emission and, consequently, make estimates of the star forming and supernova rates.

The radio continuum component outside the bar does not coincide with emission in any other observed wavelength. It is unlikely that is is related to any jet-like outflow as seen in NGC 4258, since the Hα emission shows no sign of this component. I have gathered considerable evidence that NGC 7479 is a product of a very recent, possibly still ongoing, minor merger. Molecular clouds from the satellite galaxy are tidally stripped off and they spiral in towards the center by dynamical friction and cloud-cloud collisions. When a giant association of these clouds impacts the bar, the molecular gas is compressed and star formation is triggered. After a time delay, the recently formed massive stars explode as supernovae, producing radio continuum emission. It needs to be demonstrated that this time delay, coupled with a circular orbit (different from the gas and stars trapped in the bar) can produce the observed radio continuum morphology. There is a moderately strong radio continuum source in the nucleus. It is point source –like. The spectral index estimate is uncertain, but it could have a large contribution from thermal emission.

The H I distribution has a large central hole, roughly matching the radius of the bar ($45''$). Since most of the gas in this area has been driven in to the bar, there has been a

phase transition from atomic to molecular gas. Outside the central hole, the atomic gas is largely distributed to a disk that ends around $130''$ from the center. The extent of this disk is similar to the extent of the optical disk. Outside the main disk there is a long extension of the western gas arm. This arm coincides with the strong optical arm, but continues to much larger distances than the optical counterpart. This arm is explained as a tidal arm generated opposite to an infalling companion. South of the main disk, a weaker arm can be seen. This arm is related to gas stripped apart from an infalling companion in the merger scenario.

The H I kinematics of the disk are fairly regular on the eastern side of the major axis. In contrast, there is a severe perturbation associated with the western spiral arm. This perturbation can be explained if the tangential velocity in the arm is slower than expected from the mass distribution. Either the arm is in another plane, or the arm is expanding, or both.

No H I rich companions ($M(H\ I) > 2.4 \pm 0.7\ M_\odot$) were found within $\pm 12'$ and ± 440 km/s of the center of NGC 7479.

Molecular Gas Observations

The ^{12}CO emission peaks in the nucleus, but there is also a fair amount of emission along the bar. The total amount of molecular gas in the bar is $4 \times 10^9\ M_\odot$, half of which is within $5''$ of the center. The central gas mass within $2''$ of the nucleus is more than 10% of the dynamical mass within this radius. The emission perpendicular to the bar is poorly resolved. Some gas concentrations in the bar seem to be related to nearby concentrations of the 21 cm radio continuum emission, which are, however, located outside the bar.

The strong bar radial streaming motions cause large velocity widths in the CO emission (more than 100 km/s), seen in the profiles perpendicular to the bar. The strong

central concentration within $2''$ is in a fast-rotating circular motion. Outside the center, the velocity field is complicated because of the large range of motions seen within the synthesized beam. No CO emission is seen in the bar–spiral arm transition region.

Near-Infrared and Optical Observations

The high resolution near-infrared images of the bar region reveal the bar dust lanes. Hot dust contributes to the K band emission. The southern part of the bar is 0.2–0.3 magnitudes brighter than the northern part. There is an isophote twist near the center, seen even in the K band.

The most obvious features in the visible images are the bright nucleus, bar and the western spiral arm. The arm structure on the eastern side is incoherent, and the arm seems to bifurcate in the north just beyond the end of the bar. The optical images reveal a sharp color change at about $55''$ from the center. Inside this radius the colors are reddish, whereas outside they are bluish, especially in the spiral arms and arcs. This radius is the corotation radius from the numerical models. The main linear dust lanes in the bar are close to the major axis of the bar, but slightly displaced towards the leading edges. In addition, there are several peculiar dust lanes, often intersecting the bar almost perpendicularly. Bright star forming regions can be seen all along the bar, especially in the Hα emission. The western arm has very blue colors along its whole optical extent, and lots of Hα emission. The strongest Hα emission does not come from the center, but from two H II regions in the western spiral arm just beyond the end of the bar.

The Hα velocity field indicates that there are large streaming motions associated with the bar. In the nucleus, evidence for a circularly rotating central disk is found in the Hα velocity field.

Numerical Simulations

Gas flow in the bar potential

The simulations indicate that the gas observations can be explained best if the bar pattern speed is high, placing the corotation around $55''$. The model with this corotation radius has linear gas/dust lanes that extend to within $\pm 10''$ of the nucleus, slightly displaced toward the leading edges. The velocity field matches that seen in the CO observations, except in the nuclear region. Star formation takes place near the bar shocks close to the largest gas concentrations, as seen in the observations. The radial streaming velocities along the bar are large, more than 150 km/s at intermediate distances ($15'' - 20''$) from the bar center.

Additional evidence for the high bar pattern speed is provided by the spiral arm and arc morphology. High pattern speed provides a morphology in which the spiral arms bend parallel to the bar while slightly overshooting it. In contrast, the slow pattern speed models produce arms that start almost perpendicularly to the bar end, contrary to the observations. The mass inflow rates at 1 kpc at intermediate times ($6-8 \times 10^8$ years from the beginning of the simulation) are around 5 $M_\odot$/year for all pattern speeds. The nuclear gas surface density is comparable to the observed one for high pattern speed runs, but much higher for low pattern speed models.

Interaction simulations

The simulations employed companions that had masses 5–10% of the main galaxy's disk mass. The halo mass of the main disk galaxy was twice the disk mass. The main disk included 10% of its mass in gas particles. The companions were similar in structure to the main disk, but scaled down in mass, length and velocity.

The results demonstrate that moderate mass companions can produce a strongly asymmetric spiral arm structure in the main galaxy gas and stellar distribution. Also a strong bar can be produced by the companion. Results were comparable for both retrograde and prograde spinning companions.

The velocity field shows that there is some motion along the strong asymmetric arm in addition to the circular rotation. The main problem with these simulations is that the companion is not disrupted, whereas the observations show that it must have been disrupted during its interaction with NGC 7479, since no remnant is seen in the images. The strong H II region about $15''$ north of the nucleus is the best candidate for the remains of the companion galaxy.

Synthesis of Observations and Modeling

All the observational images, with the exception of H I and Hα, have the highest luminosities in the nucleus. This indicates that a lot of gas and dust has fallen to the nucleus, and it is now active. The nature of the activity seems to include a LINER nucleus, possibly powered by a supermassive object, and a nuclear star burst.

The dust lanes, CO distribution and Hα emission all seem to be closely correlated in the bar outside the nucleus. This indicates that star formation is triggered near the bar shocks where dust and gas are compressed. I suggest that the abundance of star formation in the bar has been triggered by moderate shocks and molecular clouds pulled apart from the disrupted companion. Since the H I distribution has a large hole in the bar region, it has been compressed to the molecular form that is observed in the bar.

The spiral arm structure is best seen in the Hα emission. The models show that the strong western arm could have been generated by the minor merger. The arm is now partly driven by the strong bar. The velocity perturbations on the strong western spiral

arm imply that tangential velocities are not as high on the arm as expected from the rotation curve on the eastern side. Either the arm is less inclined than the main disk, or there are other factors that reduce rotation, such as an expansion driven by the tidal interaction.

The gas in the disk is marginally stable for gravitational collapse. The corotation radius in the models is found just beyond the end of the bar at $55''$. This radius marks a gap in the star formation along the spiral arms, and a weak ring of H I around the center.

The observational evidence for the interaction includes the long gaseous H I arm with disturbed kinematics, the asymmetric spiral structure, the dust lane structure near the bar and star formation in the bar.

Directions For Future Research

Future Observations

High resolution (sub-arc second) radio continuum mapping with the VLA at 2, 6 and 20 cm is required to estimate the true nature of the nucleus. These observations will give a reliable spectral index, and separate the flux into thermal and nonthermal components. In addition, these observations will allow us to deduce the star formation and the supernova rates.

Further light on the nuclear properties can be shed by high resolution near-infrared narrow band images and spectra. Different lines trace different components; e.g., the Fe II 1.64 μm is a strong cooling line in supernova remnants, and Brγ traces the recent star formation. The various near-infrared lines of the molecular hydrogen (H_2) indicate the excitation mechanism of the molecular gas. Finally, the CO absorption feature near 2.3 μm can be used to separate supergiant from giant emission.

Optical high resolution measurements together with appropriate modeling could also clarify the nature of activity in the nucleus, and help us understand how the gas is fed into the nucleus. However, the very large amount of dust and gas in the nucleus causes high uncertainties in the optical estimates. Further information is given by the mid-infrared lines of Ar III (9 μm), S IV (10.5 μm) and Ne II (12.8 μm). It is important to measure the X-ray emission from the nucleus at several X-ray energies. This constrains the excitation mechanism in the nucleus.

A detailed study of the bar shocks requires observations with highest possible resolution. An attempt should be made with the Hubble Space Telescope's NICMOS camera, but most likely we have to wait for future instruments with higher sensitivities. More sensitive CO observations could detect molecular gas in the bar-spiral arm transition zone. Higher resolution CO observations are also required to find out how closely the gas distribution is associated with the bar shock lanes. These observations would also resolve the central gas disk and help understand the resonance structure in this area. Higher resolution measurements of the velocity jumps of the ionized gas across the bar should be made to estimate the strength of the shocks and the related star formation.

Higher resolution and especially better sensitivity 21 cm H I observations would allow us to map the velocity field across the spiral arms very accurately. This could further constrain estimates of the kinematical perturbations associated with the merger scenario.

Future Numerical Work

The simulations made here should be repeated with a more accurate large scale K band image. The self-gravity of the gas should be included, and a realistic estimate of the three-dimensional potential should be employed. The new runs should be three-dimensional. The effects of star formation should also be included as the run advances.

A halo component should be added and a secondary component, which simulates the merging satellite, should be included. More attention should be paid to the variation of the viscous coefficients and various values of the bar turn-on time should be tried. More particles should be included in the runs to gain a better resolution.

More simulations of the minor merger scenario should be made. This would be of general interest as well. The structure of the main and satellite galaxies should be varied, as should their mass ratio, the halo-to-disk mass ratio, and star formation should be included. Different inclinations and initial values for the gas distribution and orbital geometries should be tried.

APPENDIX A
PROPERTIES OF THE 21 CM ATOMIC HYDROGEN EMISSION

Hydrogen is the most abundant element in the Universe. The mass of the stars is made up of more than 70% hydrogen when they start their lives in the main sequence. By the number of atoms, about 90 % of the initial stellar material of the stars consists of hydrogen. Because stars form in the interstellar space, there must be (or at least must have been at some point) large amounts of interstellar hydrogen gas. The observational proof did not come until the development of radio astronomy and the detection of the interstellar 21 cm emission. This line was theoretically predicted by Hendrick van de Hulst and first observed by Harold Ewen and Edward Purcell in 1951. This emission occurs at a rest frequency of

$$\nu_{10} = 1.420405751786 \pm 0.000000000020 \cdot 10^9 \, Hz \qquad (A-1)$$

which corresponds to about 21.106 cm. The emission mechanism is the hyperfine transition (electron spin flip) in the electronic state ($1^2S_{1/2}$). The total spin momentum of the atom is $\bar{F} = \bar{J} + \bar{I}$ where $\bar{J}$ is the total electronic spin momentum and $\bar{I}$ is the nuclear spin momentum. Here, $\bar{J}$ is 1/2 and $\bar{I}$ is 1/2 so $\bar{F}$ is either 1 or 0. The change in the orientation of the proton and electron magnetic moments corresponds to an energy of 6 x 10^{-6} eV or about 0.07 K. When the spins are aligned parallel to each other, there is a finite probability for them to become antiparallel. The transition probability is

$$A_{10} = 2.86888 \cdot 10^{-15} s^{-1} \qquad (A-2)$$

(Rohlfs 1986). This corresponds to a lifetime of 3.5 x 10^{14} seconds or about 10^7 years. In interstellar temperatures (typically around 100 K), the thermal equilibrium is maintained

216

by collisions, and the number of atoms at different excitation levels is determined from

$$\frac{n_1}{n_0} = \left(\frac{g_1}{g_0}\right) \exp\left(-\frac{h\nu}{kT_S}\right), \tag{A–3}$$

where the ratio of statistical weights (g_1/g_0) is 3 $(g = 2F + 1)$. Using a typical spin temperature $T_S = 100$ K, the exponential is very close to 1, and therefore the ratio of the occupation number of the upper level (n_1) and lower level (n_0) is practically 3. The collisional de-excitation rate will be substantially higher than the spontaneous emission rate. The collisional cross section of the hydrogen atoms is on the order of 10^{-16} cm^{-2}. Under typical conditions in the ISM, the density is perhaps one atom per cubic centimeter and the velocity 10 km/s. Therefore, collisions (and collisional de-excitations) take place every 300–400 hundred years. Despite the frequent de-excitations by collisions, in the large pool of interstellar hydrogen there are always atoms which decay to the lower level through a spontaneous transition, thereby emitting a 21 cm photon. It should be noted that most of the emission may actually come from warm neutral gas near the location of star formation sites. Under those conditions, the gas temperature can be greater than 3000 K. Dickey & Brinks (1988) found that in M31, as in the Milky Way, the fraction of the cool gas is only about 20–25%. A typical density in the warm atomic gas is perhaps 50 atoms per cubic centimeter. It is clear that under these conditions collisions take place even more frequently and a thermal equilibrium is quickly established. Higher electronic levels are also excited and their contribution to the spin flip emission (and absorption) must be calculated in a more detailed theory. However, the different excitation and de-excitation mechanisms only affect the spin temperature. The observed brightness temperature of the emission is independent of the spin temperature as long as the emission is optically thin, as can be seen below.

The equation of radiative transfer is

$$\frac{\partial I_\nu}{\partial \tau_\nu} = I_\nu - S_\nu \qquad (A-4)$$

where I_ν is the specific intensity, S_ν the so-called source function and τ_ν the optical depth at frequency ν. This equation can be integrated if S_ν is constant, regardless of the optical depth. With the assumption of no incident radiation, and that $S_\nu = B_\nu$, the Planck function, which at the long wavelength (Rayleigh-Jeans) limit becomes

$$B_\nu(T_S) = \frac{2kT_S\nu^2}{c^2}, \qquad (A-5)$$

where T_S is the spin temperature, we finally obtain

$$I_\nu(0) \approx 2kT_S(\nu^2/c^2)(1 - \exp(-\tau_\nu)). \qquad (A-6)$$

The brightness temperature, T_B, is defined as

$$T_B \equiv \left(\frac{c^2}{2k\nu^2}\right)I_\nu. \qquad (A-7)$$

In terms of T_B, the equation of radiative transfer is

$$T_B = T_S(1 - \exp(-\tau_\nu)). \qquad (A-8)$$

Often the 21 cm emission is optically thin. In that case equation (A–8) simplifies to

$$T_B \approx \tau_\nu T_S \qquad (A-9)$$

Now using the B_{01} and B_{10} (the Einstein transition coefficients), and χ_ν from

$$\tau_\nu = -\int \chi_\nu ds, \qquad (A-10)$$

we can write

$$\chi_\nu = (n_1 B_{01} - n_2 B_{10})\left(\frac{h\nu}{4\pi}\right)\phi_\nu \qquad (A-11)$$

which includes the absorption profile ϕ_ν, which is normalized to 1 when integrated over all frequencies. With the help of equation (A–3), the fact that $g_0 B_{01} = g_1 B_{10}$ and the expansion

$$\exp\left(-\frac{h\nu}{kT_S}\right) \approx 1 - \frac{h\nu}{kT_S} \tag{A-12}$$

equation (A–10) becomes

$$\tau_\nu = \left(\frac{B_{01}h^2\nu^2}{4\pi kT_S}\right)N_0\phi_\nu. \tag{A-13}$$

N_0 is the integrated column density of atomic hydrogen in the lower level along the line of sight. Since in thermal equilibrium the ratio of the populations of the two levels is 3, the total number of atomic hydrogen atoms will be $4N_0$. Finally, the total column density of atomic hydrogen (in cm^{-2}) can be found from

$$N_H = 3.88 \cdot 10^{14} \int_0^\infty T_B d\nu \ cm^{-2} \tag{A-14}$$

where I have used equation (A–9). This substitution may be made if the emission is optically thin. The frequency units in this expression are in Herz. The total mass of the atomic hydrogen gas in a galaxy may then be calculated by integrating this expression over the surface area of the system. Expressing this integral in units of the flux density,

$$S(Jy) = \frac{2k\Omega_b\nu^2 T_B(K)}{c^2}, \tag{A-15}$$

we finally obtain

$$M_H(M_\odot) = 2.36 \cdot 10^5 D^2 \int_0^\infty S(v)dv, \tag{A-16}$$

where D is the distance to the galaxy in megaparsecs, and the integration is over velocity (in km/s) instead of frequency.

The derivation above included several assumptions. First, we must assume a thermal equilibrium. We estimated that under typical conditions in the ISM, the hydrogen atoms

collide every 300–400 years. This time-scale is much shorter than the spontaneous emission time-scale. The collisions will therefore establish a thermal equilibrium in the 21 cm hyperfine transition. This assumption will most likely be good in every location where emission is detected. We assumed a spin temperature of 100 K except for warm gas, as noted above. This temperature is practically the same as the kinetic temperature or the excitation temperature. Kinetic temperatures of this order have been deduced from the H I absorption line measurements of extragalactic radio sources (Spitzer 1978). In H I clouds the dominant coolants are C II, O I, C I and F II. For example, in C II the major cooling line has an energy difference corresponding to a temperature of 92 K. The other important coolants have lines with characteristic temperatures in the range 63 K – 554 K. Since the balance of cooling and heating determines the kinetic temperature of the interstellar medium, kinetic temperatures close to 100 K are achieved through cooling in the above-mentioned lines.

H I emission occurs in a relatively narrow plane of a galaxy. Therefore, it is safe to assume that there is no incident radiation (unless there is an extragalactic background source). As we have discussed above, the conditions in the 21 cm line are very close to thermodynamic equilibrium. Under these conditions $S_\nu = B_\nu$, as we assumed. Because $h\nu/kT$ is ≈ 0.0007, the Rayleigh-Jeans approximation is certainly valid. The optical depth of the 21 cm emission is likely to be much less than one, so that we may use the assumption of a small τ value. This is so because the differential rotation in the plane of the galaxy causes the emission to shift in frequency. As demonstrated in Mihalas and Binney (1981), if the line profile is a Doppler profile with a typical velocity width along the line of sight of 10 km/s, occurring over about 600 pc, the optical depth in the line center is 0.3. This is most likely an overestimate, because there may not be hydrogen clouds in every position along the whole path length. These values are based

for the rotation properties of the Galaxy, but they are likely to be similar in other disk galaxies, where (differential) rotation takes place. I have also implicitly assumed that the spin (kinetic) temperature is the same along all lines of sight. If this is not the case, the expressions for the total hydrogen mass and column density need to be modified. In the absence of any detailed knowledge about this temperature, I will assume a constant temperature. One must also keep in mind that since the optical depth may be more than 0.1 in the brightest regions, the expressions (A–14) and (A–16) give only lower limits to the true values. In these regions the true surface density is

$$N_H = 3.88 \cdot 10^{14} \int\limits_0^\infty T_B(\nu) \left[\frac{\tau_\nu}{1 - \exp{(-\tau_\nu)}} \right] d\nu \ \ cm^{-2}. \tag{A–17}$$

APPENDIX B
REVIEW OF APERTURE SYNTHESIS THEORY

The observation of the atomic hydrogen distribution and kinematics at the 21 cm wavelength requires the use of radio antennas and detectors. The detailed distribution of 21 cm emission can be resolved only with an array of several radio telescopes. These telescopes are distributed in such a way that they synthesize the continuous aperture of a much larger single antenna. Measuring the correlation of signals coming from each possible pair in the array gives information on the location and amplitude of the sources in the field of view of the individual telescopes, which are all pointed at the same position in the sky. The effective resolution of this array is inversely proportional to the largest distance or baseline (B) between any antenna pair. More specifically, the smallest resolvable angular features are roughly λ/B radians. The sensitivity of this array is worse than the sensitivity of an equivalent single dish aperture, because the total collecting area of the elements is much smaller than the aperture they synthesize.

The interference of the received signal, coming from a source much farther away than the length of the baseline, forms a resultant signal of maxima and minima, in an analogous way to the optical double slit interference experiments. Each projected length of the baseline measures a different Fourier component of the intensity distribution in the observed source. This source may be thought of as a number of point sources. To obtain all the information available about this source, all the possible spacings should be measured. In practice, this is impossible, but with a multielement interferometer, aided by the changing projection of the baselines, caused by earth's rotation, a large

number (perhaps hundreds of thousands) of the correlations, also called visibilities, may be measured. Each visibility is averaged or integrated over a short time interval of order 30–120 seconds. The lower limit is set by the hardware data sampling and processing limits and the upper limit by smearing owing to the changing orientation of the baseline as seen from the source.

The Very Large Array (VLA) consists of 27 radio telescopes distributed along a Y-shaped configuration. At any given moment there are $\frac{27 \times 26}{2} = 351$ interferometer baselines. The arms are approximately in north, southeast and southwest directions. However, there is a 5° offset between the north direction and the north arm. This way exact east-west baselines between the southeast and southwest arms are avoided, and in terms of the u and v coordinates, defined in the next section, a better u-v coverage is obtained by avoiding pure u baselines. The distance from the center of the array to the nth antenna in an arm is proportional to $n^{1.716}$. This power-law design gives no redundant spacings on any arm, and has a denser sampling of u-v baselines near the center of the array, resulting in a larger, but more sensitive beam. As an example, the u-v coverage obtained in the H I observations of NGC 7479 is shown in Figure B.1. The array may be configured in four basic configurations, A, B, C and D. The highest resolution may be achieved with the A configuration, where the largest distance between two antennas is 36.4 km. In contrast, the shortest baseline in the D configuration is 35 m.

Let me first define the coordinate systems used in measuring the visibilities V(u,v,t). The u coordinate is the projection of the baseline distance B between two antennas in the east-west direction, pointing east, and v is the projection in the direction towards north. In addition, there is a third component, w, which is perpendicular to the u-v plane and is significant only if the antennas are not in the same plane. The components of the unit vector $\bar{s}$, pointing towards the source, in the same coordinate system, are l, m
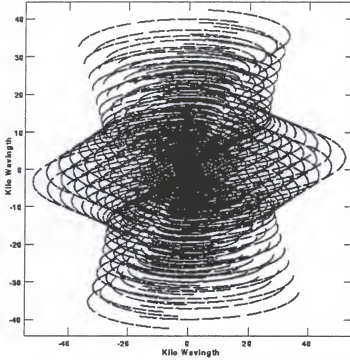
Figure B.1: The u-v coverage obtained in the observations of NGC 7479.

and $\sqrt{1 - l^2 - m^2}$. We are observing the electric field of the radiation coming from the source. This signal will be converted to a voltage at the receiver, amplified, and then correlated and averaged, before a raw visibility is recorded. This process is described in Figure B.2.

In terms of the coordinate system defined above, the product $\bar{B} \cdot \bar{s}$ becomes ul + vm + $(\sqrt{1 - l^2 - m^2})$w. If the observed field is small (the l and m coordinates are small), we may expand the square root to obtain

$$\left(\sqrt{1 - l^2 - m^2}\right)w \approx -\frac{1}{2}(l^2 + m^2)w \approx 0 \tag{B-1}$$

The result of multiplying together the cosine terms, and performing a low-pass filtering is

$$r(\tau) \propto cos(2\pi v(ul + vm)) \tag{B-2}$$

The cosine term may be represented by an exponential. The amplitude of this visibility is tied to the intensity of emission at the observed coordinates. The definition of a
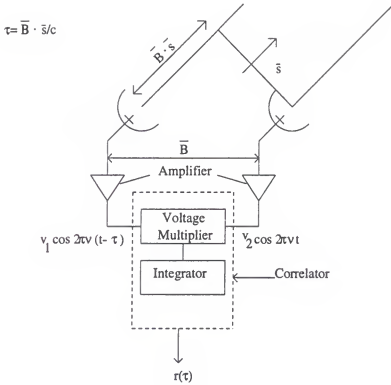
Figure B.2: A diagram illustrating the correlation of two signals from an antenna pair.

visibility is

$$V_{ij}(u,v,t) = \int\limits_{-\infty}^{+\infty} \int\limits_{-\infty}^{+\infty} A_\nu(l,m) I_\nu(l,m) \exp[-2\pi i(u_{ij}(t)l + v_{ij}(t)m)] dl dm, \qquad (B\text{--}3)$$

where

1. i and j specify the antenna pair

2. ν is the frequency of observation

3. A_ν is the normalized power pattern of an antenna in the array

4. I_ν is the intensity at the source

The observed visibilities V_{ij} will need to be calibrated both for their amplitude and their phase. This is done by making observations of powerful point sources in the sky. The so-called primary calibrators serve as flux calibrators. Their fluxes have been accurately determined, and they are *assumed* to be constant. Normally a flux calibrator (3C 48 or 3C

286) is observed at the beginning and end of a run. If the run is long and/or uses multiple configurations and frequencies, more frequent observations are necessary. Most of the calibration is done with a secondary or phase calibrator, which is usually observed every 30–40 minutes in extragalactic H I observations. It is important to observe a calibrator often enough to monitor the phase stability of the atmosphere.

In spectral line work, visibilities are obtained from several different frequencies. The appropriate frequency at the VLA is selected by inserting a delay τ into the transmission lines before correlating the signals from two antennas. These delays select discrete frequencies from the incoming signal. This corresponds to an extra term of the form $\exp[-i2\pi\nu\tau]$. We have to integrate over the frequency to obtain the spectral visibility. The frequencies are not transmitted uniformly throughout the bandwidth. The frequency passband function $b(\nu)$ must be calibrated by observations of strong, spectrally flat continuum sources.

In the system used at the VLA, the number of channels in the correlator is a power of two, so that the Fourier transform of the lag spectrum may be calculated with Fast Fourier Transform (FFT) techniques. The number of baselines multiplied by the number of channels is handled by the limited number of correlators. This limits the maximum number of available channels.

The calibration is a process where the complex gains G_{ij} are determined. These may be solved from (Perley et al. 1989)

$$V'_{ij} = G_{ij}(t)V_{ij}(t) + \varepsilon_{ij}(t) + \eta_{ij}(t), \tag{B–4}$$

where

1. V'_{ij} is the observed visibility,

2. V_{ij} is the true visibility,

3. G_{ij} is the baseline-based complex gain,

4. ϵ_{ij} is the baseline-based complex offset, and

5. η_{ij} is the complex noise

Usually the offset term is assumed to be negligible and the noise averaged out. The complex gains can be approximated as a product of antenna-based gains times a "closure error" term: $G_{ij}(t) = g_i(t)g_j^*(t)g_{ij(t)} = A_{ij}(t)\exp[i\Phi_{ij}(t)]$, where

1. $g_{i,j}(t)$ is the antenna-based complex gain for antenna i, j,

2. $g_{ij}(t)$ is the residual baseline-based complex gain, the "closure error",

3. $A_{ij}(t)$ is the antenna-based amplitude correction, $A_{ij} = a_i(t)a_j(t)a_{ij}(t)$. $a_{ij}(t)$ is the closure error in amplitude.

4. $\Phi_{ij}(t)$ is the antenna-based phase correction, $\Phi_{ij}(t) = \phi_i(t)-\phi_j(t) + \phi_{ij}(t)$. $\phi_{ij}(t)$ is the closure error in phase.

The calibration may be made by baseline-based calibration (using equation (B–4) without the offset and noise terms and substituting the flux of the calibrator, S, for the true visibility). Usually the calibration is antenna-based, which means that we determine the antenna-based amplitude and phase corrections. One reason for this is that most of the errors occur in individual antennas. Secondly, the number of antennas is much smaller than the number of baselines, making the solution simpler. Also, for an extended calibrator, the antenna-based solutions may usually always be solved for, whereas some baselines may have to be excluded because the source is resolved at longest baselines. The large number of baselines available for solution means that the equations are overdetermined and a least squares solution can be used.

The closure errors should be less than 10% in amplitude and 5° in phase. In practice, the calibration for VLA data is done with the help of the Astronomical Image Processing

System (AIPS). In spectral line work, one of the channels is always a pseudo-continuum channel, called channel 0, which covers the central 75% of the used bandwidth. Therefore, the signal (line+continuum) is much stronger than it is in the narrow-band channels. Channel 0 is used to calibrate the data for this reason. The data are calibrated on-line for system effects. Also, the data are usually Hanning-smoothed (smoothed along the frequency or velocity axis) on-line to suppress the effects of ringing of the frequency spectrum at the ends of the bandpass (Gibbs' phenomenon). This ringing is a result of the truncation of the temporal (lag) cross-correlation spectrum. In Hanning smoothing the central channel is weighted by 0.5, and the channels adjacent to it by 0.25. The frequency resolution in the smoothed channel will be twice the channel width. In practice, we create a new channel from all the even channels, thus reducing the number of channels by a factor of two. The frequency resolution in these newly created channels is the same as the channel width.

The first step in reducing the on-line calibrated and Hanning-smoothed visibilities is editing. The visibilities may be displayed on the computer using the AIPS task TVFLG. Noisy visibility values and discrepant peaks or low values are then deleted interactively. Usually this is first done on channel 0, and the flags are then copied onto the line data. Often the first record of a scan is noisy and will have to be deleted. Next, the flux for primary flux calibrators (3C 286 or 3C 48) is determined by applying well-known values. Then, the antenna-based gains for the calibrators are solved. If large closure errors (much greater than 5° in phase and 10% in amplitude in my observations) are noticed, the discrepant baselines or antennas are deleted and the calibration repeated.

Next we determine (bootstrap) the flux densities of the secondary (phase) calibrators using the flux determined for the primary calibrator and the antenna-based gain solutions. Finally, the gain solutions are linearly interpolated after boxcar smoothing (which aver-

ages over a given interval of time) and applied to the sources. The calibration table is then copied from channel 0 to the line channels. The final step in calibration, which may be performed before the gain calibration, is the calibration of the bandpass. This is done with the help of a source that has a strong signal which is practically constant across the bandpass. Usually, the flux calibrators 3C 286 and 3C 48 can be used for this purpose. The line channels are simply divided by channel 0 and normalized. The calibrated source u-v data may now be split from the multisource file. The data are now ready for imaging.

As was discussed above, each visibility measures one Fourier component of the intensity distribution in the source, also seen in equation (B–3). This equation may be Fourier inverted to give

$$I' = I(l,m)A(l,m) = \int\limits_{-\infty}^{+\infty} \int\limits_{-\infty}^{+\infty} V_{ij}(u,v) \exp[2\pi i(ul + vm)] du dv. \qquad \text{(B–5)}$$

As was discussed before, the large number of measured visibilities requires large amounts of calculations if the transform is made using a Direct Fourier Transform (DFT). In practice, the transform is always made by Fast Fourier Transform techniques. For this technique to work, the visibilities will need to be gridded onto a map which has dimensions that are a power of 2. In addition, we have the problem of "missing spacings", because the u-v plane is not evenly sampled, as is easily seen in Figure B.1. For these reasons, the data needs to be weighted before the Fourier transform can be carried out. The visibilities used in the inverse transform are obtained from

$$V^R = R\left(C * (WV)\right), \qquad \text{(B–6)}$$

where

1. V^R is the visibility to be used in the transform,

2. R is the re-sampling function,

3. C is a convolving function,

4. W is the weight and

5. V is the calibrated visibility.

The convolution is made to provide smooth estimates for the gridding procedure, because the observed visibilities are unevenly and discretely distributed in the u-v plane. Ideally C should be a function which is flat across the field to be imaged and drops sharply beyond it. This ensures that sources outside the image will not be aliased into the map when the Fourier transform is done. Also, if the source itself is strong, its sidelobes may be aliased back onto the image. The function most commonly used at the VLA is a truncated spheroidal function (Perley et al. 1989). The sampling function is Bracewell's "sha" function,

$$R(u,v) = III\left(\frac{u}{\Delta u}, \frac{v}{\Delta v}\right) = \sum_{j=-\infty}^{\infty} \sum_{k=-\infty}^{\infty} \delta\left(j - \frac{u}{\Delta u}, k - \frac{v}{\Delta v}\right), \qquad (B–7)$$

where Δu and Δv define the separation between grid points.

The weighting itself controls the shape of the synthesized beam. The synthesized "dirty beam" will be the Fourier transform of R(C*W). Expressed in another way, the dirty beam will be the image of a point source at the phase tracking center (the telescope pointing coordinates). Therefore, the choice of weighting parameters affects the beam shape critically. In the broadest sense, there are two types of weighting, density weighting and tapering. In density weighting, we assign a weight to each visibility depending on the local density of visibility samples. If we give each visibility a unit weight, the cells that have many samples (i.e. cells close to the center of the u-v plane, as seen in Figure 2.1) will be heavily weighted. This "natural" weighting produces a wide beam, because it overemphasizes the shortest baselines. On the other hand, because the source brightness, B, is proportional to flux over the synthesized beamwidth, the best sensitivity to low

surface brightness emission will be attained through the use of natural weighting. A large beam will also suppress noise, because it averages over a larger solid angle. In naturally weighted maps every visibility is included, and therefore contributes to make the sensitivity better, because sensitivity $\propto \frac{1}{\sqrt{n}}$, where n is the number of visibilities that were used in making the map.

The best resolution is obtained with "uniform" weighting. This scheme assigns weights inversely proportional to the number of samples in a cell. Because the density of the visibilities is highest in the center of the u-v plane, uniform weighting effectively suppresses the short baselines in constructing the beam. Since the long baselines are overweighted at the expense of the short baselines, the beam will have a narrow Gaussian core, but it may also have large sidelobes because the outer u-v plane is sparsely sampled. The locations of unsampled u-v grid cells will have a zero value, and in the Fourier transformation this will result in high frequency sidelobes in the beam. One way to suppress these sidelobes is to use a taper weighting function. This is usually a Gaussian that will effectively lower the weights of the outer portion of the u-v plane. In uniformly weighted maps the beam shape is largely controlled by the taper. The AIPS task IMAGR employs a slightly more complicated scheme. A new parameter, ROBUST, has been added. The density weight of a u-v visibility is assigned a value from the following formula:

$$W_2(i) = \frac{W_1(i)}{\sum P(i) + S}, \tag{B-8}$$

where

$$S = \frac{10^{ROBUST} \cdot \langle \sum P(i) \rangle}{5.0} \tag{B-9}$$

Here $W_1(i)$ is $W_i(i)^p$, where p is 0, 0.25, 0.5 or 1.0, and

$$W_i(i) = \frac{K}{\sigma^2(i)} \tag{B-10}$$

and K is a constant and $\sigma(i)$ is the uncertainty in the visibility. $P(i) = W_1(i)$ for uniform weights and $\sum P(i)$ is the weighted sum of P(i)s over all samples in the neighborhood of the cell occupied by the i'th sample. The weighting may be one of several functions, e.g. a Gaussian. The symbol $\langle\rangle$ denotes an average of the local sums over all visibilities. If robust > 4, the weighting is close to natural. On the other hand, if robust < –4, the weighting is close to uniform. With the use of the parameter ROBUST a map may be made where the beam width is close to uniformly weighted values and the noise is only slightly higher than in a naturally weighted map.

Another way to reduce the sidelobes and give an estimate to the shortest, zero-spacing flux (not measured by the interferometer), is "cleaning" the image. This procedure will be described below. Imaging requires the selection of a cell size and the map size. The map size has to be a power of 2. In practice, around extended objects, like galaxies, the whole half power beam width (HPBW) of the antennas is mapped. The synthesized beam must be sampled by at least 2 samples per beam (Nyquist sampling). Based on experience, 3–4 cells per beam has proven to be a reasonable criterion for the cell size. In this way aliasing is further reduced. Because the image coordinates and the baseline coordinates are the inverse of each other, the smaller the cell in the image plane, the larger the cell in the u-v space is. This may be expressed by

$$\Delta u \Delta l = \frac{1}{m} \qquad (B-11)$$

where Δu is the cell size in the u direction and Δl is the cell size in the image plane (in l direction) and m is the number of cells between two grid points in u direction. A similar equation applies for v and m coordinates.

In spectral line work, the continuum emission must be subtracted before further processing of the data (i.e. cleaning). The continuum subtraction may be done in the

u-v plane or in the map domain. Conventionally, the channel maps not containing any line emission are averaged, and then subtracted from the channel maps containing line emission. Another way of doing this is fitting a linear baseline to visibilities in the u-v plane, and subtracting this from the data. Because strong continuum sources are often confusing in imaging and image processing, u-v subtraction may be the preferred way to remove the continuum emission. Maps of continuum emission may be made by mapping the channels containing no line emission. AIPS offers many tasks to do the continuum subtraction in the u-v plane. For weak sources, the task UVLIN is recommended. It does the fitting to the real and imaginary parts of the visibilities.

The "dirty" image formed by the Fourier transform discussed in the previous section has been convolved with the dirty beam. The dirty beam includes sidelobes even at the 10% level. The side lobes are the response of the truncation of the u-v plane and all the missing u-v components out to infinity. Measuring the fluxes in the dirty image is not useful, because the fluxes are in units of Jy/(dirty beam), but the area of the dirty beam is not well defined. Therefore there is a need to deconvolve this dirty beam out of the image and replace it by a well-defined "clean" beam. This process is called cleaning.

The basic CLEAN algorithm was devised by J. Högbom (1974). It was improved by B. Clark (1980) to take advantage of FFTs. The basic Clark CLEAN algorithm consists of two cycles. In the minor cycle a beam patch (the center of the dirty beam with the highest sidelobe) is selected. Then points on the dirty image are selected if they have an intensity, as a fraction of the image maximum, greater than the highest sidelobe not included in the beam patch. These peaks, represented by delta functions, are then multiplied by a gain factor (0.1–0.2), convolved with the beam patch and subtracted from the dirty image. In the major cycle the point sources found in the minor cycle are transformed via FFT into visibilities, multiplied by the sampling function (the inverse of

the dirty beam) and transformed back to an image, and then subtracted from the dirty image. As a stopping criterion a preset maximum value of minor cycle iterations can be used, or a maximum flux value in the residual image may act as a cutoff. At the end, the "clean components" are convolved with a "Clean beam", normally a Gaussian fitted to the core of the dirty beam, to reduce the spurious sidelobes in the dirty beam. The residuals are added to this clean image. It should be noted that the units of the convolved clean components are Jy/(clean beam), but the units of the residuals are still Jy/(dirty beam), which is not well defined. If accurate fluxes are required, other techniques must be used to overcome this limitation (see Chapter 2).

CLEAN will interpolate across the center of the u-v plane to find a suitable "zero-spacing" flux. CLEAN is successful in doing this if the zero-spacing flux is not large. Optionally, the user can provide an estimate of the zero-spacing flux, based on the values of shortest baselines or single dish observations. If the zero-spacing flux has been underestimated, the source is seen to lie inside a "bowl" of negative surface brightness. In the extreme case of zero flux for the zero-spacing component, the bowl effect can be explained in a simple way. All real flux is positive, so the relatively small region of actual emission will be balanced by a larger region of slightly negative brightness to get a zero flux for the zero-spacing component. The imaging task IMAGR in AIPS uses the Clark CLEAN algorithm with a slight modification. Instead of subtracting the visibilities from the gridded values, it subtracts them from the ungridded u-v data. This way aliasing and gridding errors can be removed. The task APCLN subtracts the convolved clean components from the gridded data points.

The CLEAN algorithm may also be employed to subtract the continuum point sources from the u-v plane, because it will create a list of clean components in the field including the point sources, if no continuum subtraction has been made. In this way, the continuum

emission from a galaxy may be investigated after subtracting the interfering sidelobes from these sources.

APPENDIX C
PROPERTIES OF THE 2.6 MM CARBON MONOXIDE EMISSION

The most common molecule, H_2, forms mostly on the surfaces of interstellar grains. Because the formation of the H_2 molecule is an exothermal process, a third body in addition to the H atoms must be present. It is very unlikely that such collisions take place among the gaseous particles. On the other hand, the hydrogen atoms are adsorbed by the surface of an interstellar grain. The atoms may move along the surface of the grain and form H_2 molecules.

The formation of the CO molecule is believed to take place through exchange reactions. There are several ways to make CO, for example from CH and O, C_2 and O, C and O_2, CO^+ and H, and OH and C. These reactions take place in a complicated network (van Dishoeck 1988). Another possible way to form these molecules is in the extended envelopes of giant stars where the temperature is low enough (≤ 2000 K; C and N type stars). Once the CO has formed, it is relatively difficult to destroy, since the dissociation energy equals 11.09 eV (compare H_2, the dissociation energy of which is 4.48 eV, but usually photons with energies more than 14.7 eV are required for its dissociation, owing to its symmetric nature).

The kinetic energy of rotation for a molecule of angular momentum J is

$$E_J = \frac{\hbar^2}{2I}J(J+1), \tag{C-1}$$

where $\hbar$ is $h/(2\pi)$, I is the moment of inertia of the two molecule system, and J has integer values 0, 1, 2, 3, ... Introducing the rotation constant B, defined by

$$B = \frac{h}{8\pi^2 I}, \tag{C-2}$$

we can write the energy difference between two states J and J-1 as

$$E_J - E_{J-1} = hB[J(J+1) - J(J-1)] = 2hBJ. \qquad (C–3)$$

The frequency corresponding to this transition is 2BJ. The quantum mechanical selection rule for electric dipole radiation is $\Delta J = \pm 1$. For ^{12}CO, the transition $J = 1 \rightarrow 0$ occurs at 115.27 GHz, $J = 2 \rightarrow 1$ at twice this frequency, etc. The energy in the $J = 1 \rightarrow 0$ transition corresponds to a temperature of about 5.5 K (from $kT = \Delta E_J$). Therefore, this transition will probe much colder regions of the interstellar medium than the atomic hydrogen 21 cm emission. Temperatures at which we could expect to detect considerable CO emission (5–30 K) occur only inside of dusty molecular clouds which are well shielded from external heating by UV radiation.

Line strengths will depend on the value of $|\mu_{ij}|^2$, the square of the dipole moment matrix elements summed over the three spatial directions (Kutner 1984). The quantity $|\mu_{ij}|^2$ depends on the square of the permanent electric dipole moment, which for ^{12}CO is very small, $3.74 \cdot 10^{-14} Cm$ (Rohlfs 1986). Therefore, the spontaneous emission coefficient, A_J, which is directly related to $|\mu_{ij}|^2$, is relatively small, $7.4 \cdot 10^{-8} s^{-1}$.

The excitations of the CO emission take place through collisions (mostly with H_2 molecules, because it is the most abundant molecule). The collisional rate per molecule in state i for a transition to state j can be calculated from

$$C_{ij} = n_0 \langle v \sigma_{ij}(v) \rangle \qquad (C–4)$$

where n_0 is the number density of exciting H_2 molecules, v is their speed, σ_{ij} is the collisional cross section for this transition, calculated from the theory, and the average is over the velocity distribution of the colliding particles. Between states 1 and 2, when the collisions dominate (thermal equilibrium), the ratio of the collisional excitations to

collisional de-excitations will be given by

$$\frac{C_{12}(T_k)}{C_{21}(T_k)} = \frac{n_2}{n_1} \tag{C–5}$$

where T_k is the kinetic temperature. The ratio of the number of atoms at the two levels, n_2/n_1, is described by a Boltzmann distribution at temperature T_x

$$\frac{n_2}{n_1} = \frac{g_2}{g_1} \exp\left(-\frac{h\nu_{21}}{kT_x}\right), \tag{C–6}$$

which is also the definition for the excitation temperature, T_x. The quantities g_1 and g_2 are the statistical weights for the two levels. The intensity of the radiation (I_ν) at any frequency ν may be calculated from

$$I_\nu = I_\nu(0) \exp\left(-\tau_\nu\right) + S_v[1 - \exp\left(-\tau_\nu\right)], \tag{C–7}$$

where τ_ν is the optical depth at frequency ν and S_ν is the source function, which includes the contributions from both the emission and absorption in the cloud. To obtain the line emission only, one must subtract the continuum, giving

$$\Delta I_\nu = [S_\nu - I_\nu(0)][1 - \exp\left(-\tau_\nu\right)] \tag{C–8}$$

Using the blackbody representation for S_ν at the line excitation temperature and the temperature 2.7 K for the cosmic background radiation (which, in the absence of any other continuum source determines the background intensity $I_\nu(0)$), we obtain

$$\Delta I_\nu = [B_\nu(T_x) - B_\nu(2.7)][1 - \exp\left(-\tau_\nu\right)]. \tag{C–9}$$

Even though the condition (Rayleigh-Jeans limit) $h\nu \ll kT$ is not true for 2.6 mm radiation, we may still define a "radiation temperature" T_R by

$$T_R = \frac{c^2 I_\nu}{2\nu^2 k}. \tag{C–10}$$

In terms of this variable, the observed temperature (brightness temperature of the line radiation, ΔT_R), becomes

$$\Delta T_R = [J_\nu(T_x) - J_\nu(2.7)][1 - \exp(-\tau_\nu)], \qquad (C-11)$$

where

$$J_\nu(T) = \frac{h\nu}{k}\left[\frac{1}{\exp\left(\frac{h\nu}{kT}\right) - 1}\right] \qquad (C-12)$$

In practice, if the beam is large compared to the source, the right hand side of equation (C–11) needs to be multiplied by the beam filling factor f, which is the ratio of the source solid angle to the beam solid angle.

^{12}CO emission is optically thick because the observed line profiles are saturated (flat topped) and the observed ^{12}CO/^{13}CO ratio is smaller than the measured cosmic isotopic ratio. The small A_{10} coefficient ensures that collisions with H_2 dominate the excitation. Thus $T_k = T_{ex} \approx T_B$.

The density of the molecular material (essentially the density of H_2) in the molecular clouds of the galaxy can be estimated through observations of the ^{13}CO isotope, which is often optically thin. The observations of the ^{12}CO determine the excitation temperature, which is assumed to be the same for both isotopes. If so, the column density $N(^{13}$CO) can be calculated in a straightforward way. The relations between $N(^{13}$CO) and the visual extinction, A_V, and total hydrogen column density and A_V, give us a molecular gas density, assuming we know the extent of the cloud along the line of sight and a hydrogen to helium abundance ratio (around 10%). Use of this method requires that the atomic hydrogen column density is known.

The strength of the ^{13}CO emission from extragalactic objects is often so weak that this method cannot be used. Instead, we have to estimate the molecular masses with the help of the integrated CO intensity, $I_{CO} = \int T_B(CO)dV$, where T_B is the brightness

temperature of the CO emission and the integration is over the velocity width of the emission. We expect that there is a correlation between the molecular mass of the galaxy and the integrated CO intensity, because we observe a collection of gas clouds that do not shadow each other in the position-velocity space. In essence, we see an integral over cloud temperature and total projected cloud surface area. We can define a CO luminosity by

$$L_{CO} = D^2 \int I_{CO} d\Omega \tag{C-13}$$

which is equal to $\pi R^2 T_B(CO) \Delta v$ if there is a collection of uniform, spherical clouds with a radius R and mass M. Since $\Delta v = \sqrt{\frac{GM}{R}}$,

$$M = L_{CO} \sqrt{\frac{4\rho}{3\pi G T_{CO}}} \tag{C-14}$$

If the projected CO surface area to H_2 volume is constant and if, statistically, the temperatures and densities in each cloud are the same, the integrated CO signal is directly proportional to the molecular hydrogen column density in the beam (Israel 1988). This relationship can be calibrated by observations of the molecular clouds in the Galaxy. Before discussing the determination of this proportionality factor, I must emphasize that the physical conditions in the Galaxy can be very different from the extragalactic environments.

One way to calibrate the above-mentioned relationship is through Galactic determinations of $N(H_2)$ and I_{CO} using the relation between the ^{13}CO emission and A_V. An average of all observations is taken and the resulting value determines the proportionality factor. In another method, the observed CO integral of a Galactic molecular cloud may be compared to its mass estimate obtained with the virial theorem. The uncertainty in this method includes the degree of relaxation of the Galactic molecular clouds. If their lifetimes are on the order of 10^7 years, they may not have had enough time to relax

and virialize. In the third method, the dust masses of the clouds are estimated with far-infrared and submillimeter observations. A gas-to-dust mass ratio is assumed and employed to estimate their total gas masses. If the atomic mass is known from the H I observations, the H_2 mass may be obtained. The critical assumption is the constancy of the gas-to-dust mass ratio throughout the Galaxy. In the final method, the measurement of the gamma ray emission above a certain threshold energy (about 50 MeV) is assumed to reflect the hydrogen density, because these gamma rays are produced by the cosmic ray − hydrogen nucleon interactions. However, the conversion factor from this method depends on the model parameters.

Finally, I will discuss briefly the uncertainties associated with the conversion factor between the CO intensity and the molecular hydrogen mass. It is clear that the application of the Galactic conversion factor to the extragalactic measurements is justified only if the molecular cloud properties and the physical conditions, such as excitation and abundances, of the galaxy are similar to that of the Milky Way. The H_2 molecules are characterized by a high formation rate and strong self-shielding against photodissociation. CO has a lower formation rate and is less self-shielding because of its lower interstellar abundance. Therefore, the molecular cloud has a large H_2 extent and a smaller CO core. It is clear that in low metallicity environments, we would tend to underestimate the H_2 masses, if we use the standard Galactic conversion factor. In high metallicity regions, the opposite might happen. Some dwarf galaxies are characterized by very low metallicities and high star formation rates (high ionizing photon densities). We would expect that the standard conversion factor is not applicable under these circumstances. This has been confirmed by recent studies of local group galaxies (see e.g. Wilson 1995; also Verter & Hodge 1995). The conversion of CO intensities to molecular masses must be made with caution. Especially if one uses a constant conversion factor (as in this dissertation), the

uncertainties must be kept in mind. More discussion on these issues can be found e.g. in the reviews by Young & Scoville (1991), Henkel et al. (1991) and Combes (1992) and in the recent papers by Arimoto et al. (1996), Bryant & Scoville (1996), Sodroski et al. (1995). The conversion factor from the CO intensity to H_2 surface density can be a factor of 10 larger than the standard value in metal poor dwarf galaxies, while it may be lower by a factor of two near the metal-rich centers of spiral galaxies.

APPENDIX D
DESCRIPTION OF THE TREE-SPH ALGORITHM

There are probably on the order of 10^{11} stars in a typical disk galaxy. The numerical codes can handle only a very small fraction of this, because the computing time rises sharply with the number of particles (although only as N log N with the tree code). It is a common practice to distribute the total mass in stellar material evenly among the particles. These particles should not be thought of as individual stars, but rather, as clumps or clusters of stars or giant molecular clouds of gas moving in the galactic potential.

Here we meet the greatest challenge of the numerical simulation techniques. How believable are the results of the N-body computations, not only with respect to the number of particles, but with respect to other limitations as well? Clearly, the study of these issues is warranted. I refer to a recent paper by Habib et al. (1996) that studied the effects of weak friction and noise in potentials that admit both regular and stochastic orbits. They conclude that even very small irregularities can dramatically change the behavior of orbits in time-scales much shorter than a characteristic relaxation time-scale. These changes take place in a time-scale that is smaller than the age of the Universe. A study of these effects in a more realistic potential is being made presently at the University of Florida by Dr. Kandrup, Mr. Siopis and others. Especially the study of uniqueness of models and the proportion of chaotic orbits in real galaxies are extremely important.

The concern raised in the last paragraph means that detailed models for the evolution of individual galaxies are not likely to be generated for some time, if ever. However, numerical simulations can still be used to test different scenarios of evolution and to help

243

the interpretation of the observations. Many examples can be found in the literature. It is difficult to argue the value of the pioneering interaction simulations by Toomre & Toomre (1972), which reproduced most of the essential features of the observations. Therefore, keeping the obvious limitations of this approach in mind, I will continue the discussion of numerical codes, specifically the tree-SPH code (Hernquist & Katz 1989; Heller 1991).

Since close encounters between the stars of a galaxy are extremely rare, the far-field forces determine the motion. To accomplish this in the numerical codes, the forces have to be softened to avoid great perturbations in encounters between massive particles.

A fairly recent review of N-body codes is in Sellwood (1987). The pioneering work in N-body simulations was made by direct codes that require $\sim N^2$ force calculations per time step, where N is the number of particles. These codes can be used to calculate the evolution of only a few thousand particles. A more modern technique is the use of a grid that samples the available volume at regular intervals. The forces are calculated exactly only on the grid. Interpolations to the positions of the particles are then made. Since Fast Fourier Transform techniques are used, the grid size must be a power of two. The number of calculations is roughly proportional to N log N and it can handle perhaps a million particles.

This work uses a different technique to calculate the forces. The tree-code that I use is called the Fast Tree Method (FTM) and was developed by Clayton Heller (1991) as part of his Ph.D. thesis. The code uses the ideas of Barnes & Hut (1986). The whole system is first imagined to be inside a big box. This box is then divided into eight smaller daughter boxes (four in two-dimensional cases, I will discuss only the three-dimensional case here, but the restriction to two dimensions should be obvious). Each of these smaller boxes is then divided into eight daughter boxes in turn, and this process is continued until there is only one or no particle inside of a box. The empty boxes are

discarded and do not take any memory during the execution of the code. This method has been vectorized, and it is fast.

For each box, starting from the bottom, the center of mass and the quadrupole moment are calculated. For a "parent" box, these quantities can be calculated by summing over the "daughter" boxes. The quadrupole moment is calculated with respect to the center of mass of the box. The dipole moment for the center of mass disappears for symmetry reasons. The time consumed in ascending (or descending) the tree is $\sim \log_8 N$.

Next we want to calculate the forces at each particle's position, thus going down the tree again, and thus the time spent altogether is $\sim N \log_8 N$. We want to estimate which forces we are going to calculate accurately, and for which forces an approximation to the quadrupole order will be made. To do this, we evaluate the ratio of the size of a another box to its distance from the particle (actually an angle). If this angle is smaller than a preset tolerance, we will use the quadrupole approximation of the force. If the angle is greater than the tolerance, the box is "resolved", and the test is applied to daughter boxes. The tolerance is chosen in such a way that the gravitational forces of the particles in the nearest boxes are calculated exactly (with some spline softening, to be described below). The value for the critical angle used in the simulations is between 0.6 and 0.8. These values have been found to give forces which are within 1 % of the forces found by direct summation Drimmel (1995). The hierarchical tree method is fully Lagrangian (comoving). Therefore, no mesh-related limitation on the spatial resolution is imposed.

The potential per unit mass of a spatially bounded set of point particles at an exterior point is given by (Heller 1991)

$$\phi(r) = -\frac{GM}{r} - \frac{1}{2}\frac{G}{r^5}\mathbf{r} \cdot \mathbf{Q} \cdot \mathbf{r} \tag{D-1}$$

where M is the total mass of the bounded set and $\mathbf{Q}$ is the traceless quadrupole tensor

defined by

$$Q_{ij} = \sum_k m_k \left(3x_{k,i} x_{k,j} - r_k^2 \delta_{ij} \right) \tag{D-2}$$

where $x_{k,i}$ is the ith component of r_k. All quantities are evaluated with respect to the center of mass of the set.

The corresponding acceleration is

$$a = -GM \frac{\hat{\mathbf{r}}}{r^2} + \frac{G}{r^4} \, \mathbf{Q} \cdot \hat{\mathbf{r}} - \frac{5G}{2} \left(\hat{\mathbf{r}} \cdot \mathbf{Q} \cdot \hat{\mathbf{r}} \right) \frac{\hat{\mathbf{r}}}{r^4}. \tag{D-3}$$

As discussed above, the potential needs to be softened in order to simulate a nearly collisionless medium such as stars in real galaxies. The commonly used approach is to add an epsilon term to the denominator of the potential equation. This in effect saturates the force at short distances and artificial heating is thus reduced. The epsilon approximation approaches the exact Keplerian potential only slowly with increasing interparticle distance. This affects the resolution adversely. Because the multipole expansion is based on the assumption that bodies are point particles, additional errors in potential calculation are introduced if epsilon is used. In FTM, the softening is done with the help of a spline kernel, that converges to the exact Keplerian potential for r ≥ 2 x epsilon. The spline kernel, and its first derivative are continuous everywhere. The spline used in FTM can be found for example in Drimmel (1995) and Heller (1991). The smoothing lengths, epsilon, can be dynamically varied for the gas particles, resulting in much better accuracy in high density regions of a galaxy.

The time steps for the collisionless particles are computed with the help of the Courant condition. The maximum step size for particle i is calculated from

$$\delta t_i = \sqrt{\frac{\eta |F_i|}{|\dot{F}|}}, \tag{D-4}$$

where F stands for force and η is a dimensionless accuracy parameter. The real time steps have been binned to constant sizes that differ from each other by a power of two.

SPH stands for Smoothed Particle Hydrodynamics. It is a scheme to incorporate the forces from the dissipative component (gas) into the N-body calculations. A good review of SPH techniques is given by Monaghan (1992). An essential feature of SPH is the neighbor searching. Neighbors are searched for in a box that has a size 4h x 4h x 4h, where h is the so-called smoothing length. Finding the neighbors is the most time-consuming part of a tree-SPH code such as FTM.

The same gravitational tree is used for stellar and gaseous particles. The tree is descended in search for the neighbors. The gaseous particles move around (Lagrangian method) carrying the "grid" with them. They sample a continuous distribution of gas. The basic assumption of SPH is that the number density is proportional to the mass density. SPH works because the pressure forces and viscosity make the particle distribution ordered (the kernel might have problems sampling a completely random distribution). The disadvantage of SPH is that it uses artificial viscosity to simulate shocks. Naturally, it is impossible to present an arbitrarily large density gradient, such as found in real shocks, with a finite number of particles. In this sense SPH has a limited spatial resolution.

In SPH, the values of various physical fields (density, velocity, thermal energy etc.) are only known at a finite number of discrete points. It is necessary to estimate the values of these quantities by averages over finite volumes. The averages are found from the smoothed estimate,

$$\langle A(\mathbf{r}) \rangle = \int_D A(\mathbf{r}') W(\mathbf{r}, \mathbf{r}', \mathbf{h}) d\mathbf{r}', \tag{D–5}$$

where A($\mathbf{r}$) is the function to be interpolated and W is a kernel that has been normalized

to one

$$\int\limits_D W(\mathbf{r}, \mathbf{r}', h) d\mathbf{r}' = 1. \tag{D–6}$$

Also, $\langle A(\mathbf{r}) \rangle \to A(\mathbf{r})$ *as* $h \to 0$. In practice, an estimate for A can be calculated from

$$\langle A \rangle \approx \sum_j \frac{A_j}{n_j} W(\mathbf{r}, \mathbf{r}', h), \tag{D–7}$$

where n_j is the number density.

Usually the kernel has the property

$$W(\mathbf{r}, \mathbf{r}', h) \equiv W(|\mathbf{r} - \mathbf{r}'|, h), \tag{D–8}$$

and it can be shown by partial integration (Heller 1991) that the gradient

$$\langle \nabla \phi(\mathbf{r}) \rangle = \int\limits_D \phi(\mathbf{r}') \nabla W(|\mathbf{r} - \mathbf{r}'|, h) d\mathbf{r}'. \tag{D–9}$$

The expectation value for the divergence can be calculated in a similar way:

$$\langle \nabla \cdot \mathbf{v}(\mathbf{r}) \rangle = \int\limits_D \mathbf{v}(\mathbf{r}') \cdot \nabla W(|\mathbf{r} - \mathbf{r}'|, h) d\mathbf{r}'. \tag{D–10}$$

The kernel used in FTM is a spherically symmetric spline that has continuous first and second derivatives and is second order accurate (Heller 1991).

The smoothing length, h, must be chosen so that there are enough neighbors within the $(4h)^3$ box. A common choice is 32 particles. The smoothing length h is variable both in space and time. If the first guess for h includes more neighbors than the optimum number (e.g. 32), we only include the amount of nearest neighbors equal to the optimum number. If no particles are found, we will double the value of h and try again. These steps will be iterated until we arrive within some tolerance of the optimum number.

All equations in SPH must be symmetrical (i.e., the force of particle i on particle j is the same as the force of particle j on particle i). One way to do this is to average

the individual smoothing lengths h_i and h_j, and use this average in the mutual force calculation. A possible problem with this scheme is that we ignore the gradient in h between particles i and j. Another way to symmetrize the force equations is to use an average kernel, $\frac{w_i + w_j}{2}$. This method has been adopted in FTM. However, this method will give a smoothing length larger than the original for one of the particles and smaller than the original for the other. Therefore we may be outside of the tolerance limit from the optimum number of nearest neighbors. Once the force has been calculated for one particle (e.g. i with respect to j), it is included for the other particle (j with respect to i).

The SPH kernel is used to calculate the smoothed density, pressure, $\nabla \cdot \mathbf{v}$ and viscosity parameters. The phase space evolution of a particle is given by the equations

$$\frac{d\mathbf{r}}{dt} = \mathbf{v} \tag{D-11}$$

and

$$\frac{d\mathbf{v}}{dt} = -\frac{1}{\rho}\nabla P + a_{visc} - \nabla\phi. \tag{D-12}$$

The pressure gradients are calculated from

$$-\frac{\nabla P}{\rho} = \sum_j m_j \frac{\sqrt{P_j P_i}}{\rho_i \rho_j}[\nabla_i W(r_{ij}, h_i) + \nabla_i W(r_{ij}, h_j)], \tag{D-13}$$

gravity forces in the same way as in the tree-method, and viscosity forces from

$$a_{visc} = -\sum_j m_j \Pi_{ij} \frac{1}{2}[\nabla_i W(r_{ij}, h_i) + \nabla_i W(r_{ij}, h_j)], \tag{D-14}$$

where

$$\Pi_{ij} = \frac{-\alpha \bar{c}\mu_{ij} + \beta\mu_{ij}^2}{\bar{\rho}_{ij}}, \tag{D-15}$$

$$\mu_{ij} = \begin{cases} \dfrac{\mathbf{v}_{ij} \cdot \mathbf{r}_{ij}}{\bar{h}_{ij}\left[\left(\dfrac{r_{ij}}{h_{ij}}\right)^2 + \eta^2\right]}, & \mathbf{v}_{ij} \cdot \mathbf{r}_{ij} < 0 \\ 0, & \mathbf{v}_{ij} \cdot \mathbf{r}_{ij} \geq 0 \end{cases} \tag{D-16}$$

and where $\mathbf{v}_{ij} = \mathbf{v}_i - \mathbf{v}_j$, $\bar{c} = \frac{c_i + c_j}{2}$, the average speed of sound of particles i, j, $\bar{h}_{ij} = \frac{h_i + h_j}{2}$ and $\bar{\rho}_{ij} = \frac{\rho_i + \rho_j}{2}$. The first term in equation (D–15) is analogous to a bulk viscosity, whereas the second term is intended to suppress particle interpenetration. Typically, $\alpha \sim 0.5$, $\beta \sim 1.0$ and $\eta \sim 0.01$. To reduce the effective shear viscosity, Benz (1990) has introduced a switch in the form of a multiplicative factor f_{ij} on μ_{ij}. The factor f_{ij} is the average of f_i and f_j, where

$$f_i = \frac{|\nabla \cdot \mathbf{v}|_i}{|\nabla \cdot \mathbf{v}|_i + |\nabla \times \mathbf{v}|_i + 0.001 c_i / h_i}, \tag{D–17}$$

and the curl of the velocity is given by the estimate

$$\nabla \times \mathbf{v} = \frac{1}{\rho_i} \sum_j m_j \mathbf{v}_{ij} \times \nabla W_{ij}. \tag{D–18}$$

The time gradient of the specific heat is calculated from

$$\frac{du}{dt} = \sum_j m_j \left(\frac{\sqrt{P_i P_j}}{\rho_i \rho_j} + \frac{1}{2} \Pi_{ij} \right) \mathbf{v}_{ij} \cdot \frac{1}{2} [\nabla_i W(\mathbf{r}_{ij}, h_i) + \nabla_i W(\mathbf{r}_{ij}, h_j)]. \tag{D–19}$$

The first term with the pressures is the adiabatic term, the second one is the heating term associated with viscosity. Additional heating and cooling terms not associated with viscosity may be included in this equation. This equation can be used with the first adiabatic term included to monitor the total thermal energy lost. The last equation was derived from the first law of thermodynamics,

$$du = -P dV + T ds. \tag{D–20}$$

My simulations used an isothermal equation of state, which is a special case of the polytropic equation of state,

$$P = K \rho^\gamma. \tag{D–21}$$

In the isothermal case, $\gamma = 1$, and $K = c_{iso}^2$. The polytropic case requires no description of the evolution of the specific heat.

The time steps for the collisionless particles are calculated according to equation (D–4). The time steps for the SPH particles are calculated from

$$\delta t_i = C Min\left[\sqrt{\frac{h_i}{F_i}}, \frac{h_i}{\sigma_i}\right], \tag{D–22}$$

where

$$\sigma_i = h_i |\nabla \cdot \mathbf{v}_i| + c_i + 1.2(\alpha c_i + \beta max_j|\mu_{ij}|), \tag{D–23}$$

and C is the Courant number. The greater the summed force or the viscosity, the smaller the time step.

The code uses a standard leap-frog integrator for integration of the equations of motion for the stars. This is accurate to the second order. For particle i, the new positions and velocities are found from (Davies 1995)

$$r_i^{n+\frac{1}{2}} = r_i^{n-\frac{1}{2}} + \Delta t v_i^n + O(\Delta t^3), \tag{D–24}$$

$$v_i^{n+1} = v_i^n + \Delta t a_i^{n+\frac{1}{2}} + O(\Delta t^3), \tag{D–25}$$

where the superscripts refer to the time step at which the quantities are computed. For the SPH particles the acceleration depends on the velocity of the particle. In this case a prediction of the new velocity is calculated and then this predicted value is used to calculate the time-centered acceleration used in equation (D–25). Higher order accuracy is not necessary because the force expansions are only made to the quadrupole term.

As discussed above, the individual time steps are a power of two subdivision of the system time step, Δt_s, such that

$$\Delta t_k = \frac{\Delta t_s}{2^k}, k = 1, 2, ..., n, \tag{D–26}$$

where n is the power of the shortest time step. The particle is placed within the largest time bin so that

$$\Delta t_k < \Delta t_i. \tag{D–27}$$

All the particles in a certain time bin are advanced together. The system is synchronized after each set of 2^{n+1} time steps. The time step used to advance particle's positions is half the smallest particle time step. The particles are allowed to move to the next smaller time step at the end of their current time step, but are allowed to move to the next larger time step only when the two bins are synchronized. If the particle changes its time bin, its position is updated using a midpoint velocity in order to preserve the accuracy of the scheme. The leap-frog integrator may be made self-starting if initial positions and velocities have been given. A second order estimate for the positions can then be found from

$$r_i^{n+\frac{1}{2}} = r_i^n + \frac{\Delta t}{2} v_i^n + \frac{\Delta t^2}{8} a_i^n. \tag{D–28}$$

The equations describing the time evolution of the dissipative component, the gas, are integrated using a second order predictor-corrector algorithm. Both the linear and the angular momentum are conserved exactly. This method also has the advantage that the positions need not be time-synchronized with the velocities when computing diagnostic information or corrected when changing time bins. First we calculate the quantities

$$\bar{v}_i^{\;1} = v_i^0 + \Delta t F_i^0$$
$$\bar{u}_i^{\;1} = u_i^0 + \Delta t Q_i^0 \tag{D–29}$$
$$\bar{r}_i^{\;1} = r_i^0 + \Delta t v_i^0,$$

where bars denote predicted values and the superscripts 0 and 1 the initial and final times, respectively. Then we calculate $\rho_i^{\frac{1}{2}}, P_i^{\frac{1}{2}}, \nabla \cdot v_i^{\frac{1}{2}}, F_i^{\frac{1}{2}},$ and $Q_i^{\frac{1}{2}}$ where

$$v_i^{\frac{1}{2}} = \frac{1}{2}\left(v_i^0 + \bar{v}_i^{\;1}\right)$$
$$u_i^{\frac{1}{2}} = \frac{1}{2}\left(u_i^0 + \bar{u}_i^{\;1}\right) \tag{D–30}$$
$$r_i^{\frac{1}{2}} = \frac{1}{2}\left(r_i^0 + \bar{r}_i^{\;1}\right),$$

and $P_i^{\frac{1}{2}} = \mathrm{K}\left(\rho_i^{\frac{1}{2}}, u_i^{\frac{1}{2}}\right)$, where K is the equation of state. Finally, the quantities are corrected according to

$$v_i^1 = v_i^0 + \Delta t F_i^{\frac{1}{2}}$$
$$u_i^1 = u_i^0 + \Delta t Q_i^{\frac{1}{2}}$$
$$r_i^1 = r_i^0 + \frac{\Delta t}{2}\left(v_i^0 + v_i^1\right).$$

(D–31)

In practice it is sufficient to substitute the midpoint values $F^{\frac{1}{2}}$ and $Q^{\frac{1}{2}}$ from the previous time step for F^0 and Q^0 when predicting.

As shown by e.g. Heller and Shlosman (1994), the inclusion of star formation in numerical codes can dramatically change the results of a simulation. Unfortunately, the star formation process is still not very well understood. Therefore, only a schematic representation is possible at the moment, although work is being done to improve this. Some of the studies using star formation in numerical codes were made by Heller and Shlosman (1994), Friedli and Benz (1995), Katz (1992), Mihos and Hernquist (1994b) and Navarro and White (1993). Different criteria for star formation were used. For example, Heller and Shlosman (1994) use the Jeans criterion

$$\rho > \rho_{crit} = \frac{\pi c_s^2}{16 G h^2}.$$

(D–32)

Heller and Shlosman also restrict star formation only to regions where the divergence of the velocity field is negative (collapsing). Using this criterion, star formation takes place only in the bar, as demonstrated by Friedli & Benz (1993). These authors favor the Toomre stability criterion

$$Q = \frac{c_s \kappa}{\pi G \mu_g} < Q_{crit},$$

(D–33)

where κ is the epicyclic frequency and μ_g is the gaseous surface density. The numerical value of Q_{crit} is somewhat uncertain, but the observations suggest a value around 1.4

(Kennicutt 1990). This criterion is somewhat difficult to implement in a tree-code because κ is a local quantity. In grid codes it is relatively straightforward to interpolate κ from the grid. Finally, Mihos and Hernquist (1994b) used a criterion based on the Schmidt's law

$$\rho_{SFR} = C\rho^{1.5}, \tag{D–34}$$

which is an empirical criterion for star formation.

Another way to regulate star formation is through the use of time-scales. The criteria implemented for star formation in FTM is the following:

$$T_c < T_d, \tag{D–35}$$

where T_d is the local dynamical time for collapse,

$$T_d = \left(\frac{3\pi}{16G\rho_{gas}}\right)^{\frac{1}{2}}, \tag{D–36}$$

and T_c is the local cooling time. The latter is a better way to calculate the star formation threshold because it does not directly depend on the smoothing length, h, and thus on the number of neighbors used.

The tree-SPH code has been tested thoroughly by earlier users (Heller & Shlosman 1994; Davies 1995). These tests included colliding non-gravitating sheets of gas to study the resulting shock profiles, the radial pulsations of a self-gravitating polytropic gas sphere and the oscillations of a Maclaurin disk. In all cases the code modeled the analytical expectation satisfactorily.

REFERENCES

Aaronson, M. 1977 Ph.D. thesis, Harvard University.

Aguerri, J. A., Munoz–Tunon, C., Varela, A. M. and Prieto, M. 1996, in *Barred Galaxies*, eds. R. Buta, D. A. Crocker and B. G. Elmegreen, ASP Conf. series, **91**, 557.

Allen, R. J. 1992, *Ap.J.*, **399**, 473.

Arimoto, N., Sofue, Y. and Tsujimoto, T. 1996, *P.A.S.J.*, **48**, 275.

Athanassoula, E. 1992a, *M.N.R.A.S.*, **259**, 328.

Athanassoula, E. 1992b, *M.N.R.A.S.*, **259**, 345.

Athanassoula, E. 1994, in *Mass-Transfer Induced Activity in Galaxies*, ed. I. Shlosman, Cambridge University Press, Cambridge, Great Britain, p. 143.

Ball, R. 1984, Ph.D. thesis, University of Florida.

Ball, R. 1986, *Ap.J.*, **307**, 453.

Ball, R. 1992, *Ap.J.*, **395**, 418.

Ball, R., Sargent, A. I., Scoville, N. Z., Lo, K. Y. and Scott, S. L. 1985, *Ap.J. Let.*, **298**, 21.

Balzano, V. A. 1983, *Ap.J.*, **268**, 602.

Barnaby, D. and Thronson, M. A. 1992, *A.J.*, **103**, 41.

Barnes, J. E. and Hernquist, L., 1991, *Ap.J. Let.*, **370**, 65.

Barnes, J. E. and Hut, P. 1986, *Nature,* **324**, 446.

Baumgart, C. W. and Peterson, C. J. 1986, *P.A.S.P.*, **98**, 56.

Balzano, V. A. 1983, *Ap.J.*, **268**, 602.

Beckman, J. and Cepa, J. 1989, *Ap. Space Sci.*, **156**, 199.

Beckman, J. and Cepa, J. 1990, *Astr. Ap.*, **229**, 37.

Begeman, K. G. 1989, *Astr. Ap.*, **223**, 47.

Benedict, G. F. 1982, *A.J.*, **87**, 76.

Benedict, G. F., Smith, B. J. and Kenney, J. D. P. 1996, *A.J.*, **111**, 186.

Benz, W. 1990, in *The Numerical Modelling of Nonlinear Stellar Pulsations, Problems and Prospects*, ed. J. R. Buchler, Kluwer, Dordrecht, Netherlands, p. 269.

Binney, J. and Tremaine, S. 1987, in *Galactic Dynamics*, Princeton University Press, Princeton, N. J.

Blackman, C. P. 1983, *M.N.R.A.S.*, **202**, 379.

Bloemen, J. B. G. M., Strong, A. W., Mayer-Hasselwander, H. A., Blitz, L., Cohen, R. S., Dame, T. M., Grabelsky, D. A., Thaddeus, P., Hermsen, W. and Lebrun, F. 1986, *Astr. Ap.*, **154**, 25.

Bosma, A. 1981, *A.J.*, **86**, 1791.

Bottinelli, L., Gouguenheim, L. and Paturel, G. 1982, *Astr. Ap.*, **113**, 61.

Brinks, E. and Bajaja, E. 1986, *Astr. Ap.*, **169**, 14.

Bryant, P. M. and Scoville, N. Z. 1996, *Ap.J.*, **457**, 678.

Burbidge, E. M., Burbidge, G. R. and Prendergast, K. H. 1960, *Ap.J.*, **132**, 654.

Buta, R. 1993, *P.A.S.P.*, **105**, 654.

Canzian, B. 1993, *Ap.J.*, **414**, 487.

Canzian, B., Mundy, L. G. and Scoville, N. Z. 1988, *Ap.J.*, **333**, 157.

Clark, B. G. 1980, *Astr. Ap.*, **89**, 377.

Combes, F. 1992, in *Physics of Nearby Galaxies: Nature or Nurture?*, ed. T. X. Thuan, C. Balkowski and J. T. T. Van, Editions Frontiers, Gif-sur-Yvette, France.

Combes, F. 1994, in *Mass-Transfer Induced Activity in Galaxies*, ed. I. Shlosman, Cambridge University Press, Cambridge, Great Britain, p. 170.

Combes, F. and Elmegreen, B. G. 1993, *Astr. Ap.*, **271**, 391.

Combes, F. and Gerin, M. 1985, *Astr. Ap.*, **150**, 327.

Condon, J. J. 1987, *Ap.J. Suppl.*, **65**, 485.

Contopoulos, G. 1975, *Ap.J.*, **201**, 566.

Contopoulos, G. 1980, *Astr. Ap.*, **81**, 198.

Contopoulos, G. 1983, *Astr. Ap.*, **117**, 89.

Contopoulos, G., Gottesman, S. T., Hunter, J. H., Jr. and England, M. N. 1989, *Ap.J.*, **343**, 608.

Contopoulos, G. and Mertzanides 1977, *Astr. Ap.*, **61**, 477.

Contopoulos, G. and Papayannopoulos, T. 1980, *Astr. Ap.*, **92**, 33.

Crovisier, J. 1981, *Astr. Ap.*, **94**, 162.

Davies, C. L. 1995, Ph.D. thesis, University of Florida.

Davis, L. E. and Seaquist, E. R. 1983, *Ap.J. Suppl.*, **53**, 269.

de Jong, T., Clegg, P. E., Rowan-Robinson, M., Soifer, B. T., Habing, H. J., Houck, J. R., Aumann, H. H. and Raimond, E. 1984, *Ap.J. Let.*, **278**, 67.

del Rio, M. S. 1995, Ph.D. thesis, Universidad de la Laguna.

de Vaucouleurs, G. 1979, *Ap.J.*, **227**, 729.

de Vaucouleurs, G., de Vaucouleurs, A., Corwin, H. G., Jr., Buta, R. J., Paturel, G. and Furgue, P. 1991, *Third Reference Catalogue of Bright Galaxies*, Springer, New York, (RC3).

Devereux, N. A. 1987, *Ap.J.*, **323**, 91.

Devereux, N. A. 1989, *Ap.J.*, **346**, 126.

Devereux, N. A., Kenney, J. D. P. and Young, J. S. 1992, *A.J.*, **103**, 784.

Dickey, J. M. and Brinks, E. 1988, *M.N.R.A.S.*, **233**, 781.

Drimmel, R. E. 1995, Ph.D. thesis, University of Florida.

Duval, M. F. and Monnet, G. 1985, *Astr. Ap. Suppl.*, **61**, 141.

Elmegreen, B. G. 1993, *Ap.J.*, **411**, 170.

Elmegreen, B. G. and Elmegreen, D. M. 1990, *Ap.J.*, **355**, 52.

Elmegreen, D. M. and Elmegreen, B. G. 1985, *Ap.J.*, **288**, 438.

Elmegreen, D. M. and Elmegreen, B. G. 1987, *Ap.J.*, **314**, 3.

Elmegreen, D. M. and Elmegreen, B. G. 1995, *Ap.J.*, **445**, 591.

Elmegreen, B. G., Elmegreen, D. M. and Seiden, P. E. 1989, *Ap.J.*, **343**, 602.

England, M. N. 1986, Ph.D. thesis, University of Florida.

England, M. N. 1989a, *Ap.J.*, **337**, 191.

England, M. N. 1989b, *Ap.J.*, **344**, 669.

England, M. N., Gottesman, S. T. and Hunter, J. H., Jr. 1990, *Ap.J.*, **348**, 456.

Eracleous, M., Livio, M. and Binette, L. 1995, *Ap.J. Let.*, **445**, 1.

Filippenko, A. V. 1993, in *The Nearest Active Galaxies*, ed. J. Beckman, CSIC, Madrid.

Filippenko, A. V. and Sargent, W. L. W. 1985, *Ap.J. Suppl.*, **57**, 503.

Forbes, D. A., Ward, M. J., DePoy, D. L., Boisson, C. and Smith, M. S. 1992, *M.N.R.A.S.*, **254**, 509.

Friedli, D. 1994, in *Mass-Transfer Induced Activity in Galaxies*, ed. I. Shlosman, Cambridge University Press, Cambridge, Great Britain, p. 268.

Friedli, D. 1996, *Astr. Ap.*, **312**, 761.

Friedli, D. and Benz, W. 1993, *Astr. Ap.*, **268**, 65.

Friedli, D. and Benz, W. 1995, *Astr. Ap.*, **301**, 649.

Friedli, D., Wozniak, H., Rieke, M., Martinet, L. and Bratschi, P. 1996, *Astr. Ap. Suppl.*, **118**, 461.

Gomez, G., Lopez, R. 1994, *A.J.*, **108**, 195.

Gottesman, S. T., Ball, R., Hunter, J. H., Jr., and Huntley, J. M. 1984, *Ap.J.*, **286**, 471.

Grosbøl, P. J. 1985, *Astr. Ap. Suppl.*, **60**, 261.

Habib, S., Kandrup, H. E. and Mahon, M. E. 1996, *Ap.J.*, submitted.

Hawarden, T. G., Mountain, C. M., Leggett, S. K. and Puxley, P. J. 1986, *M.N.R.A.S.*, **221**, 41P.

Haynes, M. P. and Giovanelli, R. 1984, *A.J.*, **89**, 758.

Heckman, T. M. 1980, *Astr. Ap.*, **88**, 365.

Heller, C. H. 1991 Ph.D. thesis, Yale University.

Heller, C. H. and Shlosman, I. 1994, *Ap.J.*, **424**, 84.

Henkel, C., Baan, W. A. and Mauersberger, R. 1991, *Astron. Astrop. Rev.*, **3**, 47.

Hernquist, L 1989, *Nature*, **340**, 687.

Hernquist, L 1993, *Ap.J. Suppl.*, **86**, 389.

Hernquist, L and Katz, N. 1989, *Ap.J. Suppl.*, **70**, 419.

Hernquist, L and Mihos, J. C. 1995, *Ap.J.*, **448**, 41.

Hewitt, J. N., Haynes, M. P. and Giovanelli, R. 1983, *A.J.*, **88**, 272.

Hjellming, R. M. and Basart, J. P. 1982, in *An Introduction to the NRAO Very Large Array*, ed. R. M. Hjellming, NRAO, Charlottesville, Virginia.

Ho, L., Filippenko, A. V. and Sargent, W. L. W. 1993, *Ap.J. Suppl.*, **98**, 477.

Högbom, J. A. 1974, *Astr. Ap. Suppl.*, **15**, 417.

Hua, C. T., Donas, J. and Doan, H. H. 1980, *Astr. Ap.*, **90**, 8.

Huchtmeier, W. K. and Richter, O.-G. 1989, *A General Catalog of H I Observations of Galaxies*, Springer-Verlag, New York.

Hummel, E., van der Hulst, J. M., Kennicutt, R. C., Jr., Keel, W. C. 1990, *Astr. Ap.*, **236**, 333.

Hunter, J. H., Jr., Ball, R., Huntley, J. M., England, M. N. and Gottesman, S. T. 1988, *Ap.J.*, **324**, 721.

Hunter, J. H., Jr. and Gottesman, S. T. 1996, in *Barred Galaxies*, eds. R. Buta, D. A. Crocker and B. G. Elmegreen, ASP Conf. series, **91**, 398.

Huntley, J. M. 1977, Ph.D. thesis, University of Virginia.

Huntley, J. M., Sanders, R. H. and Roberts, W. W., Jr. 1978, *Ap.J.*, **221**, 521.

Hurt, R. L., Turner, J. L. and Ho, P. T. P. 1996, *Ap.J.*, **466**, 135.

Ishizuki, S., Kawabe, R., Ishiguro, M., Okumara, S. K., Morita, K.-I., Chikada, Y., Kasuga, T. and Doi, M. 1990a, *Ap.J.*, **355**, 436.

Ishizuki, S., Kawabe, R., Ishiguro, M., Okumara, S. K., Morita, K.-I. 1990b, *Nature*, **344**, 224.

Israel, F. P. 1988, in *Millimetre and Submillimetre Astronomy*, eds. R. D. Wolstencroft and W. B. Burton, Kluwer, Dordrecht, Netherlands, p. 281.

Jörsäter, S. 1984, Ph.D. thesis, Stockholm University.

Jörsäter, S. and van Moorsel, G. A. 1995, *A.J.*, **110**, 2037.

Karachentseva, V. E. 1973, *Soob. Spets. Astrof. Obs.*, **No. 8.**, 3.

Katz, N. 1992, *Ap.J.*, **391**, 502.

Kaufmann, D. E. and Contopoulos, G. 1996, *Astr. Ap.*, **309**, 381.

Keel, W. C. 1983a, *Ap.J. Suppl.*, **52**, 229.

Keel, W. C. 1983b, *Ap.J.*, **269**, 466.

Kenney, J. D. P. 1996a, in *Barred Galaxies*, eds. R. Buta, D. A. Crocker and B. G. Elmegreen, ASP Conf. series, **91**, 150.

Kenney, J. D. P. 1996b, in *The Interstellar Medium in Galaxies*, ed. J. M. van der Hulst, Kluwer, Dordrecht, Netherlands.

Kenney, J. D. P., Carlstrom, J. E. and Young, J. S. 1993, *Ap.J.*, **418**, 687.

Kenney, J. D. P. and Lord, S. D. 1991, *Ap.J.*, **381**, 118.

Kenney, J. D. P. and Young, J. S. 1989, *Ap.J.*, **344**, 171.

Kenney, J. D. P., Wilson, C. D., Pisano, D. J. and Scoville, N. Z. 1996, *Ap.J.*, submitted.

Kenney, J. D. P., Wilson, C. D., Scoville, N. Z., Devereux, N. A. and Young, J. S. 1992, *Ap.J. Let.*, **395**, 79.

Kennicutt, R. C., Jr. 1989, *Ap.J.*, **344**, 685.

Kennicutt, R. C., Jr. 1990, in *The Interstellar Medium in Galaxies*, eds. H. A. Thronson and J. M. Shull, Kluwer, Dordrecht, Netherlands, p. 405.

Kennicutt, R. C., Jr. and Kent, S. M. 1983, *A.J.*, **88**, 1094.

Knapen, J. H. 1992, Ph.D. thesis, Universidad de La Laguna.

Knapen, J. H., Beckman, J. E. 1996, *M.N.R.A.S.*, **283**, 251.

Knapen, J. H., Beckman, J. E., Heller, C. H., Shlosman, I. and de Jong, R. S. 1995, *Ap.J.*, **454**, 623.

Kuijken, K. and Merrifield M. R. 1995a, *Ap.J. Let.*, **443**, 13.

Kuijken, K. and Merrifield M. R. 1995b, *M.N.R.A.S.*, **274**, 933.

Kutner, M. L. 1984, *Fund. Cosmic Physics*, **9**, 233.

Laine, S. and Gottesman, S. T. 1996, in *Barred Galaxies*, eds. R. Buta, D. A. Crocker and B. G. Elmegreen, ASP Conf. series, **91**, 495.

Landini, M., Natta, A., Oliva, E., Salinari, P. and Moorwood, A. F. M. 1984, *Astr. Ap.*, **134**, 384.

Landolt, A. U., 1983, *A.J.*, **88**, 439.

Lewis, B. M. 1984, *Ap.J.*, **285**, 453.

Lindblad, P. A. B. 1996, Ph.D. thesis, Stockholm University.

Lindblad, P. O. and Jörsäter, S. 1988, in *Evolution of Galaxies*, ed. J. Palous, Czech. Acad. of Sciences, Czechoslovakia, p. 289.

Lindblad, P. A. B. and Kristen, H. 1996, *Astr. Ap.*, **313**, 733.

Lindblad, P. O. and Lindblad, P. A. B. 1994, in *The Gaseous and Stellar Disks of the Galaxy*, ed. I. King, ASP Conf. series, **66**, 29.

Lindblad, P. A. B., Lindblad, P. O. and Athanassoula, E. 1996, *Astr. Ap.*, **313**, 65.

Lo, K. Y., Berge, G. L., Claussen, M. J., Heiligman, G. M., Leighton, R. B., Masson, C. R., Moffet, A. T., Phillips, T. G., Sargent, A. I. and Scott, S. L. 1984, *Ap.J. Let.*, **282**, 59.

Long, K. 1991, Ph.D. thesis, Princeton University.

Lord, S. D. 1991 and Kenney, J. D. P., *Ap.J.*, **381**, 130.

Lynden-Bell, D. 1979, *M.N.R.A.S.*, **187**, 101.

Martin, P. 1996, in *Barred Galaxies*, eds. R. Buta, D. A. Crocker and B. G. Elmegreen, ASP Conf. series, **91**, 70.

Martin, P. and Roy, J.–R. 1994, *Ap.J.*, **424**, 599.

Martin, P. and Roy, J.–R. 1995, *Ap.J.*, **445**, 161.

Merritt, D. 1996, *A.J.*, **112**, in press.

Mihalas, D. and Routly, P. 1968 *Galactic Astronomy*, W. H. Freeman and Company, San Francisco.

Mihalas, D. and Binney, J. 1981 *Galactic Astronomy*, W. H. Freeman and Company, New York.

Mihos, J. C. and Hernquist, L. 1994a, *Ap.J. Let.*, **425**, 13.

Mihos, J. C. and Hernquist, L. 1994b, *Ap.J.*, **437**, 611.

Miles, J. W., Houck, J. R. and Hayward, T. L. 1994, *B.A.A.S*, **26**, 59.09.

Mirabel, I. F. and Sanders, D. B. 1988, *Ap.J.*, **335**, 104.

Monaghan, J. J. 1992, *Ann. Rev. Astron. Astrophys.*, **30**, 543.

Moore, E. M. and Gottesman, S. T. 1995, *Ap.J.*, **447**, 159.

Mulder, P. S. 1995a, Ph.D. thesis, University of Groningen.

Mulder, P. S. 1995b, *Astr. Ap.*, **303**, 57.

Navarro, J. F. and White, S. D. M. 1993, *M.N.R.A.S.*, **265**, 271.

Neff, S. G. and Hutchings, J. B. 1992, *A.J.*, **103**, 1746.

Nilson, P. 1973, *Uppsala General Catalogue of Galaxies*, Royal Soc. Sci. Uppsala, Uppsala, Sweden (UGC).

Noguchi, M. 1987, *M.N.R.A.S.*, **228**, 635.

Noguchi, M. 1988, *Astr. Ap.*, **203**, 259.

Odewahn, S. C. 1994, *A.J.*, **107**, 1320.

Odewahn, S. C. 1996, in *Barred Galaxies*, eds. R. Buta, D. A. Crocker and B. G. Elmegreen, ASP Conf. series, **91**, 30.

Okamura, S. 1978, *P.A.S.J.*, **30**, 91.

Padin, S., Scott, S. L., Woody, D. P., Scoville, N. Z. and Seling, T. V. 1991, *P.A.S.P.*, **103**, 461.

Pasha, I. I. and Smirnov, M. A. 1982, *Ap. Space Sci.*, **86**, 215.

Pence, W. and Blackman, C. P. 1984, *M.N.R.A.S.*, **207**, 9.

Perley, R. A., Schwab, F. R. and Bridle, A. H. *Synthesis Imaging in Radio Astronomy*, ASP Conf. series, **6**.

Phillips, A. C. 1996, in *Barred Galaxies*, eds. R. Buta, D. A. Crocker and B. G. Elmegreen, ASP Conf. series, **91**, 44.

Phookun, B. 1993, Ph.D. thesis, University of Maryland.

Phookun, B., Mundy, L. G., Teuben, P. J. and Wainscoat, R. J. 1992, *Ap.J.*, **400**, 516.

Phookun, B., Vogel, S. N. and Mundy, L. G. 1993, *Ap.J.*, **418**, 113.

Phookun, B. and Mundy, L. G. 1995, *Ap.J.*, **453**, 154.

Pogge, R. W. 1989, *Ap.J. Suppl.*, **71**, 433.

Pompea, S. M. and Rieke, G. H. 1990, *Ap.J.*, **356**, 416.

Quillen, A., Frogel, J. A. and Gonzalez, R. A. 1994, *Ap.J.*, **437**, 162.

Quillen, A., Frogel, J. A., Kenney, J. D. P., Pogge, R. W. and DePoy, D. L. 1995, *Ap.J.*, **441**, 549.

Rand, R. J. 1995, *A.J.*, **109**, 2444.

Regan, M. W. and Gruendl, R. A. 1995, in *Astronomical Data Analysis Software and Systems IV*, eds. R. A. Shaw, H. E. Payne and J. J. E. Hayes, ASP Conf. series, **77**, 335.

Regan, M. W. and Vogel, S. N. 1995, *Ap.J. Let.*, **452**, 21.

Regan, M. W., Vogel, S. N. and Teuben, P. J. 1997, *Ap.J. Let.*, submitted.

Richter, O.-G. and Huchtmeier, W. K. 1982, *Astr. Ap.*, **109**, 155.

Richter, O.-G. and Sancisi, R. 1994, *Astr. Ap.*, **290**, L9.

Rieke, G. H., Lebofsky, M. J., Thompson, F. J. and Tokunaga, A. T. 1980, *Ap.J.*, **238**, 24.

Rix, H.-W. 1993, *P.A.S.P*, **105**, 999.

Rix, H.-W., Rieke, M. J. 1993, *Ap.J.*, **418**, 123.

Roberts, W. W., Jr., Huntley, J. M. and van Albada, G, D. 1979, *Ap.J.*, **233**, 67.

Roche, P. F., Aitken, D. K., Smith, C. H. and Ward, M. J. 1991, *M.N.R.A.S.*, **248**, 606.

Rohlfs, K. 1977, *Lectures on Density Wave Theory*, in *Lecture Notes in Physics*, eds. J. Ehlers, K. Hepp, R. Kippenhahn, H. A. Weidenmüller and J. Zittartz, Springer-Verlag, Berlin.

Rohlfs, K. 1986, *Tools of Radio Astronomy*, Springer-Verlag, Berlin.

Sakamoto, K., Okumura, S., Minezaki, T., Kobayashi, Y. and Wada, K. 1995, *A.J.*, **110**, 2075.

Sandage, A. and Tammann, G. A. 1987, *A Revised Shapley-Ames Catalog of Bright Galaxies, 2 ed.*, Carnegie Inst., Washington (RSA).

Sanders, R. H. and Huntley, J. M. 1976, *Ap.J.*, **209**, 53.

Sanders, R. H. and Prendergast, K. H. 1974, *Ap.J.*, **188**, 489.

Sanders, R. H. and Tubbs, J. M. 1980, *Ap.J.*, **235**, 803.

Schwarz, M. P. 1981, *Ap.J.*, **247**, 77.

Schwarz, M. P. 1984, *M.N.R.A.S.*, **209**, 93.

Schwarz, M. P. 1985, *M.N.R.A.S.*, **212**, 677.

Scoville, N. Z., Carlstrom, C. J., Chandler, J. A., Phillips, J. A., Scott, S. L., Tilanus, R. P. J., and Wang, Z. 1993, *P.A.S.P.*, **105**, 1482.

Scoville, N. Z., Yun, M. S., Clemens, D. P., Sanders, D. B. and Waller, W. H. 1987, *Ap.J. Suppl.*, **63**, 821.

Sellwood, J. A. 1981, *Astr. Ap.*, **99**, 362.

Sellwood, J. A. 1987, *Ann. Rev. Astron. Astrophys.*, **25**, 151.

Sellwood, J. A. and Debattista, V. P. 1996, in Proceedings of the Nobel Symposium 98, *Barred Galaxies and Circumnuclear Activity*, eds. A. Sandquist and P. O. Lindblad, *Lecture Notes in Physics*, **474**, Springer-Verlag, Heidelberg, Germany, p. 43.

Sellwood, J. A. and Sparke, L. 1988, *M.N.R.A.S.*, **231**, 25P.

Sellwood, J. A. and Wilkinson, 1993, *Rep. Prog. Phys.*, **56**, 173.

Sempere, M. J., Combes, F. and Casoli, F. 1995a, *Astr. Ap.*, **299**, 371.

Sempere, M. J., Garcia-Burillo, S., Combes, F. and Knapen, J. H. 1995b, *Astr. Ap.*, **296**, 45.

Sérsic, J. L. and Pastoriza, M. 1965, *P.A.S.P.*, **77**, 287.

Sérsic, J. L. and Pastoriza, M. 1967, *P.A.S.P.*, **79**, 152.

Shlosman, I., Frank, J. and Begelman, M. 1989, *Nature*, **338**, 45.

Shlosman, I., Begelman, M. and Frank, J. and 1990, *Nature*, **345**, 679.

Shlosman, I. and Noguchi, M. 1993, **414**, 474.

Shostak, G. S. 1978, *Astr. Ap.*, **68**, 321.

Simpson, C. S. 1995, Ph.D. thesis, University of Florida.

Sodroski, T. J., Odegard, N., Dwek, E., Hauser, M. G., Franz, B. A., Freedman, I., Kelsall, T., Wall, W. F., Berriman, G. B., Odenwald, S. F., Bennett, C., Reach, W. T. and Weiland, J. L. 1995, *Ap.J.*, **452**, 262.

Sofue, Y. 1994, *Ap.J.*, **423**, 207.

Sofue, Y. 1996, in *Formation and Evolution of Galaxies*, eds. W. Duschl and N. Arimoto, Springer, Heidelberg, Germany.

Sørensen, S.-A., Matsuda, T. and Fujimoto, M. 1976, *Ap. Space Sci.*, **43**, 491.

Spitzer, L. 1978, *Physical Processes In The Interstellar Medium*, John Wiley & Sons, Inc., New York.

Sygnet, J. F., Tagger, M., Athanassoula, E. and Pellat, R. 1988, *M.N.R.A.S.*, **232**, 733.

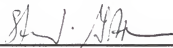Tagger, M., Sygnet, J. F., Athanassoula, E. and Pellat, R. 1987, *Ap.J. Let.*, **318**, 43.

Telesco, C. M., Campins, H., Joy, M., Dietz, K. and Decher, R. 1991, *Ap.J.*, **369**, 135.

Telesco, C. M., Dressel, L. L. and Wolstencroft, R. D. 1993, *Ap.J.*, **414**, 120.

Telesco, C. M. and Gatley, I. 1984, *Ap.J.*, **284**, 557.

Telesco, C. M. and Gezari, D. Y. 1992, *Ap.J.*, **395**, 461.

Teuben, P. J. and Sanders, R. H. 1985, *M.N.R.A.S.*, **212**, 257.

Teuben, P. J., Sanders, R. H., Atherton, P. J. and van Albada, G. D. 1986, *M.N.R.A.S.*, **221**, 1.

Thakar, A. R. and Ryden, B. S. 1996, *Ap.J.*, **461**, 55.

Toomre, A. 1964, *Ap.J.*, **139**, 1217.

Toomre, A. 1981, in *The Structure and Evolution of Normal Galaxies*, eds. S. M. Fall and D. Lynden-Bell, Cambridge University Press, Cambridge, Great Britain, p. 111.

Toomre, A. and Toomre, J. 1972, *Ap.J.*, **178**, 623.

Tremaine, S. and Weinberg, M. D. 1984, *Ap.J. Let.*, **282**, 5.

Tubbs, A. D. 1982, *Ap.J.*, **255**, 458.

Turner, J. L. 1994, in *Mass-Transfer Induced Activity in Galaxies*, ed. I. Shlosman, Cambridge University Press, Cambridge, Great Britain, p. 90.

Turner, J. L. and Ho, P. T. P. 1994, *Ap.J.*, **421**, 122.

Turnshek, D. A., Bohlin, R. C., Williamson, R. L., II, Lupie, O. L., Koornneef, J. and Morgan, D. H. 1990, *A.J.*, **99**, 1243.

van Albada, D. G. and Roberts, W. W., Jr. 1981, *Ap.J.*, **246**, 740.

van der Hulst, J. M., Terlouw, J. P., Begeman, K., Zwitser, W. and Roelfsema, P. R. 1992, in *Astronomical Data Analysis Software and Systems I*, eds. D. M. Worall, C. Biemesderfer and J. Barnes, ASP Conf. series, **25**, p. 131.

van der Kruit, P. C 1973, *Astr. Ap.*, **29**, 231.

van der Kruit, P. C., Oort, J. H. and Mathewson, D. S. 1972, *Astr. Ap.*, **21**, 169.

van Dishoeck, E. F. 1988, in *Millimetre and Submillimetre Astronomy*, eds. R. D. Wolstencroft and W. B. Burton, Kluwer, Dordrecht, Netherlands, p. 117.

Varela, A. M., Aguerri, J. A. L., Prieto, M. and Munoz-Tunon, C. 1996, in *Barred Galaxies*, eds. R. Buta, D. A. Crocker and B. G. Elmegreen, ASP Conf. series, **91**, 123.

Verter, F. and Hodge, P. 1995, *Ap.J.*, **446**, 616.

Vogel, S. N., Kulkarni, S. R. and Scoville, N. Z. 1988, *Nature*, **334**, 402.

Vogel, S. N., Weymann, R., Rauch, M. and Hamilton, T. 1995, *Ap.J.*, **441**, 162.

Wada, K. 1994, *P.A.S.J.*, **46**, 165.

Wada, K. 1996, in *Barred Galaxies*, eds. R. Buta, D. A. Crocker and B. G. Elmegreen, ASP Conf. series, **91**, 439.

Wada, K. and Habe, A. 1992, *M.N.R.A.S.*, **258**, 82.

Wada, K. and Habe, A. 1995, *M.N.R.A.S.*, **277**, 433.

Warner, P. J., Wright, M. C. H. and Baldwin, J. E. 1973, *M.N.R.A.S.*, **163**, 163.

Wilson, C. D. 1995, *Ap.J. Let.*, **448**, 97.

Worthey, G. 1994, *Ap.J. Suppl.*, **95**, 107.

Wozniak, H., Friedli, D., Martinet, L., Martin, P. and Bratschi, P. 1995, *Astr. Ap. Suppl.*, **111**, 115.

Young, J. S. and Devereux, N. A. 1991, *Ap.J.*, **373**, 414.

Young, J. S., Schloerb, F. B., Kenney, J. D. P. and Lord, S. D. 1986, *Ap.J.*, **304**, 443.

Young, J. S. and Scoville, N. Z. 1991, *Ann. Rev. Astron. Astrop.*, **29**, 581.

Young, J. S., Xie, S., Kenney, J. D. P. and Rice, W. L. 1989, *Ap.J. Suppl.*, **70**, 699.
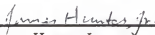
BIOGRAPHICAL SKETCH

Seppo Jalmari Laine was born on March 9, 1965, in Raisio, Finland. He obtained his High School Diploma in May 1984 and served the mandatory military duty 1984–1985, earning the rank of Second Lieutenant. He then started academic studies at the University of Turku, Turku, Finland. He earned the degree of Candidate of Philosophy in May 1990, majoring in astronomy. The same summer he left Finland for graduate study in astronomy at the University of Florida, where he has enjoyed the sunny and warm Florida weather until now. Seppo Laine is an avid ice-hockey enthusiast and is known among the astronomy students for his sweet honey parties, celebrating his favorite team TPS.

I certify that I have read this study and that in my opinion it conforms to acceptable standards of scholarly presentation and is fully adequate, in scope and quality, as a dissertation for the degree of Doctor of Philosophy.

Stephen T. Gottesman, Chair
Professor of Astronomy

I certify that I have read this study and that in my opinion it conforms to acceptable standards of scholarly presentation and is fully adequate, in scope and quality, as a dissertation for the degree of Doctor of Philosophy.

James Hunter, Jr.
Professor of Astronomy

I certify that I have read this study and that in my opinion it conforms to acceptable standards of scholarly presentation and is fully adequate, in scope and quality, as a dissertation for the degree of Doctor of Philosophy.
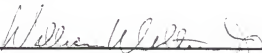
Haywood Smith, Jr.
Associate Professor of Astronomy

I certify that I have read this study and that in my opinion it conforms to acceptable standards of scholarly presentation and is fully adequate, in scope and quality, as a dissertation for the degree of Doctor of Philosophy.

Humberto Campins
Associate Professor of Astronomy

I certify that I have read this study and that in my opinion it conforms to acceptable standards of scholarly presentation and is fully adequate, in scope and quality, as a dissertation for the degree of Doctor of Philosophy.

William Weltner, Jr.
Professor of Chemistry

I certify that I have read this study and that in my opinion it conforms to acceptable standards of scholarly presentation and is fully adequate, in scope and quality, as a dissertation for the degree of Doctor of Philosophy.

Isaac Shlosman
Professor of Physics and Astronomy
University of Kentucky

This dissertation was submitted to the Graduate Faculty of the Department of Astronomy in the College of Liberal Arts and Sciences and to the Graduate School and was accepted as partial fulfillment of the requirements for the degree of Doctor of Philosophy.

December 1996

Dean, Graduate School